



Long Range Order in Ferroelectric and Antiferroelectric
Perovskites Meets Large Scale Density Functional Theory

By Jack S. Baker^{1,2}



¹Department of Physics and Astronomy, University College London

²London Centre for Nanotechnology

Supervised by Prof. David R. Bowler^{1,2}

and Dr. Pavlo Zubko^{1,2}

A dissertation submitted in partial fulfillment of the requirements for the degree of **Doctor of
Philosophy of University College London**

Declaration

I, Jack S. Baker confirm that the work presented in this thesis is my own. Where information has been derived from other sources, I confirm that this has been indicated in the thesis.

Jack S. Baker
November, 2020

Abstract

The technological applications of the ferroelectric and antiferroelectric perovskite oxides are extensive. With use cases ranging from ultrafast read/write memories to high energy density storage devices, they are the subject of a vast body of research. In particular, these materials have a rich history of discovery using *ab initio* techniques based on density functional theory (DFT). While conventional implementations of DFT can be used to great avail, unfortunately, calculations become prohibitively computationally expensive for simulations involving more than a few hundred atoms; a situation often encountered. Many then migrate to lower levels of theory embracing the mantra of ‘multiscale modelling’. While this in principle *can* be a good idea, many move away from DFT too soon; neglectful of the latest advancements in large scale DFT promising to restore quantum mechanical accuracy over larger length scales.

The scope of this thesis is tripartite. Firstly, we re-examine the $\text{Pb}(\text{Ti}, \text{Zr}, \text{Hf})\text{O}_3$ isoelectronic series and the archetypal piezoelectric solid solution $\text{PbZr}_{1-x}\text{Ti}_x\text{O}_3$ (PZT) by means of a comparative lattice dynamical study. Dynamical instabilities at q away from high symmetry points indicate competitive distortions over longer length scales than previously expected. Studying their condensation with conventional DFT can then become of a prohibitive expense. Further, a popular method designed to sidestep large scale simulations in some systems - the virtual crystal approximation - is found to be insufficient to describe the character of these distortions. Remarkably, when examining the phonon dispersions of antiferroelectric PbZrO_3 and PbHfO_3 , they are found to be dynamically unstable and suggest that a $Pnma$ structure is more stable than the established $Pbam$. This stability is corroborated at the LDA, GGA and meta-GGA levels suggesting a small modification to the known ground state.

Our second goal is to demonstrate the readiness of large scale DFT to accurately simulate the perovskite oxides. Reformulating DFT in terms of the Kohn-Sham density matrix, we use the CONQUEST code to study the structural and electronic accuracy resulting from the use of basis sets of pseudoatomic orbitals (PAOs) compared to plane wave pseudopotential calculations. Using PbTiO_3 , PbZrO_3 , PZT and other technologically important materials as test cases, we find that a carefully designed basis of PAOs can rival the accuracy of plane wave calculations for lattice constants, bulk moduli, charge densities and Bader-assigned ionic charges.

Equipped now with a method of proven robustness, we advance to our final goal: to target otherwise intractable problems for standard DFT. Simulating thousands of atoms, we investigate

ferroelectric domain morphologies in low-dimensional PbTiO_3 films finding properties ripe for exploitation in new functional devices. When mounted on a SrTiO_3 substrate, we see the emergence of exotic chiral textures as a result of an internal bias field born of the compositionally broken inversion symmetry present in any film/substrate system. Strong coupling of local polar modes to surface antiferrodistortions drives a previously unknown $p(2 \times \Lambda)$ surface reconstruction; demonstrating unequivocally the local compliance of the two order parameters. Finally, we investigate the interaction of engineered surface trenches with the domain structure and alignment of domain walls informing advances in domain wall nanoelectronics.

Impact statement

Solids condensing in the simple perovskite crystal structure give rise to a stunningly broad array of phenomena. Many such phenomena are suited for exploitation in industry and novel applications in nanotechnology. The ferroelectric & antiferroelectric perovskites treated in this thesis are no exception. Lead zirconate promises use in next-generation energy storage devices and thin films of lead titanate allow researchers to explore the formation and nature of ferroelectric domains. When combined in an alloy, they form lead zirconate titanate; industry's favourite piezoelectric.

Using simulations based on quantum theory, we show that our understanding of these materials is incomplete. We show that the crystal structure distorts over longer length scales than was previously thought. Importantly, in the case of lead zirconate and lead hafnate, these distortions are found to contribute to the stabilisation of the crystal structure. In turn, this informs a new candidate for the ground state, different to the one reported in the literature (which has been established since the 1980's). Some of these distortions can cause problems for the quantum mechanical simulation method. This is since, conventionally, the calculations take a prohibitively long time to complete when we increase the amount of material we must study. We find that adopting a non-conventional implementation of the theory circumvents this problem.

After proving the validity of our new method, we use it to study lead titanate on the nanoscale; fabricated as an ultrathin film. Our simulations provide new insights for the manipulation of ferroelectric domains and the domain walls. These findings have clear applications for new low-dimensional functional devices, especially in the field of domain wall nanoelectronics. In doing so, we also demonstrate to all that accurate simulations based on quantum theory can be applied to the perovskites on length scales longer than previously reported. The program for doing so - CONQUEST - is now, after 20 years of development, freely and publicly available. This program shows promise to be widely adopted in the community.

List of publications

The below publications were completed in the duration of this Ph.D or are in preparation. They are given in order of appearance of their content in this thesis:

A. Nakata, **J. S. Baker**, S. Y. Mujahed, J. T. L. Poulton, S. Arapan, J. Lin, Z. Raza, S. Yadav, L. Truffandier, T. Miyazaki, and D. R. Bowler, “[Large scale and linear scaling DFT with the CONQUEST code](#),” *The Journal of Chemical Physics*, vol. 152, p. 164112, Apr. 2020.

J. S. Baker and D. R. Bowler, “[First-principles soft-mode lattice dynamics of \$\text{PbZr}_{0.5}\text{Ti}_{0.5}\text{O}_3\$ and shortcomings of the virtual crystal approximation](#),” *Physical Review B*, vol. 100, p. 224305, Dec. 2019.

J. S. Baker, G. Catalan, J. K. Shenton and D. R. Bowler, “Is PbZrO_3 a *Pnma* antiferroelectric?”, in preparation (full title and author list pending).

D. R. Bowler, **J. S. Baker**, J. T. L. Poulton, S. Y. Mujahed, J. Lin, S. Yadav, Z. Raza, and T. Miyazaki, “[Highly accurate local basis sets for large-scale DFT calculations in CONQUEST](#),” *Japanese Journal of Applied Physics*, vol. 58, p. 100503, Oct. 2019.

J. S. Baker, T. Miyazaki, and D. R. Bowler, “[The pseudoatomic orbital basis: electronic accuracy and soft-mode distortions in \$\text{ABO}_3\$ perovskites](#),” *Electronic Structure*, vol. 2, p. 025002, June 2020.

J. S. Baker and D. R. Bowler, “[Polar Morphologies from First Principles: \$\text{PbTiO}_3\$ Films on \$\text{SrTiO}_3\$ Substrates and the \$p\(2 \times \Lambda\)\$ Surface Reconstruction](#),” *Advanced Theory and Simulations*, vol. 3, p. 2000154, Sept. 2020.

J. S. Baker and D. R. Bowler, “Ferroelectric domain wall alignment with engineered surface trenches in ultrathin films”, in preparation.

The below two publications were completed in the duration of the Ph.D but are *not* relevant to the content of this thesis. They are instead related to education and inclusion in science; two topics I believe to be of a high importance:

C. Sousa-Silva, L. K. McKemmish, K. L. Chubb, M. N. Gorman, **J. S. Baker**, E. J. Barton, T. Rivlin, and J. Tennyson, “[Original Research By Young Twinkle Students \(ORBYTS\): when can students start performing original research?](#),” *Physics Education*, vol. 53, p. 015020, Dec 2017.

L. K. McKemmish, K. L. Chubb, T. Rivlin, **J. S. Baker**, M. N. Gorman, A. Heward, W. Dunn, and M. Tessenyi, “[Bringing pupils into the ORBYTS of research](#),” *Astronomy & Geophysics*, vol. 58, pp. 5.11–5.11, Oct. 2017.

Acknowledgements

There are a great many people who I would like to acknowledge for their help and support throughout this Ph.D. (and my life to date). I will have no doubt forgotten many of these, so I apologise in advance for any glaring omissions.

I give thanks firstly to my close family including Francesca Lovett, Richard Lovett, Adam Baker and Mark Baker for their patience and support during my long twelve year stint in full time education. I am grateful to my caring girlfriend Kirshita Seevaratnam, *Kirshi*, for being a prime motivator in the completion of this thesis and putting up with my more-than-usual shortness during this stressful period.

I've been lucky enough to have experienced many great academic mentors over the years (before undertaking this Ph.D.). I send thanks to Frank Marsh (an excellent Physics teacher from Thorpe St. Andrew high-school), Steve Gurman (the master of Physics pedagogy at the University of Leicester), Paul Howes (who amongst other things, knows a lot about bees) and Alex Bugnar (my mentor during my time at Diamond Light Source).

I would also like to acknowledge the insight gained from academic (ok, mostly non-academic) conversations within the walls of UCL office A22 with my peers Shereif Mujahed, Kane Shenton, Jack Poulton, Alex Broad, Anu Vibhakar, Jared Jeyaretnam and Chathurangi Kumarasinghe.

I extend my gratitude to my international collaborators within the CONQUEST team for hosting me overseas and making feel so welcome. This includes Tsuyoshi Miyazaki, Ayako Nakata and Lionel Trufflandier.

Thank you to my peers in the ORBYTS (original research by young twinkle students) program who made it such a worthwhile experience in the early years of my Ph.D. I am particularly grateful to William Whyatt, Laura McKemmish and William Dunn for their efforts in this project.

I have reached out to many experts in the field in the duration of this Ph.D., many of whom have provided helpful insights. Thanks to Pavlo Zubko (my second supervisor), Marios Hadjimichael, Ron Cohen, Pablo Aguado-Puente, Mike Glazer, Gustau Catalan and Roman Burkovsky.

Finally, I am forever indebted to my excellent supervisor David Bowler, *Dave*, for his expert guidance and technical contributions to the CONQUEST code (although I thank the other developers also!) which made much of this thesis possible. Above all, thanks for listening to my latest harebrained schemes and tolerating my nocturnal working habits.

Contents

1	Introduction	27
2	An Overview of the Perovskite Oxides	33
2.1	The ABO_3 Factotum and Accomplices	33
2.2	Ferroelectricity	37
2.2.1	Signatures of ferroelectricity	37
2.2.2	A brief history	38
2.3	Antiferroelectricity	41
2.3.1	An even briefer history	42
2.4	The phenomenological Landau-Devonshire theory	43
2.5	The modern theory of electrical polarisation	47
2.6	Lattice dynamics	52
2.6.1	An overview of crystal vibrations	52
2.6.2	Soft modes	56
2.6.2.1	A microscopic theory of ferroelectricity	56
2.6.2.2	Some practical implications at 0K	57
2.7	Anomalous dynamical charges	59
2.8	Ferroelectric domain structures	60
2.9	Alignment to surface features	64
3	Theoretical Background	69
3.1	An introduction to the quantum many-body problem	69
3.2	Fundamentals of density functional theory	71
3.2.1	The Hohenberg-Kohn theorems	71
3.2.2	Independent orbitals: the Kohn-Sham <i>ansatz</i>	72
3.2.3	Exchange and correlation	75
3.3	Periodic systems: a conventional implementation	76
3.3.1	Plane waves	77
3.3.2	Pseudopotentials	78
3.3.3	Projector augmented waves	80

3.4	Scaling upwards	81
3.4.1	Limitations of conventional implementations	82
3.4.2	A local basis: pseudoatomic orbitals	83
3.4.3	The CONQUEST approach	85
3.4.4	Diagonalisation for small systems	86
3.4.5	Contracting the Hamiltonian: multi-site support functions	88
3.4.6	The $\mathcal{O}(N)$ method	90
3.4.6.1	Canonical purification	93
3.4.6.2	Density matrix minimisation	94
3.5	Phonons	95
3.5.1	Density functional perturbation theory	96
3.5.2	The finite displacement method	100
4	The Pb(Ti, Zr, Hf)O₃ Isoelectronic Series: a Lattice Dynamical Study	101
4.1	Introduction	102
4.2	Theoretical method	105
4.3	Results: PTO, PZO & PZT	108
4.3.1	Parent structures	108
4.3.2	Phonon dispersion and density of states	111
4.3.2.1	PTO & PZO	112
4.3.2.2	Virtual crystal approximation & PZT I	117
4.3.2.3	PZT II & III	118
4.3.2.4	PZT IV	121
4.3.2.5	PZT V & VI	122
4.4	PZO & PHO: a new ground state candidate	124
4.4.1	Comparison of phonon dispersions	124
4.4.2	The antiferroelectric <i>Pnma</i> phase	127
4.5	Summary	132
5	Pseudoatomic Orbitals: Electronic and Structural Accuracy	135
5.1	Introduction	136
5.2	Theoretical method	139
5.2.1	Simulation details	139
5.2.2	Comparative metrics	142
5.2.3	Generation of pseudoatomic orbitals	143
5.3	Results	145
5.3.1	Equilibrium volumes and bulk moduli	145
5.3.2	Charge density differences	149
5.3.3	Bader analysis	151

5.3.4	Soft mode distortions	156
5.3.5	Basis set optimisation	162
5.4	Summary	164
6	Ultrathin PbTiO₃ Films: Substrate Effects and Surface Defects	167
6.1	Introduction	168
6.2	Theoretical method	172
6.2.1	General details	172
6.2.2	Multi-site support functions	172
6.2.3	Linear scaling	175
6.2.4	The local polarisation	176
6.2.5	Supercell configurations: PTO on STO	178
6.2.5.1	Paraelectric	180
6.2.5.2	Monodomain in-plane ferroelectric	182
6.2.5.3	Polydomain ferroelectric	182
6.2.6	Supercell configurations: trenches on free standing PTO	183
6.2.6.1	Trenches parallel to domain walls	184
6.2.6.2	Trenches perpendicular to domain walls	185
6.3	Results: PTO on STO	187
6.3.1	Competing phases	187
6.3.2	Polarisation morphologies	189
6.3.3	The $p(2 \times \Lambda)$ surface reconstruction	194
6.4	Results: trenches on free standing PTO	196
6.4.1	The most favourable orientation	196
6.4.2	Depolarising field minimisation	197
6.4.3	Strain fields	201
6.5	Summary and Conclusions	203
7	Conclusions and Outlook	209
A	Appendices	215
A.1	Plane waves and dynamical instabilities,	215
A.2	Pseudoatomic orbitals: bulk and thin films	222
	Bibliography	227

List of Figures

2.1	The ABO_3 prototype crystal structure (upper centre) and a variety of the possible order parameters/phases that can arise simply by engineering the A and B site cations. The VESTA (v3) crystal structure visualisation program [86] is used to create crystal structure images in this figure. Indeed, this program is used <i>heavily</i> throughout this thesis, so we thank the developers here at its first use.	35
2.2	The origin of negative capacitance in dielectric/ferroelectric heterostructure capacitors. a) An illustration of a dielectric/ferroelectric capacitor heterostructure. b) The free energy as a function of polarisation within the ferroelectric and dielectric layers as well as the combined heterostructure.	36
2.3	The hysteresis curves for a ferroelectric (a) and antiferroelectric (b) material under poling by a uniform electric field. Important values of the polarisation and electric field are labelled: the saturating polarisation P_{sat} , the remenant polarisation P_r and the coercive field E_c	38
2.4	A timeline for the early years of ferroelectric research detailing the simplest known ferroelectric compound versus the year. We see clearly then that the known prototype simplified with time leaving us with the ABO_3 drosophila we have today.	39
2.5	The $Pbam$ crystal structure of PZO/PHO from two different viewing angles. The left figure has arrows on the Pb sites indicating the two-left two-right antipolar displacement pattern. The right figure allows one to more easily see the antiphase rotations of the Zr/HfO ₆ octahedra about the $[1\bar{1}0]$ axis.	43
2.6	The free energy density (as a function of polarisation), spontaneous polarisation and dielectric susceptibility/stiffness (all as a function of temperature) for second (i - iii) and first (iv - vi) order transitions as predicted by LD theory.	45
2.7	A polar and non-polar infinite 1D ionic lattice. When calculating the polarisation, we see that it is many valued; dependant on our choice of unit cell.	48

2.8	The phonon dispersion curves of $Pm\bar{3}m$ PTO as calculated with density functional perturbation theory using the projector augmented wave method [152] and the LDA functional of Perdew and Wang [153]. The ionic displacement patterns derived from the eigendisplacements of the soft modes are displayed below the dispersion. a) The M_3^+ mode featuring in-phase $a^0a^0c^+$ rotations. b) The Γ_4^- mode describing the ferroelectric distortion. c) The R_4^+ mode featuring anti-phase $a^0a^0c^-$ rotations.	54
2.9	A neutron of wavevector $\mathbf{q} = (q_x, 0, 0)$, $q_x \rightarrow 0$ but $q_x \neq 0$ is incident upon an exemplar ionic lattice (+ve ions in red, -ve ions in blue). Three polar phonon modes are excited: TO 1, TO 2 and LO. Each mode generates an internal E , but, only in the LO mode is its dot product with \mathbf{q} non-zero. The resulting force shifts the frequency upwards resulting in LO-TO splitting.	55
2.10	Experimental, simulated and example images/diagrams of ferroelectric domain morphologies. In all cases, arrows represent the direction and magnitude of the local ferroelectric mode. a) A cross-sectional HR-STEM for a $\text{STO}_{10}/\text{PTO}_{10}$ superlattice, showing that an array of vortex–antivortex pairs is present in each PTO layer defining a flux-closure domain pattern from reference [173]. a i) A magnified image of a single vortex–antivortex pair, showing the continuous and gradual rotation of the polarisation state within such vortex–antivortex pairs from reference [173]. b) A phase-field simulation demonstrating the polar wave texture as predicted in an intermediate phase in electric field switching of a PTO/STO superlattice from reference [174]. c) A first principles simulated flux-closure domain texture in the $\text{PTO}_6/\text{STO}_6$ superlattice from reference [175]. The red area marks an area where an antivortex has formed. d) A schematic of Classical Kittel domains where up the page is the out of plane direction. e) A schematic of Landau-Lifshitz type domains. All images have been used with permission from the lead authors of [173], [174] and [175]. Figure (a), (a i) and (b) are © 2017 Springer Publishing and Figure (c) is © 2012 American Physical Society.	63

2.11	Maps of structural inhomogeneities in the vicinity of surface defects of PTO/STO superlattice heterostructures. a) Map of the ϵ_{33} strain tensor element local to a surface defect on a PTO/STO superlattice from reference [55] (scale bar $2\mu\text{m}$). b) The evaluated strain gradients for the strain field in (a) from reference [55] (scale bar $2\mu\text{m}$). c-d) $500 \times 500 \text{ nm}^2$ room temperature tapping mode AFM images of surface steps and 180° stripe domains for epitaxially deposited PTO on STO. Height is displayed with a color scale range of 0.8 nm. These images are taken from reference [34]. All images have been used with permission from the lead authors of [55] and [34]. Images (a) and (b) are © 2017 American Physical Society and images (c) and (d) are © 2008 American Institute of Physics.	65
3.1	Norm-conserving pseudopotential generation data for Pb with the PBESol [229] functional as parsed from the PseudoDojo database [230] (PS=pseudo, AE=all-electron). The matching radius is given for each l -channel which is $2.4 a_0$ for $l = 0$ and 1 and $2.1 a_0$ for $l = 2$. The pseudo and all-electron radial wavefunctions for solved for the $l = 0-2$ pseudopotentials. b) Smooth pseudopotentials for $l = 0-2$ (non-local) and the local potential. We refer the reader to [230] for an explanation of the local and non-local parts of the pseudopotential.	79
3.2	The default Pb radial function solutions $R_{nl\zeta}(r)$ for $\zeta = 1$ and 2 generated by the CONQUEST PAO generator code (v1.02) using the <i>equal radii</i> method described in Chapter 5. The cutoff radii r_c are marked with vertical dotted lines. Pb 5d features only a single ζ as we choose to treat it as a semicore state. We have perturbatively polarised Pb 6p to create the Pb 6d radial functions.	84
3.3	Scaling performance for CONQUEST on the K-computer and ARCHER using a pure MPI implementation. a) Strong scaling on the UK national supercomputer, ARCHER, up to 4920 processors (from 50-5 atoms/core). Calculations were performed on bulk PTO with an L_{range} of 7.41\AA and a SZ basis of PAOs. b) A scaling demonstration for the $\mathcal{O}(N)$ algorithm on ARCHER for the same material system as (a). c) Weak scaling on the K-computer up to <i>one million</i> atoms for bulk Si. This image is © American Institute of Physics from reference [7].	91
4.1	The structures used for the phonon dispersion calculations of Section 4.3.2. A-site Pb has been removed for clarity and BO_6 octahedral complexes have been coloured to match the B-site species. Supercell models (rows 1 and 2) are labelled with Roman numerals I:VI whilst the last row indicates the PZT-VCA supercell as well as the end members PTO and PZO. Each supercell is also assigned a crystalline space-group.	107

4.2	The soft mode phonon dispersion relations for PZT I:VI, the VCA, PTO and PZO. All dispersions are over an identical fractional q -path controlled by the parameter $\zeta = 1/2$ (upper x -axis). Folded symmetry labels (described in Table 4.3) are included for PZT I:III, the VCA, PTO and PZO. We only include folded labels if a soft mode of that wavevector is present at the given q -point. In the particular case of PTO, this leads to no label for the wavevector $(1/2, 1/2, 1/2)$. Since dispersions for PZT IV:VI were calculated on the primitive cell, no folding takes place thus only one symmetry label is required.	113
4.3	Species projected phonon density of states $D(\bar{\nu})$ for PTO, PZO the VCA and the PZT supercells over the imaginary wavenumber space. For the VCA calculation, the gold curve is the PDOS of the alchemical 50/50 Ti/Zr atom whilst for the supercell models it represents the sum of B-site PDOS.	115
4.4	Visualisation of eigendisplacements described in the text following the same key as Figure 4.1 but also with grey spheres representing Pb sites. i) The T_4 modes of PTO and PZO. Both Pb and counter-rotating octahedra are removed for clarity. ii) The Γ_4^+ distortion of PZT I (c-axes into page) and the M_2^+ distortion of the VCA from three viewing angles indicating out-of-phase rotation about three axes of rotation iii) The antipolar Δ_4 distortion of PZT III. Arrows indicate the direction of the local polarisation. iv) The mixed antipolar/AFD M_3^+ distortion of PZT IV.	119
4.5	The phonon dispersions of primitive $Pm\bar{3}m$ PZO (blue) and PHO (orange). . .	124
4.6	The phonon dispersions of primitive $Pbam$ PZO (blue) and PHO (orange). . . .	125
4.7	The two most important modes comprising the difference between the $Pbam$ and $Pnma$ crystals for PZO and PHO. The magnitude of the displacement is exaggerated. a) The T_4 mode. ZrO_6/HfO_6 octahedra rotate in antiphase about the pseudocubic b axis in <i>pairs</i> . b) The Λ_3 mode. Antipolar Pb displacements are grouped by a common displacement direction with coloured boxes (red: up, blue: down, orange: left, green: right). Zr/Hf (inactive in this mode) has been removed for clarity.	127
5.1	The crystal structures for all of the test cases in this chapter. We do not explicitly show C or Ge since they are isostructural with Si in this work. Similarly, we do not show STO since one only needs to exchange the A site of PTO for Sr. For PTO and PZO, we also illustrate the paraelectric to ferroelectric and paraelectric to antiferroelectric phase transitions, respectively. The responsible displacive soft modes for the transitions are also indicated.	141

5.2	The Birch-Murnaghan equations of state for $Fd\bar{3}m$ Ge using plane waves (PW) and the default ER PAOs. This test case shows the <i>worst</i> agreement with plane waves. Each curve is shifted to the origin by the equilibrium energy and volume as this allows for clearer comparison of the bulk modulus.	148
5.3	The charge density difference between PAO calculations and plane waves for increasing PAO basis set size for cubic PTO (a) and cubic PZO (b). For each case, we display the full 3d isosurfaces and slices through the PbO and BO ₂ planes. Isosurfaces are plotted at the +0.10 (dark red), +0.020 (light red) and -0.020 (blue) electrons/Å ³ levels.	150
5.4	The charge density difference between PAO calculations and plane waves for increasing PAO basis set size for tetragonal PTO (a) and orthorhombic PZO (b). For each case, we display the full 3d isosurfaces and selected slices. Isosurfaces are plotted at the +0.10 (dark red), +0.020 (light red) and -0.020 (blue) electrons/Å ³ levels.	152
5.5	The charge density difference between PAO calculations and plane waves for increasing PAO basis set size for $Fm\bar{3}m$ cubic PZT 50/50 (a) and $Pm\bar{3}m$ cubic PZT 50/50 (b). For each case, we display the full 3d isosurfaces and selected slices. Isosurfaces are plotted at the +0.10 (dark red), +0.020 (light red) and -0.020 (blue) electrons/Å ³ levels.	153
5.6	The convergence properties of plane wave calculations where PAO calculations featuring <i>the same error</i> have been overlaid for comparison. Calculations were performed on the $Pm\bar{3}m$ PTO structure. a) Convergence with respect to the total electronic error integral of Equation 5.2 b) Convergence with respect to ΔE , the energy difference between a given calculation and the energy obtained from the 40Ha plane wave cutoff.	154
5.7	The phase transition energetics for PTO and PZO as function of normalised mode amplitude. Points/crosses are calculated data whereas lines are linear interpolations. Curves labelled with (PW) were calculated along the plane wave optimised trajectory. a) Seven curves indicating phase transition paths for the zone centre distortions in PTO. Modes with the subscript σ are strain modes coupled to the displacive Γ_4^- mode. b) Seven curves describing the phase transition path for the three most important modes in the $Pbam$ PbZrO ₃ phase transition. Each path begins with the optimised orthorhombic cell for each basis such that strain modes are “pre-frozen”.	161

6.1	The equations of state $E(V)$ for the cubic phases of STO (left) and PTO (right) using different $r_{MS} = r_{LD}$. We also include $E(V)$ for the exact diagonalisation of PAOs (where the MSSF contraction has not been made) and the $E(V)$ (PW) result obtained from a plane wave calculation using the same pseudopotentials. The PW curve has V_0 shifted to agree with the minimum of the exact diagonalisation calculation so a better comparison can be made of the energetics. The true lattice constants can be found in Table 6.1.	173
6.2	The total energy (upper) for $Pm\bar{3}m$ and $P4mm$ PTO and the energy difference (lower) between them as a function of increasing DM range. Horizontal dashed lines mark the total energy/energy difference from exact diagonalisation.	176
6.3	The initial supercell configurations for the $N_z = 3$ films before structural relaxation. Shown here are the supercells <i>not</i> including AFD modes. Each configuration is however also treated with AFD modes following the explanation in Section 6.2.5. a) The paraelectric supercell constrained such that spontaneous polarisation cannot emerge. b) The monodomain in-plane ferroelectric case ($\mathbf{P} \parallel [100]$ is shown here, but we also treat $\mathbf{P} \parallel [110]$) constrained such that spontaneous polarisation cannot develop in the out-of-plane direction. c) The polydomain ferroelectric case with equally sized up and down domains for the ferroelectric polarisation. Shown here is the $\Lambda = 6$ case.	179
6.4	The displacements of metal cations from their initial positions (described in the main text) as a function of the number of included substrate monolayers, N_{ML}	180
6.5	Energy versus the R_4^+ mode rotation angle θ_z for PTO at its bulk cubic lattice constants, strained PTO with $a = b = a_{\text{STO}}$ ($\sigma = -0.78\%$) and STO at its bulk cubic lattice constants. Calculations here are in full periodic boundary conditions in the infinite bulk crystal. The coefficients of quartic polynomials are evaluated with a least squares fitting procedure and plotted as lines. <i>Inset</i> An illustration demonstrating the R_4^+ rotation angle θ_z shown here for STO. The same angle persists in PTO.	181
6.6	The energy difference between free standing $N_z = 7$ polydomain films and the paraelectric film as a function of domain period Λ . The equilibrium period is found at $\Lambda = 12$	184
6.7	The local polarisation vector field of the relaxed $N_z = 7$ film at the equilibrium domain period $\Lambda = 12$ (as demonstrated in Figure 6.6).	185

- 6.8 a-c) Bird's eye views for surface trenches on an ultrathin PTO film. Each trench arrangement is shown with its label which was assigned in the text. +AFD is bracketed in (a) and (b) as these trench configurations are treated with and without AFD modes. (a) Parallel to the domain wall, positioned over the domain wall: \parallel^{wall} . (b) Parallel to the domain wall, positioned over a domain centroid: \parallel^{wall} . (c) Perpendicular to the domain wall: \perp + AFD. The reason this arrangement always includes AFD modes is discussed in the main text. d) Looking down the axis of a surface trench on the $N_z = 7$, $\Lambda = 12$ film. This example is the configuration shown in (a) looking down the [010] direction. Atom colouring follows the same key as Figure 6.3. 186
- 6.9 The energy difference of a given film ΔE compared with the non-polar paraelectric films versus the film thickness in PTO unit cells, N_z . Since we use a fixed amount of STO substrate, the formula unit of the film alters with N_z . This is accounted for by the upper x-axis indicating the Pb/Sr fraction. The area in grey indicates the domain of N_z for which the polydomain configuration was found to be unstable. In the key, entries followed by (c) indicate films where the mentioned modes coexist. Those followed by (sum) are simply the sum of the individual (isolated) contributions from the mentioned modes. 188
- 6.10 The local polarisation profiles as a function of film vertical position z for different film geometries with and without the interplay of AFD modes. a) The local polarisation ($|P|_{xz} = \sqrt{P_x^2 + P_z^2}$, which is $\approx P_z$ at the domain centroid apart from the $N_z = 3$ film which has a polar wave morphology) at the domain centroids for both the up and down domains of polydomain films. We display only $N_z = 3$ and $N_z = 9$ for clarity. b) The local polarisation of films initially in the $\mathbf{P} \parallel [110]$ configuration. Both P_x and P_y components are shown for $N_z = 1$ and $N_z = 2$ (where there is a finite size effect). Otherwise, $P_x \approx P_y$. c) The local polarisation (P_x) for films with $\mathbf{P} \parallel [100]$ 190
- 6.11 The local polarisation vector fields in the x-z plane for two film thicknesses not including AFD modes. a) The flux-closure domains of the $N_z = 9$, $\Lambda = 12$ film. The red area highlights a vortex/antivortex pair b) The polar wave morphology in the $N_z = 3$, $\Lambda = 6$ film. The red area indicates a cylindrical chiral bubble. . . 192
- 6.12 a) The $a^0 a^0 c^-$ TiO_6 octahedral rotation angle $\theta_z(z)$ for the different geometries of the $N_z = 9$ film. b) $\theta_z(x)$ and the x and z components of the local polarisation $P(x)$ across a domain period Λ of 12 unit cells for the $N_z = 9$ film. Since both the local polarisation and rotations are centered on Ti sites, as a visual guide, an aerial view of the film looking down $[00\bar{1}]$ is below b) aligned with the points on b). 194

6.13	Surface and interface rumpling of the Pb cations for the $N_z = 7$ ($\Lambda = 10$) film <i>without</i> AFD modes. a) The vertical deviation of the surface (upper) and interface (lower) Pb atoms from the Pb atom located at the first domain wall (along the x-axis). b) An exaggerated schematic of the surface and interface rumpling including the boundary with the substrate.	195
6.14	A close-up demonstration of the differences in the local polarisation before (a, c) and after (b, d) the introduction of a surface trench for those trench orientations running <i>parallel</i> to the domain wall. O sites are removed for clarity. a) Near the surface of the pristine film at the domain centroid. The Pb site contained within a grey box is the site used in the scale bar (lower right) b) The local polarisation near a $d = 1$ trench over the domain centroid ($\parallel^{\text{centroid}}$). The two Ti sites contained within the purple dashed box are discussed in the text. c) Near the surface of the pristine film at the domain wall. d) The local polarisation near a $d = 1$ trench over the domain wall (\parallel^{wall}). The two Ti sites contained within the orange dashed box show a near-head-to-head arrangement of local polar modes which are discussed in the text.	199
6.15	a) The local polarisation vector field of a single vortex in the relaxed $d = 2$, $\perp +$ AFD film looking down [010]. Oxygen has been removed for clarity. This figure also uses the same scale bar as Figure 6.14. b) A schematic of the $\perp +$ AFD film. The area shaded in cream/yellow indicates the segment of the film displayed in a). The arrows on the front of this shaded portion are a cartoon representation of a). c) A close up of the five local polar modes along [010] at Ti-centered unit cells near the film surface (the area on a) circled in blue). The last Ti-site on the right is at the edge of the trench. d) A close up of six local polar modes along [010] at Ti-centered unit cells near the vortex core (the area on a) circled in grey). The last Ti-site on the right is the Ti-site closest to the surface of the trench. . .	200
6.16	The out-of-plane strain for (bottom) surface unit cells $\epsilon_{33}^{\text{surf}}$ along the [100] direction for the $\parallel^{\text{centroid}}$ films. Both plots feature the underlying strain from the pristine film (the film without trenches) for comparison.	203
6.17	The out-of-plane strain for surface unit cells $\epsilon_{33}^{\text{surf}}$ along the [100] direction for: a) the $\parallel_{4\Lambda}^{\text{centroid}}$ film and b) the $\parallel_{4\Lambda}^{\text{wall}}$ film. Both plots feature the underlying strain from the pristine film (the film without trenches) for comparison. Up domains are coloured light grey while down domains are dark grey.	204
A.1	The convergence of the total energy (compared to the total energy resulting from a highly converged 1500 eV calculation) as function of plane wave cutoff energy for the NCPP and PAW calculations. Plots on vastly different scales are separated by a black dashed line.	216

A.2	The convergence of the total energy (compared to the total energy resulting from a highly converged $12 \times 12 \times 12$ calculation) as function of Γ -centred Monkhorst-Pack mesh dimensions for the NCPP and PAW calculations. Note that $Fm\bar{3}m$ PZT 50/50 is represented within a $2 \times 2 \times 2$ supercell of the primitive perovskite unit, so, the $6 \times 6 \times 6$ mesh of this calculation is designated as $12 \times 12 \times 12$ -equivalent. Plots on vastly different scales are separated by black dashed lines.	217
A.3	The convergence of forces on the B-site ions in the cubic cell with the B-site displaced 0.1\AA in the [001] direction. We show convergence as a function of fineness of Brillouin zone integration as well as the plane wave cutoff energy. Each plot has a different scale for the y-axis. For the upper right plot. PZT 50/50 calculations are plotted with their 5-atom perovskite unit cell equivalent MP mesh (i.e, a $2 \times 2 \times 2$ MP mesh in the 40-atom PZT supercell is equivalent to a $4 \times 4 \times 4$ mesh on the primitive perovskite unit cell).	218
A.4	Phonon dispersion curves using the FDM and DFPT for both PTO (top) and PZO (bottom). This calculation is performed across the primitive cell of $Pm\bar{3}m$ PTO & PZO.	223
A.5	A convergence study for the the fineness of integration grid (measured in plane-wave equivalent cut-off energy, E_{cut}) for the bulk $Pm\bar{3}m$ and $P4mm$ phases of PTO. The upper and middle panels are for convergence of the total energy whilst the lower panel measures the energy difference ΔE between the phases in meV/atom.	224
A.6	The convergence of reciprocal space integrals using uniform Monkhorst-Pack meshes for the bulk phases of PTO and the $N_z = 2$ film (detailed in Chapter 6). The upper panels show the convergence of the total energy with increasing grid dimensions. The middle panel shows the same test but as a difference with the highly converged (to $\approx 5 \times 10^{-7}$ eV in the total energy) $12 \times 12 \times 12$ mesh. The lower panel also compares with the $12 \times 12 \times 12$ mesh, but measures the energy difference between the considered phases.	225

List of Tables

4.1	The space-groups, Wyckoff positions and <i>primitive</i> supercell dimensions of the relaxed, cubic-constrained structures. All structures are representable in the $2 \times 2 \times 2$ primitive perovskite supercell as illustrated in Figure 4.1. Wyckoff positions are stated using the site multiplicity and Wyckoff letter as made standard by the Bilbao Crystallographic Server [323]. Supercell dimensions are given in lengths of the mutually orthogonal axes a, b & c with the exception of PZT I whose axes are at an angle $\alpha = \beta = \gamma = 60^\circ$ with the full form of the lattice vectors displayed.	109
4.2	The diagonal elements of the stress tensor σ , high frequency dielectric tensor ϵ^∞ and averaged born effective charges \bar{Z}^* of the unique elements for the primitive cubic perovskite unit cell following the convention of reference [162]. For PZT, these calculations were performed at a_{vg} whilst PTO & PZO were performed at a_{PTO} & a_{PZO} respectively.	112
4.3	Brillouin zone labels the reader may find useful for interpreting Figures 4.2, 4.5 and 4.6 and references to high symmetry points in the text. Wavevectors are presented in fractional \mathbf{q} . High symmetry points are in bold font while other points are in plain font.	114
4.4	The 10 most unstable modes, for each structure, measured along the phonon dispersion path in Figure 4.2 (with the exception of PTO, featuring only 7 instabilities over the dispersion path). Modes are listed in descending imaginary wavenumber $\bar{\nu}$ across the page. Each entry features a symmetry label for the irrep and a multiplicity M. Since PZT II, III, IV and VI feature directional polar modes, affected wavenumbers are given in the format $\bar{\nu}_{[010]}/\bar{\nu}_{[110]}/\bar{\nu}_{[111]}$. The full tabulation of all dynamical instabilities can be found in appendix A.1.	116
4.5	The relative stability ΔE (in meV/FU) of the <i>Pbam</i> and <i>Pnma</i> phases compared to cubic <i>Pm$\bar{3}m$</i> for PZO and PHO. $\Delta E = E(\text{Pbam}/\text{Pnma}) - E(\text{Pm}\bar{3}m)$.	128
4.6	The (fractional) Wyckoff positions (x, y, z) and orthorhombic lattice vectors for 40 atom <i>Pbam</i> PZO and PHO. We compare LDA-PW, PBESol and the SCAN functionals complete with comparison to 10K neutron diffraction data.	129

4.7	The (fractional) Wyckoff positions (x, y, z) and orthorhombic lattice vectors for 80 atom $Pnma$ PZO and PHO. We compare LDA-PW, PBESol and the SCAN functionals. We warn the reader, that by convention, the pseudocubic a and b axes are interchanged when compared to $Pbam$	130
4.8	The total decomposed mode amplitudes A_p (described in the text) for each irrep using the $Pm\bar{3}m$ phase as the parent and the $Pbam/Pnma$ phase as the daughter. Data is presented in the format “LDA-PW PBESol SCAN”. $RSS = \sqrt{\sum_i A_{p,i}^2}$	131
5.1	The orbitals treated as valence by the pseudopotentials used in this work. Those orbitals in bold font are treated as semi-core in the PAO calculations (i.e, are described by only a single ζ regardless of the basis set size) and those which are underlined are <i>not</i> present in the pseudopotential but are treated as polarisation states in the PAO calculations.	140
5.2	The cutoff radii r_c for the default PAOs used in this work under the equal energies and equal radii constructions for the PBE and PBESol functionals. Those table entries left blank appear for orbitals treated as semi-core (being described by only a single ζ).	144
5.3	The equilibrium volumes V_0 and bulk moduli B_0 obtained from least-squares fits to the Birch Murnaghan equation of state [357] (Equation 5.1). EE indicates results from the equal energies PAO construction while ER indicates results from the equal radii method. PW is the converged plane wave result.	146
5.4	The total integrated electronic error N_{error}^e (normalized per 5-atom ABO_3 perovskite unit, containing 44 electrons) as defined in Equation 5.2 for the SZP, DZDP & TZTP PAO basis sets for each of the considered structures in Figure 5.1.	149
5.5	The Bader partitioned ionic charges q_B , volumes V_B and average valence charge densities \bar{n}_B for each ionic species and each of the considered crystal structures calculated for each basis set. Where ionic species have symmetry inequivalent sites, we take the mean value over all sites. We give also the mean relative error (MRE) ϵ and mean absolute relative error (MARE) ϵ^{abs} measured in % error versus plane waves.	155
5.6	The mode amplitudes normalised to the parent cell A_p (described in the text) for the irreps characterising the $Pm\bar{3}m \rightarrow P4mm$ phase transition in PTO.	157
5.7	The mode amplitudes normalised to the parent cell A_p (described in the text) for the irreps characterising the $Pm\bar{3}m \rightarrow Pbam$ phase transition in PZO. The modes are listed in descending total distortion.	158
5.8	The strain mode amplitudes, A_p , for the $Pm\bar{3}m \rightarrow P4mm$ phase transition of PTO and the $Pm\bar{3}m \rightarrow Pbam$ phase transition of PZO.	158

5.9	The optimised, mutually orthogonal, pseudocubic lattice constants a , b and c for the distorted PTO/PZO phases and the PZT 50/50 arrangements.	159
5.10	The phase transition energies for the cubic to tetragonal/orthorhombic transitions in PTO/PZO. This quantity is defined by the difference in total energy between the relaxed cubic phase and the relaxed distorted phase for each basis.	160
5.11	The cutoff radii r_c for the default (ER; equal radii) and optimised LDA-CAPZ PTO basis described in the text. Unlike before, we now treat the Pb 5d states as semicore.	163
6.1	The values of the equilibrium volumes V_0 , equilibrium lattice constants a_0 , bulk moduli B_0 and bulk modulus derivatives B'_0 as obtained from a least squares fit of $E(V)$ to the Birch-Murnaghan equation of state. Exact diagonalisation refers to the result obtained without the MSSF contraction, i.e. the Hamiltonian is built with primitive PAOs with dimensions $N_{\text{PAO}} \times N_{\text{PAO}}$ like in Chapter 5.	174
6.2	The relative stabilities of the relaxed films with trenches as detailed in Section 6.2.6. The energy is measured relative to the $\parallel^{\text{centroid}} + \text{AFD}$ arrangement apart from films subscripted with 4Λ which are measured relative to $\parallel_{4\Lambda}^{\text{centroid}}$. Energies are normalised per formula unit. This is assigned as the number of atoms in the parallel trench arrangements with the <i>same</i> trench separation. That is, for $d = 1, 2$ and 3 , the energy is given per 428, 412 and 396 atoms, respectively, but, for the films subscripted 4Λ , the energy is given per 1760 atoms.	197
A.1	The analytical phonon wavenumbers of dynamical instabilities at the considered wavevectors chosen in 4 for PTO, PZO and PZT 50/50. Modes are listed in descending order in imaginary wave number from left to right. Each mode is assigned a symmetry label and a multiplicity, M	222

1 | Introduction

Conventional simulations based on density functional theory (DFT) and plane waves have undoubtedly accelerated discovery in the ferroelectric and antiferroelectric perovskites. Indeed, much of their impact can be measured on the grounds that our current understanding of the microscopic origin of ferroelectricity in the prototypes BaTiO_3 and PbTiO_3 (previously understood on the basis of a classical shell model [1, 2]) is based upon the predictions of plane wave DFT [3]. The long-term success of this conventional method has brought it into a status of maturity within computational condensed matter physics, chemistry and materials science. With this maturity has come an ingrained acceptance (within a large portion of the community, at least) that the technique is *not* viable for simulations beyond a few hundred atoms; a consequence of an $\mathcal{O}(N^3)$ (where N is the number of atoms) asymptotic scaling wall in its numerical implementation in standard codes [4, 5]. This belief is *still* held despite the enormous effort of the past twenty years in breaking this scaling wall, bringing to fruition an implementation of DFT scaling linearly with the number of atoms, or, $\mathcal{O}(N)$ [4, 6–12]. While it is true that $\mathcal{O}(N)$ methods now allow for full DFT calculations involving many thousands to millions of atoms [13], the method has not yet worked its way into the “simulation tool-box” of many.

The reason for this is many-faceted. Firstly, DFT practitioners have become experts at fitting the problem at hand into a supercell comprised of only a small collection of atoms. More often than not, in the process of doing so they no longer solve precisely the problem they intended, but, a model of reduced complexity. One may then assert that, more than anything, we have become comfortable with the limitations of conventional DFT rather than truly circumventing the need for more atoms in our simulations. The next reason is less psychological and more practical. Within the vast zoo of conventional DFT codes[†] exist many with user friendliness at the forefront [14, 15]. This makes these codes accessible for theorists and dabbling experimentalists alike; “plug and play” quantum mechanics is realised. While this often obfuscates the inner workings of the code making it a “black box”, this is *most of the time* permissible if one simply wishes to perform standard total energy calculations (provided care has been taken in convergence studies).

On the other hand, $\mathcal{O}(N)$ codes have historically not provided such out-of-the-box functionality. A lot of this is down to problems emerging from the use of a local basis. For

[†]Although, a lot of the animals in this zoo are remarkably similar.

example, basis sets of pseudoatomic orbitals (PAOs; used for much of this thesis, described in Chapter 3, Section 3.4.2) cannot be improved in a systematic manner, unlike plane waves, which can[†]. This introduces an additional preparatory step where we must make a judicious choice of basis set and carefully study the parameters of its creation. Addressing this problem is the focus of Chapter 5 and as we will show, the default basis sets of PAOs which ship with the CONQUEST (Concurrent O(N) QUantum Electronic STructure) code [7, 17] are now remarkably accurate, offering near plane wave accuracy in most situations. The last issue we shall discuss relates to access to ample computational resources. Although conventional DFT calculations can be (and often are) a task for high performance computing (HPC) centres, useful $\mathcal{O}(N)$ calculations demand HPC. Within the CONQUEST code, we recommend ≈ 10 -20 atoms (5 at a push) per physical core for optimal load balancing; quickly making simulations of tens of thousands of atoms require a few thousand physical cores! This requirement precludes many from using such a code, leaving these calculations to expert HPC users familiar with the parallelisation strategies for which the efficiency of $\mathcal{O}(N)$ calculations rely. As we detail in Chapter 3, Section 3.4.5, using the multi-site support function (MSSF) method [18, 19] can allow access to high accuracy calculations of a few thousand atoms without such a high demand for computational resources. It is this method which we use for a large part of Chapter 6.

To solve some problems, we have no choice but to use a larger number of atoms. Many of these scenarios can be realised within the perovskite oxides; the crystal structure central to this thesis. This class of material, however, is more than a mere vector to exploit the functionality of large scale DFT. They are highly technologically important. Since the phenomena of ferroelectricity was observed in BaTiO_3 in the 1940's [20–22] there has been a boom in exploitative technologies reliant on giant piezoresponses and switchable polarisation states. The former is responsible for ultrasonic transducers; used in loudspeakers, headphones, microphones as well as in sonar and many sensors and actuators. The latter is the basis for ferroelectric memories[‡]; devices which store the direction of the spontaneous polarisation state of a ferroelectric as a binary 0 or 1 [23]. These technologies have in recent years faced challenges as the insatiability of device miniaturisation has continued. It is known that ferroelectric devices of reduced dimensionality see their spontaneous polarisation degraded, eventually leading to a net polarisation of zero [23, 24]. While it was originally thought that this signalled a finite size for the existence of ferroelectricity, it was later realised that the net zero polarisation was the result of equally sized and antiparallel ferroelectric domains separated by a domain wall [23].

The appearance of multiple domains and domain walls was once believed to be a great drawback for low-dimensional ferroelectric technologies. While this is true if the device is

[†]Systematically improvable local basis sets *do* exist, (like b-splines [16] (blips), period sinc functions [9] (psincs) and Daubechies wavelets [12]) but, are known to converge slowly and to sometimes require immoderate optimisation.

[‡]There are two popular models for non-volatile memory using ferroelectrics. Those which utilize a capacitor set up for random access memory - FeRAM and those which inform a variation on the field effect transistor - FeFETs.

reliant upon a stable and unidirectional polarisation, it is not true if the device is intended for use as a dielectric or piezoelectric. That is, polydomain films are known to give rise to enhanced piezoelectric coefficients and dielectric properties in comparison to the bulk crystal [25]. The domain walls themselves have now become an area of intense study. In particular, Seidel showed that the domain walls in the (otherwise insulating) room temperature multiferroic[†] BiFeO₃ were conducting [26]. This shows promise to be exploited in new low-dimensional nanocircuits whereby 2D conducting channels can deliver current to mounted nanocomponents [27–29] or themselves become nanocomponents [29]. It is for this reason that there is an invested interest in the field to manipulate and guide ferroelectric domain walls. One approach for doing so is to temporarily (and reversibly) ‘write’ domains using targeted electric fields; a technique known as ‘domain wall injection’ [30, 31]. Another is to more permanently write domain walls by use of etched surface trenches. This method is informed by the experimental observation that domain walls tend to preferentially align to run parallel to surface defects; an effect first observed in thin films of PbTiO₃ in the early 2000’s [32–34].

Now the antiferroelectrics have also become technologically useful, principally as energy storage materials. That is, when used in a dielectric capacitor, antiferroelectrics can give rise to higher energy densities as well as higher power and charge release densities in comparison to standard ferroelectric and linear dielectric capacitors [35]. It is almost surprising that applications of antiferroelectrics have been realised when one takes into account just how little we know about the physics of these materials. Despite being discovered nearly 70 years ago [36], the very definition of the phenomenon remains cloudy [37]. In addition to this, the nature of the archetypal antiferroelectric PbZrO₃ is still a cause for debate and has in recent years undergone an intense re-examination [37]. Most of this debate is related to the mechanism of the paraelectric to antiferroelectric phase transition [38–41], but, as we introduce in this thesis, subtle distortions at low temperatures may even suggest a different crystalline space group assignment to the established *Pbam* [42].

It is now appropriate to clearly define the scope and goals of this thesis. These can be divided into three parts:

1. To demonstrate the need for large scale DFT calculations within the ferroelectric/antiferroelectric perovskites by establishing the importance of competitive long range order in technologically important examples.
2. To demonstrate the readiness of large scale DFT to accurately solve problems within the ferroelectric/antiferroelectric perovskites by use of compact and accurate PAO basis sets.
3. Finally, to deploy large scale DFT simulations to solve problems related to the formation of ferroelectric domains and their manipulation that are otherwise intractable for conventional

[†]A multiferroic is a material simultaneously possessing more than one ferroic order parameter. In the case of BiFeO₃, the material is spontaneously ferroelectric and antiferromagnetic - a *magnetoelectric*.

methods.

The first goal is addressed in Chapter 4. Using conventional methods, we critically examine the lattice dynamics of PbTiO_3 , PbZrO_3 and PbHfO_3 ; the $\text{Pb}(\text{Ti}, \text{Zr}, \text{Hf})\text{O}_3$ isoelectronic series [43]. The first two members of this series, in solid solution, form the most well known piezoelectric material, $\text{PbZr}_{1-x}\text{Ti}_x\text{O}_3$, or, PZT. In the region around $x \approx 0.52$ (what is known as the morphotropic phase boundary) PZT is famous for giving rise to a giant electromechanical response which has long been exploited in industrial applications [44]. Within this chapter, we compare the first principles obtained lattice dynamics of several arrangements of near morphotropic ($x = 0.5$) PZT to find that phonons with \mathbf{q} away from high symmetry points, or, *long wavelength modes*, are in most cases dynamically unstable in the high temperature paraelectric phases [43]. Further, the instability of these modes rival that of the more well known ferroelectric and Glazer-type [45, 46] antiferrodistortive modes. Supercell calculations commensurate with these long wavelength modes will consequentially require more and more atoms. Further, we assess the usefulness of the virtual crystal approximation in simulations of solid solutions. Historically, this method has been used to circumvent the need for large supercell calculations [47–49]. We find, however, that the method inaccurately predicts the character of phonon eigendisplacements. Now shown explicitly, this is a confirmation of the suspicions of the DFT community that the method cannot accurately describe local atomic distortions [50]. In a re-examination of PbZrO_3 and PbHfO_3 , we find long wavelength modes also compete. Informed by this, we analyse the stability of the established *Pbam* antiferroelectric phase. Surprisingly, we find that this phase too is dynamically unstable and the stability can be increased by allowing for a phase transition to the subgroup *Pnma*.

The second goal is fulfilled in Chapter 5. We carefully compare the default methods for the generation of PAOs within CONQUEST. We study the effects of basis set completeness by analysing the lattice constants and bulk moduli of perovskites and other materials [51] in comparison to plane wave pseudopotential calculations. Then, motivated by the arguments of Cochran [1, 2] and Anderson [52] on the soft mode theory of ferroelectricity, we assert that errors in the electronic charge density can propagate to large errors in the description of ferroelectric phases [53]. We see this come to light for small default basis sets of PAOs (where the error in the charge density can be large) giving rise to a large super-tetragonality errors in the description of PbTiO_3 . We find that larger PAO basis sets see the eradication of this error, which, in many cases, lead to errors in the structural and electronic properties reducing to less than half a percent when compared with plane wave pseudopotential calculations.

Now content with the accuracy of the approach taken in CONQUEST, we advance to the third and final goal. In Chapter 6, we simulate low-dimensional PbTiO_3 films using large scale DFT in CONQUEST [54]. We begin by investigating the effects of broken inversion symmetry present inherent in any film/substrate system. Using the most popular substrate for the fabrication of PbTiO_3 films, SrTiO_3 , we unveil a chiral phase transition between striped

ferroelectric domains and a polar wave phase with cylindrical chiral bubbles. We reason that this is born from the internal bias field present from the broken inversion symmetry. Since such a bias field depends very sensitively on the boundary conditions for the film, it can be easily manipulated allowing control over chiral polar order on the nanoscale. Further, we observe strong coupling between local polar and antiferrodistortive modes which gives rise to a surface reconstruction commensurate with the domain period of the polydomain film. Such a mechanism offers a promising pathway for the local manipulation of ferroelectricity should one be able to engineer antiferrodistortions into a heterostructure, or, vice versa. Finally, we use the full force of the $\mathcal{O}(N)$ algorithm to investigate the effects of engineered surface trenches on the alignment of domain walls in free standing PbTiO_3 films. We confirm the experimental observation that the film geometry is more stable should the domain wall run parallel to the surface trench. We reason that this stability arises from limited modulations to both the underlying polar texture and surface strain fields of the pristine film. We also find that the introduction of such trenches gives rise to giant strain and fields in the vicinity of the trench in line with experimental observations [55]; previously suggested to contribute to the domain wall alignment mechanism for large trenches.

Before delving into the results of this thesis, in Chapter 2, we provide a convenient overview of many of the important phenomena which appear in the perovskite oxides. We detail the fundamental theories which underlie much of our understanding of the ferroelectric perovskites and provide historical accounts for the study of ferroelectricity and antiferroelectricity. Following this, in Chapter 3, we survey the underpinnings of the quantum many-body problem and the foundations of DFT. We pay special attention the modes of operation within the CONQUEST code and methods for the calculation of phonon spectra. In the 7th and final chapter, we evaluate the impact of this thesis and suggest new avenues for future research including what we believe to be a logical continuation of this work.

2 | An Overview of the Perovskite Oxides

Chapter abstract

The perovskite oxides are the polymaths of condensed matter physics. They are well known to draw from a far-reaching repertoire of useful and exotic properties enabled by their complex and rich pressure-temperature (PT) phase diagrams and their sensitivity to epitaxial strain, small compositional modulations, dimensionality and interfacial effects. A broad description of these properties has now been covered in many detailed review articles including references [56–58]. Following these articles, it is the purpose of this chapter to provide an overview of the vast variety of physical phenomena this materials class are known to give rise to. We pay special attention to the phenomena of ferroelectricity, antiferroelectricity and the formation of ferroelectric domains and discuss recent advances in these areas. In doing so we make reference to physical systems relevant to this thesis. We detail important theories underpinning our understanding of these materials including the Landau-Devonshire (LD) theory of phase transitions [59–63] and the Berry-phase theory of electrical polarisation [64–68], (now also known as the *modern theory of polarisation*). We describe the fundamentals of lattice dynamics with the goal of describing the soft mode theory of phase transitions [1, 2, 52, 69, 70] as well as the key concept of dynamical charge tensors [71–73]. We finish the chapter with remarks upon recent advances related to ferroelectric domain wall control by means of engineered surface defects. This is a promising avenue for the development of low-dimensional nanocircuits.

2.1 The ABO_3 Factotum and Accomplices

The ABO_3 crystal structure (Figure 2.1) is a factotum[†] of exotic phenomena. Compounds adopting this crystal structure or its family of similar crystal structures (double perovskites, hybrid perovskites, layered perovskites etc.) can give rise to distinctly different phenomena based upon the choice of the A and B-site ions, position on the PT phase diagram, epitaxial strain, doping conditions and much more. Interfacial phenomena are of a particular technological relevance. Such phenomena appear at the interface of two different perovskites in systems known as *heterostructures*. In the repeated and layered case, these are known as *superlattices*. At

[†]Translated from New Latin literally meaning "do everything". A factotum is jack-of-all trades.

the interface of the ABO_3 perovskites $LaAlO_3$ (LAO) and $SrTiO_3$ (STO), a two-dimensional electron gas (2DEG) forms as the result of an electronic reconstruction due to the so called *polar catastrophe* [74]. This is surprising seeing as both constituents of the heterostructure are insulating and non-magnetic when the 2DEG is conducting (even superconducting [75, 76]) and under the right conditions can be ferromagnetic [77], can develop a large in-plane magnetoresistance [76] and can even become photoconductive [78]. This leads to applications in field effect devices and photovoltaics as suggested in a study on the similar $LaVO_3$ /STO interface [79]

Many of the exotic properties found within this crystal family (illustrated in Figure 2.1) are the direct consequence of the competing/coupling degrees of freedom of the system. Such competitions/couplings are made possible due to the closely related energetics of spin, charge, orbital and structural degrees of freedom [58]. For this reason we sometimes observe the cooperative alignment of electric dipoles or spin leading to ferroelectricity (discussed further in Section 2.2) and ferromagnetism. It is also possible, in some scenarios, to simultaneously observe different ferroic order parameters in a group of materials known as the *multiferroics*, host to valuable magnetoelectric properties [80]. A whole array of new couplings are obtained when we consider heterostructures. Take for example the 1:1 (or *digital*) $PbTiO_3$ (PTO) STO superlattice, i.e, alternating repeating units of PTO and STO with a period of a single unit cell. It was found that structural modes otherwise unrelated to the electrical polarisation are able to support it. In this case, these structural modes were related to rotations of the oxygen octahedra, or *antiferrodistortive* (AFD) modes able to couple to the polarisation leading to the phenomena of hybrid improper ferroelectricity by trilinear coupling [81]. Such effects become apparent when examining the LD free energy expansion of the system; an expansion discussed generally in Section 2.4. We are not limited to coupling just AFD modes. It is also possible to couple Jahn Teller distortions (thus introducing orbital degrees of freedom) to create similar effects [82–84]. It is possible to observe trilinear couplings in pure ABO_3 perovskites, not just heterostructures. It has been suggested that the paraelectric to antiferroelectric (AFE) phase transition in $PbZrO_3$ (PZO) is driven by a trilinear coupling of an AFD mode, an antipolar mode and a mode resembling both antipolar and AFD order [85].

The PTO/STO heterostructure has more to offer. Take the case where we are in a capacitor heterostructure setup with a dielectric (STO) and ferroelectric (PTO) layer like is shown in Figure 2.2a. Although initially sounding strange, in a certain temperature window, we can observe a *negative capacitance* within the ferroelectric layer [87, 88]. How? First, consider the free energy curves as a function of polarisation for the dielectric and ferroelectric layers in isolation as shown in Figure 2.2b. For the dielectric layer, this curve is a simple parabola with a minimum at zero polarisation. For the PTO layer, below the ferroelectric phase transition temperature $T_0^{PTO, bulk}$, this curve has a characteristic double well appearance with a local maximum at zero polarisation. So long as the combined heterostructure is held at $T_0^{PTO+STO} < T < T_0^{PTO, bulk}$

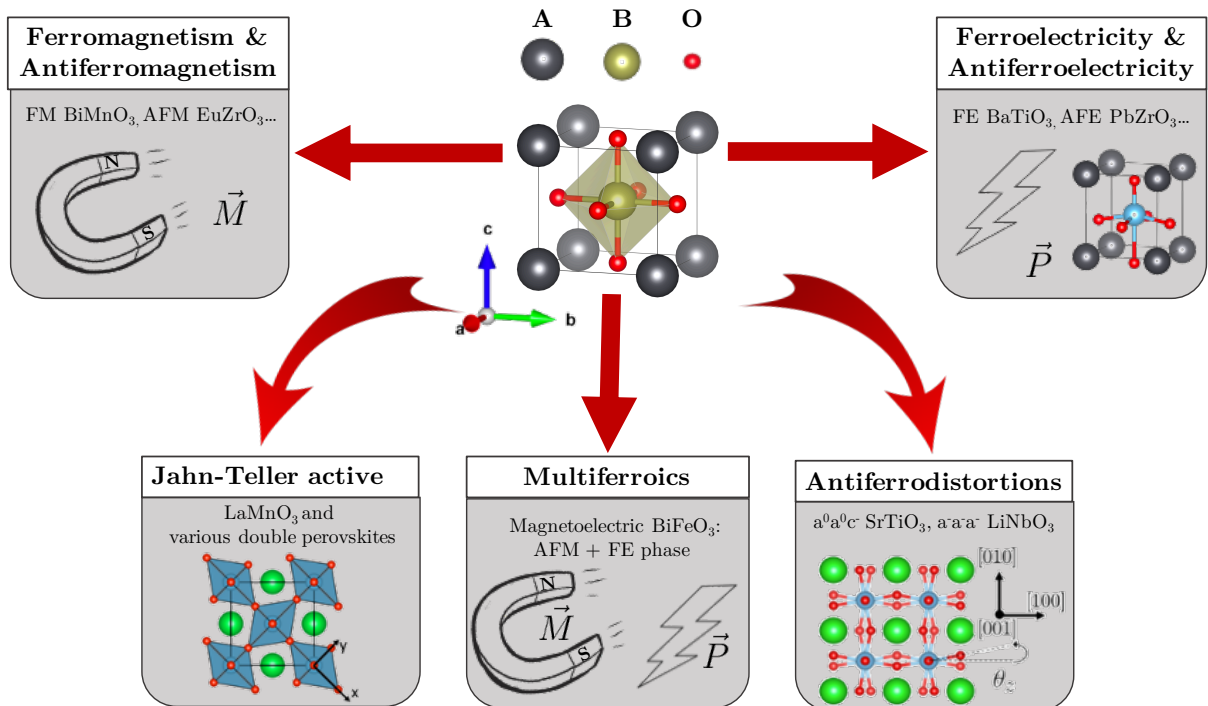


Figure 2.1: The ABO₃ prototype crystal structure (upper centre) and a variety of the possible order parameters/phases that can arise simply by engineering the A and B site cations. The VESTA (v3) crystal structure visualisation program [86] is used to create crystal structure images in this figure. Indeed, this program is used *heavily* throughout this thesis, so we thank the developers here at its first use.

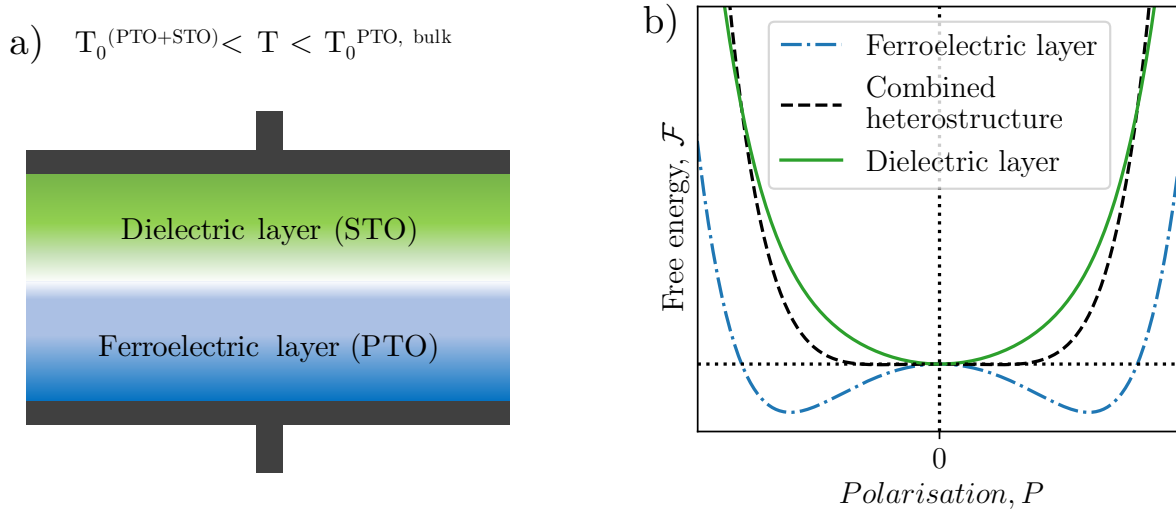


Figure 2.2: The origin of negative capacitance in dielectric/ferroelectric heterostructure capacitors. a) An illustration of a dielectric/ferroelectric capacitor heterostructure. b) The free energy as a function of polarisation within the ferroelectric and dielectric layers as well as the combined heterostructure.

(where $T_0^{\text{PTO}+\text{STO}}$ is the temperature at which the *entire* heterostructure becomes polarised) the free energy of the joint system must have a minimum at zero polarisation (as shown by the black curve in Figure 2.2). Importantly, the minimum of the combined heterostructure coincides with the local maximum of the free energy in the ferroelectric layer. This local maximum is enclosed by two areas of *negative curvature* in the directions of positive or negative polarisation. Since the dielectric stiffness κ is proportional to this curvature, in the ferroelectric layer, it is *locally negative*. The formation of ferroelectric domains and domain wall motion are also known to widen the temperature range that this effect is observed [88]. Also, rather exotically, *sheaths* of negative permittivity have recently been found at the peripheries of polar skyrmions in the PTO/STO system [89].

It has been theoretically proposed that thin films of ferroelectric PTO on dielectric STO substrates (at a depth > 14 unit cells) are able to form a 2DEG and two dimensional hole gas (2DHG) pair [90]. Although sharing the polar catastrophe scenario with the LAO/STO interface, in this case, the polar discontinuity is a result of the ferroelectric polarisation of PTO and *not* charged layers as is the case for LAO (nominally, LaO is +1 and AlO₂ is -1 whilst PbO and TiO₂ layers are charge neutral). This 2DEG/HG pair has not yet been experimentally observed since the stabilisation of a ferroelectric monodomain phase in PTO thin films competes with the formation of ferroelectric domains which strongly reduce the depolarising field and thus remove the need for the formation of mobile interface screening charges.

Random solid-solutions adopting the general structure of $\text{AB}_x\text{B}'_{1-x}\text{O}_3$ are of a great technological importance. A notable example (and relevant to this thesis) is that of $\text{PbZr}_x\text{Ti}_{1-x}\text{O}_3$ (PZT). At a concentration $x \approx 0.52$ [90, 91], we have the most abundantly used

piezoelectric material. That is, a material where lattice strain and the electrical polarisation are coupled. This electromechanical coupling peaks at $x \approx 0.52$ for PZT in a small region known as the *morphotropic phase boundary* (MPB). This boundary exhibits complex lattice dynamics where a flat energy surface for polarisation rotation exists between the ferroelectric tetragonal (polarisation parallel to [001]) and rhombohedral (polarisation parallel to [111]) phases via intermediate monoclinic phases [90, 92, 93].

2.2 Ferroelectricity

A substance possessing both a spontaneous *and* switchable electrical polarisation (the electrical dipole moment per unit volume of the sample) is considered ferroelectric. The etymology of the word can be understood when considering its magnetic counterpart; a ferromagnetic material. Here, the prefix “*ferro*”, that is, containing iron (sometimes “ferrous”) derives from the simple fact that many ferromagnetic materials indeed contain iron. Now the prefix “*ferro*”, by extrapolation, is used to describe any phenomena relating to an order parameter which is both spontaneous and switchable by application of a conjugate field. That is, the magnetisation (the magnetic dipole moment per unit volume of the sample) of a ferromagnetic material is switchable in orientation through application of a magnetic field while the electrical polarisation of ferroelectric material is switchable by application of an electric field. We see now that the two phenomena share the same definition albeit with the replacement of the electrical polarisation with the magnetisation.

2.2.1 Signatures of ferroelectricity

Here we discuss two reliable signatures which indicate whether the material in question is indeed a ferroelectric. The first is a trace of the material’s $P(E)$. Examining Figure 2.3, we can see that the conditions indicated in the definition of a ferroelectric are fulfilled. At $E = 0$ we see that there still exists a polarisation in the material. This is the remanent polarisation P_r (or spontaneous polarisation, P_s). We see that with large E we can increase P further but arrive at a point where no further advances can be made. This is the saturating polarisation P_{sat} . We now reduce E eventually entering a region where E becomes antiparallel to P . Not too long after this, we find that $P = 0$ then flips sign thereafter[†]. The field at which this occurs is known as the coercive field E_c . We see now that the second condition of a ferroelectric has been met; the polarisation is switchable. We recognise now that the trace of $P(E)$ is that of a hysteresis curve, a sought-after experimental signature of ferroelectricity. However, one must be careful in the identification of ferroelectric hysteresis. It has been demonstrated that lossy dielectrics can show a similar signature in the controversy known as the ‘ferroelectric banana’ [95]. This effect

[†]The reader is alerted that this is a much simplified discussion of the switching process. In reality, domain wall motion drives the switching dynamics. This is a topic of current research [94].

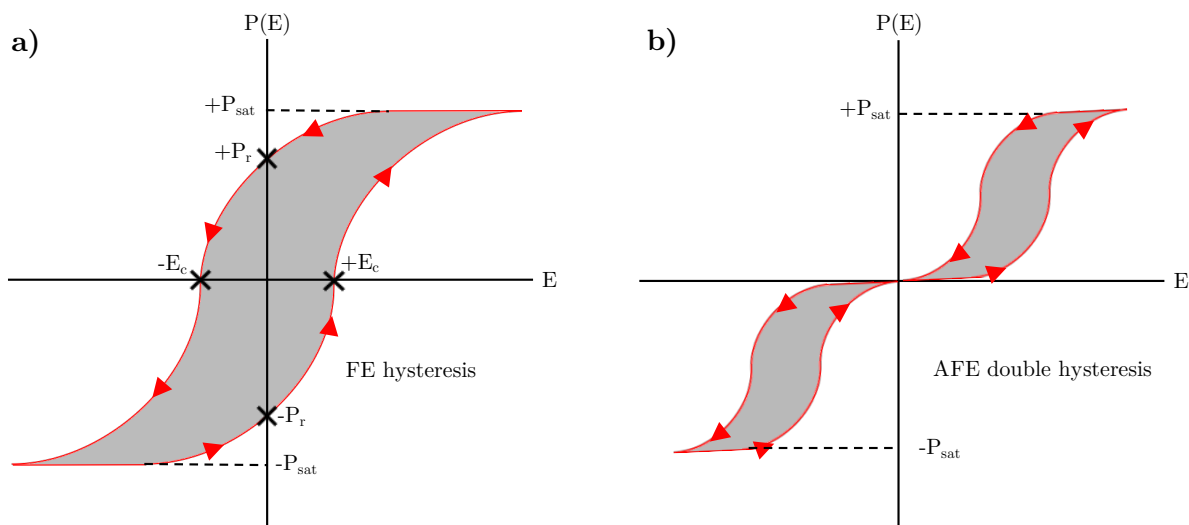


Figure 2.3: The hysteresis curves for a ferroelectric (a) and antiferroelectric (b) material under poling by a uniform electric field. Important values of the polarisation and electric field are labelled: the saturating polarisation P_{sat} , the remanent polarisation P_r and the coercive field E_c .

results in *cigar shaped* curves which appear to share the features of a real ferroelectric hysteresis curve but instead display the leakage current in the capacitor setup used in the measurement [95]. Recently, machine learning techniques have been deployed to distinguish non-ferroelectric loops from ferroelectric ones with some success [96].

The other important signature of ferroelectricity can be appreciated from theoretical standpoint; a double well in the free energy as a function of electrical polarisation, $F(P)$. We touched on this in Section 2.1 when describing the phenomenon of negative capacitance in dielectric/ferroelectric capacitors [88]. $F(P)$ should become double well below the phase transition temperature, or *Curie temperature* T_C . In either of the two wells in the free energy, the system should be polarised at a magnitude P_r (or P_s) and be thermodynamically stable. It is also important that the system is unstable at the local maximum of $P = 0$, the stable system *must* be spontaneously polar. We discuss this concept further in Section 2.6 showing explicitly how such a free energy surface can lead to a third signature of ferroelectricity; dielectric anomalies.

2.2.2 A brief history

The study of ferroelectric materials has a rich history starting from as early as 1921 when Valasek observed for the first time a ferroelectric hysteresis loop (and a piezoelectric response, although previously measured in 1880 by the Curie brothers [97]) in the complex Rochelle salt crystal structure[†] [99] (Figure 2.4, lower). In fact, the term *ferroelectric* had not yet been coined and was instead referred to as *Seignette electricity* named after the apothecary who had first

[†]The crystal structure of the Rochelle salt, or, Potassium sodium tartrate tetrahydrate ($\text{KNaC}_4\text{H}_4\text{O}_6 \cdot 4\text{H}_2\text{O}$) is rather complex and was not discovered until twenty years after the discovery of ferroelectricity in the compound [98].

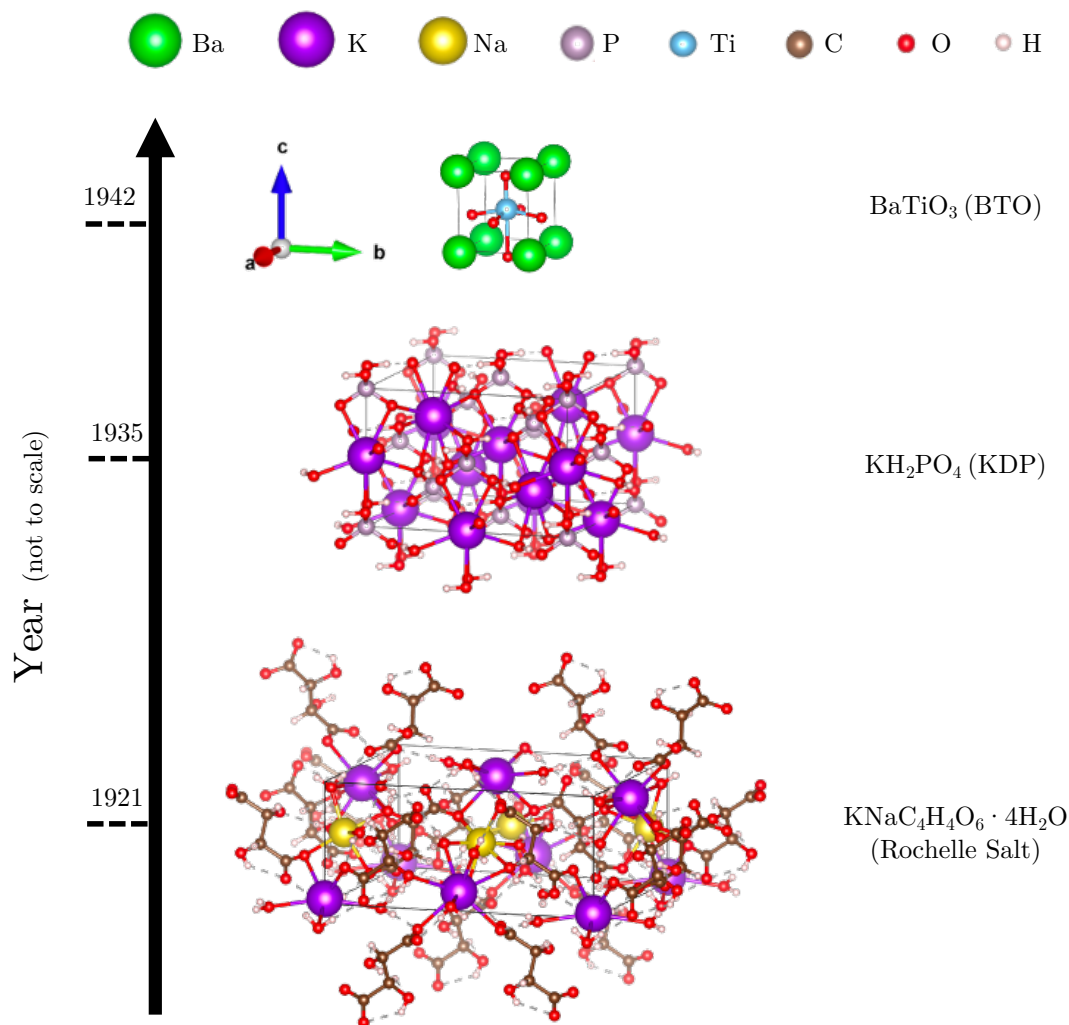


Figure 2.4: A timeline for the early years of ferroelectric research detailing the simplest known ferroelectric compound versus the year. We see clearly then that the known prototype simplified with time leaving us with the ABO₃ drosophila we have today.

synthesized it in 1665, Elie Seignette, in La Rochelle, France. Its use was originally intended as a mild purgative medicine which is somewhat at odds with the blockage in the flow of early ferroelectric research caused by this clearly non-prototypic material. With a unit cell of 112 atoms [98], complex crystal chemistry and difficult experimental conditions, the Rochelle salt was hardly a *drosophila*[‡]. So, from the point of view of wanting to find a physical description of ferroelectricity, this turned out to be not such a great starting point. It likely slowed the development of the field in the early years up until the discovery of ferroelectricity in KH₂PO₄ (KDP; Figure 2.4, middle) in 1935 [101].

KDP has a much simpler structure than the Rochelle salt and its chemistry was already understood [102]. Because of this, a theory for the onset of ferroelectricity in the compound was

[‡]The drosophila (particularly *D. melanogaster*) is a fruit fly used extensively as a model organism in genetics research due to its simple genome (which has now been fully sequenced [100]). Used metaphorically in the text, the Rochelle salt was no model system.

quickly devised related to the different possible arrangements of hydrogen bonds and a preferred axis for the alignment of the $(\text{H}_2\text{PO}_4)^-$ dipoles. [103]. What is often overlooked was the role of the similar compound ammonium dihydrogen phosphate (ADP) in the KDP era. ADP is *not* a ferroelectric like KDP but is instead an antiferroelectric, (discussed in Section 2.3). ADP was found to have a marked piezoelectric response [104] which was exploited for submarine detection [105] by sonar in World War II, replacing the by now obsolete Rochelle salt transducers which were never *really* fit for purpose since the material is deliquescent (has a tendency to absorb water).

The (admittedly short) age of KDP/ADP application ended shortly after the discovery of the first ferroelectric ABO_3 perovskite [22]: BaTiO_3 (BTO; Figure 2.4, upper) [20, 21]. Devoid of hydrogen bonding, strongly ionic and with only 5 atoms per unit cell, we have finally found our prototype. The history surrounding the discovery of ferroelectricity in BTO in the midst of World War II is in itself fascinating and I would recommend reading [106] for a full account. The theory of the ferroelectric transition and application in piezoelectric ceramics would now flourish following the explosion of perovskite ferroelectrics in the decade that would follow. Some notable examples include LiNbO_3 [107], KNO_3 [108], PbTiO_3 [109] and the solid solution families of $\text{PbZr}_{1-x}\text{Ti}_x\text{O}_3$ (PZT) [110] and $\text{Na}_{1-x}\text{K}_x\text{NbO}_3$ [111]. Now equipped with simple ferroelectric crystals, Devonshire [59, 60] would apply the phenomenological phase transition theory of Landau and Ginzburg [112] to explain the ferroelectric transition in BTO. The reader is also referred to the historical musings of Ginzburg [113] regarding the theory and his contributions behind the iron curtain of the USSR.

Cochran and Anderson would independently and simultaneously develop the soft mode[†] theory of ferroelectricity [1, 2, 52]. This theory is rather central to displacive ferroelectric phase transitions and is described in detail in Section 2.6. This theory would then have the weight of experimental observation added to it following numerous Raman spectroscopy [114, 115], inelastic neutron scattering [116] and IR reflectance [117] studies. Indeed, the theory of Cochran and Anderson would prove to be far more general than describing just the ferroelectric phase transition, extending to soft phonon modes away from the zone centre [114] and even a theory of magnetic phase transitions, or, *magnon softening* [118, 119].

Heading now into late 1960's and early 1970's, piezoelectric ceramics were now a commodity dominated by PZT transducers. An accurate account of the developments in this era can be found in the seminal book of Jaffe, *Piezoelectric Ceramics* [44]. It was during this period that the theory of ferroelectricity would advance once more following the works of Aizu who found and tabulated *all* of the spacegroups capable of the ferroelectric phase transition [120–122]. It is clear now that a centrosymmetric crystal class *cannot* possess a spontaneous polarisation. When also considering symmetries which allow for a divertible polarisation in a direction *not* opposite

[†] Although the soft mode theory was indeed developed by Cochran and Anderson, the idea of a soft mode was founded much earlier by Raman studying the α - β transformation in quartz [69].

to the current direction, there are in total thirty three crystal classes where ferroelectricity is possible [120].

Also during the 1970's the first signatures of improper ferroelectrics began to appear in $\text{Gd}_2(\text{MoO}_4)_3$ [123, 124]; classified by the onset of ferroelectricity being only a secondary order parameter in the phase transition. In addition, we note that although being discovered in the 1950's, the 1970's and 1980's also produced important studies on the dielectric properties of the relaxor ferroelectrics. These are crystals with a cubic symmetry condensing polar nano-domains below a critical temperature known as the Burns temperature [125]. They are known to give rise to a giant electromechanical response and a peak in the dielectric spectrum much broader than a standard ferroelectric. The general properties of the relaxor ferroelectrics are described in [126, 127] and references therein.

We turn our attention now to a great advance in the theory of ferroelectric crystals. That is, before the 1990's the calculation of a ferroelectric's intrinsic macroscopic polarisation was not possible for infinite crystals described with periodic boundary conditions; the most common setup for simulations of solids. It was only after the work of Vanderbilt, King-Smith [65] and Resta [66] paired with the Berry-phase formalism [64] that this problem was solved. This work became known as the modern theory of polarisation and is described in Section 2.5. Now well into the 1990's, calculations utilising Density Functional Theory (discussed in great detail in Chapter 3) exploded onto the scene. In particular, the work of Cohen used the theory to produce a first principles explanation for the origin of ferroelectricity in the perovskite oxides [3, 128]. Using the prototypical ferroelectrics BTO and PTO, it was found that Oxygen 2p-Titanium 3d orbital hybridisation is essential for the onset of ferroelectricity [3]. It was also found that the two perovskites differed in their ground states due to the partially covalent character of Pb-O bonds versus the nearly completely ionic Ba-O bonds [3].

2.3 Antiferroelectricity

The definition of an antiferroelectric material is not as clear-cut as a ferroelectric one. There have been several proposed definitions which are discussed and compared in [37]. We proceed now with what *I believe* to be the most intuitive definition. That is, much like ferroelectrics, antiferroelectrics can be considered as being related to their magnetic analogue, antiferromagnets. In an antiferromagnet, local magnetic dipole moments oppose one another such that the substance has a net zero magnetisation. In an antiferroelectric, local electrical dipole moments (often due to the counter-displacements of metal cations as can be seen for PZO in Figure 2.5) oppose one another resulting in the substance having a net zero electrical polarisation. Further, the reaction of an antiferroelectric to an applied electric field is rather different to a ferroelectric (Figure 2.3b). As a result of having zero spontaneous polarisation ($\mathbf{P}(\mathbf{E} = 0) = 0$), the hysteresis loop must take on a *pinched* shape. There is some energy cost to align the counter-aligned dipoles which is

overcome at some finite E . Once overcome, the crystal now exists in a poled ferroelectric phase which defines another criterion for an antiferroelectric material; a competing ferroelectric phase. The result of this is a *double* hysteresis curve as shown in Figure 2.3b. Such a property makes this class of material particularly useful in energy storage devices [35].

2.3.1 An even briefer history

While Kittel's definition of an antiferroelectric [129] dates back to as early as 1951, comparatively little is known about these materials in relation to their ferroelectric counterparts. Accompanying Kittel's definition, in the same year, were the observations made by Shirane et. al [36] of antiferroelectricity in PZO and in 1952 of antiferroelectricity in $(\text{Pb-Ba})\text{ZrO}_3$ and $(\text{Pb-Sr})\text{ZrO}_3$ solid solutions [130]. It was here that the definition of this class of compounds was added to further by suggesting a competing ferroelectric phase: "*It is concluded, from these situations, that the antiferroelectric phase in pure PbZrO_3 must be very peculiar, the free energy of this phase being closely adjacent to those of a ferroelectric phase as well as another antiferroelectric phase.*" [130]. Such is the peculiarity of this phase that the currently accepted spacegroup ($Pbam$; the crystal structure is displayed in Figure 2.5) was only decided upon in 1982 by the accurate XRD/neutron diffraction studies of Fujishita et al. [42] after a number of failed space group assignments by other studies[†]. Although it was long expected, it was later found that PZO's isoelectronic partner, PbHfO_3 (PHO) was also a $Pbam$ antiferroelectric, isostructural with PZO [131].

Despite the complexity of the PZO and PHO crystal structure, these are still considered the drosophila of antiferroelectrics. Should we cast our minds back to Section 2.2.2 (and to the not-so-drosophila Rochelle Salt), it is clear that this complexity would wreak havoc for attempts to determine the mechanism for the paraelectric to antiferroelectric phase transition. In fact, this is *still* a topic for debate. Some argue that the $Pbam$ phase is a 'missed' incommensurate phase driven by the softening of a single lattice mode via flexoelectric coupling [38]. Some regard this theory as being too exotic and claim that the work of Vales-Castro et. al [39] rules out this mechanism since neither the flexoelectric or flexocoupling coefficients are anomalously high at the Curie temperature. Further, the recent first-principles finite-temperature simulations of Xu et. al [40] suggest that near the paraelectric to antiferroelectric phase transition temperature, no true soft modes exist at all, suggesting the transition is order-disorder based [40]. This is in contrast to the first-principles effective Hamiltonian model of Fthenakis and Ponomareva [41] who *do* find explicit mode softening. As if there weren't enough spanners in the works, the first-principles determined Landau expansions of Íñiguez et. al [85] suggest that PZO (and probably PHO) isn't even a proper antiferroelectric, but, an improper one. That is, the antipolar Pb-O mode is only secondary to the phase transition.

[†]The road to finding the currently proposed crystal structure of antiferroelectric PZO is documented nicely in the paper by Fujishita et al. [42].

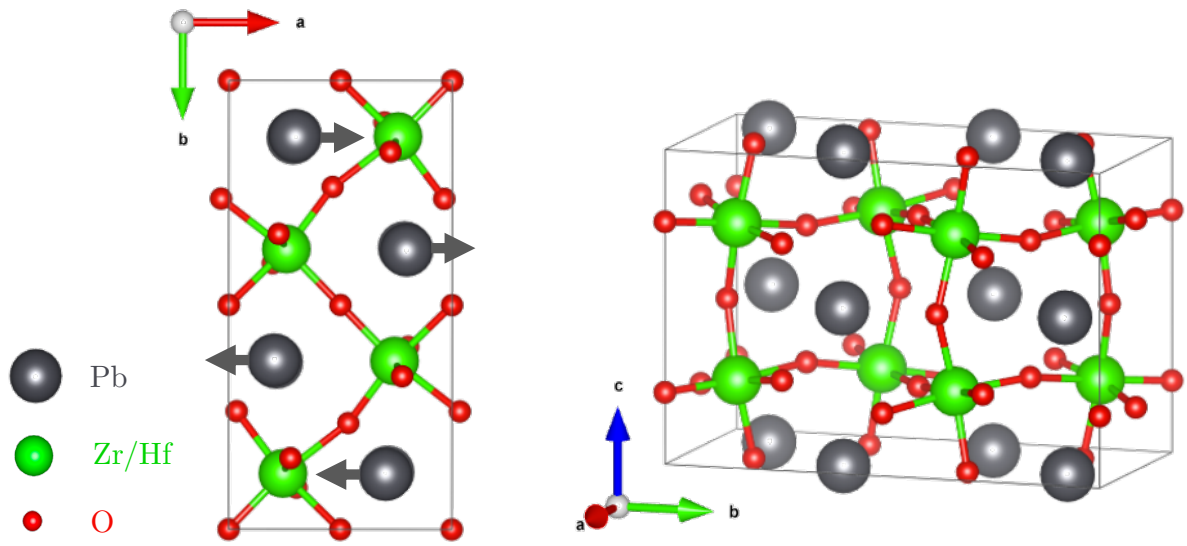


Figure 2.5: The $Pbam$ crystal structure of PZO/PHO from two different viewing angles. The left figure has arrows on the Pb sites indicating the two-left two-right antipolar displacement pattern. The right figure allows one to more easily see the antiphase rotations of the Zr/HfO_6 octahedra about the $[1\bar{1}0]$ axis.

It is remarkable that it was only this year (2020) that evidence of a true and ‘proper’ displacive antiferroelectric transition has emerged within francisite $Cu_3Bi(SeO_3)_2O_2Cl$ [132]. This appears as a single soft mode at the zone boundary (fractional $q = (0, 0, 1/2)$) measured by X-ray scattering, Raman spectroscopy and supported with first principles results[‡]. If the history of ferroelectricity has taught us anything, the discovery of this archetypal transition will likely expand our knowledge greatly towards a full understanding of the antiferroelectric phenomenon.

2.4 The phenomenological Landau-Devonshire theory

The work enclosed within this thesis tackles ferroelectric phenomena from an atomistic perspective. Another treatment, however, exists from a purely macroscopic perspective founded only upon symmetry considerations and thermodynamics. It is the aim of this section to introduce the reader to this purely phenomenological theory, presenting a simple picture of the behaviour of a uniform, bulk ferroelectric near the phase transition temperature. This approach is known formally as Landau-Devonshire (LD) theory [59, 60]. We note that whilst this theory generalises for spatial gradients of the polarisation, with and without boundary conditions (Landau-Ginzburg-Devonshire theory, or, LGD theory) these discussions are beyond the scope of this section. The reader is instead referred to [61–63] and references therein.

We begin by presenting a postulate of thermodynamics. That is, the free energy F (specifically

[‡]Although, it is noted in [132] that the displacements predicted by the first-principles model (at 0K) are at odds with the measured finite temperature displacement pattern.

the Gibbs free energy) of a system in equilibrium can be specified completely by some special variables pertaining to the system of interest. In the case of a spatially uniform ferroelectric these are the temperature T , the polarisation P , the electric field E , the strain η and the stress σ . In most cases, in fact, the free energy can be specified only by the three Cartesian components of the polarisation, the six independent elements of the stress tensor and by the temperature. It is useful here to work instead with the free energy density \mathcal{F} ($F = \int \mathcal{F}dV$) which we now Taylor expand in the vicinity of the phase transition, choosing the origin of the energy for the unpolarised phase to be zero

$$\mathcal{F}_P = \frac{1}{2}aP^2 + \frac{1}{4}bP^4 + \frac{1}{6}cP^6 - EP + \mathcal{O}(P^8). \quad (2.1)$$

See that we have chosen to neglect stress and strain effects in this expansion, but, we will come back to this later. The equilibrium of Equation 2.1 is found with elementary calculus (by setting $\partial\mathcal{F}_p/\partial P = 0$)

$$E = aP + bP^3 + cP^5. \quad (2.2)$$

We then obtain the linear dielectric susceptibility χ of the non-polar phase (i.e, above the phase transition temperature) by finding the minimum of Equation 2.2 with respect to P and then setting $P = 0$

$$\chi_{T>T_0} = \frac{1}{a} = \frac{P}{E}. \quad (2.3)$$

Within the framework of LD theory we now make the assumption that the quadratic coefficient a is a linear function of the temperature close to the Curie point

$$a = a_0(T - T_0) \quad (2.4)$$

where a_0 is a positive constant. By inspection, then, we see that the reciprocal dielectric susceptibility (or dielectric stiffness, κ) is the quadratic coefficient a

$$\kappa_{T>T_0} = \chi_{T>T_0}^{-1} = a_0(T - T_0). \quad (2.5)$$

It is clear now that our system follows a Curie-Weiss law, implying some physical motive for our choice of $a(T)$. We can now rewrite Equation 2.1 with the additional temperature dependence

$$\mathcal{F}_P = \frac{1}{2}a_0(T - T_0)P^2 + \frac{1}{4}bP^4 + \frac{1}{6}cP^6 - EP + \mathcal{O}(P^8). \quad (2.6)$$

If we then assume that the coefficients b and c are positive (c is in fact positive for *all* known ferroelectrics [61]), we can see from Equation 2.6 that the behaviour of \mathcal{F}_P above T_0 is parabolic but below T_0 develops a double well in the free energy density (Figure 2.6i). These

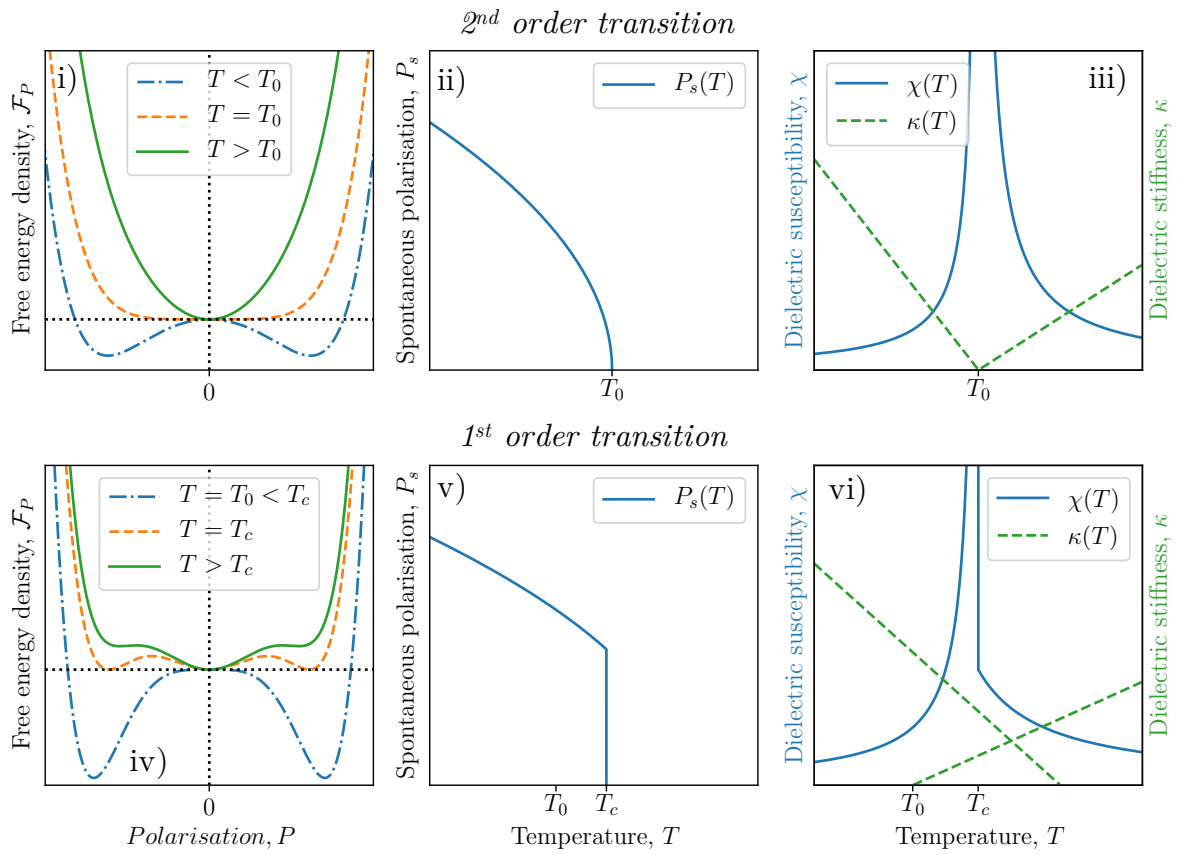


Figure 2.6: The free energy density (as a function of polarisation), spontaneous polarisation and dielectric susceptibility/stiffness (all as a function of temperature) for second (i - iii) and first (iv - vi) order transitions as predicted by LD theory.

two degenerate minima have finite polarisation in the absence of an applied field so correspond to the spontaneous polarisation

$$P_s = \pm \left[\frac{a_0}{b} (T - T_0) \right]^{\frac{1}{2}}. \quad (2.7)$$

This gradual and continuous change in P near the Curie point is characteristic of a *second order* phase transition. This transition is not common in the perovskite oxides but has been observed for the onset of ferroelectricity in triglycine sulfate [133]. Given the same conditions, we can also extract the dielectric susceptibility below T_0^\dagger

$$\chi_{T < T_0} = \frac{1}{2a_0(T_0 - T)}. \quad (2.8)$$

We should now consider the case where the quartic coefficient $b < 0$ and $a_0 > 0, c > 0$. In this case, we observe some rather different behaviour. We see now that even if $T > T_0$, the free energy density has multiple minima (Figure 2.6iv). We see a local minimum at $P = 0$ and two mirrored minima at finite P . As we reduce temperature, the minima at finite P eventually become more thermodynamically favoured than $P = 0$. The point at which this occurs is the curie temperature, T_c . What separates this behaviour from the second order transition is the sudden change in P at the phase transition temperature (Figure 2.6v) such that it discontinuously falls to zero at $T = T_c$. This is known as a *first order* transition, describing the onset of ferroelectricity in many perovskite oxides including the prototype BTO [59, 60]. We can also derive $P_s(T)$ (Figure 2.6v), $\chi(T)$ and $\kappa(T)$ (Figure 2.6vi) following the same procedure as before.

We move now to consider the effects of strain (η) on the LD free energy density. This turns out to be an important effect for most ferroelectrics due to a non-trivial coupling between strain and polarisation. In fact, if we consider a uniaxial ferroelectric, cubic above T_c , (like $P4mm$ BTO or PTO) we see the development of tetragonality parallel to the polar axis at zero applied stress σ . The tetragonal strain is therefore also a spontaneous quantity in a phenomenon known as ferroelasticity. A simple symmetry argument deduces that the lowest order of strain/polarisation coupling *must be* quadratic in P , ηP^2 . A linear coupling, for example, would impact the free energy density differently depending on the sign of P . This must be nonsense since in our pseudocubic crystal, polarisation can develop along any one of the six symmetry equivalent directions. Let us then expand the free strain energy density \mathcal{F}_η

$$\mathcal{F}_\eta = \frac{1}{2} K \eta^2 + Q \eta P^2 + \mathcal{O}(P^4) - \eta \sigma \quad (2.9)$$

for coefficients K and Q . The first term is Hookean whilst the second is the result of the symmetry of the transition. In general, other symmetries are allowed although we will continue

[†]That is, by setting $P = P_s$ in the derivative of Equation 2.2 and solving the resulting quartic equation.

with our pseudocubic example. Consider now the thermodynamic minima with respect to both η and P of the combined free energy density $\mathcal{F} = \mathcal{F}_P + F_\eta$

$$\frac{\partial \mathcal{F}}{\partial P} = \frac{\partial \mathcal{F}}{\partial \eta} = 0. \quad (2.10)$$

The minimum with respect to η provides some interesting insight. For example, setting $P = 0$ we once more find Hooke's law, $\eta = \sigma/K$. Another case which is of importance in this thesis is where we apply a stress to force the strain to zero. This condition occurs when we mount a thin film upon a substrate, forcing the film to take on the lattice constant of the substrate; known as a *clamped* system. Lastly, we apply the condition of zero applied stress to find the spontaneous ferroelastic strain

$$\eta_s = -\frac{QP^2}{K} \quad (2.11)$$

confirming that at the lowest possible order of the expansion that $\eta_s \propto P^2$. Should we then set $\eta_s = \eta$ for the combined free energy density, we find that the quartic coefficient (of P) in the expansion becomes

$$b' = \frac{1}{4}(b - 2Q^2/K). \quad (2.12)$$

Recall that for a first order transition we have $b < 0$. Now with b' , the transition is even more strongly first order, increasing also T_0 . We see also that should $2Q^2/K > b > 0$ a first order transition now becomes second order for a clamped system. We observe this effect in clamped BTO [134]. Indeed, choosing a substrate with a different misfit strain allows one to tune the quartic coefficient of the free energy expansion to either strengthen or dull the ferroelectric instability. Such an approach is often referred to as epitaxial strain engineering. This approach has also been used to drive a second order transition in strained PTO [135] as well as driving in-plane ferroelectricity in the incipient ferroelectric STO [136].

2.5 The modern theory of electrical polarisation

The modern theory of electrical polarisation was born from what was at the time perceived to be a logical fallacy. Specifically, this fallacy was for the calculation of the macroscopic polarisation of solids with periodic boundary conditions [67]. This comes about by taking a naive definition of the polarisation, that is, the dipole moment, \mathbf{d} , of a unit cell of the sample divided by the unit cell volume Ω

$$\mathbf{P} = \frac{\mathbf{d}}{\Omega} \quad (2.13)$$

where \mathbf{d} is defined in the standard way using the positions, \mathbf{r}_i , of an ensemble point charges

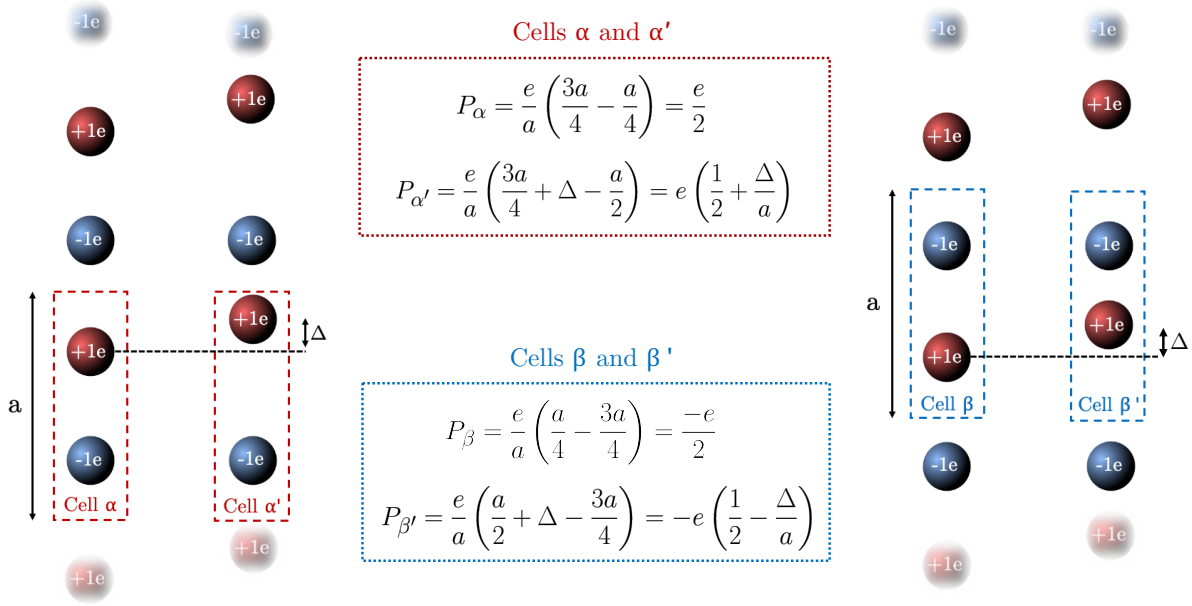


Figure 2.7: A polar and non-polar infinite 1D ionic lattice. When calculating the polarisation, we see that it is many valued; dependant on our choice of unit cell.

q_i

$$\mathbf{d} = \sum_i q_i \mathbf{r}_i. \quad (2.14)$$

The reason this definition becomes troublesome is because, against our intuition, it leads to the polarisation becoming a many valued quantity [65–67, 137]. This strange occurrence is a consequence of the infinite definitions of a unit cell in any Bravais lattice. Take for example the case of an infinite 1D perfectly ionic lattice with alternating charges of $+1e$ and $-1e$ (Figure 2.7). Let us evaluate the polarisation (which in 1D is the dipole moment per unit length) for two valid unit cells α and β for the *non-polar* lattice where ions are at the lattice sites $a/4$ and $3a/4$. We see clearly from Figure 2.7 that $P_{\alpha} = e/2 \neq P_{\beta} = -e/2$. In fact, if we repeat this process for other valid unit cells on the same lattice we will find that the polarisation takes on a range of values constituting what is known as a polarisation lattice: $-\infty \leftarrow -5e/2, -3e/2, -e/2, e/2, 3e/2, 5e/2 \rightarrow \infty$, or, $eP_q/2 \pm neP_q$ where P_q is the *polarisation quantum*[†]. It is important to note that in this case the polarisation lattice is symmetrical about the origin which is indicative that the system is non-polar [68]. This many valued nature of the polarisation greatly troubled the theoreticians of the time leading to claims that the polarisation is not a valid quantity for systems with periodic boundaries and that a finite sample must be used to calculate \mathbf{P} . This thought is rather worrisome in itself since then the polarisation would depend on the details of the surface termination!

[†] P_q is defined by the change in polarisation for a unit cell by displacing an electron a full unit cell along a lattice vector. In our 1D lattice, we see then that $P_q = -1e$ [137].

Some sense can be made from this many valued quantity if we examine how a measurement of the spontaneous polarisation is taken in experiment. What is usually used is the Sawyer-Tower configuration [138]. This is setup is rather simple. The material for which we wish to measure the spontaneous polarisation of is placed between two electrodes. The polarisation of the material then causes a build-up of surface charge at one electrode (as a mechanism of screening the depolarising field) and a build-up of holes at the other electrode. If we then switch the direction of the polarisation of the sample (as is possible by electric field for a ferroelectric), the electrons and holes flow through a circuit connected across the electrodes such that there are electrons where there were once holes and vice versa. The current generated from this switching flows through a reference capacitor which then measures *twice* the spontaneous polarisation ($2P_s$). It is clear from this measurement that what was actually measured was the *difference* in polarisation ΔP between the up and down polarised states and *not* the polarisation itself. Let us then extend this logic to our infinite 1D ionic lattice. Consider now unit cells α' and β' in the polarised ionic lattice of Figure 2.7. The cations have been displaced a small amount Δ relative to the anions (in a manner similar to what you would observe in a true ferroelectric phase transition). We once again find that the polarisation for two unit cells are not the same, $P_{\alpha'} \neq P_{\beta'}$. Taking the difference with the non-polar cells α and β , however, yields the same result independent of our choice of unit cell

$$\Delta P_{\alpha} = P_{\alpha'} - P_{\alpha} = \Delta P_{\beta} = P_{\beta'} - P_{\beta} = e \frac{\Delta}{a}. \quad (2.15)$$

It is now clear that for a calculation of the electrical polarisation, we must instead talk about the *polarisation difference* and not the polarisation itself. To do so in practice, we must calculate the polarisation of two structures (usually a non-polar paraelectric reference and polar ferroelectric structure) then take their difference. We must be careful, however, to ensure that both structures share the same polarisation quantum P_q . This is usually checked by evaluating several points on what is known as a *polarisation branch*. That is, we calculate polarisation as a gradual function of the ferroelectric distortion - a branch - ensuring that the cases of maximal and minimal distortion connect as a smooth function without discontinuity. In the case of our infinite 1D ionic lattice, branches are simple linear functions of Δ , uniformly shifted upwards or downwards in polarisation by P_q depending on our choice of unit cell. Such a process may now be possible to bypass in some cases following the newly developed Berry flux diagonalisation approach described in [139].

The perfect ionic lattice example is purely pedagogical of course. Real systems are usually regarded as having a continuous electronic charge density $n(\mathbf{r})$ as well as point ion-like cores. Whilst the polarisation contribution from the latter is calculable in the manner considered before, the calculation of the former takes more consideration. It is clear that $n(\mathbf{r})$ need not be localised to certain areas of a unit cell. Our system of interest could have a significant covalent character

in its bonding which causes a problem for identifying a clear polarisable unit. Further, the Bloch functions $\psi_{n\mathbf{k}}(\mathbf{r})$ underlying any lattice periodic wavefunction are intrinsically delocalised in space. It is then useful to consider not the Bloch functions but their Fourier transformed counterparts; Wannier functions (WFs) $W_n(\mathbf{r} - \mathbf{R})$ [140]

$$W_n(\mathbf{r} - \mathbf{R}) = \frac{\Omega}{(2\pi)^3} \int_{\text{1BZ}} e^{i\mathbf{k}\cdot(\mathbf{r}-\mathbf{R})} u_{n\mathbf{k}}(\mathbf{r}) d^3\mathbf{k} \quad (2.16)$$

in unit cell \mathbf{R} and where the integral is over the first Brillouin zone. This format is particularly useful since we can, in real space, find the expectation value of the position operator[†] $\langle \hat{\mathbf{r}} \rangle$ and treat the electrons belonging to the WF of band n as all being at this position. This position is known as the Wannier centre $\bar{\mathbf{r}}_n$

$$\bar{\mathbf{r}}_n = \int W_n^*(\mathbf{r}) \hat{\mathbf{r}} W_n(\mathbf{r}) d^3\mathbf{r}. \quad (2.17)$$

Using the momentum space representation of the position operator $\hat{\mathbf{r}} = -i\frac{\partial}{\partial\mathbf{k}}$ [141] and substituting for Equation 2.16, we find that in terms of the lattice periodic part of the Bloch functions (a proof for this step can be found in [142])

$$\bar{\mathbf{r}}_n = \frac{i\Omega}{(2\pi)^3} \int_{\text{1BZ}} e^{i\mathbf{k}\cdot\mathbf{R}} \left\langle u_{n\mathbf{k}} \left| \frac{\partial u_{n\mathbf{k}}}{\partial\mathbf{k}} \right. \right\rangle d^3\mathbf{k}. \quad (2.18)$$

We can now simply proceed as before, but, separating the electronic contributions from the ionic cores

$$\mathbf{P} = \frac{1}{\Omega} \left(\sum_i (q_i \mathbf{r}_i)^{\text{ions}} + \sum_n^{\text{occ}} (q_n \bar{\mathbf{r}}_n)^{\text{WFs}} \right). \quad (2.19)$$

As before, Equation 2.19 is a many valued quantity, now on a 3D polarisation lattice. We then proceed to take the difference between two configurations (again, usually between a high symmetry non-polar and a polar crystal), $\Delta\mathbf{P}$. With the help of Equations 2.18 and 2.19, we have

$$\begin{aligned} \Delta\mathbf{P} &= \mathbf{P}_s \\ &= \left[\frac{1}{\Omega} \sum_i q_i (\mathbf{r}_i^f - \mathbf{r}_i^0) \right]^{\text{ions}} - \frac{2ie}{(2\pi)^3} \sum_n^{\text{occ}} \left[\int_{\text{1BZ}} e^{i\mathbf{k}\cdot\mathbf{R}} \left\langle u_{n\mathbf{k}}^f \left| \frac{\partial u_{n\mathbf{k}}^f}{\partial\mathbf{k}} \right. \right\rangle - \left\langle u_{n\mathbf{k}}^0 \left| \frac{\partial u_{n\mathbf{k}}^0}{\partial\mathbf{k}} \right. \right\rangle d^3\mathbf{k} \right] \end{aligned} \quad (2.20)$$

for initial non-polar structure 0 and final polar structure f . Once again, care must be

[†]Some care must be taken when considering $\langle \hat{\mathbf{r}} \rangle$ in systems in periodic boundary conditions. That is, following the seminal work of Resta, the position operator (in standard Schrödinger representation in real space) for an isolated system is not commensurate with a periodic one. A new definition for $\langle \hat{\mathbf{r}} \rangle$ is given in [67].

taken to ensure both the initial and final structures exist on the same polarisation branch. Notice that the second term of Equation 2.20 is the Berry phase developed by $u_{n\mathbf{k}}$ as it evolves along the path of wavevector \mathbf{k} [64, 65, 143]. It is for this reason that this approach is often referred to as the Berry phase theory of polarisation. The Berry phase formalism appears also in other areas of physics, well known for describing the Aharonov-Bohm effect [144] and the properties of topological insulators [145].

From the definition in Equation 2.20, there are two paths to proceed for evaluating \mathbf{P}_s in practice. The first is to explicitly calculate the WFs[†] for the initial and final structures. This is usually performed by computing the Wannier centres of the maximally localised Wannier functions (MLWFs) for which the mean square of their positional spread is minimised with respect to the phase of the Bloch functions [146]. We then take the difference in the two values of \mathbf{P} calculated trivially applying Equation 2.19.

The second approach is to perform the integral on the RHS of Equation 2.20. We first calculate the matrix elements $\langle u_{n\mathbf{k}} | \partial u_{n\mathbf{k}} / \partial \mathbf{k} \rangle$ by integrating along a string of \mathbf{k} -points. We note that since $\partial / \partial \mathbf{k}$ is a vector derivative, we must calculate these matrix elements along three non-collinear directions [137]. We then for each component of the polarisation take multiple strings of \mathbf{k} -points, calculate the Berry phase and average the value (thus performing the BZ integral) over the number of strings used. We must take care here to converge these calculations both with respect to the number of \mathbf{k} -points in each string and with respect to the total number of strings. We should also check that the calculated Berry phase for each \mathbf{k} -point string exists on the same polarisation branch. Failing to do so can cause the resulting polarisation from averaging over strings to erroneously become close to zero.

We finish this Section remarking upon a useful definition sometimes used in this thesis for the calculation of the spontaneous polarisation in the limit of large supercells (where the cell dimensions $L \rightarrow \infty$) as suggested by Resta [147]. That is, the case where the BZ integral on the RHS is converged with a single \mathbf{k} -point; the Γ point. We simply replace this term with

$$\lim_{L \rightarrow \infty} \Delta P^{\text{elec}} = -\frac{e}{\pi L^2} [\text{Im} \ln \det \mathbf{S}^f - \text{Im} \ln \det \mathbf{S}^0] \quad (2.21)$$

where $\mathbf{S}^{f/0}$ is the connection matrix of the KS states for the initial non-polar or final polar structure with elements

$$S_{ij}^{f/0} = \langle \psi_n^{f/0} | e^{i\frac{2\pi\hat{\mathbf{r}}}{L}} | \psi_{n'}^{f/0} \rangle. \quad (2.22)$$

This is sometimes known as the *two point Berry phase formula*; often used for the calculation of polarisation in Car-Parrinello simulations [148–150].

[†]Since the Bloch functions are defined only to within a phase factor, the WFs cannot be uniquely defined. However, in accordance with Equation 2.20 we only need the sum over the Wannier centres to be well defined, which it is.

2.6 Lattice dynamics

The phenomenological LD theory described in Section 2.4 adequately explains the observed phenomena near T_c of a ferroelectric phase transition. We must note, however, that the central order parameter (along with other variables) for which we performed the expansion of the free energy density was assumed *a priori* to be the polarisation P . In fact, it is clear that LD theory makes no account for the microscopic origin of any order parameter but instead describes the consequences of their onset. The soft mode theory described in this section addresses this shortcoming for the observed phase transitions in many crystals. We note that whilst the soft mode concept was developed originally for the description of the onset of ferroelectricity (and is what we address mostly in this section), it has since become a far more general theory describing many other structural phase transitions.

2.6.1 An overview of crystal vibrations

The soft mode concept is one rooted in the field of lattice dynamics. This field is concerned with the temperature induced oscillations of a system of nuclei forming the basis of a crystal lattice. The collective excitations of this oscillating mechanical field are known as *phonons* [72] and are the main concern of this section. The evaluation of phonon modes (which equate to a particular nuclear displacement pattern) and their frequencies are usually conducted assuming the quasi-harmonic approximation. That is, nuclear vibrations behave as if they are a system of interconnected harmonic oscillators [72]. We can then Taylor expand, to second order, the total energy of this system in mechanical equilibrium with nuclei κ located at the Cartesian coordinates $R_{\kappa,\alpha}$ [151]

$$E = E_0 + \sum_{\kappa,\alpha} \frac{\partial E}{\partial u_{\kappa,\alpha}} \cdot u_{\kappa,\alpha} + \frac{1}{2} \sum_{\kappa,\alpha,\kappa',\alpha'} u_{\kappa,\alpha} \cdot \phi_{\alpha,\alpha'}^{\kappa,\kappa'} \cdot u_{\kappa',\alpha'} + \dots \quad (2.23)$$

where E_0 is the total energy of the equilibrium system, α is a Cartesian direction, $u_{\kappa,\alpha}$ is a displacement from the equilibrium configuration and $\phi_{\alpha,\alpha'}^{\kappa,\kappa'}$ is the real space force constant matrix

$$\phi_{\alpha,\alpha'}^{\kappa,\kappa'} = \frac{\partial^2 E}{\partial u_{\kappa,\alpha} \partial u_{\kappa',\alpha'}} = \frac{\partial F_{\kappa\alpha}}{\partial u_{\kappa',\alpha'}} \quad (2.24)$$

which we note has an infinite range for a system with periodic boundary conditions. We can see that the second term of Equation 2.23 must vanish at the equilibrium since the forces $F_{\kappa,\alpha} = -\partial E / \partial u_{\kappa,\alpha} = 0$. The periodic boundary conditions permit a plane-wave solution for the displacements [151]

$$\mathbf{u}_{\kappa} = \mathcal{W}_{m\kappa,\mathbf{q}} e^{i\mathbf{q} \cdot \mathbf{R}_{\kappa} - \omega_{m,\mathbf{q}} t} \quad (2.25)$$

for phonon propagation wavevector \mathbf{q} , polarisation vector $\mathcal{W}_{m\kappa,\mathbf{q}}$ and oscillation frequency

$\omega_{m,\mathbf{q}}$. Substituting into Equation 2.23, after some manipulation, yields the eigenproblem

$$D_{\alpha,\alpha'}^{\kappa,\kappa'}(\mathbf{q})\mathcal{W}_{m\kappa,\mathbf{q}} = \omega_{m,\mathbf{q}}^2\mathcal{W}_{m\kappa,\mathbf{q}} \quad (2.26)$$

where $D_{\alpha,\alpha'}^{\kappa,\kappa'}(\mathbf{q})$ is the dynamical matrix [151] defined as

$$D_{\alpha,\alpha'}^{\kappa,\kappa'}(\mathbf{q}) = \frac{1}{\sqrt{M_\kappa M_{\kappa'}}} \sum_{\mathbf{R}} \phi_{\alpha,\alpha'}^{\kappa,\kappa'} e^{i\mathbf{q}\cdot\mathbf{R}}. \quad (2.27)$$

We see then that the dynamical matrix is the Fourier transform of the force constant matrix normalised by the nuclear mass M_κ [151]. Solving the eigenproblem of Equation 2.26 yields the vibrational frequencies $\omega_{m,\mathbf{q}}$ and thus the important phonon dispersion relations as shown in Figure 2.8 for cubic PTO. The mathematics laid out above may seem rather formal but are simply an extension of a one dimensional simple harmonic oscillator obeying Hooke's Law[†] to three dimensions in periodic boundary conditions. This paints the picture that the quasi-harmonic dynamical matrix is just a collection of spring constants, K .

If we are able to calculate the dynamical matrix of a system, we can solve the eigenproblem of Equation 2.26 giving us access to the nuclear displacement patterns (the eigendisplacements) and their frequencies of oscillation (the eigenfrequencies). Methods for calculating $D_{\alpha,\alpha'}^{\kappa,\kappa'}(\mathbf{q})$ using electronic structure calculations are discussed in Chapter 3, Section 3.5. Once we have these quantities, they can be used to calculate many of the thermodynamical variables of the system [151].

As we will later learn, the ferroelectric distortion arises from a polar phonon mode at the zone centre $\mathbf{q} = (0, 0, 0)$ [109, 154]. It is appropriate then to discuss an issue implicit in the above formalism for polar modes of this wavevector. This issue is with the eventual undefined nature of longitudinal-optical-transverse-optical (LO-TO) splitting as $\mathbf{q} \rightarrow 0$. An interesting discussion of the physical origin of this phenomenon can be found in reference [155]. LO-TO splitting is best understood with the aid of a figure. Modes participating in LO-TO splitting are usually accessible to neutron scattering, so, we imagine we have a neutron of momentum $\hbar\mathbf{q} = \hbar(q_x, 0, 0)$ incident upon one of the mutually orthogonal axes of a cubic crystal as shown in Figure 2.9. This neutron excites three polar modes. One in the direction of \mathbf{q} (the LO mode) and two mutually orthogonal to \mathbf{q} (the TO modes; TO 1 and 2). Now, since these modes are polar, an internal electric field is generated in the axis of the oscillation. We now take the dot product of \mathbf{q} with this electric field, finding that the only non-zero contribution comes from $\mathbf{E} \parallel \mathbf{q}$; the LO mode. This amounts to an additional restoring force only for the LO phonon, causing its frequency to be shifted upwards. This effect is accounted for implicitly in the calculation of $D_{\alpha,\alpha'}^{\kappa,\kappa'}(\mathbf{q})$ for all \mathbf{q} apart from $\mathbf{q} = (0, 0, 0)$. Here, we find that $\mathbf{q} \cdot \mathbf{E}$ is exactly zero for all three excited modes such that no splitting occurs. The result is a sudden and discontinuous degeneracy of the LO and TO modes

[†]Since $F = -Kx$ for a Hookean spring and $F = -m\omega^2x$ for a simple harmonic oscillator, we see that $(K/m)x = \omega^2x$ which is rather reminiscent of Equation 2.26.

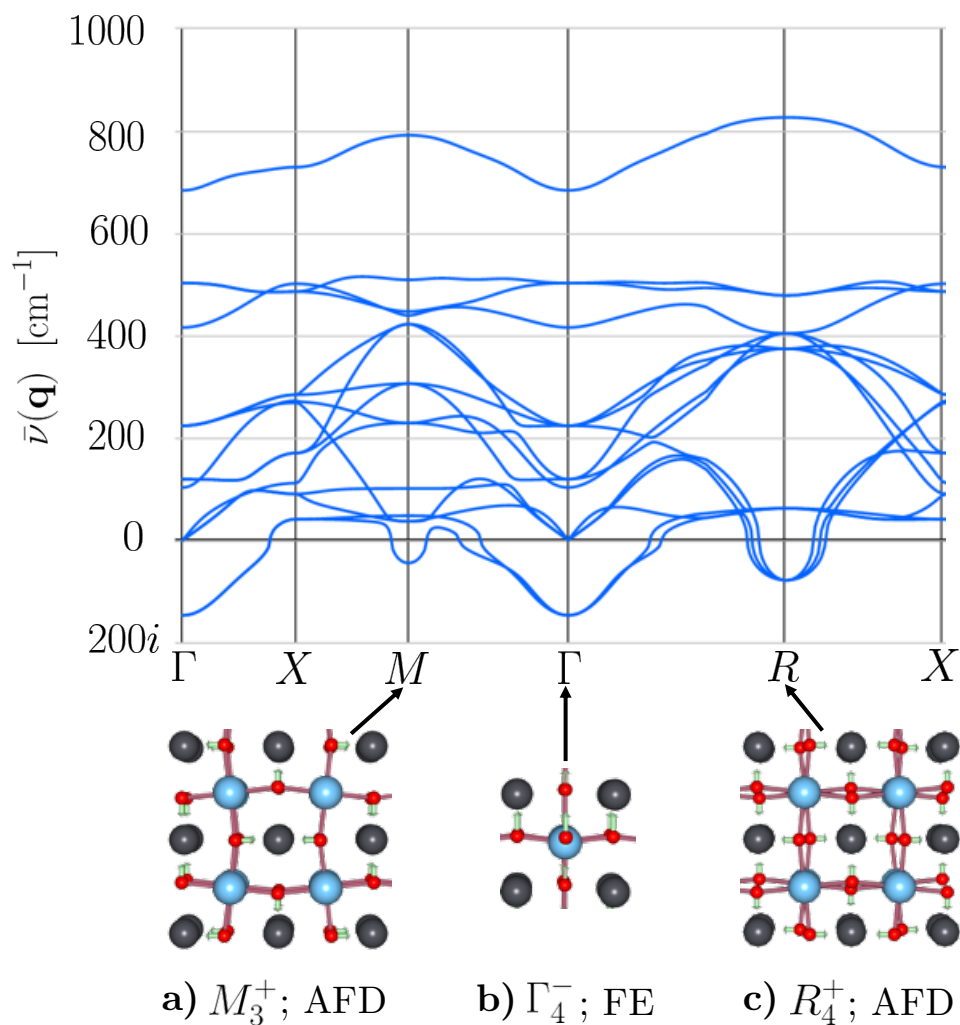


Figure 2.8: The phonon dispersion curves of $Pm\bar{3}m$ PTO as calculated with density functional perturbation theory using the projector augmented wave method [152] and the LDA functional of Perdew and Wang [153]. The ionic displacement patterns derived from the eigendisplacements of the soft modes are displayed below the dispersion. a) The M_3^+ mode featuring in-phase $a^0a^0c^+$ rotations. b) The Γ_4^- mode describing the ferroelectric distortion. c) The R_4^+ mode featuring anti-phase $a^0a^0c^-$ rotations.

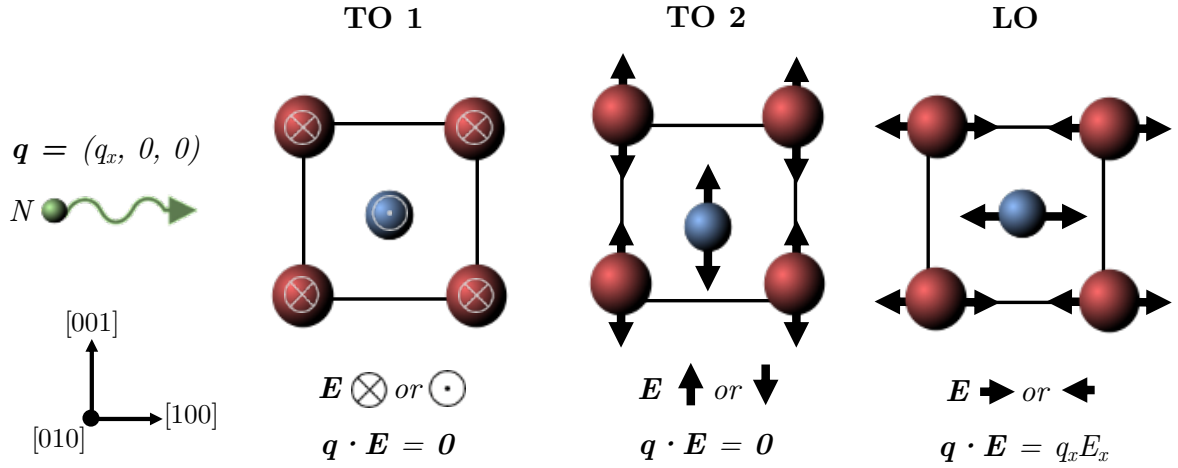


Figure 2.9: A neutron of wavevector $\mathbf{q} = (q_x, 0, 0)$, $q_x \rightarrow 0$ but $q_x \neq 0$ is incident upon an exemplar ionic lattice (+ve ions in red, -ve ions in blue). Three polar phonon modes are excited: TO 1, TO 2 and LO. Each mode generates an internal E , but, only in the LO mode is its dot product with \mathbf{q} non-zero. The resulting force shifts the frequency upwards resulting in LO-TO splitting.

at the Brillouin zone centre. For small \mathbf{q} in a cubic crystal, it is found that this frequency shift of the LO mode can be calculated with the well known Lydanne-Sachs-Teller (LST) relation [156]

$$\frac{\epsilon_0}{\epsilon_\infty} = \frac{\omega_{LO}^2}{\omega_{TO}^2} \quad (2.28)$$

for low/high frequency dielectric constants $\epsilon_0/\epsilon_\infty$ and LO/TO phonon frequencies ω_{LO}/ω_{TO} . In general, however, we find that to include all symmetries (not just cubic) we must instead add an additional non-analytical correction (NAC) term [151] to Equation 2.27 and evaluate the shifted eigenfrequencies by solving the eigenproblem of Equation 2.26

$$\text{NAC } \Delta D_{\alpha, \alpha'}^{\kappa, \kappa'}(\mathbf{q} \rightarrow \mathbf{0}) = \frac{1}{\sqrt{M_\kappa M_{\kappa'}}} \frac{4\pi e^2}{\Omega} \frac{(\mathbf{q} \cdot \mathbf{Z}_\kappa^*)_\alpha (\mathbf{q} \cdot \mathbf{Z}_{\kappa'}^*)_{\alpha'}}{\mathbf{q} \cdot \epsilon_\infty \cdot \mathbf{q}}. \quad (2.29)$$

Note that this equation is still undefined for \mathbf{q} of *exactly* zero, but, defines the limiting case for which we usually use to interpolate the phonon dispersion near $\mathbf{q} = (0, 0, 0)$. A property of this correction which can be a cause for alarm for an observer of a phonon dispersion plot is its directionality for non-cubic crystals. That is, some bands become discontinuous as we approach Γ from different directions. This is completely natural consequence of ϵ_∞ becoming anisotropic and \mathbf{Z}^* gaining more unique elements (perhaps even becoming non-diagonal) in the non-cubic space group. Explicitly, we see from Equation 2.29 that two different small \mathbf{q} wavevectors, say $(\delta q, 0, 0)$ and $(0, \delta q, 0)$ would yield a different value for the NAC. I must emphasise that such discontinuities are *not* fictitious and are an observable phenomenon in inelastic neutron scattering [157].

2.6.2 Soft modes

The conceptual idea of a *soft mode* is profound to the field of structural phase transitions. It is fortunately quite simple to understand within the remit of the lattice dynamics discussed in the previous section (Section 2.6.1). The idea is rooted in a particular normal lattice mode exhibiting an anomalously strong (but gradual) reduction in its vibrational frequency as temperature is decreased [1, 2, 52, 70]. Close to the Curie temperature, T_c , the vibrational frequency is so small that we are left with a now-static nuclear displacement pattern *frozen in* to the original crystal[†]. This defines a symmetry lowering structural phase transition where the character of the eigendisplacements \mathbf{u}_κ (Equation 2.25) describe exactly the details of the transition (although not its equilibrium amplitude). Although this idea is generalised to normal modes at *any* wavevector within the first Brillouin zone [70], zone centre modes are of a particular interest to this work. Zone centre soft modes were the first to be studied in the perovskite oxides and are responsible for the ferroelectric phase transition [1, 2, 52].

2.6.2.1 A microscopic theory of ferroelectricity

We proceed now following the arguments of Cochran [2] in his seminal work on crystal stability and the theory of ferroelectricity. Cochran showed that it was possible to derive the Curie-Weiss behaviour of ferroelectric near T_c from a purely atomistic perspective; reconcilable with the macroscopic and phenomenological LD theory approach presented in Section 2.4. Let us begin by quoting two empirical relationships describing the zone centre vibrational frequencies of the LO and TO lattice modes of a diatomic cubic crystal. These equations are derived from a classical shell model which was (at the time) found to perform well in describing the lattice dynamics of sodium iodide [158]. These are

$$\mu\omega_{TO}^2 = R'_0 - \frac{4\pi}{9\Omega}(\epsilon_\infty + 2)(Z'e)^2, \quad (2.30)$$

$$\mu\omega_{LO}^2 = R'_0 + \frac{8\pi}{9\Omega\epsilon_\infty}(\epsilon_\infty + 2)(Z'e)^2 \quad (2.31)$$

for ion reduced mass μ , effective ionic charge Z' , short range restoring force spring constant R'_0 and unit cell volume Ω . Primed quantities here depend on the parameters of the given shell model which can be found in [158]. The first term on the RHS Equations 2.30 and 2.31 is representative of short range restoring forces. You should see that including just this term would be the result of equating the restoring force of a simple harmonic oscillator ($F = -m\omega^2x$) to the restoring force of a Hookean spring ($F = -R'_0x$). The second terms of the same equations represent long range Coulombic forces. Note that this term differs between Equations 2.30 and

[†]For the sake of clarity, the reason such modes are known as ‘soft’ is that this reduction in frequency is the result of weaker or *softer* spring constants for the bonds describing the particular eigenmode.

2.31 as a manifestation of LO-TO splitting as described in Section 2.6.1.

We examine now what happens as $\omega_{TO} \rightarrow 0$ when $T \rightarrow T_c$ as would occur in a mode softening. We argue that since the terms on the RHS of Equation 2.30 are linearly temperature dependent due to vibrational modes having anharmonic contributions [1, 2]. We then postulate that near T_c

$$\frac{\mu\omega_{TO}^2}{R'_0} = 1 - \frac{4\pi(\epsilon_\infty + 2)(Z'e)^2}{9\Omega R'_0} = \gamma(T - T_c) \quad (2.32)$$

where γ is a positive temperature coefficient. If we now use the LST relationship [156] of Equation 2.28 it can be shown that

$$\frac{\epsilon_0 - 1}{4\pi} \simeq \frac{\epsilon_0 - \epsilon_\infty}{4\pi} = \frac{(\epsilon_\infty + 2)^2(Z'e)^2}{9\Omega R'_0\gamma(T - T_c)} = \frac{C}{T - T_c} \quad (2.33)$$

such that a Curie-Weiss law is followed with Curie constant

$$C = \frac{(\epsilon_\infty + 2)^2(Z'e)^2}{9\Omega R'_0\gamma} \simeq \frac{\epsilon_\infty + 2}{4\pi\gamma}. \quad (2.34)$$

We have now shown from a microscopic origin the same anomaly in the dielectric susceptibility as was predicted by the phenomenological LD theory in Section 2.4. This is important because it allows us to consider the nature of the forces which drive the ferroelectric instability. Clearly from Equation 2.32, ω_{TO} is a decreasing function of decreasing temperature; exactly zero frequency at $T = T_c$ where the TO mode has frozen into the crystal. Consider now what must occur for the terms on the RHS of Equation 2.30 to allow for $\omega_{TO} = 0$. That is, the short range restoring forces must be equal to the long range Coulombic ones. It can be deduced then that short range restoring forces stabilise the crystal in its cubic structure against the destabilising Coulomb forces which quench ω_{TO} , favouring ferroelectricity.

2.6.2.2 Some practical implications at 0K

It is useful to discuss now the implications of this microscopic theory when working at a temperature of 0K. As we will learn in Chapter 3, Section 3.2, our main simulation method, DFT, is a theory which operates (most of the time [159]) at 0K. At $T = 0$, we are of course working below the phase transition temperature and some artefacts of this do arise. Take now the example of PTO. Despite being a high temperature phase, the cubic $Pm\bar{3}m$ crystal structure of PTO is metastable at 0K. This is since the high symmetry structure is such that the forces on each ion are equal and opposite thus defining a static equilibrium. We then ask the question, in such a metastable phase, what would happen to the frequency ω_{TO} ? We see that below T_c , the RHS of Equation 2.32 becomes negative. If we then evaluate ω_{TO} we find that it is an *imaginary frequency*.

A lattice ‘vibration’ of an imaginary frequency is clearly not a vibration in any standard sense.

Its meaning, however, can be derived simply with some high-school Physics [160]. Making use of Hooke's law and the vibrational frequency of a simple harmonic oscillator (here chosen to model the vibration of ions), we have

$$\omega = \sqrt{\frac{K}{m}} = \sqrt{\frac{-1}{m} \frac{dF}{dx}}. \quad (2.35)$$

Consider now the sign of dF/dx . $dF/dx < 0$ gives real ω ; a small ionic displacement dx produces a restoring force $-dF$. $dF/dx > 0$ gives imaginary ω ; the displacement dx now produces non-restorative dx . In this latter case, our 'springs' *push* the ions in a pattern defined by the eigendisplacements of the particular mode and force a structural phase transition. When such a situation arises in any crystal lattice, we refer to it as a *dynamical instability*.

Referring back to our metastable cubic PTO crystal, we see that when we calculate the phonon dispersion relations ($\omega_m(\mathbf{q})$ or its reciprocal, the wavenumber as $\nu_m(\mathbf{q})$ shown in Figure 2.8) we have real ω for most branches but near three important regions: the Γ , R and M -points we have imaginary ω [43, 154]. If we examine the corresponding eigendisplacements \mathbf{u}_κ at each of these points we find some important distortions. At the Γ -point we find the eigendisplacements of a ferroelectric distortion (Figure 2.8b) and at the R and M points we find the eigendisplacements of $a^0 a^0 c^-$ (Figure 2.8c) and $a^0 a^0 c^+$ (Figure 2.8a) AFD distortions respectively [43, 154].

It is commonplace to label these modes using group theory. Each mode is assigned an irreducible representation or *irrep* from a list of possible labels for a given parent spacegroup [161]. In the case of PTO, the soft mode irreps of the parent $Pm\bar{3}m$ spacegroup are Γ_4^- , R_4^+ and M_3^+ respectively [43, 154, 161]. If a structure has multiple dynamical instabilities, it is not guaranteed that the groundstate structure will include all of these. Again, our $Pm\bar{3}m$ PTO example has three instabilities but only one (the ferroelectric Γ_4^- mode) condenses in the phase transition to the $P4mm$ spacegroup. It is also not the case that only one irrep must condense during the phase transition. In the $Pm\bar{3}m$ paraelectric to $Pbam$ AFE phase transition of PZO, the AFE structure condenses *six* distinct irreps [38]. It is then the task of simulation to explore each of the dynamical instabilities (and their combinations with each other) to determine which combination of irreps produces the lowest groundstate energy. One way of doing so would be to include one irrep at a time. Once an irrep has been introduced (at its equilibrium amplitude, found by relaxing the structure) we calculate $\omega_m(\mathbf{q})$ for the new structure and check for imaginary ω_m . This process is repeated until $\omega_m(\mathbf{q}) \in \mathbb{R}$ throughout the entire first Brillouin zone. We must also consider that the final structure after this process could be dependant on the irrep path taken, so, for completeness, we must check all available paths.

2.7 Anomalous dynamical charges

It is now convenient to discuss in more detail the concept of dynamical charges. These are related to the change in polarisation induced by atomic motion. The magnitude of these charges are found to be anomalously large [162] (compared to the nominal or static charges, say) in the perovskite oxides serving as a signature of the instability of a crystal against the ferroelectric distortion. There are in fact several definitions for the dynamical charge which relate to the different relationships between the electric field \mathbf{E} and polarisation \mathbf{P} and on the boundary conditions of the system [73] (i.e. is this system periodic or isolated?). The most common definition used in the study of the perovskite oxides is the *Born effective charge* [71, 72] or *transverse charge* which is defined at a macroscopic field of $\mathbf{E} = 0$ in periodic boundary conditions. This quantity is a Cartesian tensor whose matrix elements are defined as

$$Z_{\kappa,\alpha\beta}^* = \Omega \left. \frac{\partial P_\beta}{\partial u_{\kappa,\alpha}} \right|_{\mathbf{E}=0} \quad (2.36)$$

for atomic species κ , Cartesian directions α and β and displacements of a symmetry-equivalent periodic sublattice of ions $u_{\kappa,\alpha}$. It is useful to consider these charges as being comprised of two components. We can explore the nature of these components in a pedagogical sense by evaluating the dynamical charge of an isolated diatomic molecule in one dimension. A convenient definition for the static charge in this scenario would be $Z(x) = d(x)/x$ (note the 1D dipole moment $d(x)$ from Equation 2.14). We can then evaluate the dynamical charge

$$Z^*(x) = \frac{\partial d(x)}{\partial x} = \frac{\partial}{\partial x}[xZ(x)] = Z(x) + x \frac{\partial Z(x)}{\partial x}. \quad (2.37)$$

The first term on the RHS of Equation 2.37 is just the static charge. The second term is an additional *dynamical contribution* (sometimes referred to as the *anomalous contribution*) relating to the rate of change of the static charge when the atom is displaced. This contribution is the direct result of changes in the overlaps of atomic orbitals thus varying the degree of orbital hybridisation. This effect is referred to in the seminal work of Dick and Overhauser [163] as “exchange charge polarisation”. In systems like the perovskite oxides where $Z_{\kappa,\alpha\beta}^*$ has a large dynamical contribution, cation displacements force electrons to move in the opposite direction to the displacement. The opposite is true for anion displacements; holes are forced in the opposite direction to the displacement. $Z_{\kappa,\alpha\beta}^*$ can be calculated easily in first principles calculations either by evaluating Equation 2.36 with a finite differences approach (since we know how to calculate P following Section 2.5) or with a perturbation theory approach [164–166]. Such calculations have made it possible to probe which orbital hybridisations are responsible for the anomalous $Z_{\kappa,\alpha\beta}^*$ using band-by-band decompositions. For BTO, the large anomalous charge of Ti ($\approx +7.25$, compared to a nominal charge of just 4) can be understood by changes in the hybridisation of O 2p and Ti 3d orbitals. That is, the Wannier centre of the O 2p bands is found to displace in

a direction opposite to Ti producing the effect described above [73]. In fact, this mechanism persists for most ATiO_3 perovskites [73]. Notably, for PTO, Pb-O hybridisation also makes an important contribution [3, 167].

An obvious consequence of anomalous Born effective charges is that relatively small ionic displacements can generate large dipole moments, large values for the spontaneous macroscopic polarisation of a ferroelectric phase and giant destabilizing coulombic fields [162] (which you will recall from Section 2.6 drives the ferroelectric transition against short range restoring forces). In fact, a minor reworking of Equation 2.36 yields the linear approximation for the spontaneous polarisation, $P_{s,\alpha}$, first noted by Resta [66]

$$P_{s,\alpha} = \frac{1}{\Omega} \sum_{\kappa,\beta} Z_{\kappa,\alpha\beta}^* \Delta u_{\kappa,\beta} \quad (2.38)$$

where $\Delta u_{\kappa,\beta}$ is an atomic displacement from a non-polar reference structure (which is often a cubic $Pm\bar{3}m$ phase). We note that this definition has no conceptual issues with the modern theory of polarisation as described in Section 2.5 since we are calculating a polarisation difference $\Delta \mathbf{P} = \mathbf{P}_s$ between a non-polar reference and a distorted structure on the same polarisation branch [137]. This approach allows one to estimate \mathbf{P}_s of a ferroelectric phase using only atomic displacements and the Born effective charge tensors of a high symmetry phase. It may seem counter-intuitive that a constant value of $Z_{\kappa,\alpha\beta}^*$ can be used in such a calculation since we may expect this to alter over the distortion path due to changes in orbital hybridisations. Recall, however, (from Equation 2.37) that the anomalous contribution originates from the *rate of change* of orbital hybridisation and not the current level of hybridisation [154]. The former may be fairly constant throughout a distortion path[†] (although one should check this) allowing Equation 2.38 to provide good estimates of \mathbf{P}_s . Equation 2.38 can also be used to define a local metric of the polarisation. This is a particularly useful probe when considering inhomogeneous systems where dipole moments alter locally (like near a domain wall or surface). Such a procedure is usually carried out by partitioning the system into many ‘local unit cells’ and measuring their displacements from a cubic phase. We make use of this approach regularly in Chapter 6 to create local polarisation vector fields to provide a visualisation of complex polar textures.

2.8 Ferroelectric domain structures

In our previous discussions, we have considered only the case where the ferroelectric polarisation is entirely uniform throughout a sample. Such a scenario is not physical reality. In fact, even in a sample free of obvious inhomogeneities (like defects and strain fields), we still see the organisation of local electrical dipole moments into distinct domains, separated by a domain

[†]Examining Z_{Ti}^* in the cubic (+7.06) and ferroelectric tetragonal (+6.71) phases of PTO (with an LDA-DFT calculation) shows a drop of just 4.95% over the phase transition path [162]. This difference is even smaller for the other species.

wall (DW). This phenomenon is the result of the finiteness of a real sample. Let us conduct a thought experiment. Should we take a uniformly polarised finite crystal, merely the condition that the crystal is polarised means that positive charge is displaced towards one surface and negative charge is displaced towards the opposite surface (often termed the polarisation charges [168, 169]). This separation of charge has now made our sample a capacitor with an electric field opposite to the direction of the polarisation that had created it. This field is able to suppress the polarisation so is often termed the *depolarising field* [168, 169]. Now, the configuration of the local electrical dipole moments in our sample will reorganise themselves into domains (albeit with some non-trivial dynamics), reducing the electrostatic energy cost associated with the polarisation charges. The exact domain structure that will form will depend very sensitively on the electrostatic boundary conditions for the sample as well as the energy cost for the formation of a DW. This delicate interplay makes the study of ferroelectric domain structures a rich and interesting one.

The symmetry of the ferroelectric crystal being studied in part determines the morphology on the resulting domain structure. For example, the tetragonal $P4mm$ ferroelectrics (like PTO and BTO) can only form DWs where the polarisation traverses an angle of 180° or 90° . This is due to the six symmetry equivalent axes for the polarisation of the parent cubic $Pm\bar{3}m$ space group. This is in contrast to the room temperature multiferroic BiFeO_3 (BFO) whose spontaneous polarisation is aligned along one of the eight equivalent $[111]$ directions of its pseudocubic parent. In this case, there are three possible DWs: 180° , 109° and 71° [168]. Of particular interest to this thesis are the polar domain morphologies in the vicinity of 180° DWs in thin ferroelectric films. That is, alternating domains with $\mathbf{P} \parallel [001]$ and $\mathbf{P} \parallel [00\bar{1}]$ in a stripe pattern (where $[001]$ is the out-of-plane direction for the film). This domain pattern forms as a result of strong depolarising fields. At the nanoscale (and the limit of *ultrathin* films) it is true that the depolarising field generated by the polarisation charges completely suppresses out-of-plane ferroelectricity for a film with a single domain. It can be shown with simple electrostatics (assuming a uniformly polarised film in a vacuum) that the depolarising field for such an out-of-plane polarised film is given by [170]

$$E_d = -\frac{P_z}{\epsilon_0} \quad (2.39)$$

for out-of-plane polarisation P_z . If we take P_z to be the polarisation of bulk $P4mm$ PTO (measured between $57\text{-}100 \mu\text{C}/\text{cm}^2$ [171]), we can see that the depolarising field is truly gigantic, $\sim 10^2$ GV/m and well beyond the required field to suppress the polarisation completely. The polarisation charges can thus be heavily reduced should the film break into distinct domains allowing out-of-plane polarisation to exist. To further reduce polarisation charges, local dipole moments close to the surface/interfaces of the film tend to continuously and smoothly rotate to be parallel to the surface/interface forming domain caps. This defines what are often termed

flux-closure domains as seen in Figures 2.10a, 2.10ai, 2.10c. The local dipole moments gradually rotate across the DW with the walls themselves now being the centre of counter-rotating polar vortices (seen clearly in Figure 2.10ai). Under electric bias fields, the polar texture can be manipulated to adapt a more ‘wave-like’ structure like is seen in Figure 2.10b. In general, flux closure domains can be considered an intermediary between the sharp Kittel type domains (Fig 2.10d) and Landau-Lifshitz type domains (Fig 2.10e). Despite all of this, the polarisation charges cannot be entirely screened by the formation of domains because stray fields formed in the vicinity of DWs add to the electrostatic energy cost. Undeterred by this, PTO films as thin as three unit cells [32, 33, 172] have been shown to preserve out-of-plane polarisation in a polydomain phase.

The presence of stray fields at DWs motivated Kittel to consider the relationship between the strength of such fields and the equilibrium domain period Λ for 180° stripe domains in ferromagnetic films [176]. As it turns out, the same arguments can be made when we replace the ferromagnetic order parameter with the ferroelectric one. It was first realised that smaller domains generated smaller stray depolarising fields. Kittel found that the energy density of a domain F_{domain} must be proportional to its period [176]

$$F_{\text{domain}} \propto U\Lambda \quad (2.40)$$

for volume energy density U . One can then minimise the energy by simply reducing Λ . One then has to consider that as Λ is decreased, the density of DWs in the sample must also increase at a rate $\propto \Lambda^{-1}$. Since there is an energy cost for the formation of DW, this must also become a factor in determining the domain period. Kittel stated that the DW energy density F_{wall} is related to the surface area of the DW which itself must be related to the thickness of the film, t

$$F_{\text{wall}} \propto \frac{\sigma t}{\Lambda} \quad (2.41)$$

for DW energy density σ . Should we then minimise the total energy density with respect to the domain period (that is, set $\partial/\partial\Lambda(F_{\text{domain}} + F_{\text{wall}}) = 0$) we arrive at the famous Kittel scaling relationship

$$\Lambda \propto \sqrt{t}. \quad (2.42)$$

The above has been shown to hold true for many ferroelectric films and superlattices. The constant of proportionality for the Kittel law depends on many different materials properties generally tending to be much larger for ferromagnets than ferroelectrics meaning ferroelectric domains (and their DWs) have generally much smaller periods than their ferromagnetic counterparts. This offers a clear advantage when it comes to device miniaturisation.

Aside from the flux-closure polar morphology, other interesting and potentially useful arrangements of electrical dipole moments can exist. These include polar waves [174] (Figure

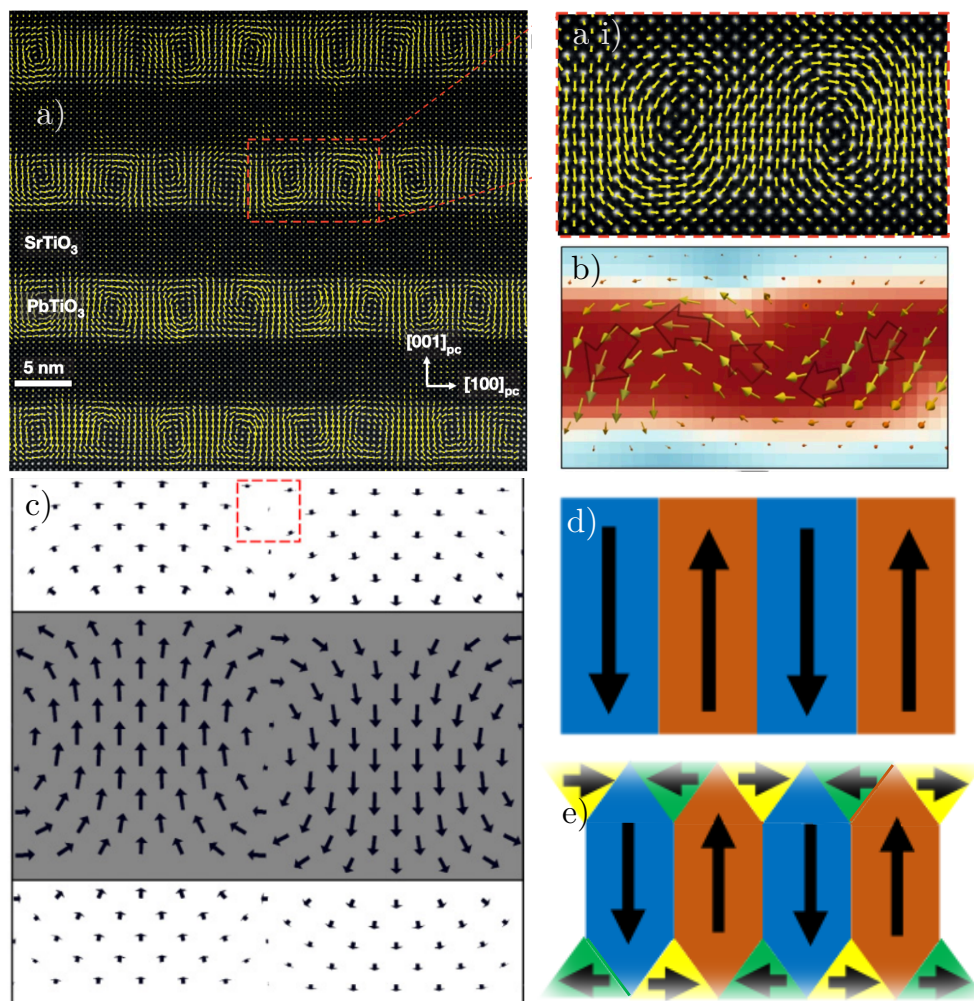


Figure 2.10: Experimental, simulated and example images/diagrams of ferroelectric domain morphologies. In all cases, arrows represent the direction and magnitude of the local ferroelectric mode. a) A cross-sectional HR-STEM for a $\text{STO}_{10}/\text{PTO}_{10}$ superlattice, showing that an array of vortex–antivortex pairs is present in each PTO layer defining a flux-closure domain pattern from reference [173]. a i) A magnified image of a single vortex–antivortex pair, showing the continuous and gradual rotation of the polarisation state within such vortex–antivortex pairs from reference [173]. b) A phase-field simulation demonstrating the polar wave texture as predicted an an intermediate phase in electric field switching of a PTO/STO superlattice from reference [174]. c) A first principles simulated flux-closure domain texture in the $\text{PTO}_6/\text{STO}_6$ superlattice from reference [175]. The red area marks an area where an antivortex has formed. d) A schematic of Classical Kittel domains where up the page is the out of plane direction. e) A schematic of Landau-Lifshitz type domains. All images have been used with permission from the lead authors of [173], [174] and [175]. Figure (a), (a i) and (b) are © 2017 Springer Publishing and Figure (c) is © 2012 American Physical Society.

2.10b), disclinations [177] and even the stabilisation of polar skyrmion phases [89, 178, 179]. Many of these morphologies can possess a finite spontaneous toroid moment (ferrotoroidicity) and subsequently give rise to electrotoroidic, pyrotoroidic and piezotoroidic responses [174, 180, 181]. Interestingly, those morphologies with toroidal order are able to interact with time dependent magnetic fields by producing a curling electric field by Faraday's Law [181]. This field is hypothesized to be able to switch the toroidal moment to another stable configuration offering (amongst other things) an exciting alternative to ferromagnetic and ferroelectric memories [180, 181].

Before closing this section we stress that domain formation is not the only mechanism existing to screen the depolarising field in thin films. In fact, domain structure formation within thin films is mostly achieved under open circuit boundary conditions. Consider instead a thin film sandwiched between two metallic electrodes. In this scenario, free charges within these electrodes can migrate to the interface with the film to screen the polarisation charges [182] (although, domains have been shown to persist in DFT calculations of BTO interfaced with metallic SrRuO₃ in a capacitor setup [183]). Indeed, the same mechanism is possible through the adsorption of atmospheric adsorbates (like OH) and has been demonstrated by varying the partial pressure of oxygen at an open surface [184]. In the absence of externally supplied mobile carriers, it is possible that the film itself becomes conducting near the interfaces thus forming interfacial 2DEG/HGs in the *polar catastrophe scenario* [90, 185, 186]. Finally, it is often overlooked that the depolarising field can be greatly reduced by the simple continuity of polarisation across an interface. This is of course not possible at the interface with the vacuum but has been observed in ferroelectric/dielectric superlattices where the dielectric layer can become polarised [187, 188].

2.9 Alignment to surface features

As we have seen in Section 2.8, a large body of interesting physics stems from the discussion of the possible polar morphologies that can be achieved in thin films. We note now, however, that an increasing amount of research is now focused on the properties of the DWs. It has been found that the 180° and 109° DWs in BFO are conducting at room temperature using conductive atomic force microscopy [26]. Although the origin of this conductivity is still not a settled topic, the very fact that sub-nm 2D conducting channels can exist in an otherwise insulating material has very exciting ramifications in nanoelectronics. If one is able to manipulate and guide these conducting DWs, the prospect of nanocircuits becomes a reality. Should this manipulation be a reversible process (which can be achieved with applied fields [30]) we are then able to write nanocircuits onto a 'blank ferroelectric slate' and remove them just as easily. This field is known as agile circuit technology [27, 31].

There is promise that nanocircuits could be written permanently by etching patterns into the

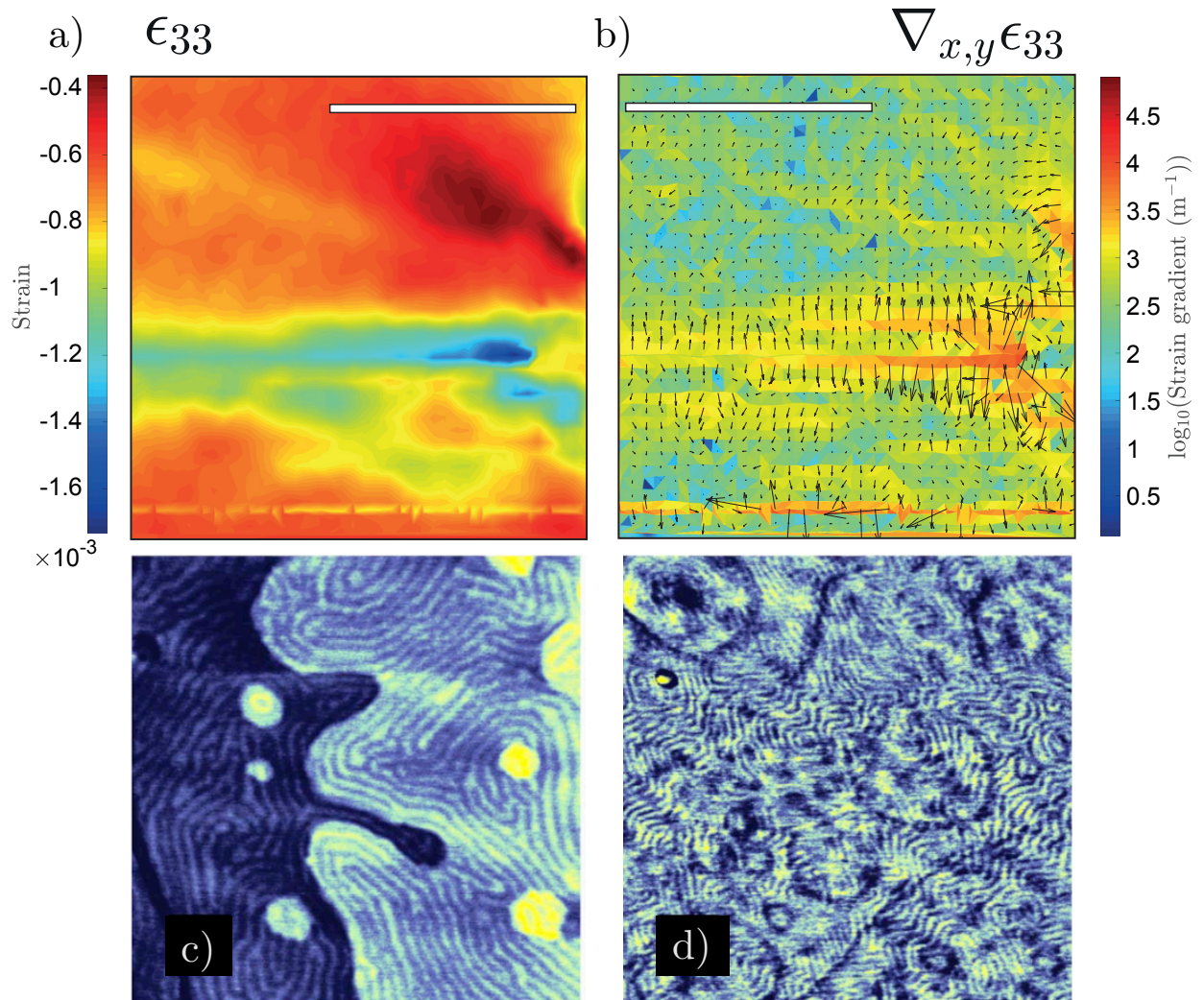


Figure 2.11: Maps of structural inhomogeneities in the vicinity of surface defects of PTO/STO superlattice heterostructures. a) Map of the ϵ_{33} strain tensor element local to a surface defect on a PTO/STO superlattice from reference [55] (scale bar $2\mu\text{m}$). b) The evaluated strain gradients for the strain field in (a) from reference [55] (scale bar $2\mu\text{m}$). c-d) $500 \times 500 \text{ nm}^2$ room temperature tapping mode AFM images of surface steps and 180° stripe domains for epitaxially deposited PTO on STO. Height is displayed with a color scale range of 0.8 nm . These images are taken from reference [34]. All images have been used with permission from the lead authors of [55] and [34]. Images (a) and (b) are © 2017 American Physical Society and images (c) and (d) are © 2008 American Institute of Physics.

surfaces of ferroelectrics. Although such circuits would not be considered agile, they could be accomplished without the delicate control of applied fields. It was first noticed in early studies of PTO films on STO substrates that DWs align with crystallographic steps of the substrate [32]. This effect was imaged explicitly with AFM on the surface of epitaxial PTO [34] as shown in Figures 2.11c and 2.11d. XRD confirmed alignment of the stripe domains to the edges of surface steps and other surface defects [34]. It was shown that this alignment occurs in most thicknesses of ultrathin films ($< 11\text{nm}$) apart from at low temperature and low thickness ($< 3\text{nm}$) where the stripe domain pattern tends to randomly align. There is now an effort to engineer these surface defects. One study used focused Ar ion beams to mill surface defects [55]. Large inhomogeneous strain and strain gradients (Figures 2.11a and 2.11b) were found in the vicinity of the defects suggesting that the alignment mechanism could be flexoelectric [55]. Another study also used focused ion beams to etch surface defects on PTO/STO superlattices [189]. Like in reference [55], a nanofocused X-ray beam was used to probe the local alignment of the stripe domains in the vicinity of the defect. It was found that domain walls strayed no more than 20° away from the defect edge. Within this study, time dependent LGD theory was used to suggest that the alignment mechanism is elastic; resulting from lowering of the bulk and electrostrictive contributions to the free energy of the system since lateral mechanical constraints are released [189].

There has been some effort to understand this alignment mechanism from the perspective of atomistic simulations. An effective Hamiltonian method (parameterised from first principles) was used to investigate alignment to surface steps in thin PTO films [190]. Interestingly, this study found that the domain centroids (and not the DWs) recentered to align with the steps. It was verified that the resulting domain configurations from steps parallel to the DW direction are more energetically favourable than steps perpendicular to the DWs [190]. Notably, the latter case was found to be an unstable structure for films thinner than 20\AA (with a step height of 4\AA). DFT calculations have also provided some insight [191, 192]. One study showed that DWs were pinned to the edges of crystallographic steps above a critical compressive strain [191] in contrast to the effective Hamiltonian study mentioned previously [190]. It was also found that FE modes local to the steps were enhanced when PbO terminated but suppressed at TiO_2 steps due to charge transfer mechanisms [191, 192].

It is then clear that there is little consensus in this area both for the mechanism of the alignment (elastic, flexoelectric or a combination?) or for what specifically in the stripe domain structure is pinned (the DW or the domain centroid?). Within this thesis, we add to this discussion using large scale DFT methods. That is, previous DFT simulations of [191, 192] failed to treat explicitly the interaction of a polydomain film with a surface trench. They were limited only to treating monodomain in-plane polarisation (which they found had a tendency to spontaneously form a polydomain film upon introduction of a surface step [191]) due to the computational expense of DFT. The Monte-carlo simulations in [190] did treat the polydomain phase but (i)

do not offer the same level accuracy of DFT (ii) did not treat the effect of a surface defect in isolation; instead studying a periodic array of crystallographic steps. It is clear that large scale simulations could provide insight into (ii) using a large supercell.

3 | Theoretical Background

Chapter abstract

The simulations enclosed within this thesis stand on the shoulders of a theory familiar (at least in name) to condensed matter theorists, chemists and experimentalists alike: density functional theory, or, DFT. Subsequently, most of this chapter is dedicated to its origins, implementation and limitations. After presenting the foundations on which the theory sits, we provide an overview of its standard implementation in periodic boundary conditions with plane waves and pseudopotentials or with the projector augmented wave method. We then move to pay special interest to the reformulated implementation of the theory within the CONQUEST code [7, 17, 193, 194] which allows for large scale DFT simulations for systems comprised of thousands (and even millions [13]) of atoms; well beyond what is possible with conventional implementations. This is the code of choice for simulations in Chapters 5 and 6 allowing us to simulate long range order in the perovskite oxides with quantum mechanical accuracy. Lastly, we discuss the linear response and finite displacement methods for the calculation of phonons which are central to Chapter 4.

3.1 An introduction to the quantum many-body problem

A problem at the very foundations of quantum chemistry and condensed matter physics is in how one extracts the wavefunctions from systems of interacting electrons and nuclei. In principle, once one has the wavefunction, we have access to *all* of the properties of the system of interest [195]. The problem is, the exact evaluation of the wavefunction for the fully interacting system (the many-body wavefunction) is tremendously difficult once one has more than a couple of electrons. Fully analytical solutions are only known for 1-electron-1-nucleus systems (i.e Hydrogen and the hydrogenic ions [196]) and numerical evaluations become intractable around 5 electrons. This is particularly troublesome seeing as most systems of interest are *much more complex* than this. The problem is made clearer if we consider the Hamiltonian of an interacting

system of N electrons and I nuclei at coordinates \mathbf{r}_N and \mathbf{R}_I respectively

$$\hat{\mathbf{H}}^{\text{MB}} = -\frac{1}{2} \left(\sum_N \nabla_N + \sum_I \frac{1}{M_I} \nabla_I \right) - \sum_{N,I} \frac{Z_I}{|\mathbf{r}_N - \mathbf{R}_I|} + \frac{1}{2} \sum_{N \neq M} \frac{1}{|\mathbf{r}_N - \mathbf{r}_M|} + \frac{1}{2} \sum_{I \neq J} \frac{Z_I Z_J}{|\mathbf{R}_I - \mathbf{R}_J|} \quad (3.1)$$

where we have used atomic units[†]. The first two terms featuring the Laplacian operators are the kinetic energies of the electrons and nuclei respectively. The third term is for the Coulomb interactions of electrons and nuclei and the last two terms are for the Coulomb interactions of electrons with electrons and nuclei with nuclei respectively. Note that for the last two terms the sums exclude self-interaction terms as well as featuring a prefactor of 1/2 to eliminate double counting. Consider now the degrees of freedom the full many-body wavefunction must possess when operated upon with this Hamiltonian in the time-independent (non-relativistic) Schrödinger equation

$$\hat{\mathbf{H}}^{\text{MB}} \Psi^{\text{MB}}(\mathbf{r}_1, \mathbf{r}_2 \dots \mathbf{r}_N, \mathbf{R}_1, \mathbf{R}_2 \dots \mathbf{R}_I) = E \Psi^{\text{MB}}(\mathbf{r}_1, \mathbf{r}_2 \dots \mathbf{r}_N, \mathbf{R}_1, \mathbf{R}_2 \dots \mathbf{R}_I). \quad (3.2)$$

In three dimensions this is $3N + 3I$. It is immediately clear that *even if* we could solve for this many-body system, the storage of the wavefunction would be implausible. Take for example a single atom of Pb with 82 electrons. The many-body wavefunction then has 249 degrees of freedom. If we are to store this wavefunction on a uniform, coarse grid of 10 points per degree of freedom, we would need 10^{249} points in total. If each point is stored as a 64-bit double in memory, our many-body wavefunction would occupy $\sim 10^{238}$ terabytes of disk space - *far* in excess of current estimates for the total number of atoms in the observable universe ($\sim 10^{80}$; the Eddington number [197]).

Let us now try to make this problem more tractable. A good first step is to separate the electronic and nuclear degrees of freedom in what is known as the Born-Oppenheimer (BO) approximation [72, 198]. One way of looking at this approximation is that it is permissible when the timescale associated with nuclear motion greatly exceeds the electronic timescale. That is, within the BO approximation, we expect electrons to instantaneously adapt to a new nuclear potential. This is very often justified as electrons are much less massive than the nuclei. Alternatively, the BO approximation is well justified when the energy gap between ground and excited electronic states exceeds the energy scale of the nuclear motion, causing beyond-BO effects where this condition isn't met [199, 200]. A step which almost always follows the BO approximation is to treat the nuclei as classical point particles. This is generally a good approximation with the exception of some light nuclei where a full quantum mechanical treatment may be required. The problem is now reduced to finding the solutions for just the

[†] $1/(4\pi\epsilon_0) = \hbar = e = m_e = 1$.

electronic wavefunctions in the presence of a static field of classical point charges. This makes the computation of nucleus-nucleus and electron-nucleus terms tractable, but, we are still left with the many-body nature of the electron-electron terms and thus a 3N-dimensional wavefunction. This problem is clearly *still* intractable following the same arguments from before.

It is then the purpose of much research in quantum chemistry to find approximate solutions to the exact many-body electronic wavefunction. Whilst many such methods exist (and a variety are summarised succinctly in [201]) the focus of this thesis is aimed towards the DFT solution. As demonstrated in the previous chapter, DFT has a history for making accurate predictions in ferroelectric materials, so, makes for a good choice when studying the systems in this thesis. What now follows is a brief introduction to the theory in terms of its core tenets and limitations.

3.2 Fundamentals of density functional theory

This section details the necessary foundations of DFT. While it is safe to assume that these discussions are now textbook, we include them here for easy reference in the proceeding sections. For an in-depth discussion of the topic, we direct the reader to the comprehensive reference texts by Martin [202], Parr [203], Dreizler [204] and Burke [205] and for a more gentle, pedagogical introduction, the book by Kohanoff [206].

3.2.1 The Hohenberg-Kohn theorems

As we have noted before, the many-body wavefunction (due to its many coordinates) is an intractable object to store in memory, let alone solve. This motivates a search for a different fundamental concept from which we can evaluate the ground state properties of a system. As it turns out, we can steer away from the full many-body wavefunction by instead considering the ground state charge density $n_0(\mathbf{r})$. Let us now examine the theorems of Hohenberg and Kohn (HK) or the *HK theorems* [207] which demonstrate why such a change of focus is valid.

HK theorem I: *let $n_0(\mathbf{r})$ be the (possibly degenerate) ground-state density for an N -electron system. Then, $n_0(\mathbf{r})$ determines not only the electron number*

$$N = \int n_0(\mathbf{r}) d^3\mathbf{r} \quad (3.3)$$

but also uniquely[†] defines the external potential[‡] $v_{\text{ext}}(\mathbf{r})$, the Hamiltonian $\hat{\mathbf{H}}$ and thereby everything there is to know about this system.

[†]The uniqueness of $v_{\text{ext}}(\mathbf{r})$ for a given $n(\mathbf{r})$ doesn't guarantee that $v_{\text{ext}}(\mathbf{r})$ exists for *any* $n(\mathbf{r})$. An electron density $n(\mathbf{r})$ for which the associated $v_{\text{ext}}(\mathbf{r})$ *does* exist, is called v -representable.

[‡]Apart from by an additive constant - i.e, if one were to shift the potential uniformly up or down by a constant amount, the same $n_0(\mathbf{r})$ would result.

We refer the reader to [207] for the original *reductio ad absurdum* proof of this theorem. Practically, HK I means that one need not evaluate the many-body wavefunction directly to obtain the ground state properties of the system. Instead, the much more palatable 3-dimensional $n_0(\mathbf{r})$ gives us access to these. Further, the theorem asserts that for a given external potential[†], v_{ext} we can uniquely define $n_0(\mathbf{r})$.

HK theorem II: *For any given external potential $v_{\text{ext}}(\mathbf{r})$, a ground state total energy functional of the density exists and can be found subject to the variational principle*

$$E_{\text{tot}} \leq F[n(\mathbf{r})] + \int v_{\text{ext}}(\mathbf{r})n(\mathbf{r})d^3\mathbf{r} \quad (3.4)$$

where $F[n(\mathbf{r})]$ is a universal, system independent functional whose exact form is so far unknown. Equation 3.4 only reaches equality when $n(\mathbf{r}) = n_0(\mathbf{r})$, the ground state charge density.

The proof of this theorem is found simply by applying the variational principle of quantum mechanics[‡] [209]. This theorem offers a significant advantage from a computational standpoint. If a procedure can be devised to search for the ground state density, its convergence can be strictly monitored since no density can yield an energy lower than the ground state density. Even given these two theorems, we are still left with two glaring questions:

1. Naively, the charge density is related to the many-body wavefunction by $n(\mathbf{r}_1) \equiv n(\mathbf{r}) = N \int |\Psi(\mathbf{r}_1, \mathbf{r}_2, \dots, \mathbf{r}_N)|^2 d\mathbf{r}_2 \dots d\mathbf{r}_N$. This doesn't help, however, since we still need to evaluate the intractable many-body wavefunction. Given this, how to we practically calculate $n(\mathbf{r})$?
2. If the exact functional form of $F[n(\mathbf{r})]$ is unknown, how do we evaluate the ground state energy in accordance to Equation 3.4?

A scheme for answering the first question now follows in Section 3.2.2 while details about the form of $F[n(\mathbf{r})]$ and approximations for calculating it are outlined in Section 3.2.3.

3.2.2 Independent orbitals: the Kohn-Sham *ansatz*

In 1965, Kohn and Sham (KS) would make a vital step towards DFT becoming the tractable and widespread method it is today [210]. Their idea (or *ansatz*) allows us to calculate the charge density $n(\mathbf{r})$ without having to evaluate the many-body wavefunction. Instead, electrons are now

[†]Which following the arguments of the previous section, is defined classically by a set of point-like nuclear charges. However, this term can in principle include other applied fields.

[‡]The variational proof holds only for v -representable $n(\mathbf{r})$. A more general proof is the constrained search approach of Levy [208].

single, non-interacting particles which move through an *effective potential* which describes a fully interacting system [210]. Each independent electron can be treated with a spin coordinate σ . We, however, omit this choosing instead to treat the spin-degenerate system which sufficiently describes the materials treated in this thesis. Should we evaluate these single particle orbitals, we can find $n(\mathbf{r})$ rather simply as

$$n(\mathbf{r}) = 2 \sum_i f_i |\psi_i(\mathbf{r})|^2. \quad (3.5)$$

where f_i is the occupation of the i^{th} KS orbital, ψ_i . The kinetic energy of the independent electrons

$$E_{\text{kin}}^{\text{KS}}[n(\mathbf{r})] = -\frac{1}{2} \sum_i f_i \int \psi_i^*(\mathbf{r}) \nabla^2 \psi_i(\mathbf{r}) d^3\mathbf{r} \quad (3.6)$$

and the classical electrostatic Hartree energy

$$E_{\text{Ha}}[n(\mathbf{r})] = \frac{1}{2} \int \int \frac{n(\mathbf{r})n(\mathbf{r}')}{|\mathbf{r} - \mathbf{r}'|} d^3\mathbf{r} d^3\mathbf{r}' \quad (3.7)$$

together allow a definition of the universal functional $F[n(\mathbf{r})]$

$$F[n(\mathbf{r})] = E_{\text{kin}}^{\text{KS}}[n(\mathbf{r})] + E_{\text{Ha}}[n(\mathbf{r})] + E_{\text{XC}}[n(\mathbf{r})] \quad (3.8)$$

where the final terms represents the contribution from electronic exchange and correlation effects. It is for this term in particular that the exact functional form is unknown. It is defined to be the term which absorbs all of the error in the difference between the fully interacting system and the KS auxiliary system[†]

$$E_{\text{XC}}[n(\mathbf{r})] = E_{\text{kin}}[n(\mathbf{r})] - E_{\text{kin}}^{\text{KS}}[n(\mathbf{r})] + E_{\text{ee}}[n(\mathbf{r})] - E_{\text{Ha}}[n(\mathbf{r})] \quad (3.9)$$

where $E_{\text{kin}}[n(\mathbf{r})]$ is the true kinetic energy of the many-body system and $E_{\text{ee}}[n(\mathbf{r})]$ is the full electron-electron term for the many-body system.

This can be a useful definition, but, it doesn't help us actually calculate it. While some approximations for doing so are outlined in the following section, one should note now that KS-DFT in principle is an *exact* solution to the quantum many-body problem should we know *exactly* the form of $E_{\text{XC}}[n(\mathbf{r})]$. Fortunately, for most systems the exchange and correlation energy is much smaller than the other terms which are described exactly, so, even simple approximations for $E_{\text{XC}}[n(\mathbf{r})]$ can yield accurate results.

[†]When considering the interaction of a spin-degenerate homogeneous electron gas with a positive background charge, one can define an approximation of the correlation energy E_C in a similar way to Equation 3.9. Richard Feynman once called this arrangement for E_C the 'stupidity energy', E_S [211]. Perhaps E_{XC} is then the 'even stupider energy', E_{ES} .

Crucially, the KS approach allows us to replace the many-body Schrödinger equation (Equation 3.2) with N^{KS} (the total number of KS orbitals) Schrödinger-esque equations where the KS-Hamiltonian operates on the single particle orbitals

$$\hat{\mathbf{H}}^{\text{KS}}\psi_i(\mathbf{r}) = \left(-\frac{1}{2}\nabla^2 + v_{\text{KS}}^{\text{eff}}(\mathbf{r})\right)\psi_i(\mathbf{r}) = \epsilon_i\psi_i(\mathbf{r}) \quad (3.10)$$

where the effective KS potential is $v_{\text{KS}}^{\text{eff}}(\mathbf{r}) = v_{\text{Ha}}(\mathbf{r}) + v_{\text{ext}}(\mathbf{r}) + v_{\text{XC}}(\mathbf{r})$ and, like the energy terms, is an explicit functional of the density $v_{\text{KS}}^{\text{eff}} \equiv v_{\text{KS}}^{\text{eff}}[n(\mathbf{r})]$. We see now that once we have selected an approximate XC functional and have represented ψ_i with a suitable basis set expansion (discussed in Sections 3.3.1 and 3.4.2) we can solve Equation 3.10 for each ψ_i yielding the KS-energy as

$$E_{\text{KS}} = 2 \sum_i f_i \epsilon_i + \Delta E_{\text{Ha}} + \Delta E_{\text{XC}} \quad (3.11)$$

where the last two terms are the double counting corrections for the Hartree and XC contributions respectively [202, 204]. Explicitly

$$\Delta E_{\text{Ha}} = -E_{\text{Ha}}, \quad (3.12)$$

$$\Delta E_{\text{XC}} = E_{\text{XC}} - \int (v_{\text{XC}})n(\mathbf{r})d^3\mathbf{r}. \quad (3.13)$$

The total energy of the system is Equation 3.11 in addition to the classical nuclei-nuclei interactions which need only be calculated *once* for a given set of nuclear coordinates. One might naively think that each of the N^{KS} KS equations need only be solved once also. This, however, is not true. We can of course solve Equation 3.10 by constructing some $v_{\text{KS}}^{\text{eff}}(\mathbf{r})$ with some $n(\mathbf{r})$ (see HK theorem I), but, since we don't yet know whether this $n(\mathbf{r})$ is anywhere close to $n_0(\mathbf{r})$ (and why would we?), we have no reason to believe that the resulting total energy is the ground state total energy. In practice we must initially guess[†] some $n(\mathbf{r})$ and use this to construct a trial $v_{\text{KS}}^{\text{eff}}(\mathbf{r})$ for which we then solve the KS equations. Since this process yields not only the KS eigenvalues but also the eigenvectors[‡], we can use the latter to define a new set of ψ_i . By Equation 3.5, we can then yield a new density. We can then use this new density[§] to yield a new potential and so on. This process is repeated until the input density matches the density of the next step to some tolerance. Indeed, one can instead monitor the convergence of other quantities like the KS potential or the total energy. Once converged, we decide that we have arrived at an approximation for $n_0(\mathbf{r})$ subject to our choice of basis set expansion and approximation for

[†]Usually, this initial guess is based upon the atomic charge densities.

[‡] $n(\mathbf{r})$ can also be calculated without use of the eigenvectors as we will learn in Section 3.4.6.

[§]In practice, the density from a previous step in the SCF loop is mixed with another following some scheme in an attempt to reduce the inherent numerical instabilities in the SCF cycle [212].

$E_{XC}[n(\mathbf{r})]$. This process is known as the self-consistent field (SCF) procedure.

3.2.3 Exchange and correlation

With the exception of the BO approximation and the move to treat nuclei classically, our formulation of DFT has thus far been an exact one. But, as we have noted, the exact form of $E_{XC}[n(\mathbf{r})]$ is unknown so some approximations must now be made. Let us then discuss some well known approximations and the nature of electronic exchange and correlation.

Both the exchange and correlation interactions are purely quantum mechanical effects that cannot be described by the other terms of $F[n(\mathbf{r})]$ (Equation 3.8). The exchange term arises from the additional repulsion of electrons of like spins as a consequence of the Pauli exclusion principle and the antisymmetric wavefunctions which follow. The exchange interaction is treated exactly in other *ab initio* techniques. Most notably, Hartree-Fock (HF) theory achieves this through the use of an explicit exchange term generated by Slater determinants [213]. In a similar spirit to Equation 3.9, the difference between the HF-energy and the exact total energy is known as the correlation energy. Broadly, electron correlation can be understood by considering the contribution to the energy of one electron as influenced by the presence of all other electrons. One may wrongly assume that such effects are accounted for by the Hartree term of Equation 3.7, but, this can only describe the *mean-field* interaction of an electron with a classical charge distribution generated from all of the electrons. In addition to this, the Hartree term causes further headaches since the charge distribution a given electron interacts with includes this very electron - i.e, the electron fictitiously interacts with itself giving rise to a self interaction error (SIE) [202, 214]. Such an error is cause for some concern in DFT calculations and schemes for (approximately) correcting this error sometimes exist within the chosen exchange and correlation functional [215, 216].

The most well known approximate XC functional is undoubtedly the local density approximation, the LDA[†], suggested by HK in their original paper [207]. Here, we approximate the exchange and correlation contributions at a point as if the spatial charge density was that of a homogenous electron gas (HEG). This contribution is then folded into a real system with an inhomogenous $n(\mathbf{r})$. The LDA *can* become exact if the charge density varies slowly enough on the scale of the local Fermi wavelength and screening length. This condition, however, cannot be satisfied in real systems. The LDA has the functional form

$$E_{XC}^{LDA}[n(\mathbf{r})] = \int \epsilon_{XC}(n(\mathbf{r}))n(\mathbf{r})d^3\mathbf{r} \quad (3.14)$$

where $\epsilon_{XC}(n(\mathbf{r}))$ is the XC energy per electron of a HEG with density $n(\mathbf{r})$. The correlation part for this term is often fitted to the accurate Monte-Carlo simulations of Ceperley and Alder [217]. The LDA provides reasonable results for structural, elastic and vibrational properties

[†] “Most well known? did you mean B3LYP?” said the computational chemist.

but fails to produce accurate cohesive properties (typically over-binding solids) and activation energies [202]. The LDA (amongst other semi-local functionals) is also known to significantly underestimate the electronic band-gap [215]. Another popular choice for the exchange and correlation terms is a generalised gradient approximation (GGA). This requires the inclusion of the magnitude of the gradient of the charge density. This is then separated into the exchange contribution from a HEG and a separate function F_{XC}

$$E_{XC}^{GGA}[n(\mathbf{r})] = \int \epsilon_{XC}(n(\mathbf{r}), |\nabla n(\mathbf{r})|)n(\mathbf{r})d^3\mathbf{r} = \int \epsilon_X(n(\mathbf{r}))F_{XC}(n(\mathbf{r}), |\nabla n(\mathbf{r})|)n(\mathbf{r})d^3\mathbf{r}. \quad (3.15)$$

The choice of F_{XC} defines the particular version of the GGA, for which, there are many (which are exhaustively included in the well-known `Libxc` library [218]). The GGA is known to correct the over-binding problem in LDA as well as improving activation energies. The LDA lattice constant underestimation is corrected but often by too much, thus, over-softening bonds [219]. This point is particularly salient for the perovskite ferroelectrics since bond over-softening leads to the so called ‘super-tetragonality error’ and vastly overestimated ferroelectric distortions [171]. It is for this reason that the most popular flavour of GGA, the Perdew-Burke-Ernzerhof (PBE) functional [219] is often unsuitable for studying tetragonal ferroelectrics. Band-gaps are known to marginally improve for the GGA but are still vastly underestimated [215].

Other more accurate or *higher rung* functionals too exist. That is, DFT functionals are said to occupy rungs on a *Jacob’s ladder* of chemical accuracy [220]. While the LDA and GGA sit on the lowest rungs of this ladder, hybrid functionals are close to the top. By incorporating some amount of exact exchange from HF theory, band gaps, atomisation energies, bond lengths and vibrational frequencies can all be achieved at a high accuracy but with a high computational cost. A further class of functionals are the meta-GGAs (M-GGAs). These are a logical improvement on the GGA through inclusion of the laplacian of the orbitals i.e. the kinetic energy. The M-GGAs attempt to achieve the same accuracy as a hybrid but without the high computational cost. In particular, the strongly-constrained and appropriately-normed (SCAN) [221] M-GGA has been shown to be very effective in predicting many properties of the perovskite oxides [171, 222], but, is known to suffer from numerical instabilities in self-consistent calculations [223].

3.3 Periodic systems: a conventional implementation

Within the methodology of the previous section, we set out a tractable computational scheme for which the total energy of a system of interacting electrons and nuclei can be evaluated using DFT. We turn now to some further details on how this is conventionally implemented for simulations of typical condensed matter systems. Condensed matter systems (unlike isolated molecules) are naturally comprised of at least an Avogadro’s number ($N_A = 6.022 \times 10^{23}$) of atoms and

therefore more than N_A electrons. Clearly we *cannot solve* $\sim N_A$ KS equations. We instead must choose our solid to be infinite in extent, but, represented by a repeating unit in periodic or *Born-von Karman* boundary conditions [224]. We have then made the standard transform from a set of discrete electronic states to bands defined over the continuous wavevector \mathbf{k} described with Bloch's theorem [225]. The total energy (amongst other quantities) now becomes an integral over the first Brillouin zone (1BZ) [202]. At first glance, our transform seems unhelpful as we have merely replaced the $\sim N_A$ of electrons with an infinite number of wavevectors. Fortunately, these integrals can be replaced with a sum over $N_{\mathbf{k}}$ special \mathbf{k} -points on a grid following the pioneering work of Monkhorst and Pack[†] [227]. We can then evaluate the total energy of a condensed system through solving $\approx N_{\text{cell}} \times N_{\mathbf{k}}$ KS equations each SCF cycle where N_{cell} is the total number of electrons in the chosen repeating unit of the crystal. In practice, $N_{\mathbf{k}}$ can be reduced further using the symmetry operations of the crystal (where the general procedure for doing so is described in reference [228]). The remaining unique points belong to what is known as the irreducible Brillouin zone (IBZ) [202] over which we perform a weighted sum.

3.3.1 Plane waves

In its numerical implementation, the KS orbitals must be represented by some underlying basis set expansion. The most obvious (and commonplace) choice within a periodic solid is motivated by Bloch's theorem [225]

$$\psi_{n\mathbf{k}}(\mathbf{r}) = e^{i\mathbf{k}\cdot\mathbf{r}} u_{n\mathbf{k}}(\mathbf{r}). \quad (3.16)$$

Notice now that the KS orbitals are labelled with band index n and wavevector \mathbf{k} . These $\psi_{n\mathbf{k}}$ are macroscopic over the infinite crystal, but, the Bloch function $u_{n\mathbf{k}}$ is periodic over the repeating unit of the crystal. We can then choose to expand the Bloch functions using a discrete set of plane waves [202]

$$u_{n\mathbf{k}}(\mathbf{r}) = \sum_{|\mathbf{G}| \leq \mathbf{G}_{\text{max}}} c_{n\mathbf{k}}^{\mathbf{G}} e^{i\mathbf{G}\cdot\mathbf{r}} \quad (3.17)$$

where the reciprocal lattice vectors \mathbf{G} are defined by $\mathbf{G} \cdot \mathbf{L} = 2\pi m$ where \mathbf{L} is a lattice vector of the crystal and m is an integer. The KS orbitals can then be written as a sum of plane waves

$$\psi_{n\mathbf{k}}(\mathbf{r}) = \sum_{|\mathbf{G}| \leq \mathbf{G}_{\text{max}}} c_{n\mathbf{k}}^{\mathbf{G}} e^{i(\mathbf{k}+\mathbf{G})\cdot\mathbf{r}}. \quad (3.18)$$

This is a truncated expansion where we include only those \mathbf{G} -vectors whose magnitudes are less than some maximum value \mathbf{G}_{max} . This truncation is often set by the plane wave kinetic

[†]Other schemes for integrating over the 1BZ also exist [226] but the approach of Monkhorst and Pack [227] is the most frequently used.

energy cutoff $E_{\text{cut}} = G_{\text{max}}/2$ (in atomic units). Increasing E_{cut} increases the accuracy of the calculation in a variational manner, but, since this includes more plane waves in the expansion, the calculation consumes more computational resources [202].

3.3.2 Pseudopotentials

Thanks to Bloch’s theorem, we now need only consider the electrons within a single repeating unit of an infinite crystal, N_{cell} . This number can be reduced even further with a firm chemical argument. That is, the vast majority of the electronic properties of materials are the result of the chemistry of the *valence electrons*. In contrast, those electrons deeper within the nuclear potential (the core electrons) play little-to-no role in bonding. In light of this, there is a strong motivation to remove core electrons from our simulations entirely. If, in spite of this, we still decided to proceed by including both the core and valence electrons in our simulations (an ‘all-electron’ calculation) we run into another issue. For small electron-nucleus separations (like one would expect for core electrons) the Coulomb potential describing their interaction diverges rapidly. As a consequence, wavefunctions oscillate rapidly in the core region (as can be seen in Figure 3.1a) requiring a large number of plane waves (or plane wave-equivalent basis functions like blips, [16] psincs [9] and Daubechies wavelets [12]) to accurately represent. So, should we devise some scheme to remove the explicit treatment of core electrons from our simulations, not only are we now considering fewer electrons, we now require fewer plane waves to describe the remaining electrons; a computational saving double whammy!

We then replace the strong ionic potential and the core electrons with a softer pseudopotential (Figure 3.1b) which produces a set of pseudowavefunctions rather than the all-electron valence wavefunctions. The accuracy of the method is ensured by the matching the pseudo and true valence wavefunctions beyond a cutoff radius r_c from the atomic/ionic site. This matching procedure can be seen clearly in Figure 3.1. It is not only important that the pseudo and real wavefunction match beyond this point, their norms must also match within the core region. This condition, known as norm conservation (producing norm-conserving pseudopotentials, NCPPs [231]), ensures that the resulting charge densities from the pseudo and all-electron wavefunctions are the same, or

$$\int_0^{r_c} r^2 |\psi^{\text{AE}}(\mathbf{r})|^2 d\mathbf{r} = \int_0^{r_c} r^2 |\psi^{\text{PP}}(\mathbf{r})|^2 d\mathbf{r} \quad (3.19)$$

for all-electron and pseudo wavefunctions ψ^{AE} and ψ^{PP} [231]. The constraint of norm-conservation can be relaxed should we follow the *ultrasoft* scheme of Vanderbilt [232] (USSPs). Instead, an augmentation charge must be added to correct for the charge deficit in the core region. USSPs allow for convergent calculations with even fewer plane waves albeit with some loss of accuracy. We make use of norm-conserving pseudopotentials for most of the work in this thesis (particularly the style popularised by D. R. Hamann [233]), but, as detailed in the next section

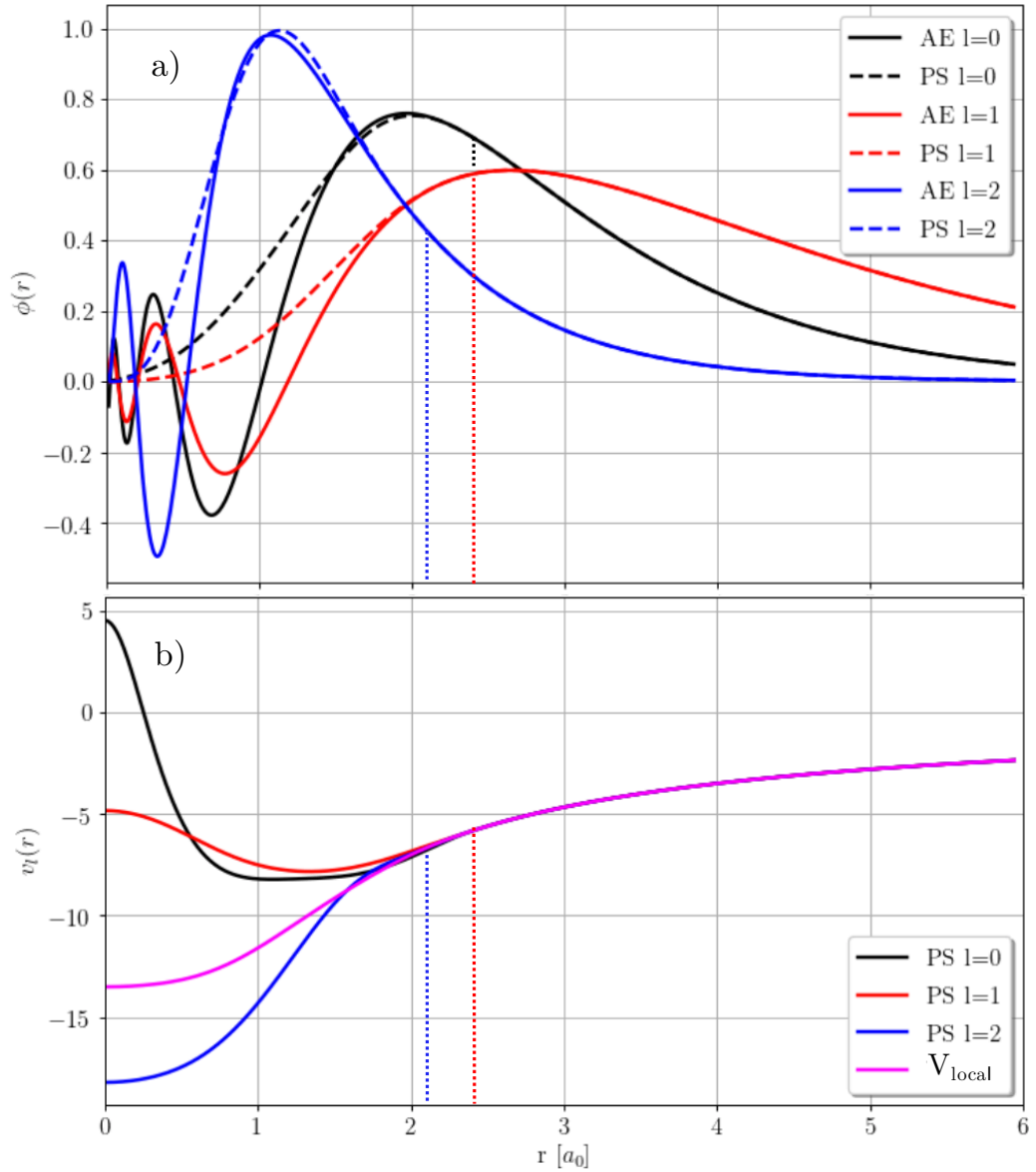


Figure 3.1: Norm-conserving pseudopotential generation data for Pb with the PBESol [229] functional as parsed from the PseudoDojo database [230] (PS=pseudo, AE=all-electron). The matching radius is given for each l -channel which is $2.4 a_0$ for $l = 0$ and 1 and $2.1 a_0$ for $l = 2$. The pseudo and all-electron radial wavefunctions for solved for the $l = 0-2$ pseudopotentials. b) Smooth pseudopotentials for $l = 0-2$ (non-local) and the local potential. We refer the reader to [230] for an explanation of the local and non-local parts of the pseudopotential.

(Section 3.3.3) we also make use of an efficient alternative.

3.3.3 Projector augmented waves

A good alternative to the pseudopotential method is that of projector augmented waves (PAW) as developed by Peter Blöchl [152]. Here, the aim is to represent the physical (all-electron) wavefunctions $\psi(\mathbf{r})$ by auxiliary (pseudo) wavefunctions $\tilde{\psi}(\mathbf{r})$ and physical core wavefunctions. The goal is to produce smooth $\tilde{\psi}(\mathbf{r})$ which can be represented with a limited basis set expansion (usually of plane waves) in the interstitial regions of the simulation box and to represent the core regions with a set of partial waves (usually numerical atomic orbitals, NAOs, discussed in Section 3.4.2). The relationship between $\psi(\mathbf{r})$ and $\tilde{\psi}(\mathbf{r})$ is made using the transformation operators $\hat{\mathcal{T}}$ and $\hat{\mathcal{U}}$. In Dirac notation

$$|\psi\rangle = \hat{\mathcal{T}}|\tilde{\psi}\rangle \iff |\tilde{\psi}\rangle = \hat{\mathcal{U}}|\psi\rangle \quad (3.20)$$

such that $\hat{\mathcal{T}} = \hat{\mathcal{U}}^{-1}$. Considering now just $\hat{\mathcal{T}}$, its closed form can be found by separating its contributions into local onsite regions (often referred to as the *augmentation* regions) and interstitial regions where the physical and auxiliary wavefunctions coincide

$$\hat{\mathcal{T}} = 1 + \sum_A \hat{\mathbf{S}}_A \quad (3.21)$$

where \mathbf{S}_A is the onsite part of the transform for each atomic site A . This term is set to zero beyond some cutoff radius from the atomic site which defines the augmentation region. Let us now consider the form of the physical and auxiliary wavefunctions in this region by expanding them in terms of the auxiliary and physical onsite partial waves $\tilde{\phi}_i$ and ϕ_i

$$|\psi\rangle = \sum_i c_i |\phi_i\rangle, \quad (3.22)$$

$$|\tilde{\psi}\rangle = \sum_i c_i |\tilde{\phi}_i\rangle. \quad (3.23)$$

We see that thanks to Equation 3.20, the expansion coefficients c_i are equal should $|\phi_i\rangle = \hat{\mathcal{T}}|\tilde{\phi}_i\rangle$. We can then write

$$|\psi\rangle = |\tilde{\psi}\rangle + \sum_i c_i (|\phi_i\rangle - |\tilde{\phi}_i\rangle). \quad (3.24)$$

We then rewrite the expansion coefficients using the inner product of local projector functions $\langle \tilde{p}_i |$ with the auxiliary wavefunctions, $c_i = \langle \tilde{p}_i | \tilde{\psi} \rangle$ providing us with a useful form of $\hat{\mathcal{T}}$

$$\hat{\mathcal{T}} = 1 + \sum_i (|\phi_i\rangle - |\tilde{\phi}_i\rangle) \langle \tilde{p}_i | \quad (3.25)$$

where the form of the projector functions are chosen to be both confined to the augmentation region and to be orthonormal to the auxiliary on-site partial waves. i.e, their matrix element is the kronecker delta: $\langle \tilde{p}_i | \tilde{\phi}_j \rangle = \delta_{ij}$. We can now build the form of the physical wavefunction using the auxiliary wavefunction and the local projectors in the revealing form

$$|\psi\rangle = |\tilde{\psi}\rangle + \sum_i (|\phi_i\rangle - |\tilde{\phi}_i\rangle) \langle \tilde{p}_i | \tilde{\psi} \rangle. \quad (3.26)$$

We see that the projectors probe the character of the auxiliary wavefunction to replace incorrect orbital character with the correct ones. We treat the core partial waves under the frozen core approximation, but, other than this, the usual basis set truncation error and choosing the augmentation region, the PAW method allows for the extraction of the physical wavefunctions at a small computational cost. In fact, simulations performed with PAWs consume comparable computational resources to a ultrasoft pseudopotential calculation[†] with an accuracy close to the all-electron calculation.

3.4 Scaling upwards

The size of the repeating unit for which we perform our simulations in our Born-von Karman box is largely determined by the symmetries of the system we wish to study. Those systems with a higher number of symmetry operations (both point and translational) can, in general, be represented with a smaller repeating unit host to a smaller number of electrons which therefore consumes less computational resources in the evaluation of the DFT total energy[‡]. Whilst this is a useful property for calculations with perfect and infinite crystals, this luxury is rarely extended to experimental reality. Symmetry is broken by defects and the emergence of order parameters in phase transitions which then require a much larger repeating unit than the original high symmetry crystal.

This is particularly salient for the perovskite ferroelectrics/antiferroelectrics following the discussions of the previous chapter. Even for the defect-free crystal, the high symmetry $Pm\bar{3}m$ phase of many perovskites is dynamically unstable at low temperatures at various propagation wavevectors \mathbf{q} in the 1BZ. These instabilities can lead to unit cell doubling when the AFD R_4^+ mode condenses (like in $I4/mcm$ STO [235]), octupling when the AFE Σ_2 mode condenses (like in $Pbam$ PZO [38]) and even increasing the number of atoms *16-fold* as we show for low energy AFE phases in PZO and PHO in Chapter 4. Extending beyond this, studying FE domain structures like those which appear in thin films will require simulations with thousands of atoms. This is the topic of Chapter 6. The consideration of realistic experimental order in random solid

[†]Indeed, USSPs and PAWs are formally related as pointed out by Kresse & Joubert [234].

[‡]The observant reader will note that in spite the smaller number of electrons in the repeating unit, integrals in \mathbf{k} -space will now require a finer grid for convergence. Whilst this is true, high symmetry crystals have a *very* small IBZ so the actual number of \mathbf{k} -points to be computed is usually much reduced.

solutions like PZT intrinsically requires a large number of atoms and increased computational resources. Unfortunately, certain scaling bottlenecks make it difficult for us to treat such systems within the conventional implementation of DFT we have described in the previous section. We shall now take a deeper look at why and propose how these bottlenecks can be remedied.

3.4.1 Limitations of conventional implementations

Conventional simulations based on DFT offer $\mathcal{O}(N^3)$ asymptotic scaling for the ground state solution time where N is the total number of atoms in the simulation box [4]. This scaling behaviour is troublesome as it quickly makes useful calculations beyond a few hundred atoms intractable on most high performance computing platforms. The origin of this $\mathcal{O}(N^3)$ scaling behaviour is rooted in the particular solution method for solving the KS equations (Equation 3.10). In the conventional procedure, we build a Hamiltonian matrix for each irreducible \mathbf{k} -point on our reciprocal space integration grid and solve for its eigenvalues and eigenvectors using standard *matrix diagonalisation*[†] [236]. This technique scales cubically with the dimensions of the matrix [236] which are typically $N_{\text{basis}} \times N_{\text{basis}}$ where N_{basis} is the total number of basis functions in the simulation box. Since $N_{\text{basis}} \propto N$ we arrive at the aforementioned $\mathcal{O}(N^3)$ asymptotic scaling.

For the plane wave basis set, convergent calculations often require ~ 100 (sometimes more) basis functions per atom which will rapidly balloon the size of the Hamiltonian as we increase the number of atoms. This, in turn, makes it intractable to diagonalise stunting our efforts to treat a larger system (although, in Section 3.4.5, we show a technique where we *can* use matrix diagonalisation for systems of a *few thousand* atoms). Such a large number of basis functions are required since the plane wave is the solution of the free electron [237]; bearing very little resemblance to the orbitals they intend to expand. Plane waves pose other issues for the scalability of DFT. Such a basis is delocalised in space which causes issues for parallelisation on many computing cores since spatial partitioning (and *divide and conquer* methods) for the basis functions becomes difficult [4]. Also, plane wave codes are reliant of the efficiency of fast Fourier transforms (FFTs) which are infamous for their poor parallelisability for large scale problems [4]. It is, of course, still possible to parallelise over \mathbf{k} -points, but, the usefulness of this procedure diminishes with system size since we require fewer and fewer total points. Their spatial delocalisation can also lead to wasteful calculations on integration grids within our simulation box. This is particularly obvious for systems with significant vacuum regions which contain negligible charge density.

[†]In the majority of plane wave codes, instead directly diagonalising a large $\mathbf{H}^{\mathbf{k}}$, we can yield the KS states by minimising the KS energy with respect to the plane wave coefficients, as shown in the seminal work of Car and Parrinello [148]. When the KS energy is directly minimised, $\mathcal{O}(N^3)$ scaling still arises but is instead from the orthogonalisation of bands [5].

3.4.2 A local basis: pseudoatomic orbitals

We can begin to alleviate the problems listed above should we switch out plane waves for a local basis set. Local basis sets are atom centered functions which are often more chemically intuitive than plane waves for describing orbitals. They subsequently require less functions to describe the KS orbitals than do plane waves. Arguably the most intuitive basis is the Slater type orbital [238]. This is since their functional form is similar to the exact solutions of the hydrogenic radial Schrödinger equation [196] (Although, unlike the true hydrogenic solutions, Slater type orbitals have no radial nodes [238]). In practice, these basis functions are often not used due to difficulties with integration [239] and are instead replaced with Gaussian functions [240]; a popular choice of basis for many codes (including the pioneering code; Gaussian [241]). One drawback of using Gaussian functions is that they typically have long tails which make them rather delocalised in space (although much less so than a plane wave). Such a property is undesirable for $\mathcal{O}(N)$ DFT as we discuss in Section 3.4.6.

Another good choice is to use the numerical solutions for the atomic orbitals of a given atomic species. This can be done at the all-electron level where the resulting orbitals are often referred to as numerical atomic orbitals (NAOs) or within the pseudopotential formalism as pseudoatomic orbitals (PAOs; although sometimes still referred to as NAOs) [6, 242–250]. The functional form of a PAO is the product of a radial function $R_{nl\zeta}(\mathbf{r})$ with the appropriate spherical harmonic $Y_m^l(\hat{\mathbf{r}})$ [196]

$$\chi_{nlm\zeta}(\mathbf{r}) = R_{nl\zeta}(\mathbf{r})Y_m^l(\hat{\mathbf{r}}) \quad (3.27)$$

where each basis function is labelled with the relevant quantum numbers: the principal quantum number n , azimuthal (angular momentum) quantum number l and the magnetic (z -projection of l) quantum number m . The subscript ζ is representative of the completeness of the basis set. That is, for any given nlm any number of ζ 's can be chosen to represent the orbital. Increasing the total number of ζ 's increases the flexibility of the basis - i.e, in the double- ζ (DZ) representation, each nlm has two ζ 's indexed as $\zeta = 1$ and $\zeta = 2$.

A popular method for the construction of multiple- ζ basis sets is the *split-norm* method. This scheme is inspired by the *split valence* method which is standard in quantum chemistry codes using a linear combination of Gaussian functions in the basis set expansion [240]. Here, the radial functions of additional ζ 's are yielded by 'splitting' the slowest decaying radial functions to act as independent radial functions [250]. For a DZ basis, this is achieved by ensuring that the $\zeta = 2$ radial function reproduces the tail of the $\zeta = 1$ function beyond a matching radius, and runs smoothly inwards. Further ζ 's can be obtained repeating the procedure at different radii. Within the CONQUEST code, we use a modified procedure where each ζ is a new and explicit solution to the radial Schrödinger equation of the pseudoatom. The assessment of this mechanism is the focus of much of Chapter 5. Even when including multiple- ζ 's in the basis

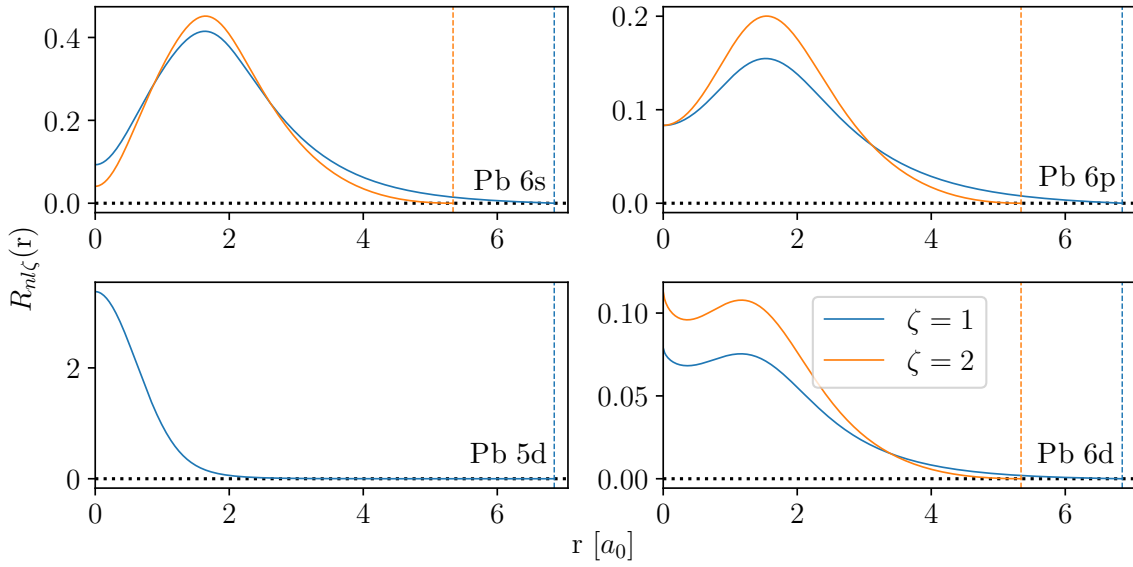


Figure 3.2: The default Pb radial function solutions $R_{nl\zeta}(r)$ for $\zeta = 1$ and 2 generated by the CONQUEST PAO generator code (v1.02) using the *equal radii* method described in Chapter 5. The cutoff radii r_c are marked with vertical dotted lines. Pb 5d features only a single ζ as we choose to treat it as a semicore state. We have perturbatively polarised Pb 6p to create the Pb 6d radial functions.

set expansion, our basis can still remain rather rigid. To combat this, we introduce *polarisation functions* to the basis set [250]. These are PAOs with a higher angular momentum (typically $l + 1$ of the highest occupied valence orbital) aimed at increasing the angular flexibility of the basis. These can be obtained simply as a new solution to the pseudoatomic Schrödinger equation or perturbatively by applying a small electric field to the orbital to be polarised [250].

To ensure that our PAOs are localised in space, the radial functions are found in the presence of a spherical confining potential [247]. How one applies such a potential to obtain the optimal balance between accuracy and efficiency of the basis is an open question which we address in Chapter 5. The resulting spatial localisation is such that each basis function decays smoothly to *exactly zero* beyond some cutoff radius ($\chi_{nlm\zeta}(\mathbf{r}) = 0; |\mathbf{r}| \geq r_c$). This ensures that important matrices (including the Hamiltonian and overlap matrices) are sparse allowing for the employment of efficient and scalable sparse matrix algebra [4, 251]. This strict localisation also means that operations between basis functions no longer need to take place in areas of vacuum. We note that matrix sparsity can also be achieved by discarding matrix elements whose magnitude is below some threshold [4, 252]. We provide in Figure 3.2 some exemplar radial functions produced by the CONQUEST PAO generator (v1.02). Including all of these functions would define a DZDP basis set for Pb.

The switch to PAOs from plane waves is not without drawbacks. While increasing the number of ζ 's does usually increase the quality of the basis, unlike plane waves, this process is not systematic [6] so we must be careful in our choice of basis and conduct considerable testing.

Also, when moving to atom centered orbitals like PAOs, we must consider an additional term in the calculation of the forces which takes into account that (unlike plane waves) basis functions *move with* the atoms. These are known as *Pulay forces* [253].

3.4.3 The CONQUEST approach

The DFT package of choice for a large portion of this thesis is the CONQUEST code [7, 17, 194]. CONQUEST is a local orbital code designed for large scale DFT calculations on thousands (and even millions [13]) of atoms. The code now primarily uses PAOs (and are the focus of this section) as basis functions although B-splines or ‘blips’ are also in use [254]. It can operate in several modes depending on the application. We address the modes used in this thesis in an order commensurate with an increasing number of atoms. That is, Section 3.4.4 deals with how one might simulate a few hundred atoms, Section 3.4.5 pertains to simulations of a few thousand atoms and Section 3.4.6 demonstrates how one can surpass *one million* atoms. We must first, however, present a short overview of the unifying parts of the code which are distinct from typical implementations of DFT.

Let us reformulate our approach to be based upon the single particle KS density matrix (which we will refer to from this point onwards as the *density matrix*)

$$\rho(\mathbf{r}, \mathbf{r}') = \sum_n f_n \psi_n^*(\mathbf{r}) \psi_n(\mathbf{r}'). \quad (3.28)$$

The next step is to assume that the density matrix has a finite number of non-zero eigenvalues. This allows us to represent the density matrix in its separable form [255, 256]

$$\rho(\mathbf{r}, \mathbf{r}') = \sum_{i\alpha, j\beta} \phi_{i\alpha}(\mathbf{r}) K_{i\alpha j\beta} \phi_{j\beta}(\mathbf{r}'). \quad (3.29)$$

This form of the density matrix introduces some recurring formalities for the operation of CONQUEST. Firstly, we describe the *support functions* $\phi_{i\alpha}(\mathbf{r})$ (SFs; sometimes called *non-orthogonal generalised Wannier functions*, NGWFs, by those associated with the ONETEP package [9]). The SFs are local orbital functions (indexed α, β) at atomic sites (i, j) which move with the atoms strictly localised within a sphere. $K_{i\alpha, j\beta}$ is known as the density matrix in the basis of support functions (or sometimes, the density kernel) which we will address fully in the forthcoming.

Within this reformulated approach, some energy functionals need reconsidering. Since the density can easily be evaluated as

$$n(\mathbf{r}) = 2\rho(\mathbf{r}, \mathbf{r}) \quad (3.30)$$

the Hartree and exchange & correlation energies can be found using the same functionals as

before. The kinetic energies of the independent electrons and the electron-pseudo-core interaction (the pseudopotential energy), however, must be re-addressed [16, 255]. The kinetic energy is now given as

$$E_{\text{kin}}^{\text{KS}} = \sum_{i\alpha, j\beta} \int \phi_{j\beta}(\mathbf{r}) K_{i\alpha, j\beta} \nabla^2 \phi_{i\alpha}(\mathbf{r}) d\mathbf{r} \quad (3.31)$$

which within CONQUEST (using PAOs), this integral is evaluated through considering the two components of the PAOs. That is, the spherical harmonic contributions are evaluated analytically while we FFT the radial part and scale by k^2 (the FFT reciprocal space coordinate) to yield the Laplacian term. The integral is then performed in 1D with a sum over a *very* fine grid. For more information on this process, we refer the reader to Appendix A of [247]. The pseudopotential energy is rewritten as

$$E_{\text{PS}} = 2 \sum_{i\alpha, j\beta} \int V_{\text{PS}}(\mathbf{r}, \mathbf{r}') \phi_{i\alpha}(\mathbf{r}) K_{i\alpha, j\beta} \phi_{j\beta}(\mathbf{r}') d\mathbf{r} d\mathbf{r}' \quad (3.32)$$

which in implementation is evaluated by multiplying $n(\mathbf{r})$ at each grid point by the total pseudopotential at each grid point and summing over all grid points. For more details of this procedure we refer to reader to Section III A of [16].

3.4.4 Diagonalisation for small systems

SFs are mapped to an underlying local basis of PAOs in the expansion

$$\phi_{i\alpha}(\mathbf{r}) = \sum_s d_{i\alpha}^s \chi^s(\mathbf{r}) \quad (3.33)$$

for support function coefficients $d_{i\alpha}^s$ and local basis functions $\chi^s(\mathbf{r})$. The way we choose to map SFs to PAOs distinguishes the in many cases the mode of operation of CONQUEST. The simplest case is to use so-called *primitive PAOs* where only one PAO is mapped to a SF. This is the same as setting $s = 1$ in Equation 3.33. Whilst this is the most accurate setting (since $d_{i\alpha}^s$ can be found exactly should the Hamiltonian be diagonalised) it also comes with the largest computational burden. This is since the Hamiltonian matrix elements are defined

$$H_{i\alpha, j\beta} = \int \phi_{i\alpha}(\mathbf{r}) \hat{\mathbf{H}} \phi_{j\beta}(\mathbf{r}) d\mathbf{r}. \quad (3.34)$$

We can instead choose to treat the SFs as an expansion of all the PAO basis functions used to represent a given orbital. For a d state (5 total orbitals) and a triple- ζ PAO basis (15 total PAOs), each of the d orbitals can now be represented with a basis set expansion of three PAOs. When doing so, we of course no longer have the exact SF coefficients from the diagonalisation, so, we must perform an optimisation for the coefficients. A contraction which is used for a

large amount of this thesis stems from using a linear combination of basis functions within a localisation region in what we call the multi-site support function method [18, 19] (which we detail in Section 3.4.5) although we can also choose to make an expansion as a combination of all of the orbitals on a given atomic site which we call the on-site support function method [257].

Once we have chosen our mapping of PAOs to SFs, we must select our method for the evaluation of the DFT ground state (i.e., the energy, charge density and its derived quantities). Principally, we make a choice on how to evaluate the density matrix in the basis of support functions; the \mathbf{K} -matrix. One approach is to solve the generalised eigenproblem form of the KS equations

$$H_{i\alpha j\beta} c_{j\beta}^n = \epsilon_n S_{i\alpha j\beta} c_{j\beta}^n \quad (3.35)$$

which arises from treating the KS orbitals as a linear combination of the SFs

$$\psi_n(\mathbf{r}) = \sum_{i\alpha} c_{i\alpha}^n \phi_{i\alpha}^n. \quad (3.36)$$

Notice how for Equation 3.35 we must explicitly calculate the overlap matrix elements $S_{i\alpha j\beta}$

$$S_{i\alpha j\beta} = \int \phi_{i\alpha}^*(\mathbf{r}) \phi_{j\beta}(\mathbf{r}) d\mathbf{r} \neq \delta_{i\alpha, j\beta}. \quad (3.37)$$

This is since our basis functions are non-orthogonal so cannot be equal to the Kronecker delta $\delta_{i\alpha, j\beta}$. Once evaluated, we can solve Equation 3.35 simply by diagonalising[†] the Hamiltonian to yield the eigenvalues ϵ_n and eigenvectors $c_{j\beta}^n$. With this eigenvector information, we can find the \mathbf{K} -matrix elements directly

$$K_{i\alpha j\beta} = \sum_n f_n c_{i\alpha}^n c_{j\beta}^{n*}. \quad (3.38)$$

Using this form of \mathbf{K} , we can evaluate Equation 3.29, although, we need only evaluate the diagonal from Equation 3.30. Since we also have the eigenvectors, we can define the KS orbitals using Equation 3.36 which in turn can be used to evaluate the kinetic energy from Equation 3.6. Without the eigenvector information (which is the case when using the $\mathcal{O}(N)$ algorithm as we will learn in Section 3.4.6), we can still evaluate the kinetic energy but must use Equation 3.31. The total energy can now be calculated in the standard way. Regardless of our choice of basis set expansion, this approach leads to $\mathcal{O}(N^3)$ scaling since we have performed the troublesome matrix diagonalisation when solving Equation 3.35. Even so, this is usually fast for systems up to a few hundred atoms since relatively few PAO basis functions are needed compared to plane waves. It is possible to avoid doing this diagonalisation entirely using a method based upon iterative sparse matrix algebra in real space. This is the $\mathcal{O}(N)$ scaling method which we

[†]In the diagonalisation mode, we must still perform integrals over \mathbf{k} -space, but, we drop this label in Equation 3.35 for notational clarity.

describe in Section 3.4.6.

3.4.5 Contracting the Hamiltonian: multi-site support functions

We have so far shown that it is possible to reformulate DFT in terms of the density matrix and have shown how we can solve for the total energy of small systems using a 1:1 PAO:SF mapping and matrix diagonalisation. This section seeks to provide a description of the multi-site support function method (MSSF) method as implemented in CONQUEST. This allows us to treat a few thousand atoms by a clever contraction of the Hamiltonian dimensions. For further discussion, the reader is referred to [18, 19, 258, 259] and references therein.

We now consider representing a support function as a linear combination of PAOs not just at a single atomic site, but, including its neighbours within a localisation region, r_{MS}

$$\phi_{i\alpha}(\mathbf{r}) = \sum_k^{i,\text{neighbours}} \sum_{\zeta \in k} C_{i\alpha,k\zeta} \chi_{k\zeta}(\mathbf{r}) \quad (3.39)$$

where k is an atomic site enclosed within a sphere of radius r_{MS} about target atom i , inclusive of i . The coefficients C now span a subspace of a local molecular orbital (MO), which relinquishes us from atomic symmetry constraints which previously did not allow for a minimal representation of support functions in the contraction [247]. In practice, this means, for example, that a primitive TZTP basis can now be contracted to its SZ size whereas before, atomic symmetry constraints only permitted the contraction to SZP. The MSSF coefficient matrix \mathbf{C} is sparse since only the atoms within r_{MS} are taken into account as neighbor atoms. The overlap matrix elements in the basis of MSSFs can be written

$$S_{i\alpha,j\beta} = \sum_{k\zeta} \sum_{k'\zeta'} C_{i\alpha,k\zeta} \langle \chi_{k\zeta} | \chi_{k'\zeta'} \rangle C_{k'\zeta',j\beta} = \sum_{k\zeta} \sum_{k'\zeta'} C_{i\alpha,k\zeta} S_{k\zeta,k'\zeta'}^{\text{PAO}} C_{k'\zeta',j\beta} \quad (3.40)$$

where we have identified that the closure $\langle \chi_{k\zeta} | \chi_{k'\zeta'} \rangle$ is the overlap matrix of Equation 3.37 in the primitive PAO basis, \mathbf{S}^{PAO} . This matrix has nonzero values only if the distance between the two atoms (k and k') is smaller than twice the PAO cutoff radius, r_c . Therefore, the evaluation of Equation 3.40 can be performed with sparse matrix algebra

$$\mathbf{S} = \mathbf{C} \mathbf{S}^{\text{PAO}} \mathbf{C}^\dagger \quad (3.41)$$

where the range of \mathbf{S} written with MSSFs now extends to twice of $(r_{\text{MS}} + r_c)$. The charge density can also be rewritten using MSSFs

$$n(\mathbf{r}) = \sum_{i\alpha,j\beta} \sum_{k\zeta} \sum_{k'\zeta'} C_{i\alpha,k\zeta} \chi_{k\zeta}(\mathbf{r}) K_{i\alpha,j\beta} C_{j\beta,k'\zeta'} \chi_{k'\zeta'}(\mathbf{r}) \quad (3.42)$$

although, it is more efficient to evaluate $n(\mathbf{r})$ in the primitive PAO representation since the matrices have a smaller range

$$n(\mathbf{r}) = \sum_{k\zeta} \sum_{k'\zeta'} \chi_{k\zeta}(\mathbf{r}) K_{k\zeta, k'\zeta'}^{\text{PAO}} \chi_{k'\zeta'}(\mathbf{r}) \quad (3.43)$$

where the \mathbf{K} -matrix in the PAO representation, \mathbf{K}^{PAO} is obtained by the transform

$$\mathbf{K}^{\text{PAO}} = \mathbf{C}^\dagger \mathbf{K} \mathbf{C}. \quad (3.44)$$

We note that whilst in principle, the \mathbf{K} -matrix can be evaluated using either diagonalisation or the linear scaling approach, we currently encounter issues with numerical instability when evaluating \mathbf{S}^{-1} using the linear scaling approach with MSSFs. This is an area of active development within CONQUEST. Using $n(\mathbf{r})$ from Equation 3.43, we can calculate the Hamiltonian matrix in the basis of primitive PAOs, \mathbf{H}^{PAO} whose range is shared with \mathbf{S}^{PAO} . We then transform this matrix to the contracted MSSF form using

$$\mathbf{H} = \mathbf{C} \mathbf{H}^{\text{PAO}} \mathbf{C}^\dagger \quad (3.45)$$

whose range is shared with \mathbf{S} . We see clearly now that the square dimensions of the Hamiltonian matrix using the MSSF method are the column or row dimensions of \mathbf{C} or \mathbf{C}^\dagger . Since these coefficients are contracted to the SZ size using the MSSF expansion, the Hamiltonian is now SZ in size typically reducing its dimensions by a factor of ≈ 3 . Diagonalisation calculations are now $\approx 27\times$ faster due to the cubic scaling of the operation.

We have so far not addressed how the coefficient matrix \mathbf{C} is evaluated. While it is possible to calculate these with a variational optimisation procedure and iterative diagonalisation, this is time consuming since convergence can be slow. So, to find the optimal balance between efficiency and accuracy, we use the local filter diagonalisation (LFD) method to evaluate the coefficients [258, 259]. This requires the solution of a local eigenproblem for a subset of atoms s enclosed by a sphere of radius $r_{\text{LD}} (\geq r_{\text{MS}})$ for each target atom

$$\mathbf{H}_s \mathbf{C}_s = \epsilon_s \mathbf{S}_s \mathbf{C}_s \quad (3.46)$$

for subspace eigenvalues ϵ_s , MO coefficients \mathbf{C}_s and where \mathbf{H}_s and \mathbf{S}_s are the local subsets of the system-wide Hamiltonian and overlap matrices respectively. By projecting \mathbf{C}_s onto a set of trial vectors \mathbf{t} , we obtain the contraction coefficients \mathbf{C}'

$$\mathbf{C}' = \mathbf{C}_s f(\epsilon_s) \mathbf{C}_s^T \mathbf{S}_s \mathbf{t} \quad (3.47)$$

where $f(\epsilon_s)$ is the Fermi-Dirac distribution. By setting the chemical potential of this distribution to a value around the Fermi energy (for this local system, not the system-wide Fermi

energy), the effect from unoccupied local MOs with high energy can be eliminated [18, 19]. While the trial vectors are arbitrary in principle, a good choice is to use the atomic orbitals on the target atoms as trial vectors. Lastly, C' is mapped onto the corresponding position in the contraction coefficient vectors, whose elements are extracted for use in Equation 3.39.

There is a final consideration to be made concerning the timing for the calculation of the MO coefficients during the SCF procedure. A simple approach would be to perform a full SCF procedure (to some tolerance) with constant C . Once this SCF cycle is completed, a new C can be obtained and then a new SCF cycle completed. This would then be repeated until convergence criteria in the total energy is met. While this is a reliable procedure, the requirement to perform many SCF cycles can be wasteful from a computational standpoint. Instead, we can choose to update C at each step of a single SCF cycle. While this could require more evaluations of the local eigenproblem of Equation 3.46 (and the matrices which are transformed by C), the overhead associated with doing so is often far less than the cost associated with further diagonalisations of the system-wide Hamiltonian. We call this procedure *mixed-LFD-SCF* and is used in the MSSF calculations in this thesis.

The MSSF method therefore introduces two new adjustable parameters to the DFT calculation; r_{LD} and r_{MS} . The former expands the space used for the local filter diagonalisation and the latter modifies the representation of $\phi_{i\alpha}(\mathbf{r})$. The accuracy of the contraction can be improved by increasing both of these subject to $r_{MS} \leq r_{LD}$. In practice, convergence can be achieved for relatively modest values of both (1-2 lattice constants of the bulk in condensed systems). Using this method, high accuracy calculations (close to plane wave accuracy, as we see in Chapter 6) with a few thousand atoms can feasibly be performed on most standard HPC systems. Structural relaxations of ≈ 1000 atoms to a stringent force tolerance can be expected to take 1-2 weeks of calculation wall-time (although this should be taken with a grain of salt, since relaxation times are very system dependent property and depend on the starting point) on ≈ 200 physical cores. Simulations of ≈ 2000 atoms may need ≈ 500 physical cores to meet the memory requirements, dependent on the memory-per-node on the HPC system.

3.4.6 The $\mathcal{O}(N)$ method

So far, our approach has relied upon matrix diagonalisation so suffers from the $\mathcal{O}(N^3)$ scaling wall for conventional DFT, regardless of the basis set used [4]. Users of conventional codes may be conditioned to believe that this is the only approach since the electronic terms in the total energy are derived from the eigenvalues, the charge density is built from the eigenvectors and the kinetic energy requires the KS orbitals, which, in turn, require the eigenvectors. This could leave one puzzled about how to obtain these seemingly central quantities, when, in fact, the HK theorems make so such indication that any eigenproblem need be solved. Instead, we detail an approach where the ground state $n(\mathbf{r})$ is found variationally through the direct minimisation of the single body KS density matrix $\rho(\mathbf{r}, \mathbf{r}')$ of Equation 3.29.

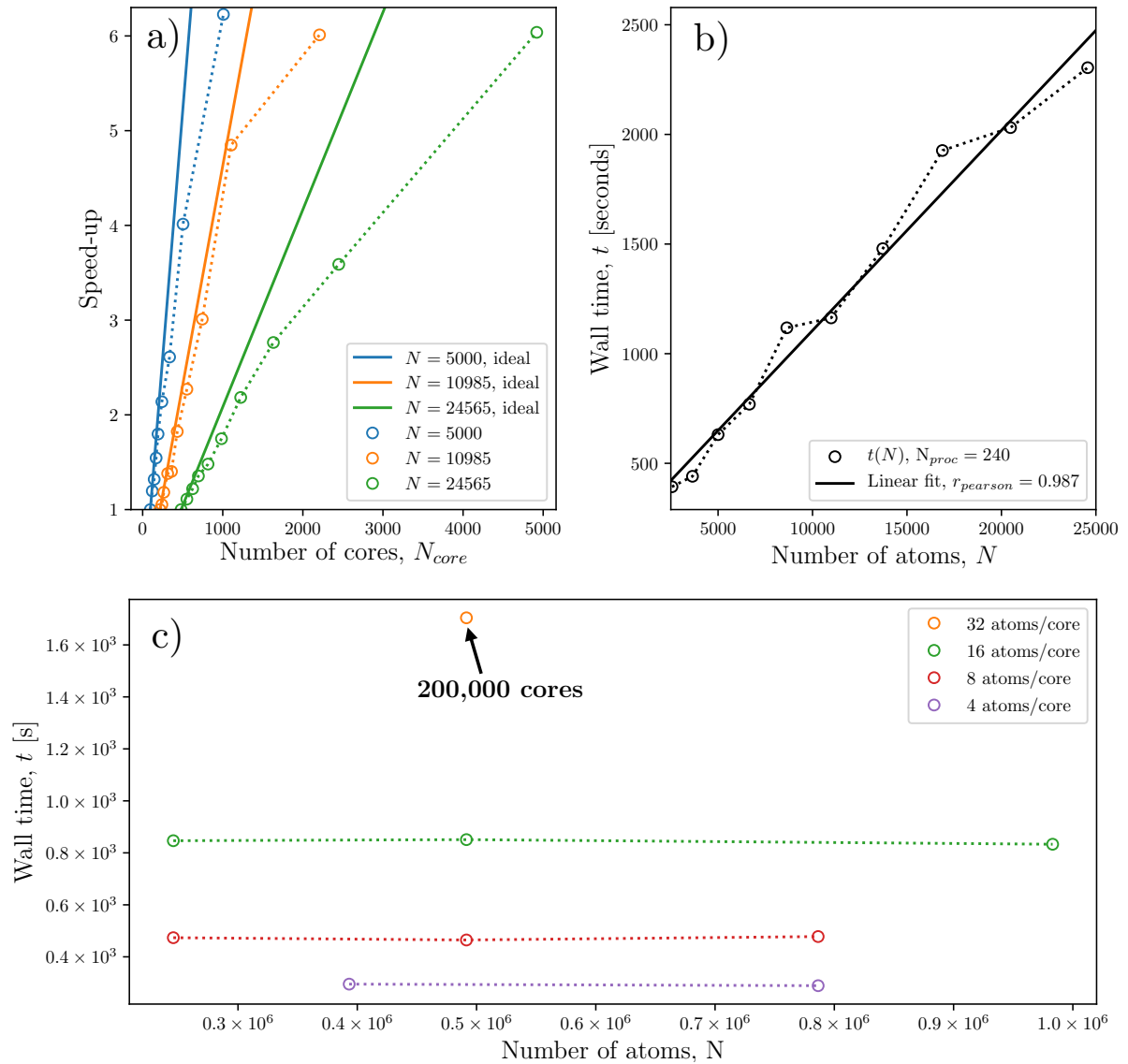


Figure 3.3: Scaling performance for CONQUEST on the K-computer and ARCHER using a pure MPI implementation. a) Strong scaling on the UK national supercomputer, ARCHER, up to 4920 processors (from 50-5 atoms/core). Calculations were performed on bulk PTO with an L_{range} of 7.41\AA and a SZ basis of PAOs. b) A scaling demonstration for the $\mathcal{O}(N)$ algorithm on ARCHER for the same material system as (a). c) Weak scaling on the K-computer up to *one million* atoms for bulk Si. This image is © American Institute of Physics from reference [7].

We first consider a property of $\rho(\mathbf{r}, \mathbf{r}')$ vital to achieving $\mathcal{O}(N)$ scaling. That is, it is known that $\rho(\mathbf{r}, \mathbf{r}')$ is ranged as a consequence of quantum interference effects in a concept often referred to as *nearsightedness* [260]. Formally,

$$\rho(\mathbf{r}, \mathbf{r}') \rightarrow 0, \quad |\mathbf{r} - \mathbf{r}'| \rightarrow \infty. \quad (3.48)$$

That is, there is a loss of quantum phase coherence between distant points. The decay-rate of $\rho(\mathbf{r}, \mathbf{r}')$ is exponential in gapped systems (increasing with the size of the gap) but algebraic in metals at $T = 0$ [4]. This means that insulating systems can be well represented with a short-ranged density matrix whereas the implicit non-locality of electrons in metals will require a considerably longer ranged $\rho(\mathbf{r}, \mathbf{r}')$. Practically, we choose a truncation range for $\rho(\mathbf{r}, \mathbf{r}')$ to acceptably converge the total energy, forces and stresses from the following minimisation to the result obtained by directly diagonalising the Hamiltonian. This should be the focus of a careful convergence study on the system of interest where one should check that the relevant quantity is converged to a tolerance. Beyond this truncation range, we set the matrix element to exactly *zero* which leads to our density matrices becoming sparse. Since the Hamiltonian and overlaps matrices are also sparse (as noted in Section 3.4.2 as a result of finite ranged basis functions), sparse algebra operations between these matrices (matrix multiplications, additions etc.) will have an execution time which scales linearly with the number of atoms [251]. As we shall formulate in Sections 3.4.6.1 and 3.4.6.2, we can yield the ground state density matrix using only these operations so can achieve a solution for the energy scaling as $\mathcal{O}(N)$.

We must enforce some constraints before outlining our minimization to ensure our solution remains physical. Firstly, the number of electrons (given as $2\text{Tr}[\mathbf{KS}]$) must remain constant. Many methods exist for imposing the correct electron number [16, 261–264] and the approach used in CONQUEST is detailed in Section 3.4.6.2. Next, we consider that $\rho(\mathbf{r}, \mathbf{r}')$ is a projector onto the occupied subspace. It is then required to have eigenvalues λ of either zero or one ($\hat{\rho} = \hat{\rho}^2$); a condition known as idempotency. This is in practice difficult to enforce so is replaced with the easier to achieve condition of $0 \leq \lambda \leq 1$. This is known as *weak idempotency* [262, 265].

The $\mathcal{O}(N)$ scaling algorithm in CONQUEST is split into two distinct parts [266]. Firstly, a density matrix is constructed using the iterative, canonical purification of Palser & Manopolous (PM) [267]. We then use this matrix to initialise the density matrix minimization (DMM) technique of Li, Nunes and Vanderbilt (LNV) [262]. The motivation for the two part scheme is as follows. The PM approach is good at finding density matrices that are idempotent, however, the algorithm is non-variational. This makes it completely arbitrary as to when to halt the algorithm. Further, the density matrix produced at the end of the PM stage will depend on the initial density matrix. The LNV approach is good for searching through idempotent density matrices to find the one that yields the true ground state. This part of the algorithm is fully variational so the

DMM can be halted once a minimum has been reached. The ground state density matrix can then be used to determine the total energy of the system. This method displays excellent strong and weak scaling performance on most hardware as shown in Figures 3.3a and 3.3c. In Figure 3.3b we explicitly display the linear growth of the wall-time between $\approx 3,000 - 25,000$ atoms for a constant number of processors.

3.4.6.1 Canonical purification

The PM canonical purification method [267] exploits a modified McWeeny purification [268] polynomial in an attempt to iteratively achieve the ground state density matrix. In its original form, the McWeeny polynomial is given as [268]

$$f(x) = 3x^2 - 2x^3. \quad (3.49)$$

This polynomial has stable fixed points at $x = 0$ and $x = 1$ (where $f(x) = x$ and $f'(x) = 0$). If we were to repeatedly apply this function to the density matrix, we would find that its eigenvalues would tend towards zero or one, thus, enforcing the idempotency constraint. So, after each iteration, some nearly idempotent density matrix \mathbf{L}_n becomes more nearly idempotent at \mathbf{L}_{n+1} .

In order to also fix the number of electrons, one can modify the function to allow its unstable fixed point c (where $f(x) = 0$ and $f'(x) \leq 1$) to move anywhere between zero and one. This extra flexibility allows us to conserve $N_e = 2\text{Tr}[\mathbf{L}\mathbf{S}]$. What follows now is the original fixed- N_e PM algorithm modified to the non-orthonormal case following the arguments of Bowler and Gillan [266]. Namely, the transforms $\tilde{\mathbf{L}} = \tilde{\mathbf{S}}^{-1/2}\mathbf{L}\tilde{\mathbf{S}}^{-1/2}$ and $\tilde{\mathbf{H}} = \tilde{\mathbf{S}}^{1/2}\mathbf{H}\tilde{\mathbf{S}}^{1/2}$ are applied, where matrices capped with a tilde are in a non-orthonormal basis. We first define the averaged chemical potential of the system

$$\bar{\mu} = \frac{\text{Tr}[\tilde{\mathbf{S}}^{-1/2}\mathbf{H}\tilde{\mathbf{S}}^{-1/2}]}{N_{\text{orb}}} = \frac{\text{Tr}[\mathbf{H}\tilde{\mathbf{S}}^{-1}]}{N_{\text{orb}}} \quad (3.50)$$

where N_{orb} is the total number of orbitals in the system. For notational clarity, we now drop *tildes* from non-orthonormal matrices. We initialize the algorithm with the optimal trial matrix given as a function of \mathbf{H} and with the correct N_e

$$\mathbf{L}_{\text{init}}^{\text{PM}} = \frac{\zeta}{N_{\text{orb}}}(\bar{\mu}\mathbf{S}^{-1} - \mathbf{S}^{-1}\mathbf{H}\mathbf{S}^{-1}) + \frac{N_e}{N_{\text{orb}}}\mathbf{S}^{-1} \quad (3.51)$$

where ζ is given by

$$\zeta = \min \left\{ \frac{N_e}{H_{\text{max}} - \bar{\mu}}, \frac{N_{\text{orb}} - N_e}{\bar{\mu} - H_{\text{min}}} \right\} \quad (3.52)$$

and H_{max} and H_{min} are estimated by the Gershgorin limits [269] on the spectrum on the

Hamiltonian. We now enter the following algorithm

$$\mathbf{L}_{n+1} = \begin{cases} [(1 - 2c_n)\mathbf{L}_n + (1 + c_n)\mathbf{L}_n\mathbf{S}\mathbf{L}_n - \mathbf{L}_n\mathbf{S}\mathbf{L}_n\mathbf{S}\mathbf{L}_n]/(1 - c_n), & \text{if } c_n \leq \frac{1}{2} \\ [(1 + c_n)\mathbf{L}_n\mathbf{S}\mathbf{L}_n - \mathbf{L}_n\mathbf{S}\mathbf{L}_n\mathbf{S}\mathbf{L}_n]/c_n, & \text{if } c_n > \frac{1}{2} \end{cases} \quad (3.53)$$

where the unstable fixed point c_n is evaluated by

$$c_n = \text{Tr} \left[\frac{\mathbf{L}_n\mathbf{S}\mathbf{L}_n - \mathbf{L}_n\mathbf{S}\mathbf{L}_n\mathbf{S}\mathbf{L}_n}{\mathbf{L}_n - \mathbf{L}_n\mathbf{S}\mathbf{L}_n} \right]. \quad (3.54)$$

The algorithm in Equation 3.53 should be terminated once $E[\mathbf{L}_{n+1}] > E[\mathbf{L}_n]$ as truncation errors will begin to dominate in further steps.

3.4.6.2 Density matrix minimisation

The LNV method [262] requires the minimization of the grand potential Ω

$$\begin{aligned} \Omega &= \text{Tr}[(\mathbf{H} - \mu\mathbf{S})\mathbf{K}] \\ &= \text{Tr}[\mathbf{H}'(3\mathbf{L}\mathbf{S}\mathbf{L} - 2\mathbf{L}\mathbf{S}\mathbf{L}\mathbf{S}\mathbf{L})] \end{aligned} \quad (3.55)$$

where $\mathbf{H}' = \mathbf{H} - \mu\mathbf{S}$ and where we have once again used Equation 3.49 to enforce the weak idempotency condition. That is

$$\mathbf{K} = 3\mathbf{L}\mathbf{S}\mathbf{L} - 2\mathbf{L}\mathbf{S}\mathbf{L}\mathbf{S}\mathbf{L}. \quad (3.56)$$

The initial \mathbf{L} at this stage is the output of the PM stage after a set number of iterations or after the energy termination condition is met. If we choose to work at a fixed chemical potential μ , we can now simply evaluate the gradient of Ω . This gradient then becomes the search direction σ for a line minimization $\mathbf{L} + \alpha\sigma$

$$\nabla\Omega = \frac{\partial\Omega}{\partial\mathbf{L}} = 6(\mathbf{S}\mathbf{L}\mathbf{H}' + \mathbf{H}'\mathbf{L}\mathbf{S}) - 4(\mathbf{S}\mathbf{L}\mathbf{S}\mathbf{L}\mathbf{H}' + \mathbf{S}\mathbf{L}\mathbf{H}'\mathbf{L}\mathbf{S} + \mathbf{H}'\mathbf{L}\mathbf{S}\mathbf{L}\mathbf{S}). \quad (3.57)$$

This step is able to change to electron number N_e . This is troublesome as we must work at fixed N_e . To counter this, we must then project out the electron variation direction ∇N_e from the search direction

$$\nabla N_e = \frac{\partial N_e}{\partial\mathbf{L}} = 12(\mathbf{S}\mathbf{L}\mathbf{S} - \mathbf{S}\mathbf{L}\mathbf{S}\mathbf{L}\mathbf{S}). \quad (3.58)$$

Once the energy minimisation has been completed, we use this electron variation direction to search for the correct electron number [266]. Once the minimisation is completed to some tolerance we retrieve \mathbf{K} from Equation 3.56 which is used to evaluate $\rho(\mathbf{r}, \mathbf{r})$ (and therefore $n(\mathbf{r})$)

in accordance with Equation 3.29. We then repeat these steps in an SCF procedure. We have, however, developed a more efficient scheme for the SCF cycle in the $\mathcal{O}(N)$ mode of operation which allows for charge density mixing concurrently with the LNV iterations. In this scheme which we call “mixed-L-SCF”, the \mathbf{K} -matrix is optimised by the Pulay residual minimisation scheme-direct inversion of the iterative subspace (RMM-DIIS) [270] at each LNV step. This is used to update $n(\mathbf{r})$ and the KS potential. We see then that charge density mixing is completed implicitly through the update of \mathbf{K} .

3.5 Phonons

In Chapter 2, Section 2.6.1, we detailed the importance of phonon calculations in predicting phase transitions in the perovskite oxides as well as introducing the foundational theory and approximations present for most lattice dynamical calculations. Building on this, we move to describe two methods for their explicit calculation from first principles DFT: density functional perturbation theory (DFPT) [164–166, 271, 272] (also known as the linear response method) and the finite displacement method (FDM) [151, 273–277] (also known as the direct method, the frozen phonon method, the supercell method or the small displacement method). While we now compare and contrast the two methods, further details pertaining to each method are explained in Sections 3.5.1 and 3.5.2. We describe DFPT more fully since this method is used for the majority of the phonon calculations in this thesis.

Both the FDM and DFPT aim to evaluate the dynamical matrix \mathbf{D} exactly at a set of \mathbf{q} then interpolate smoothly over all \mathbf{q} within the 1BZ to allow for calculations of phonon dispersion curves and the phonon density of states. In a nutshell, the main difference between the FDM and DFPT is that the interatomic force constants of the former are calculated in real space while these are computed directly in reciprocal space for the latter [166]. This means that for the FDM, the only \mathbf{q} -points that can be evaluated exactly are those which are commensurate with the supercell geometry [151]. For example, should we use the primitive cell as the supercell for a FDM calculation (which is not a good idea most of the time!) we can only calculate phonons at the Γ -point exactly so cannot evaluate the dispersion. Should we create a $2 \times 2 \times 2$ supercell instead, we now have access to the zone boundary \mathbf{q} for which we can now perform an interpolation for the band structure. Increasing the supercell size further then samples an increasingly dense mesh of \mathbf{q} -points which increases the accuracy of our interpolations. In a DFPT calculation, we can work with the primitive cell. The force constants are evaluated on the same \mathbf{k} -point grid as (or a grid commensurate with) the electronic structure calculation. That is, each $\psi_{n\mathbf{k}}$ is perturbed allowing for exact \mathbf{q} -point evaluations at arbitrary \mathbf{q} so long as this \mathbf{q} exists on the \mathbf{k} -mesh of the electronic problem. While this has its advantages, it usually means that for calculations of polar solids, the \mathbf{k} -mesh must be shifted to be centered on Γ such that important FE modes *are not* interpolated. This is in contrast the FDM where it is impossible to not include Γ for any

supercell.

It is not always clear whether the FDM or DFPT is the most appropriate choice for any given situation. It may seem obvious that the cost of accurate FDM calculations should be rather large since for accurate dispersions, a large supercell is required. However, very few calculations using this supercell may be needed to yield the dispersion since the number of symmetry inequivalent atomic sites and displacement directions may be low. This is in contrast to DFPT where many calculations must take place on the primitive cell for each of the considered \mathbf{q} -points which may be large. A more detailed comparison of the scaling of both methods can be found in [166]. One disadvantage is that a tremendous amount of data is written to disk in DFPT Calculations in comparison to the FDM. This is since a large number of perturbed wavefunctions, potentials and densities must be stored. Even for systems of tens of atoms this can add up to Terabytes of data in accurate calculations.

3.5.1 Density functional perturbation theory

Here we present an overview of the linear response formalism for calculating the interatomic force constant matrix. For a more detailed outlook and information pertaining to its implementation with plane waves, we refer the reader to the excellent review article of Baroni et al [166]. Since this process is rather complicated, we first summarise the procedure before entering the details. The quantity we desire is the electronic part of the force constant matrix. This requires the evaluation of the linearised Hellman-Feynman [278, 279] form of the Hessian matrix of the DFT total energy (Equation 3.68). This form of the Hessian requires the first order response of the charge density $n(\mathbf{r})$ to a deviation \mathbf{u}_s from the equilibrium atomic positions τ_s (Equation 3.72). The response of the charge density, in turn, requires the response of the KS orbitals $\psi_{n\mathbf{k}}$ which are evaluated using first order perturbation theory [209] (Equation 3.74). To complete this perturbation, we require the response of the KS potential (Equation 3.75) which itself depends on the response of charge density. This interdependence requires an SCF procedure analogous to the evaluation of the KS total energy. This process is carried out directly in reciprocal space which gives us straightforward access to the dynamical matrix elements since the reciprocal space force constant matrix need only be scaled by the atomic masses $(M_\kappa M_{\kappa'})^{-\frac{1}{2}}$.

Let us begin by making a change in notation from the lattice dynamics discussed in Chapter 2, Section 2.6.1. We further define the ionic site index I ; choosing this index to label the unit cell l and the position of an atom within this cell s such that $I = \{l, s\}$. This allows us to define the ionic coordinate \mathbf{R}_I as

$$\mathbf{R}_I = \mathbf{R}_l + \tau_s + \mathbf{u}_s(l) \quad (3.59)$$

where \mathbf{R}_l is the position of the l^{th} unit cell in the crystal lattice. The condition of translational

invariance[†] means that the interatomic force constant matrix depends on unit cells l and l' by the difference $\mathbf{R} = \mathbf{R}_l - \mathbf{R}_{l'}$. Expressing the real-space interatomic force constant matrix as the Hessian of the DFT total energy, we then have

$$\phi_{s,s'}^{\alpha,\alpha'}(l,l') = \frac{\partial^2 E}{\partial u_s^\alpha(l) \partial u_{s'}^{\alpha'}(l')} = \phi_{s,s'}^{\alpha,\alpha'}(\mathbf{R}_l - \mathbf{R}_{l'}). \quad (3.60)$$

Taking the Fourier transform, we have

$$\sqrt{M_s M_{s'}} D_{s,s'}^{\alpha,\alpha'}(\mathbf{q}) = \tilde{\phi}_{s,s'}^{\alpha,\alpha'}(\mathbf{q}) = \sum_{\mathbf{R}} \phi_{s,s'}^{\alpha,\alpha'}(\mathbf{R}) e^{-i\mathbf{q}\cdot\mathbf{R}} = \frac{1}{N_c} \frac{\partial^2 E}{\partial u_s^{\alpha*}(\mathbf{q}) \partial u_{s'}^{\alpha'}(\mathbf{q})} \quad (3.61)$$

where N_c is the total number of unit cells in the crystal and $\mathbf{u}_s(\mathbf{q})$ is defined as

$$\mathbf{R}_l[\mathbf{u}_s(\mathbf{q})] = \mathbf{R}_l + \tau_s + \mathbf{u}_s(\mathbf{q}) e^{i\mathbf{q}\cdot\mathbf{R}_l}. \quad (3.62)$$

We then find the phonon frequencies $\omega(\mathbf{q})$ solving the eigenproblem of Equation 2.26 in Chapter 2, leading to the secular equation

$$\det \left| D_{s,s'}^{\alpha,\alpha'}(\mathbf{q}) - \omega^2(\mathbf{q}) \right| = 0. \quad (3.63)$$

We are able to solve Equation 3.63 for individual phonons of wavevector \mathbf{q} following the reciprocal space formulation of translational invariance. That is, a phonon of wavevector \mathbf{q} does not induce a force response in the crystal at any other wavevector $\mathbf{q} \neq \mathbf{q}'$. This allows us to easily calculate the force constant matrix in reciprocal space. Where the real space matrix is needed, we can easily Fourier transform back.

One may recall that in DFT, we make the BO approximation [198] to decouple the electronic and nuclear degrees of freedom and separately choose to treat the nuclei (or in most cases, the pseudo-core) as classical point charges. This splits $\tilde{\phi}_{s,s'}^{\alpha,\alpha'}(\mathbf{q})$ into two parts; the electronic and ionic contributions

$$\tilde{\phi}_{s,s'}^{\alpha,\alpha'}(\mathbf{q}) = {}^{el} \tilde{\phi}_{s,s'}^{\alpha,\alpha'}(\mathbf{q}) + {}^{ion} \tilde{\phi}_{s,s'}^{\alpha,\alpha'}(\mathbf{q}). \quad (3.64)$$

The ionic term does not depend on the electronic structure and is simple to evaluate (yet algebraically prolonged) from the second derivative of the Ewald summation of the ionic cores[‡]

[†]Translational invariance simply means that if all of the ions in a crystal lattice are uniformly translated by the same magnitude and direction, the resulting force on each ion would be zero.

[‡]This term is derived in appendix B of reference [166].

$$\begin{aligned}
{}^{ion}\tilde{\phi}_{s,s'}^{\alpha,\alpha'}(\mathbf{q}) &= \frac{4\pi e^2}{\Omega} \sum_{\mathbf{G}} \frac{e^{-(\mathbf{q}+\mathbf{G})^2/4\eta}}{(\mathbf{q}+\mathbf{G})^2} Z_s Z_{s'} e^{i(\mathbf{q}+\mathbf{G})\cdot(\tau_s-\tau_{s'})} (q_\alpha + G_\alpha)(q_{\alpha'} + G_{\alpha'}) \\
&\quad - \frac{2\pi e^2}{\Omega} \sum_{\mathbf{G} \neq 0} \frac{e^{\mathbf{G}^2/4\eta}}{\mathbf{G}^2} \left[Z_s \sum_l Z_l e^{i\mathbf{G}\cdot(\tau_s-\tau_l)} G_\alpha G_{\alpha'} + \mathbf{c}\cdot\mathbf{c} \right] \delta_{s,s'} \\
&\quad + e^2 \sum_{\mathbf{R}} Z_s Z_{s'} e^{i\mathbf{q}\cdot\mathbf{R}} [\delta_{\alpha,\alpha'} f_2(x) + f_1(x) x_\alpha x_{\alpha'}]_{\mathbf{x}=\tau_s-\tau_{s'}-\mathbf{R}} \\
&\quad - e^2 \delta_{s,s'} \sum_{\mathbf{R}} \sum_l Z_s Z_l [\delta_{\alpha,\alpha'} f_2(x) + f_1(x) x_\alpha x_{\alpha'}]_{\mathbf{x}=\tau_s-\tau_l-\mathbf{R}} \quad (3.65)
\end{aligned}$$

where \mathbf{G} -space summations exclude $\mathbf{q} + \mathbf{G} = 0$, \mathbf{R} -space summations exclude $\tau_s - \tau_{s'} - \mathbf{R} = 0$ and η is an arbitrary constant chosen to optimally converge the summations. The functions f_1 and f_2 are defined

$$f_1 r = \frac{3\text{erfc}(\sqrt{\eta}r) + 2\sqrt{\frac{\eta}{\pi}}r(3 + 2\eta r^2)e^{-\eta r^2}}{r^5}, \quad (3.66)$$

$$f_2 r = -\frac{\text{erfc}(\sqrt{\eta}r) - 2\sqrt{\frac{\eta}{\pi}}re^{-\eta r^2}}{r^3} \quad (3.67)$$

where $\text{erfc}(y) = 1 - \text{erf}(y)$ is the complementary error function (erf).

The electronic term is found by doubly applying the Hellman-Feynman theorem to the KS total energy. This yields

$${}^{el}\tilde{\phi}_{s,s'}^{\alpha,\alpha'}(\mathbf{q}) = \frac{1}{N_c} \left[\int \left(\frac{\partial n(\mathbf{r})}{\partial u_s^\alpha(\mathbf{q})} \right)^* \frac{\partial V_{\text{ion}}(\mathbf{r})}{\partial u_{s'}^{\alpha'}(\mathbf{q})} d\mathbf{r} + \int n(\mathbf{r}) \frac{\partial^2 V_{\text{ion}}(\mathbf{r})}{\partial u_s^{*\alpha}(\mathbf{q}) \partial u_{s'}^{\alpha'}(\mathbf{q})} d\mathbf{r} \right] \quad (3.68)$$

where $V_{\text{ion}}(\mathbf{R})$ is

$$V_{\text{ion}}(\mathbf{r}) = \sum_{l,s} v_s[\mathbf{r} - \mathbf{R}_l - \tau_s - \mathbf{u}_s(l)] \quad (3.69)$$

and where v_s is the ionic pseudopotential of the s^{th} site. Following Equations 3.62 and 3.69, the V_{ion} derivative terms in Equation 3.68 read

$$\frac{\partial V_{\text{ion}}(\mathbf{r})}{\partial u_s^\alpha(\mathbf{q})} = - \sum_l \frac{\partial v_s(\mathbf{r} - \mathbf{R}_l - \tau_s)}{\partial \mathbf{r}} e^{i\mathbf{q}\cdot\mathbf{R}_l}. \quad (3.70)$$

It is the charge density response term that is at the heart of the linear response formulation of DFPT. The approach taken is to linearise the equation for the charge density in a periodic system

as described with Bloch's theorem

$$n(\mathbf{r}) = 2 \sum_{\mathbf{k}} \sum_n^{\text{occ}} |\psi_{n\mathbf{k}}(\mathbf{r})|^2 \quad (3.71)$$

to achieve

$$\Delta n(\mathbf{r}) = 4 \sum_{\mathbf{k}} \sum_n^{\text{occ}} \psi_{n\mathbf{k}}^*(\mathbf{r}) \Delta \psi_{n\mathbf{k}}(\mathbf{r}) \quad (3.72)$$

where we have introduced a finite difference operator $\Delta^{\{\mathbf{R}_I\}}$ which we define as

$$\Delta^{\{\mathbf{R}_I\}} A = \sum_I \frac{\partial A}{\partial \mathbf{R}_I} \Delta \mathbf{R}_I \quad (3.73)$$

where we drop the superscript $\{\mathbf{R}_I\}$ in Equation 3.72 for notational clarity. The $\psi_{n\mathbf{k}}$ response can then be found using the well-known first-order perturbation theory of Messiah [209]

$$(\hat{H}_{KS} - \epsilon_{n\mathbf{k}}) |\Delta \psi_{n\mathbf{k}}\rangle = (\Delta V_{KS} - \Delta \epsilon_{n\mathbf{k}}) |\psi_{n\mathbf{k}}\rangle \quad (3.74)$$

for KS Hamiltonian \hat{H}_{KS} and first order correction to the KS potential ΔV_{KS} . $\Delta \epsilon_{n\mathbf{k}} = \langle \psi_{n\mathbf{k}} | \Delta V_{KS} | \psi_{n\mathbf{k}} \rangle$ is the first-order variation to the KS eigenvalue $\epsilon_{n\mathbf{k}}$. The KS potential response is given as

$$\Delta V_{KS}(\mathbf{r}) = \Delta V_{\text{ion}}(\mathbf{r}) + e^2 \int \frac{\Delta n(\mathbf{r}')}{|\mathbf{r} - \mathbf{r}'|} d\mathbf{r}' + \left. \frac{dv_{xc}[n]}{dn} \right|_{n=n(\mathbf{r})} \Delta n(\mathbf{r}). \quad (3.75)$$

Equations 3.72-3.75 then define a set of self-consistent equations analogous to the self-consistent equations of the original DFT calculation where the KS eigenproblem has been replaced with the set of linear equations in 3.74. Once the solution has (to some tolerance) converged, the response from Equation 3.72 can be used to evaluate the appropriate term in Equation 3.68.

Although we will not show this here (but a thorough treatment can be found in Section C1 of the review article of Baroni et. al [166]), a great advantage of the linear response method is that the system of linear equations described in Equation 3.74 are decoupled from each other for perturbations at different \mathbf{q} . We then perform *monochromatic*[†] perturbations treating each \mathbf{q} separately, decomposing the set of SCF equations into their individual Fourier components, expressed only with the lattice periodic part of the Bloch functions. This monochromatic scheme means that the computational effort is comparable to the ground state calculation of the unperturbed system and is independent of \mathbf{q} . We do, however, require several \mathbf{q} to accurately interpolate the band structure, so, the procedure outlined above must then be carried out $N_{\mathbf{q}}$ times where $N_{\mathbf{q}}$ is the total number of points on the chosen \mathbf{q} -point mesh.

[†]That is, phonons calculated at a single wavevector \mathbf{q} which are independent of all other \mathbf{q} .

3.5.2 The finite displacement method

Compared with DFPT, the FDM is simple to understand. The calculation of phonon frequencies depends on the real space force constant matrix representing the proportionality between displacements and forces when the displacements are small enough for this relationship to be linear. In an FDM calculation, all that needs to be done is to calculate the real space force constant matrix $\phi_{s,s'}^{\alpha,\alpha'}$ for each of the symmetry inequivalent sites s and Cartesian directions α according to

$$\phi_{s,s'}^{\alpha,\alpha'}(\mathbf{R}) = \frac{F_{s\alpha}^+ - F_{s\alpha}^-}{2u_{s',\alpha'}} \quad (3.76)$$

where we have used a central differences approach [280] to the force derivative with respect to the atomic displacements and $F_{s\alpha}^{\pm}$ are the forces after a small displacement $\pm u_{s',\alpha'}$. We must carefully monitor the convergence of $\phi_{s,s'}^{\alpha,\alpha'}$ with respect to the supercell size. This is since the $\phi_{s,s'}^{\alpha,\alpha'}$ in the formula for $D_{s,s'}^{\alpha,\alpha'}(\mathbf{q})$ is the force constant matrix for the *infinite lattice* whereas calculations with the FDM can only be completed with a choice of supercell. This means we can only obtain information at wavevectors coincident with the reciprocal lattice vectors of the supercell. So, to approach the infinite lattice case the supercell size must be systematically increased [151]. Once we have satisfactorily converged the real space force constant matrix, we Fourier transform this into \mathbf{q} -space using Equation 3.61 which we can interpolate to evaluate at any \mathbf{q} . When performing phonon calculations on polar solids using the FDM, we must be mindful of the non-analytical form of the dynamical matrix near the zone centre (as discussed in Chapter 2, Section 2.6.1). Failure to do so will lead to incorrect interpolation of the LO bands since they will falsely become degenerate with the TO branch near Γ .

In contrast to DFPT (which is implemented with bespoke code in an electronic structure package), FDM calculations are most often performed using a standalone code. This is since they only require the induced forces after a small atomic displacement; quantities readily available in output from most atomistic codes (not limited to DFT codes). Two popular codes are PHON [151] as developed by Dario Alfè and Phonopy [277] by Atsushi Togo. We make use of the latter in this thesis.

4 | The $\text{Pb}(\text{Ti}, \text{Zr}, \text{Hf})\text{O}_3$ Isoelectronic Series: a Lattice Dynamical Study

Chapter abstract

A comparative lattice dynamical study is performed on PbTiO_3 , PbZrO_3 , PbHfO_3 and the solid solution $\text{PbZr}_{0.5}\text{Ti}_{0.5}\text{O}_3$ throughout the first Brillouin Zone. We use accurate density functional perturbation theory [164–166] and finite displacement method [151, 277] calculations to extract phonon dispersions, densities of states and the eigendisplacement character of individual modes. While we mainly focus on the dynamical instabilities of the high temperature cubic phases, we later study the low temperature AFE phases of PbZrO_3 and PbHfO_3 . This move is motivated by the ubiquity of long wavelength instabilities we find in the dispersions of their cubic phases. While such instabilities are less prevalent in PbTiO_3 , they persist in our ordered $\text{PbZr}_{0.5}\text{Ti}_{0.5}\text{O}_3$ supercells giving rise to a variety of exotic modes of mixed antipolar & AFD character. When considering the ability of the virtual crystal approximation (VCA) [47, 48] to describe the lattice dynamics of $\text{PbZr}_{0.5}\text{Ti}_{0.5}\text{O}_3$, we find that the dispersion agrees well with the highest symmetry rock salt ordered supercell, but poorly approximates other arrangements. It is also quantitatively demonstrated that the VCA is unable to capture the correct character of modes in the supercell arrangements; the VCA cannot be used to accurately predict the low temperature structure of PZT. The lattice dynamics of PbZrO_3 and PbHfO_3 are found to be strikingly similar sharing instabilities of identical character which are slightly more unstable for PbZrO_3 . Importantly, the purported low temperature *Pbam* AFE ground state for both materials is found to be dynamically unstable. The eigendisplacements of the soft mode drive a symmetry and (marginally) energy lowering transition to an 80-atom *Pnma* phase. Given that this structure now appears as the most stable arrangement in what are considered the AFE archetypes, and, has been known to appear in other chemically dissimilar perovskites [281–285], this new *Pnma* phase could be one of the most common antiferroelectric arrangements in the perovskite oxides.

4.1 Introduction

The three members of the Pb(Ti, Zr, Hf)O₃ isoelectronic series: PbTiO₃ (PTO), PbZrO₃ (PZO) and PbHfO₃ (PHO) form a set of ferroic archetypes with high technological importance. The first member, PTO, is one of the most well known ferroelectric (FE) materials (perhaps only second to BaTiO₃, BTO) in possession of a large spontaneous polarisation measuring between 57-100 $\mu\text{C}/\text{cm}^2$ [171]. This makes PTO a perfect material for application in ferroelectric memory technologies and a variety of other applications listed succinctly in [23] and [286]. Member number two, PZO, was the first antiferroelectric (AFE) to be discovered [36, 130] and is certainly the most studied. The characteristic AFE double hysteresis curve present in PZO under applied electric fields makes it particularly useful in energy storage devices [35]. The last member, PHO, is less well known and has been the subject of far fewer studies than the first two members. Indeed, PHO is an AFE considered to be isostructural with PZO [131, 287]. This paired with the fact that antiferroelectricity was discovered in PZO first has seen PHO pushed to the sidelines when studying the nature of the antiferroelectric transition.

Even more functionality can be extracted from this series should we combine the members in solid solution. Most notably, doing so with PTO and PZO forms PbZr_xTi_{1-x}O₃ (PZT); the most abundantly used piezoelectric material. This is due to its giant electromechanical response and well developed, low cost synthesis [44, 288]. Together, this has ensured the technological relevance of the material; well adapted for exploitation in ultrasonic transducers [289, 290], ceramic capacitors and actuators [291]. More exotically, PZT has been proposed for use in potential piezoelectricity-induced room temperature superconductors where a supercurrent is induced along a metal/piezoelectric interface [292, 293]. For these applications, it is most common to consider PZT at around $x \approx 0.52$ [91, 92] in the region near the morphotropic phase boundary (MPB). This is a compositional boundary at the peak of the electromechanical response. This boundary exhibits complex lattice dynamics where a flat energy surface for polarisation rotation exists between the FE tetragonal ($\mathbf{P} \parallel [001]$) and rhombohedral ($\mathbf{P} \parallel [111]$) phases via intermediate monoclinic phases [91, 93, 294].

Following this, it is clear that a thorough understanding of the lattice dynamics of these materials must play a central role in understanding the phase transitions. The idea of a *soft mode* [1, 2, 52] is at the forefront of this discussion. We discussed this idea in detail in Chapter 2, Section 2.6. In simulation, soft modes can be identified by considering the symmetry (and energy) lowering distortions of a high-symmetry cubic phase as indicated by imaginary frequencies at certain wavevectors in the phonon spectrum [1, 2, 52, 69]. Using this method it is found that a single lattice mode of irreducible representation (irrep) Γ_4^- is responsible for the $Pm\bar{3}m$ paraelectric to $P4mm$ FE transition in PTO [109, 295, 296]. In contrast to this, the $Pm\bar{3}m$ paraelectric to $Pbam$ AFE transition in PZO and PHO is characterised by six distinct lattice modes with irreps Σ_2 , R_4^+ , S_4 , R_5^+ , X_3^- and M_5^- [38, 297]. The exact nature of the AFE transition

in PZO, however, is still a matter for debate [37, 38, 41, 297, 298] which we have discussed in Chapter 2, Section 2.3.1. At first glance, a classification of the responsible modes for the phase transitions in morphotropic PZT appears helpful. This, however, is muddled by the fact such a classification is not possible for a truly random alloy. Even for ordered PZT it proves much more difficult since the character and frequencies of the relevant modes may vary with Ti/Zr concentration as well as with the specific ordering of the B-site substitutions in the crystal lattice, for which, in a periodic crystal the number of permutations are infinite.

If we are to study PZT near the MPB with first principles calculations, we should consider two paths. Both paths impose fictitious symmetry when compared to the real random compound. The first is to explore the different permutations of Ti/Zr substitutions within a supercell of finite size. True morphotropic PZT requires simulation in a large supercell so $x = 0.5$ is often chosen as a surrogate. This is the most common approach taken and has been successful in the calculation of structural [299, 300], piezoelectric [301, 302] and electronic properties [303]. Using this method, phonon dispersion relations across a small area of the first Brillouin zone have also been calculated for [1:1] PZO/PTO superlattices [50]. For (001) and (110) ordered structures, FE modes were isolated to Ti/Zr layers whilst the (111) ordered superlattice displays one mode behaviour with competing FE and AFD character. This study, however, was limited in scope by only considering modes at the zone centre. The second option is to use a mixed potential scheme such as the VCA. This approach, like the supercell method, predicts anomalous dynamical charges and with reasonable accuracy, the location of the MPB [47–49] but is unable to accurately represent distortions to local structure. The extent to which this is true, however, is unknown thus a quantitative comparison based on the characteristics of the soft mode distortions would be valuable. This approach, however, does allow access to a wide range of Ti/Zr concentrations at a fraction of the computational cost of a large supercell calculation.

This chapter has two goals. The first is to provide a complete comparative study of the phonon dispersion relations in near-morphotropic periodic[†] $PbZr_{0.5}Ti_{0.5}O_3$ within density functional theory (DFT) using the VCA and supercell method complete with comparison to the end members PTO and PZO. We do so also with special consideration of longer wavelength[‡] modes which previously have been neglected but are now suspected to play a role in the lattice dynamics of PZO [304] and PHO [305]. We compare the characters of the dynamical instabilities by considering distortions at high symmetry points (and other points) via eigendisplacement analysis and the projected phonon density of states (PDOS). Doing so gives access to displacement patterns and to the species specific character of all the dynamical instabilities. For these simulations, we select

[†] Although we do not expect $PbZr_{0.5}Ti_{0.5}O_3$ to *naturally* condense with periodic B-site order (i.e, it is a random solid solution), considering periodic arrangements allows us to study limiting cases and consider artificial digital superlattices like PZT II and III (Figure 4.1).

[‡] Long wavelength modes are often referred to in the literature as incommensurate modulations. We avoid this term here since in the context of DFT simulations of *infinite* crystals, there is no wavevector truly incommensurate with the lattice! We note that while zone centre modes have an infinite wavelength, we are instead referring to modes with fractional q away from high symmetry points.

the $2 \times 2 \times 2$ supercell of the primitive perovskite unit for our simulations to coincide with measured mean cluster size distributions for Ti/Zr ordering in PZT [306]. Such supercells have recently been used as local phases to build a complex multiphase model of the material able to predict the experimental pair distribution function to a high accuracy [307]. We obtain the irreducible representations (irreps) of the soft mode distortions and identify their incipient order parameters which in the case of longer wavelength modes we find can impose dual order and complex octahedral rotation patterns (not representable with Glazer notation [45, 46]). By doing so, we provide further insight into the complex lattice dynamics occurring near the MPB. Further, it will provide a guide for future investigations detailing the consequences of using the supercell or VCA methods for future studies of PZT and heterostructures for which PZT is an ingredient.

The second goal is achieved in a follow-up study to the one laid out above. Directed attention is now given to the purported $Pbam$ ground state crystal structure of PZO and PHO which we compare and contrast. That is, we find that the cubic dispersions of PZO (and of $PbZr_{0.5}Ti_{0.5}O_3$) feature many long wavelength dynamical instabilities, some of which are more unstable than those condensing to form the $Pbam$ crystal structure. In light of this, we calculate the phonon dispersions of PZO and PHO in their $Pm\bar{3}m$ paraelectric and $Pbam$ antiferroelectric phases. While the isostructural nature of the two materials informs us that the lattice dynamics may be similar, to our knowledge, this similarity has not been quantified in any comparative study performed with first principles calculations. Indeed, to our knowledge, the lattice dynamics of PHO has only been simulated using classical rigid-ion and shell models [308, 309]. While the focus remains on the dynamical instabilities, it should be noted that if the $Pbam$ structure is the ground state at zero Kelvin, there should be *no dynamical instabilities* in the phonon spectrum. We find that this is not the case and discover that a soft mode at the Z -point of $Pbam$ drives a transition to a lower energy 80-atom $Pnma$ phase. We compare this new phase to the previously established $Pbam$ and discuss the prospect of observing this phase in experiment.

The rest of this chapter is organised as follows. In Section 4.2 we detail the theoretical methods for the calculations, including details for the calculation of the electronic ground state, phonon dispersions and details for the specific implementation of the VCA. Past this point, the chapter is split into two parts. The first part begins in Section 4.3 with a comparative study of the dynamical instabilities of near morphotropic PZT, PTO and PZO. Within this study, in Section 4.3.1 we discuss the properties of the fully relaxed PZT parent structures. Then, in Section 4.3.2 we present the full phonon dispersion relations and PDOS along with a discussion and tabulation of the relevant soft modes and their frequencies. We begin with a comparison between the end members PTO & PZO. The other dispersions are then paired based on their similarity and discussed together with the exception of $Pm\bar{3}m$ ordered PZT supercell which is dedicated its own section. Modes important to the discussion are shown graphically. The second part of this chapter begins in in Section 4.4. Within this study, in Section 4.4.1 we compare the phonon dispersions and dynamical instabilities of PHO and PZO. Following an instability in the AFE

phase, in Section 4.4.2 we describe a new 80-atom $Pnma$ crystal structure lower in energy than $Pbam$. The results of both studies are then discussed together and summarised in Section 4.5.

4.2 Theoretical method

Calculations are performed using the implementation of DFT as present in the `ABINIT` code (v8.10.2) [310, 311]. Section 4.3 and subsections therein use scalar-relativistic, norm-conserving pseudopotentials (NCPPs) generated by the `ONCVSP` code (v0.3) [233] as made available on the `PseudoDojo` website [230]. These pseudopotentials treat the Pb $5d^{10}6s^26p^2$, Ti $3s^23p^64s^23d^2$, Zr $4s^24p^65s^25d^2$ and O $2s^22p^4$ orbitals as valence and include partial core corrections. For the $2 \times 2 \times 2$ $PbZr_{0.5}Ti_{0.5}O_3$ supercells, Brillouin zone integrals are performed with sums over Γ -centered $4 \times 4 \times 4$ Monkhorst-Pack [227] meshes. A plane-wave cutoff energy of 1088.46 eV (40 Ha) is employed to ensure the accuracy of our calculations. Exchange & correlation effects are represented by the `PBESol` [229] functional as present in `Libxc` (v3.0.0) [218]. This functional is known to produce high accuracy structural properties compared with experiment [171] justifying its use in a study of structural distortion. This method returns the paraelectric cubic $Pm\bar{3}m$ lattice constants of PTO and PZO as $a_{PTO} = 3.918 \text{ \AA}$ (-0.304%) and $a_{PZO} = 4.140 \text{ \AA}$ (+0.242%) where bracketed values are errors compared with experiment [312, 313].

Section 4.4, in contrast to Section 4.3 uses the projector augmented wave (PAW) method for phonon calculations [152]. This is since simulations utilising PAWs typically converge the relevant properties at a lower plane wave cutoff energy compared to NCPPs. This is a vital saving since low symmetry antiferroelectric phases will require many unique perturbations in the phonon calculations. For the PAW calculations, we find that a plane wave cutoff energy of 680.29 eV (25 Ha) provides satisfactory convergence when using the PAW data sets made available in the `JTH` library (v1.1) [314]. These data sets represent the same orbitals as the NCPP calculations for the already mentioned species, although, for Hf , we treat the $5s^25p^66s^26d^2$ orbitals as valence. Calculations prepared for phonon dispersions using PAWs use Γ -centered $6 \times 6 \times 6$ ($Pm\bar{3}m$) and $5 \times 3 \times 3$ ($Pbam$) Monkhorst-Pack meshes for Brillouin zone integrations. When comparing the relative energetics of different phases, however, we upgrade this to Γ -centered $8 \times 8 \times 8$ ($Pm\bar{3}m$) and Γ -centered $7 \times 5 \times 3$ ($Pbam$) meshes to accurately resolve phases close in energy. We remind the reader that the complex $Pbam$ crystal structure of PZO and PHO was shown in Figure 2.5 within Chapter 2. To our knowledge, no PAW data sets exist for the `PBESol` functional[†] which are both compatible with `ABINIT` and exist for the required elements, so, we now perform calculations using the local density approximation (LDA) functional of Perdew and Wang [153]. Compared with `PBESol`, lattice constants will now be underestimated and

[†]We note that much of the community use the available PBE PAW data sets for calculations with most GGA flavours. We, however, choose not to in order to preserve consistency between the PAW data and the chosen functional.

bonds will become stiffer; shifting upwards the frequency of real modes. We now produce the paraelectric cubic $Pm\bar{3}m$ lattice constants of PZO and PHO as $a_{\text{PZO}} = 4.107 \text{ \AA}$ (-0.556%) and $a_{\text{PHO}} = 4.072 \text{ \AA}$ (-1.40%) where bracketed values are errors compared with experiment [313, 315]. We note that convergence tests for all of the NCPP and PAW calculations in this chapter can be found in appendix A.1.

We make particular use of the linear response features in ABINIT for the calculation of phonon dispersions using density functional perturbation theory (DFPT) [164, 166]. Dynamical matrices are calculated on the \mathbf{q} -point directly corresponding to the \mathbf{k} -point mesh of the supercell calculation to ensure high accuracy. Dispersions are extracted using a Fourier interpolation scheme between points on this mesh [164, 166]. Since the perovskite oxides are known to give rise to giant LO-TO splitting [162], the non-analytic correction (NAC; Equation 2.29 in Chapter 2) at the Γ -point [164], correcting for the undefined nature of the long-range Coulomb interactions [155] is particularly important. This correction requires knowledge of the electronic dielectric tensor ϵ^∞ and Born effective charges \mathbf{Z}_i^* where i labels each atomic site in the supercell. Both are obtained also using DFPT in response to a homogeneous electric field [164, 316].

For calculations involving use of the VCA, we use the implementation in ABINIT. It is used to create an 'alchemical' virtual atom of Ti/Zr character by linearly mixing the pseudopotentials of the individual species

$$V_{\text{VCA}}^{\text{ps}} = xV_{\text{Zr}}^{\text{ps}} + (1 - x)V_{\text{Ti}}^{\text{ps}}. \quad (4.1)$$

This can be further broken down into local contributions and short-range non-local corrections [317]. Phonon dispersion calculations using DFPT *and* the VCA are currently not fully supported in the code so we instead use the (formally equivalent) finite displacement method (FDM) as implemented in the Phonopy code (v2.1) [277] using a $4 \times 4 \times 4$ supercell of the primitive perovskite unit and a displacement of 0.01 \AA . For this calculation where $x = 0.5$, the virtual atom takes on the intermediate mass of Ti and Zr, equal to 69.55 AMU. The NAC is accounted for following the same method as used in the DFPT calculations. For means of validation, a comparison of the phonon dispersions for primitive PTO & PZO using both DFPT and the FDM are given appendix A.1.

In Section 4.3.2, we treat the six unique B-site configurations of $\text{PbZr}_{0.5}\text{Ti}_{0.5}\text{O}_3$ within the $2 \times 2 \times 2$ supercell labelled with Roman numerals I:VI. These supercells are shown in Figure 4.1. Although PTO, PZO and VCA calculations are representable in the primitive perovskite cell, we still choose to use the $2 \times 2 \times 2$ supercell such that phonon dispersions are calculated along the same \mathbf{q} -path as for structures I:VI and share the same total number of phonon branches ($3 \times N_{\text{atom}} = 120$). PZT supercells are constrained to be cubic with dimensions $(2a_{\text{Vg}}, 2a_{\text{Vg}}, 2a_{\text{Vg}})$ where $a_{\text{Vg}} = 4.029 \text{ \AA}$, the lattice constant set by Vegard's law [318]. For $x = 0.5$, this is a simple average of a_{PTO} and a_{PZO} found for the NCPP calculations. This choice of lattice constant

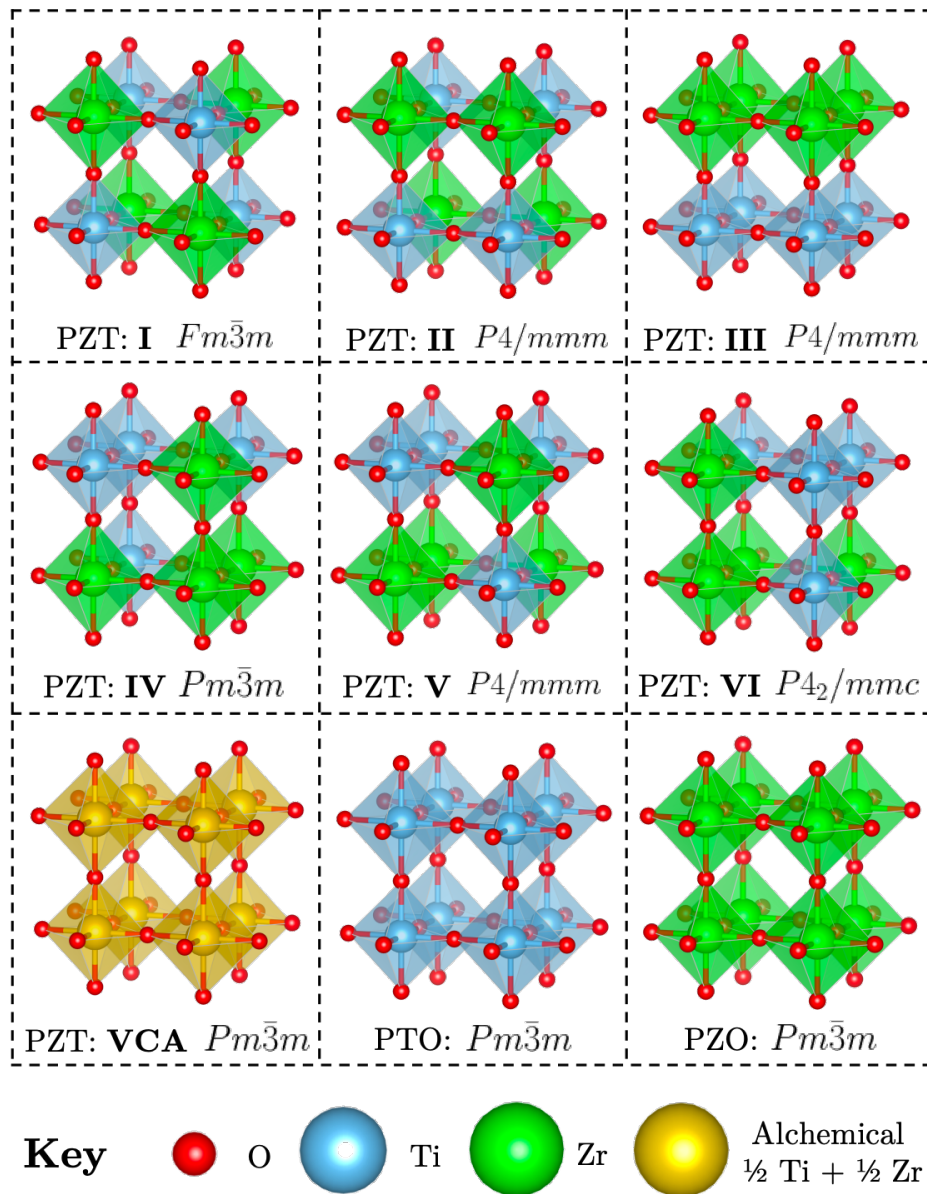


Figure 4.1: The structures used for the phonon dispersion calculations of Section 4.3.2. A-site Pb has been removed for clarity and BO_6 octahedral complexes have been coloured to match the B-site species. Supercell models (rows 1 and 2) are labelled with Roman numerals I:VI whilst the last row indicates the PZT-VCA supercell as well as the end members PTO and PZO. Each supercell is also assigned a crystalline space-group.

favours no particular B-site ordering that may be biased in different experimental conditions. Further, structural data for high temperature cubic PZT is scarce since the technologically relevant large piezoelectric coefficients stem from the low temperature tetragonal/rhombohedral phases. Simulations for PTO, PZO and PHO are performed at their theoretical lattice constants. That is, for each phase, stresses are relaxed until the magnitude of each component of the Cartesian stress tensor falls below 1×10^{-3} GPa. Before the phonon calculations, internal degrees of freedom are relaxed to a stringent force tolerance of 1×10^{-6} eV/Å to prevent soft modes forming from non-equilibrium vibrations. To further illuminate the mode characters, we also calculate the phonon PDOS for each structure. To do so, we calculate the dynamical matrix on a dense $49 \times 49 \times 49$ grid of q-points and integrate with the tetrahedron method [319].

Throughout this work, we make use of group theoretical software. We use the programs FINDSYM (v6.0) [320] and ISODISTORT (v6.5) [321] as made available in the ISOTROPY software suite. We also make use of the web-based phonon spectrum visualisation tools made available by H. Miranda [322].

4.3 Results: PTO, PZO & PZT

4.3.1 Parent structures

Table 4.1 details the structural and symmetry properties of the relaxed primitive cells. We find that a simple metric like the number of Wyckoff sites (and their deviation from the ideal perovskite sites) suggests which arrangements have comparable lattice dynamics. This is used as a basis for the discussion in Section 4.3.2. These primitive cells are then translated into the $2 \times 2 \times 2$ supercell of the primitive PbBO₃ unit (B=Zr or B=Ti) and are shown in Figure 4.1. These form a set of parent structures from which we later perform mode decompositional analysis. Table 4.2 shows other important structural, dynamical and dielectric properties also important to the discussion in this Section.

PTO/PZO/VCA cells show the usual cubic $Pm\bar{3}m$ symmetry. These are joined by PZT I ($Fm\bar{3}m$) and IV ($Pm\bar{3}m$) which also support a cubic local minimum. The former adopts rock-salt-like ordering with continuous B-sites aligned along the [111] direction whilst the latter shows a separation of Ti and Zr sites into opposite corners of the supercell. As a consequence, these parents show isotropic behaviour in both the stress and high frequency dielectric tensors (Table 4.2). This is in contrast to the other four PZT parents which are members of lower symmetry tetragonal spacegroups (even whilst constrained to a_{vg}) thus showing anisotropic behaviour in these tensors about a single axis. It is typical behaviour across all of the PZT parents (bar the VCA) to compress areas of TiO₆ coordination making way for the larger ZrO₆ octahedra. When constrained to a_{vg} , PZT I is the most energetically stable configuration whilst III is the most unstable with an energy difference of 114 meV/PbBO₃ unit between them. Remarkably, if we perform a full cell shape and size relaxation, this energy difference marginally narrows to

111 meV/PbBO₃ showing the small contribution of strain energy to the non-polar phases of PZT.

Table 4.1: The space-groups, Wyckoff positions and *primitive* supercell dimensions of the relaxed, cubic-constrained structures. All structures are representable in the $2 \times 2 \times 2$ primitive perovskite supercell as illustrated in Figure 4.1. Wyckoff positions are stated using the site multiplicity and Wyckoff letter as made standard by the Bilbao Crystallographic Server [323]. Supercell dimensions are given in lengths of the mutually orthogonal axes a, b & c with the exception of PZT I whose axes are at an angle $\alpha = \beta = \gamma = 60^\circ$ with the full form of the lattice vectors displayed.

PTO/PZO/VCA ($Pm\bar{3}m O_h\bar{1}$)	
$a = a_{PTO}/a_{PZO}/a_{Vg}$	
Pb 1b	(1/2, 1/2, 1/2)
Ti/Zr/(1/2 Ti + 1/2 Zr) 1a	(0, 0, 0)
O 1d	(1/2, 0, 0)
PZT: I ($Fm\bar{3}m O_h\bar{5}$)	
$\mathbf{a} = (0, a_{Vg}, a_{Vg}), \mathbf{b} = (a_{Vg}, 0, a_{Vg}), \mathbf{c} = (a_{Vg}, a_{Vg}, 0)$	
Pb 2c	(1/4, 1/4, 1/4)
Zr 1a	(0, 0, 0)
O 6e	(x, 0, 0), x=0.74232
Ti 1b	(1/2, 1/2, 1/2)
PZT: II ($P4/mmm D_{4h}\bar{1}$)	
$a = \sqrt{2}a_{Vg}, b = \sqrt{2}a_{Vg}, c = a_{Vg}$	
Pb 2f	(0, 1/2, 0)
Zr 1d	(1/2, 1/2, 1/2)
Ti 1b	(0, 0, 1/2)
O 4k	(x, x, 1/2), x=0.75838
O 1c	(1/2, 1/2, 0)
O 1a	(0, 0, 0)
PZT: III ($P4/mmm D_{4h}\bar{1}$)	
$a = b = a_{Vg}, c = 2a_{Vg}$	
Pb 2g	(0, 0, x), x=0.26377
Zr 1c	(1/2, 1/2, 0)
Ti 1d	(1/2, 1/2, 1/2)

O 2f	(0, 1/2, 0)
O 2h	(1/2, 1/2, x), x=0.26279
O 2e	(1/2, 1/2, 1/2)

PZT: IV ($Pm\bar{3}m O_h\bar{1}$)

$$a = 2a_{\text{vg}}$$

Pb 8g	(x, x, x), x=0.74307
Zr 1a	(0, 0, 0)
Zr 3d	(1/2, 1/2, 0)
Ti 3c	(0, 1/2, 1/2)
Ti 1b	(1/2, 1/2, 1/2)
O 6e	(x, 0, 0), x=0.74807
O 12h	(x, 1/2, 0), x=0.26024
O 6f	(x, 1/2, 1/2), x=0.74667

PZT: V ($P4/mmm D_{4h}\bar{1}$)

$$a = 2a_{\text{vg}}$$

Pb 8r	(x, x, z), x=0.75030, z=0.74302
Zr 1a	(0, 0, 0)
Zr 2f	(0, 1/2, 0)
Zr 1d	(1/2, 1/2, 1/2)
Ti 1b	(0, 0, 1/2)
Ti 2e	(0, 1/2, 1/2)
Ti 1c	(1/2, 1/2, 0)
O 4l	(x, 0, 0), x=0.74975
O 2g	(0, 0, z), z=0.73908
O 4m	(x, 0, 1/2), x=0.75053
O 4n	(x, 1/2, 0), x=0.74198
O 4i	(0, 1/2, z), z=0.73972
O 4o	(x, 1/2, 1/2), x=0.75804
O 2h	(1/2, 1/2, z), z=0.75582

PZT: VI ($P4_2/mmc D_{4h}\bar{9}$)

$$a = 2a_{\text{vg}}$$

Pb 8n	(x, x, 1/4), x=0.25710
-------	------------------------

Zr 2a	(0, 0, 0)
Zr 2c	(0, 1/2, 0)
Ti 2d	(0, 1/2, 1/2)
Ti 2b	(1/2, 1/2, 0)
O 2e	(0, 0, 1/4)
O 2l	(x, 0, 1/2), x=0.25134
O 4j	(x, 0, 0), x=0.26117
O 4i	(0, 1/2, z), z=0.74154
O 4k	(x, 1/2, 1/2), x=0.25375
O 4m	(x, 1/2, 0), x=0.26
O 2f	(1/2, 1/2, 1/4)

Table 4.2 indicates that at a_{vg} , PZT is held at a non-vanishing pressure. The VCA exhibits the largest σ_{RMS} of 2.62 GPa whilst II and III show stronger uniaxial stress about the axes of compositional modulation indicating a proclivity for expansion in these directions. PZT I:VI show remarkably similar \mathbf{Z}^* and ϵ^∞ indicating that Ti/Zr cation ordering has little influence on these quantities. It is also notable that \mathbf{Z}^* of PZT I:VI deviates only a small amount from the mean \mathbf{Z}^* of PZO and PTO. The VCA shows good agreement with the supercell method for \bar{Z}_{Pb}^* and $\bar{Z}_{O_\perp}^*$ but underestimates strongly the magnitudes of the alchemical \bar{Z}_B^* and $\bar{Z}_{O_\parallel}^*$. The VCA also features a strong discrepancy in ϵ^∞ compared to both the mean and supercell approach. Although not tabulated, it should be noted that PZT II, IV, V and VI feature off-diagonal elements in the Born effective charge tensor only for \bar{Z}_{Pb}^* . These components are small and do not exceed 0.34 electronic charges in magnitude but do vary in sign despite the positive nature of the Pb cation. It should also be noted that using a similar method, a previous study reports off-diagonal elements not of Pb, but of the O 4k site, always negative in sign [50].

4.3.2 Phonon dispersion and density of states

We now describe *in detail* the soft mode lattice dynamics of PTO, PZO and the PZT 50/50 arrangements. Figure 4.2 shows the phonon dispersions for PZT I:VI, PTO, PZO and the VCA calculated within the supercells indicated in Figure 4.1. Although we have calculated all bands (shown in the supplemental material of [43]), we consider only the space where $\bar{v}(\mathbf{q}) \in i\mathbb{R}$ thus presenting a set of symmetry lowering phase transitions along the fractional \mathbf{q} -path $(0, 0, 0) \Rightarrow (0, 1/2, 0) \Rightarrow (1/2, 1/2, 0) \Rightarrow (0, 0, 0) \Rightarrow (1/2, 1/2, 1/2)$. It is at these supercell wavevectors exactly that we analyze the character of the distortions. The soft mode character has an important impact on the properties of the of the crystal. This is then inferred with PDOS calculations (Figure 4.3) and, for some important modes, is reported with eigendisplacement analysis. Table 4.4 serves as a companion to the dispersion identifying modes symmetries, their multiplicities

Table 4.2: The diagonal elements of the stress tensor σ , high frequency dielectric tensor ϵ^∞ and averaged born effective charges \bar{Z}^* of the unique elements for the primitive cubic perovskite unit cell following the convention of reference [162]. For PZT, these calculations were performed at a_{vg} whilst PTO & PZO were performed at a_{PTO} & a_{PZO} respectively.

	σ_{11} [GPa]	σ_{22} [GPa]	σ_{33} [GPa]	\bar{Z}_{Pb}^*	\bar{Z}_{B}^*	$\bar{Z}_{\text{O}_{\parallel}}^*$	$\bar{Z}_{\text{O}_{\perp}}^*$	ϵ_{11}^∞	ϵ_{22}^∞	ϵ_{33}^∞
PTO	≈ 0	≈ 0	≈ 0	3.88	7.19	-5.91	-2.58	8.49	8.49	8.49
PZO	≈ 0	≈ 0	≈ 0	3.90	5.94	-4.90	-2.47	6.93	6.93	6.93
Mean	≈ 0	≈ 0	≈ 0	3.89	6.55	-5.41	-2.53	7.71	7.71	7.71
VCA	-1.51	-1.51	-1.51	3.90	6.13	-4.99	-2.52	7.06	7.06	7.06
I	0.56	0.56	0.56	3.89	6.54	-5.36	-2.53	7.59	7.59	7.59
II	0.64	-1.60	0.64	3.89	6.55	-5.38	-2.53	7.59	7.67	7.59
III	-1.85	-1.85	0.50	3.86	6.48	-5.31	-2.51	7.54	7.54	7.52
IV	-0.67	-0.67	-0.67	3.87	6.49	-5.32	-2.52	7.55	7.55	7.55
V	-0.56	-0.56	0.59	3.88	6.53	-5.35	-2.53	7.60	7.60	7.57
VI	-0.62	-0.60	-0.60	3.87	6.51	-5.34	-2.52	7.56	7.57	7.57

and numerical values of imaginary frequencies. Table 4.3 presents the \mathbf{q} -vectors associated with the high symmetry labels which also serves as a companion to Figure 4.2.

4.3.2.1 PTO & PZO

We begin with a discussion of end members PTO & PZO. Our choice of supercell for these calculations reveals folded spectra not previously reported in the literature. We have also, however, calculated dispersions over the primitive cell and found good agreement with previous calculations using similar method [154, 171] (see appendix A.1). For PTO we report 7 unique soft modes at the appropriate wavevectors compared to 26 in the more complex spectrum of PZO. As expected, the most unstable mode in PTO is found to be Γ_4^- featuring Pb/Ti countermotion against the O anions inducing a net polarisation and incipient FE distortion. Although the Γ_4^- distortion exists in PZO, it is harder and features Zr motion *alongside* O requiring that the smaller macroscopic polarisation is as the result of Pb-O separation. PTO shows oxygen octahedron rotational instabilities at the R & M points. These are the R_4^+ and M_3^+ AFD modes respectively. In real space, these correspond to out-of-phase and in-phase rotations of the BO_6 octahedra about a single axis, or $a^0a^0c^-$ & $a^0a^0c^+$ in Glazer's notation, respectively. These modes are generally not competitive in PTO but this is *not* true for PZO. The R_4^+ distortion is the softest mode in PZO and is a prime mover for the AFE phase transition known to make up $\approx 60\%$ of the total distortion [85] (when the rotation is about the $[1\bar{1}0]$ axis).

Branches mostly harden along the $(0, 0, 0) \Rightarrow (0, 1/2, 0)$ path in PTO resulting in an antipolar mode Δ_5 and a long wavelength AFD mode T_4 . The latter shares a likeness with both $a^0a^0c^-$ and $a^0a^0c^+$ distortions but with a doubled periodicity of four perovskite units along the axis of rotation. Of the four TiO_6 octahedra in the mode, two neighbouring octahedra rotate counterclockwise and the other two clockwise about the axis of rotation as seen in Figure 4.4i

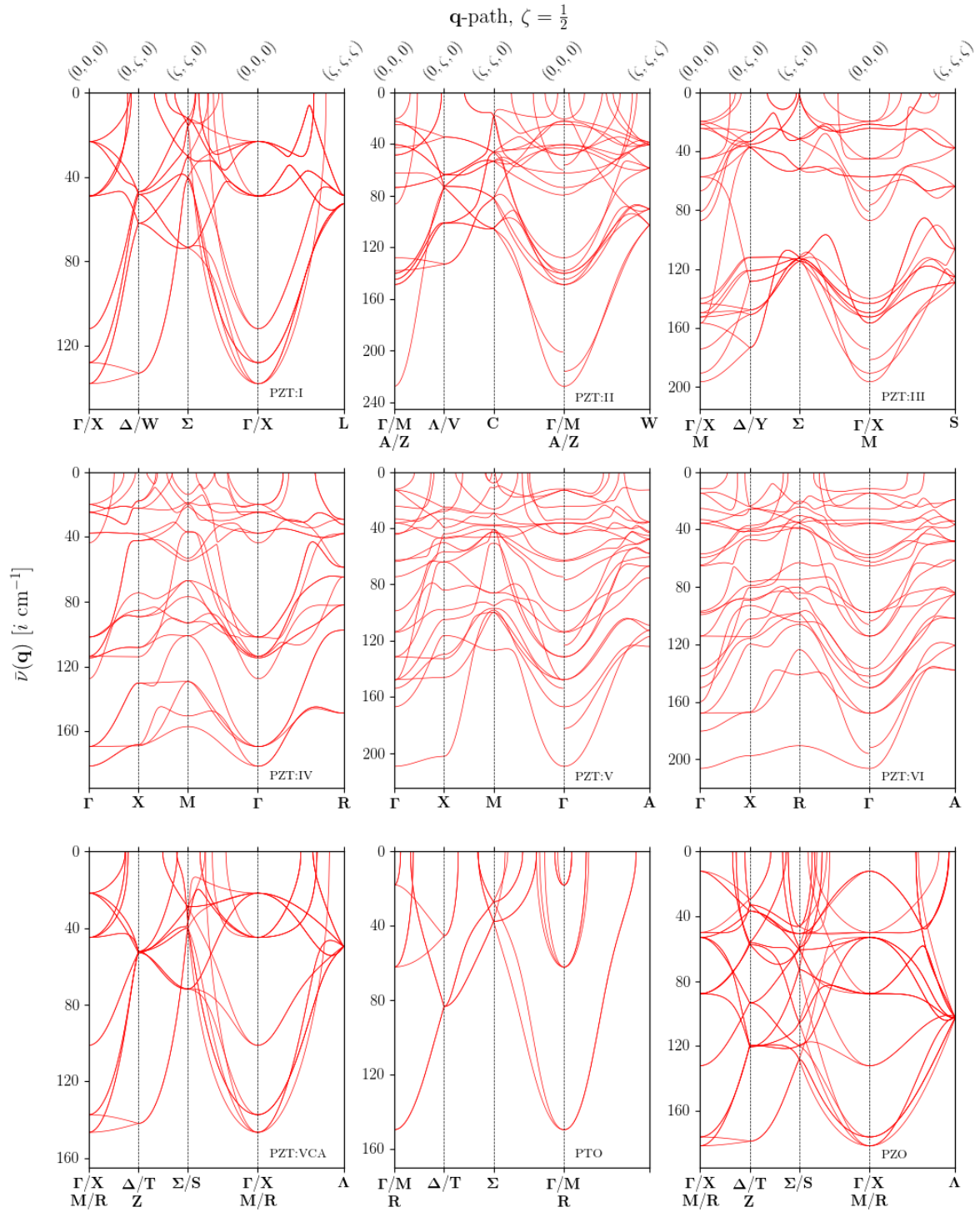


Figure 4.2: The soft mode phonon dispersion relations for PZT I:VI, the VCA, PTO and PZO. All dispersions are over an identical fractional \mathbf{q} -path controlled by the parameter $\zeta = 1/2$ (upper x -axis). Folded symmetry labels (described in Table 4.3) are included for PZT I:III, the VCA, PTO and PZO. We only include folded labels if a soft mode of that wavevector is present at the given \mathbf{q} -point. In the particular case of PTO, this leads to no label for the wavevector $(1/2, 1/2, 1/2)$. Since dispersions for PZT IV:VI were calculated on the primitive cell, no folding takes place thus only one symmetry label is required.

Table 4.3: Brillouin zone labels the reader may find useful for interpreting Figures 4.2, 4.5 and 4.6 and references to high symmetry points in the text. Wavevectors are presented in fractional q . High symmetry points are in bold font while other points are in plain font.

<i>Pm</i> $\bar{3}m$							
R	(1/2, 1/2, 1/2)	X	(0, 1/2, 0)	Δ	(0, 1/4, 0)	M	(1/2, 1/2, 0)
T	(1/2, 1/2, 1/4)	Z	(1/4, 1/2, 0)	Σ	(1/4, 1/4, 0)	S	(1/4, 1/2, 1/4)
Λ	(1/4, 1/4, 1/4)						
<i>Fm</i> $\bar{3}m$							
W	(1/2, 1/4, 3/4)	X	(1/2, 0, 1/2)	Σ	(1/4, 1/4, 1/2)	Δ	(1/4, 0, 1/4)
L	(1/2, 1/2, 1/2)						
<i>P4</i> /mmm							
C	(1/4, 1/4, 1/4)	X	(0, 1/2, 1/4)	V	(1/2, 1/2, 1/4)	M	(1/2, 1/2, 0)
W	(0, 1/2, 1/4)	A	(1/2, 1/2, 1/2)	Δ	(0, 1/4, 0)	Z	(0, 0, 1/2)
Y	(1/4, 1/2, 0)	Λ	(0, 0, 1/4)	Σ	(1/4, 1/4, 0)	S	(1/4, 1/4, 1/2)
<i>P4</i> ₂ /mmc							
X	(0, 1/2, 0)	R	(0, 1/2, 1/2)	A	(1/2, 1/2, 1/2)		
<i>Pbam</i>							
R	(1/2, 1/2, 1/2)	S	(1/2, 1/2, 0)	T	0, 1/2, 1/2	U	(1/2, 0, 1/2)
X	(1/2, 0, 0)	Y	(0, 1/2, 0)	Z	(0, 0, 1/2)		

(left). Although there is also a general hardening of branches along the same path in PZO, the softest is almost dispersionless resulting in another AFD mode of symmetry T_4 . Although over the same wavevector as the T_4 mode of PTO, this mode is better described as a $a^0a^0c^-$ -like distortion where rotating octahedra are separated by static ones (Figure 4.4i, right). Both PTO and PZO now become harder at (1/2, 1/2, 0) resulting in several antipolar modes and for the first time in this study, single modes with a mixed antipolar/AFD character. These modes often manifest in a sublattice of BO₆ octahedra rotating with a Glazer-like pattern with adjacent PbBO₃ units showing local polar distortions. These local polar distortions are aligned such that there is no net polarisation induced by the mode. An example of this is the Σ_2 distortion of PTO, although it has relatively low soft mode frequency ($27.05i \text{ cm}^{-1}$). Modes of this character are considerably softer in PZO including the S_4 distortion which features local AFD modes (with a complex non-Glazer-like rotation pattern) and antipolar cation displacements. This mode is also known to make a small contribution to the AFE PZO ground state [85].

Along the (0, 0, 0) \Rightarrow (1/2, 1/2, 1/2) path, the dispersion now becomes real in PTO. For PZO, the dispersion remains imaginary. We see a hardening resulting in two strongly degenerate modes of symmetry Λ_2 & Λ_3 . The former is an 8-fold degenerate AFD mode whilst the latter is 16-fold degenerate featuring Pb-O antipolar displacements. The character of these modes are reminiscent of some of the known modes contributing to the PZO ground state. This suggests that

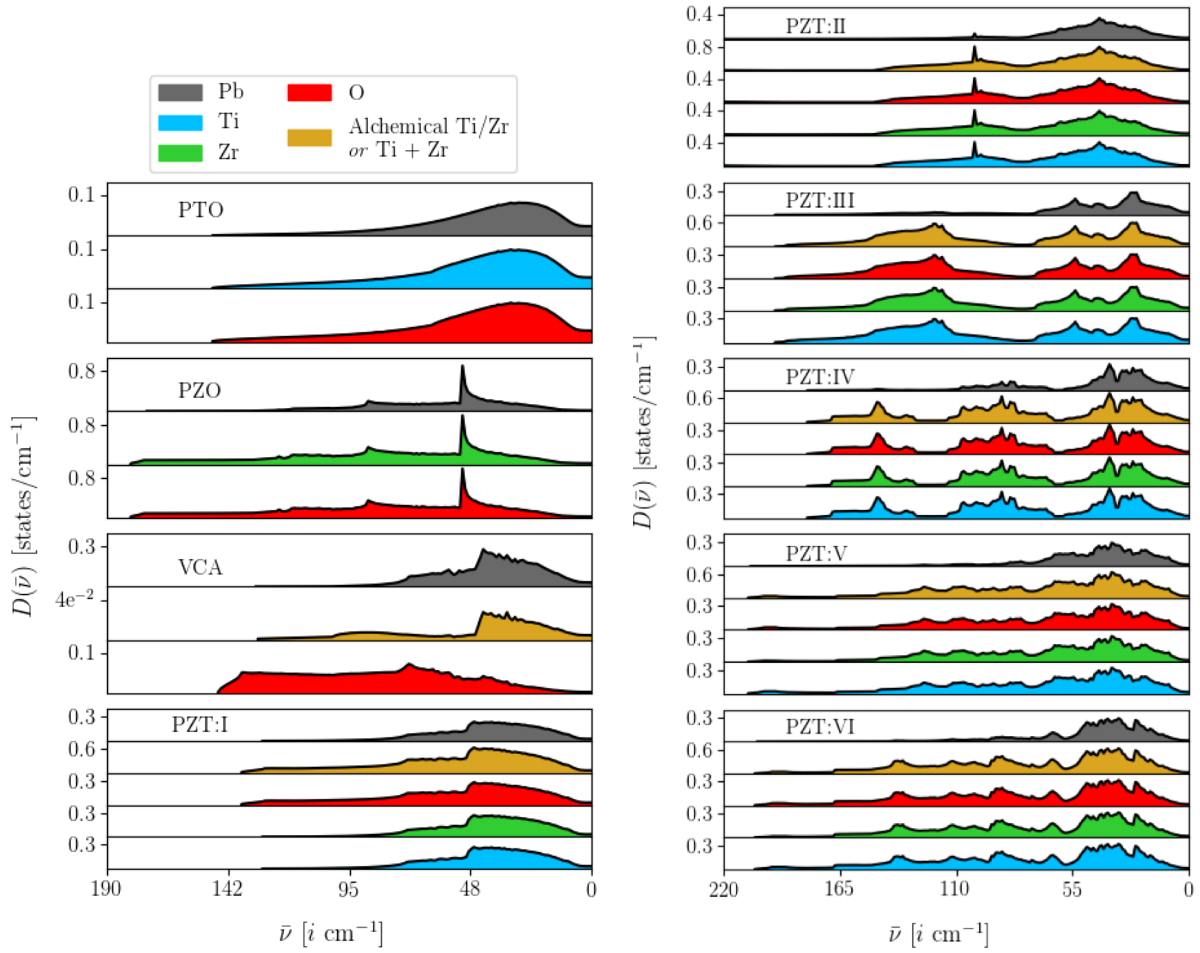


Figure 4.3: Species projected phonon density of states $D(\bar{\nu})$ for PTO, PZO the VCA and the PZT supercells over the imaginary wavenumber space. For the VCA calculation, the gold curve is the PDOS of the alchemical 50/50 Ti/Zr atom whilst for the supercell models it represents the sum of B-site PDOS.

the inclusion of these distortions, with others, could create another similar low energy competing phase. Figure 4.3 shows that the two end-members have a striking dissimilarity in the PDOS. All species for PTO show a rather featureless smooth function, peaking at $\approx 24i$ cm⁻¹ whilst PZO shows a peaked PDOS penetrating further into the imaginary space indicating that cubic PZO is more dynamically unstable than PTO. The peak at $\approx 50i$ cm⁻¹ is in part due to the dispersionless behaviour of a Pb-O antipolar branch extending from $(1/2, 1/2, 0) \Rightarrow (0, 0, 0)$. This behaviour continues for most of the $(0, 0, 0) \Rightarrow (1/2, 1/2, 1/2)$ path also. It is noteworthy that the Pb character vanishes for the softest part of the PZO PDOS leaving just modes of Zr-O character.

Table 4.4: The 10 most unstable modes, for each structure, measured along the phonon dispersion path in Figure 4.2 (with the exception of PTO, featuring only 7 instabilities over the dispersion path). Modes are listed in descending imaginary wavenumber $\bar{\nu}$ across the page. Each entry features a symmetry label for the irrep and a multiplicity M. Since PZT II, III, IV and VI feature directional polar modes, affected wavenumbers are given in the format $\bar{\nu}_{[010]}/\bar{\nu}_{[110]}/\bar{\nu}_{[111]}$. The full tabulation of all dynamical instabilities can be found in appendix A.1.

	M	$\bar{\nu}$ [i cm ⁻¹]	M	$\bar{\nu}$ [i cm ⁻¹]	M	$\bar{\nu}$ [i cm ⁻¹]			
PTO	Γ_4^-	2	149.60	Δ_5^+	4	83.40	R_4^+	3	62.12
	T_4	2	45.40	Σ_3	4	37.61	Σ_2	4	27.05
	M_3^+	3	18.02						
PZO	R_4^+	3	181.52	T_4	2	178.75	M_3^+	3	176.09
	Γ_4^-	2	132.14	S_4	4	128.32	T_5	4	120.45
	Σ_2	4	119.69	Z_4	4	119.53	S_3	4	105.37
	Λ_2	8	103.13						
VCA	M_2^+	3	146.58	Δ_5	2	141.95	R_5^-	3	137.38
	Γ_4^-	2	101.18	S_1	4	71.78	T_2	4	52.87
	Z_1	4	52.18	T_5	4	52.14	Λ_3	16	49.55
	X_5^-	6	44.89						
I	Γ_4^+	3	138.10	Δ_4	2	133.08	X_3^+	3	128.11
	Γ_4^-	2	111.99	Σ_2	4	73.53	Δ_5	4	62.02
	L_3^-	8	52.83	X_5^-	6	49.09	$L_3^{-'}$	8	48.70
	W_5	4	48.29						
II	M_3^-	1	227.52	Γ_5^-	1	144.78/201.13/215.93	Z_5^-	2	148.78
	A_5^-	2	140.02	Z_1^-	1	137.91	Λ_4	2	132.92
	Γ_3^+	1	127.97	C_1	4	105.26	Λ_5	4	101.14
	W_2	4	90.22						
III	Γ_5^-	1	196.63/196.63/196.63	M_2^+	1	190.76	Γ_3^-	1	174.29/174.29/181.62
	Δ_4	2	173.52	X_2^+	2	156.67	M_5^+	2	152.61
	Δ_3	2	150.97	X_3^+	2	149.79	Y_3	2	147.85
	X_2^-	2	143.46						
IV	Γ_4^-	2	181.41	Γ_4^+	3	169.33	X_3^+	1	168.90
	X_5^+	2	168.18	M_2^-	1	157.00	M_3^+	1	150.48
	R_4^+	3	148.69	$X_5^{+'}$	2	130.13	M_5^+	2	129.20
	$\Gamma_4^{-'}$	2	114.61						
V	Γ_5^-	1	209.42/209.42/209.42	X_3^-	1	202.33	Γ_3^-	1	153.93/153.93/182.48
	Γ_3^+	1	167.07	$\Gamma_5^{-'}$	1	148.18/148.18/123.20	Γ_5^+	1	147.67
	X_4^+	1	146.16	X_1^-	1	132.83	$\Gamma_5^{+'}$	2	131.48
	X_2^-	1	129.84						
VI	Γ_5^-	1	206.22/206.22/206.22	X_2^+	1	197.36	Γ_3^-	1	180.33/195.87/191.69
	R_1^-	1	190.45	Γ_5^+	2	167.85	X_4^+	1	167.42
	X_3^+	1	167.00	$\Gamma_5^{-'}$	1	159.78/146.71/150.21	Γ_4^+	1	149.99
	Γ_3^+	1	142.07						

4.3.2.2 Virtual crystal approximation & PZT I

There is a remarkable visual similarity in the dispersion relations between PZT I and the VCA. At first glance, this suggests that the within mixed potential scheme the dynamics of alternating Zr and Ti atoms in the rock-salt structure are well approximated. We do, however, see more unique branches for PZT I and find that the lowest lying modes of the VCA penetrate further into the soft space than its rock-salt ordered counterpart. It is also true that both approaches resemble PZO more so than PTO. This can be seen when assessing the modes at wavevector $(0, 0, 0)$. At this point, PZT I, the VCA and PZO share a similar hierarchy of modes. PZT I and the VCA also share identical multiplicities. In descending order in imaginary wavenumber, we have out-of-phase AFD, in-phase AFD, FE then a number of antipolar modes. It is illuminating in this case, to perform a full analysis of the character. It soon becomes apparent that the VCA features AFD modes about all three axes of rotation. The amplitudes of these rotations about two of the axes are small and much larger for the remaining axis. We could then consider these modes as rotations about a single axis but with small, erroneous rotations about the other axes. This is in contrast to PZT I where the softest AFD mode (Γ_4^+) has (like both end members) an $a^0a^0c^-$ displacement pattern, shown in Figure 4.4 ii) a). In the VCA, this rotation (M_2^+) retains its out-of-phase characteristic but now rotates about all three axes of rotation with different amplitudes thus exhibiting the $a^-b^-c^-$ rotation pattern shown in Figure 4.4 ii) b-d). The next softest mode in PZT I (X_3^+) has the $a^0a^0c^+$ pattern whilst the in-phase rotations in the VCA (R_5^-), as before, have differing amplitudes about all three axes of rotations. This is the $a^+b^+c^+$ rotation pattern. The rotation patterns in the VCA are *not* seen in any of the PZT supercell models indicating that rotations about more than one axis are a fictitious artifact of the method, better illustrating the inaccuracy of the VCA in the prediction of local atomic displacements.

The character of the FE Γ_4^- modes are also dissimilar in nature. For PZT I, all ions play a role in the development of polarisation including Ti and Zr displacement of a similar magnitude. For the VCA, the alchemical B-site plays much less of a role. We can then infer (without the full Berry-phase calculation) that the incipient polarisation is smaller in magnitude in part owed to the smaller B-site displacements but also due to the smaller value of \bar{Z}_B^* (Table 4.2). A lack of alchemical B-site character is in fact common place for the VCA as evidenced in Figure 4.3 where although optically coupled to Pb motion, has an almost vanishingly small PDOS. This suggests that within the VCA, the B-site is dynamically inert. This leaves the softest modes of the VCA to have nearly a pure O character. It is only for Pb that we see similarity in the PDOS between the VCA and PZT I. We see a peak in the Pb $D(\bar{\nu})$ for PZT I at $\approx 48i \text{ cm}^{-1}$ which is shifted $\approx -2i \text{ cm}^{-1}$ in the VCA. The Pb peak in PZT I coincides with the other species. Such a coupling is in fact true for all PZT configurations and end members PTO/PZO. It is unique to the VCA that we see little coupling between Pb & O. This can be regarded as a knock-on effect of the inert B-site. Since Pb & B-site vibrations are weakly coupled, the usual B-site

displacements which would otherwise follow Pb are not present. It is these displacements which more greatly influence O motion since Pb has only a weaker mixed ionic/covalent interaction with O. Whilst we expect the general fictitious character of the eigendisplacements to persist across all concentrations within the VCA, it is likely that the magnitude of the error may vary. We expect largely fictitious eigendisplacements when Ti/Zr concentrations are comparable but expect the effect to diminish in the limit of high/low concentrations where the mixed potential becomes very similar to the original, unmixed pseudopotential.

Moving away from (0, 0, 0) towards (0, 1/2, 0) both PZT I and the VCA give rise to longer wavelength AFD and antipolar modes. The T₂ and Δ₄ modes of the VCA and PZT I, respectively, display the same rotation pattern as the aforementioned T₄ distortion in PTO. This mode is significantly more unstable in PZT I. Despite the VCA appearing to have a higher degeneracy for the antipolar soft modes at $\approx 50i \text{ cm}^{-1}$, modes are still unique splitting only by $\approx 0.5i \text{ cm}^{-1}$. One of these modes, Z₁, is not purely antipolar and once again we see the mixed AFD/antipolar character displaying non-Glazer-like rotations coupled with Pb cation motion.

like PZO, both the VCA and PZT I become their hardest along the (0, 1/2, 0) \Rightarrow (1/2, 1/2, 0) path. This leads to further antipolar modes at the Σ and S points. Notably, PZT I gains an additional soft mode from the real domain along this path, Σ₁. This is distinct from the other Pb-O modes since it features antipolar Pb-B displacements with no significant O character. For the VCA, there is also a 4-fold degenerate mode Z₁ once again with mixed antipolar/AFD character. The most distinct differences in the dynamical behaviour between the VCA and PZT I now comes along the path (0, 0, 0) \Rightarrow (1/2, 1/2, 1/2). Many of the harder antipolar branches in the VCA move to the real domain. These modes do begin to harden in PZT I but then re-soften to become degenerate with other branches at the L-point giving rise to two long wavelength modes both of symmetry L₃⁻. Now commonplace, they share a mixed antipolar/AFD character split by $\Delta\bar{\nu} = 4.13i \text{ cm}^{-1}$. We distinguish between modes sharing an irrep by priming those with the lower imaginary frequency as seen in Table 4.4. Each mode has 8-fold degeneracy despite L₃⁻ having a longer wavelength AFD rotation pattern than L₃⁻. This splitting closes for the VCA giving rise to one 16-fold degenerate mode of symmetry Λ₃ displaying a similar mixed antipolar/AFD character.

4.3.2.3 PZT II & III

We move now to consider the dispersions of PZT II & III. These are the [110] and [001] ordered superlattices respectively. These structures were considered in a previous work in a study of the instabilities at the Γ-point [50] using the LDA. Consistent with the previous work, we find that both PZT II & III have strong TO FE instabilities of Γ₃⁻ & Γ₅⁻ symmetry respectively. The softest TO mode of the [110] ordered structure is not seen in our dispersion path due to the anisotropy of LO-TO splitting in non-cubic crystals. This anisotropy can be reasoned by the form of the NAC. Recall that the NAC is a function of both \mathbf{Z}_i^* & ϵ^∞ . The former gains more unique elements

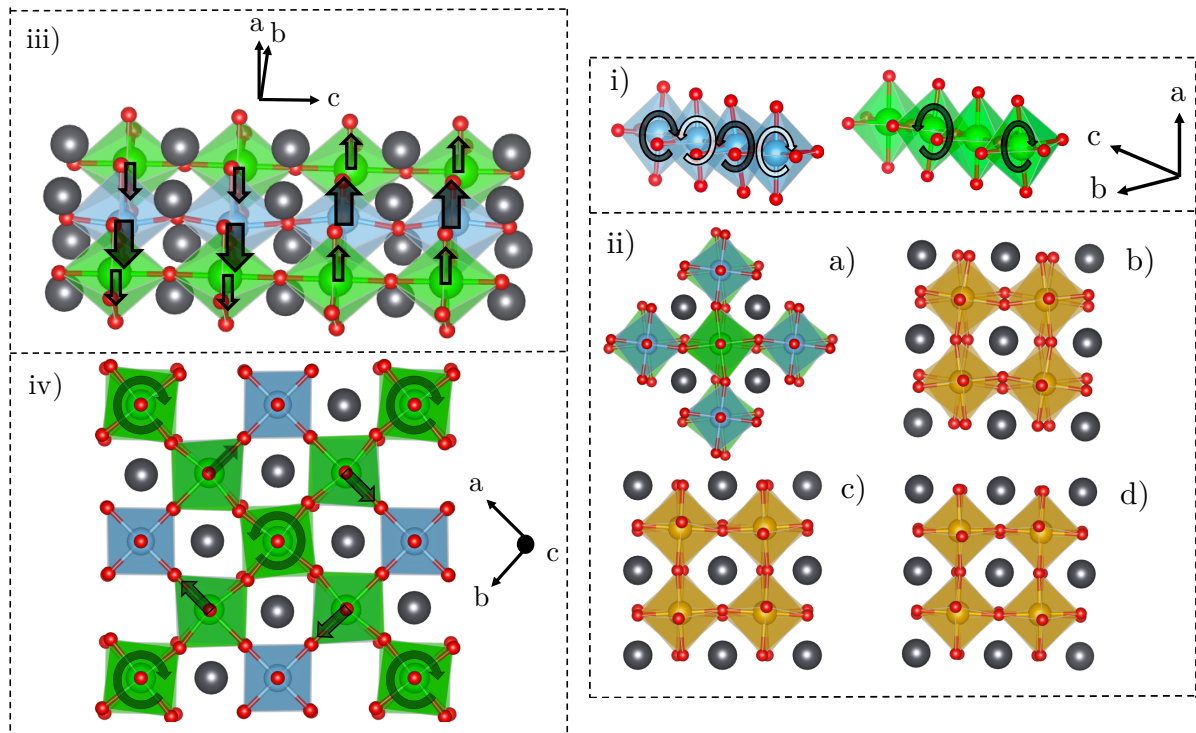


Figure 4.4: Visualisation of eigendisplacements described in the text following the same key as Figure 4.1 but also with grey spheres representing Pb sites. i) The T_4 modes of PTO and PZO. Both Pb and counter-rotating octahedra are removed for clarity. ii) The Γ_4^+ distortion of PZT I (c-axes into page) and the M_2^+ distortion of the VCA from three viewing angles indicating out-of-phase rotation about three axes of rotation iii) The antipolar Δ_4 distortion of PZT III. Arrows indicate the direction of the local polarisation. iv) The mixed antipolar/AFD M_3^+ distortion of PZT IV.

in lower symmetry crystals and the latter is no longer isotropic as evidenced in Table 4.2. The affected elements of the dynamical matrix are then corrected by a different amount based on the direction of the q -vector as it approaches Γ . This effect is seen in PZT II, II, V & VI since they are all members of a tetragonal spacegroup. These anisotropies are also accessible in experiment as evidenced by inelastic neutron scattering in tetragonal PTO [157]. Taking just the analytic part of the Γ_3^- mode of PZT II returns an eigenfrequency of $242.28i \text{ cm}^{-1}$, slightly softer than what is predicted by the LDA [50].

We find that both PZT II & III give rise to soft LO modes, again, in agreement with the previous work. [110] ordering is generally more dynamically unstable than [001] ordering showing a distinct separation between the most imaginary FE/antipolar modes and groupings of Glazer AFD modes. What was not considered in a previous study [50] was competition of polar modes with other order parameters. The antipolar mode M_3^- of PZT II is closely competitive with Γ_5^- . This mode is an antipolar arrangement of Ti-O displacements completely isolated to local PTO environments, leaving undistorted areas of PZO units. There are also a plethora of unique Glazer tilt modes owed to inequivalent directions in the crystals and thus inequivalent axes of rotation. The softest of these is an $a^0a^0c^-$ mode with the axes of rotation along the [001] (or [010]) direction, the direction of compositional modulation. This is followed by a several antipolar modes and harder FE modes. In PZT III, rotational instability is highly competitive with FE order due to the M_2^+ mode. This mode shows in-phase rotation of ZrO_6 octahedra, leaving the TiO_6 octahedra static in a manner reminiscent of the T_4 distortion of PZO. This shows there is no mechanical coupling along the axis of rotation between octahedra centered on a different B-site species. Whilst rotations of all octahedra are also unstable (both out-of-phase M_5^+ and in-phase X_2^-), they are harder. Further, both of these modes rotate along homogeneous B-site chains whereas the M_2^+ mode rotates along the heterogeneous direction where no other Glazer type instability exists.

The character of AFD modes in PZT II alters as we approach the wavevector $(0, 1/2, 0)$. This mode shows out-of-phase rotations of the ZrO_6 octahedra but with a doubled periodicity. Rotating octahedra are also separated by static ZrO_6 octahedra this time showing a lack of inter-layer coupling even along the homogeneous direction. A long wavelength AFD mode also exists for PZT III at this wavevector of irrep Y_3 . This modes shows the same character of the T_4 mode of PTO with the axis of rotation being along the homogeneous direction. This wavevector for PZT III, however, is dominated by antipolar instability with the most unstable being the Δ_4 mode. This mode appears with two separate polar domains with a domain period of 4 perovskite units, separated by a 180° domain wall as depicted in Figure 4.4 iii). Local PTO units are significantly more polar than local PZO units.

Like in PZT I, the VCA, PTO and PZO, the most imaginary bands at $(0, 1/2, 0)$ have a steep gradient to the hard wavevector $(1/2, 1/2, 0)$. This results in tight groupings of antipolar and mixed antipolar/AFD modes for PZT III but only antipolar modes for PZT II. The dispersion

now returns to $(0, 0, 0)$. We note that along this direction of approach ($[110]$), anisotropy in LO-TO splitting allows for softer LO FE modes to appear in both PZT II & III and softer still along the $[111]$ direction. This results in sharp discontinuities in the spectra. From $(0, 0, 0)$ to the long wavelength $(1/2, 1/2, 1/2)$ point, hardening occurs for both PZT II & III giving rise to 5 distinct distortions for each arrangement. For PZT II, these are the $W_{1:4}$ (where the subscript indicates all modes with integers 1 through 4) and W'_1 distortions. Each of these modes has a pure antipolar character. Further, the splitting of the isosymmetrical modes W_1 and W'_1 is large ($64.16i \text{ cm}^{-1}$) due to the inclusion of Zr displacement in W'_1 where W_1 features static Zr. PZT III possesses similar characteristics in its long wavelength distortions, $S_{1:4}$ and S'_4 . Unlike PZT II, two of these distortions have the mixed AFD/antipolar character whilst the remaining are purely antipolar. The S_4 - S'_4 splitting is also large ($61.19i \text{ cm}^{-1}$) but is now the result of the inclusion of local AFD displacements in S_4 whilst S'_4 is purely antipolar.

The general character of the distortions in both PZT II & III can be inferred from the PDOS (Figure 4.3). We see that for both arrangements, all species are optically coupled to one-another, but, like before, the Pb character starts to diminish as we penetrate further into the soft domain. Whilst both PZT II & III both give rise to two separated islands of states in the PDOS, a sharp peak exists on the softer island of PZT II at $\approx 100i \text{ cm}^{-1}$. This is owing to the nearly dispersionless behaviour of the antipolar branch connecting the Λ_5 and C_1 modes. The 4-fold degenerate W_1 anti-polar mode also appears at this wavenumber (along with Λ_5 and C_1) containing significant Pb character.

4.3.2.4 PZT IV

We discuss now PZT IV in isolation, which, despite sharing $m\bar{3}m$ symmetry with PZT I, shows radically different dynamical behaviour as well as being generally more unstable. For the first time in this study, also, we consider dispersion over what is the primitive unit cell so we pass through high symmetry points without any folding of the BZ. Unlike PZT I, the softest mode at $(0, 0, 0)$ is now a Γ_4^- distortion which although suggests a FE ground state, is not guaranteed. This is because the phonon frequency gives us only information on the instability of the mode and *not* on the magnitude of energy lowering once the soft lattice mode has condensed in the crystal. This distortion shows stronger local polarity in directions with continuous PTO units. The presence of Zr along a polar direction dampens the distortion. For the first time in this study, no pure Glazer type AFD instabilities are found to exist in a single mode. These are replaced with isolated in-phase AFD instabilities the softest of which is the Γ_4^+ mode. This mode features a rotating layer (isolated by static $PbBO_3$ layers) with a ratio of 8:1 ZrO_6 to TiO_6 octahedra. In this case, the dominance of the PZO rich environment (which favours rotation) is able to overpower the single PTO unit (favouring FE distortion) into rotation. One other rotational instability exists at this point, $\Gamma_4^{+'}$. This mode shares the same characteristics as Γ_4^+ , but the rotating layer contains fewer ZrO_6 octahedra making the mode more stable than its counterpart. It is notable that there

are three separate occurrences of the FE Γ_4^- irrep: Γ_4^- , $\Gamma_4^{-'}$ and $\Gamma_4^{-''}$. The latter (although much harder than the others) is distinct not only due to its weak B-site displacements but also its alternating Pb cation motion transverse to the direction of polarisation giving rise to a mode of a mixed FE & antipolar character at the zone centre.

Most bands harden only slightly along the path to X much in contrast to the superlattice type arrangements. Antipolar type distortions at this wavevector are much harder than previous arrangements featuring only Pb-O motion. There is now only a slight hardening in the dispersion along the $\Gamma \Rightarrow X$ path once again leading to a selection of antipolar and AFD modes. The X_3^+ and X_5^+ modes are particularly unstable. The first is a long wavelength AFD mode much like Γ_4^+ but with out-of-phase rotations. These rotational modes are very closely competing split by $<1i$ cm^{-1} in the favour of X_3^+ . The second, X_5^+ is an isolated antipolar distortion where local PTO units are polar in the direction of compositional homogeneity. PZO units are once again resistant to polarisation and are left static. After a small degree of hardening along the path to M, we find 15 unique distortions of antipolar and mixed AFD/antipolar character; the largest concentration of such states in this study. The softest is antipolar M_2^- bearing great resemblance to X_5^+ but over a greater wavelength.

The M_3^+ mode is the clearest example of a mixed AFD/antipolar mode. This is shown in Figure 4.4 iv). It features a central in-phase rotation similar to Γ_4^+ . PbBO₃ units perpendicular to the axis of rotation now show local polar displacements in a pattern enclosing the central rotating unit. Softer modes of this character can be seen at the R-point. Here we find that the most unstable branches are dominated by the mixed AFD/antipolar character. In-fact, the most unstable mode of this character, amongst all PZT arrangements, is found here and is the triply degenerate R_4^+ . This shares great similarity to M_3^+ but rotations are out of phase and about two axes making the rotation pattern $a^0b^-b^-$ -like. Other modes at this wavevector are also visually similar to M_3^+ but now the local polar regions include Pb & Ti cation motion where before local polarity was just as the result of O displacing against static Zr.

PZT IV is the only arrangement to form three distinct islands in the PDOS. The two more stable islands feature coupled ionic motion between all species, but, as before the most imaginary states have a diminished Pb character. It is clear that the first (and least imaginary) island is comprised entirely of antipolar states and the second of antipolar and mixed AFD/antipolar states. The softest island features the purely rotational states but also FE and mixed AFD/antipolar order. Unlike previous arrangements, there is a significant peak in the most unstable island at $\approx 140i$ cm^{-1} as a result of a significant amount of mixed AFD/antipolar modes. This suggests that such a mode character could play a role in a low energy structure of this arrangement.

4.3.2.5 PZT V & VI

The last of the arrangements we consider together are PZT V & VI. A striking dissimilarity between these two arrangements and the rest is the increased number on unique bands in the soft

space. The vast majority of these states are singly degenerate in response to the large number of uniquely coordinated ions. At the Γ -point, both arrangements are dominated by a highly imaginary FE distortion of symmetry Γ_5^- . Both distortions display greater local polarisation in the direction of compositional homogeneity in Ti. Local PZO units are polarized but as in the end member PZO, Zr play less of a role. Both arrangements feature other polar modes where like PZT IV, alternating Pb cation motion is in a direction perpendicular to the polarisation suggesting a dual FE & antipolar character.

Like PZT III and IV, PZT V favours isolated rotations separated by static octahedra. One example of this is Γ_3^+ mode where rotating layers feature a higher number of Zr sites and static layers have a higher number of Ti sites. It is true once more that purely Glazer type rotations are not seen in the spectra of PZT V. These are replaced with Glazer-like modes where one layer rotates more strongly than the other. The most unstable example of this is the Γ_5^+ mode which is strongly $a^0a^0c^-$ -like, but, the rotating layer with the higher Ti/Zr ratio rotates at a diminished amplitude. For both V & VI, the most imaginary polar branch is almost dispersionless along the path to X resulting in the softest mode at the X_3^- and X_2^+ for each arrangement, respectively. Both modes are antipolar featuring no Pb cation motion but heavy Ti-O countermotions. Like previous PZT arrangements at this wavevector, we see non-Glazer-like isolated AFD modes and a variety of harder antipolar modes.

For PZT VI, we see that the most imaginary TO branch is not only dispersionless along the previously mentioned path but is for much of the BZ until we see a rapid hardening as we approach Λ . Even here however, the branch remains unstable. This shares some similarity with the dynamical behaviour seen in the dispersion relations of $BaTiO_3$ (BTO), but, for BTO the result is a confinement of the instability to three quasi-two-dimensional slabs of q-space intersecting at Γ since the branch becomes real towards the R-point. With the exception of this branch, the character of modes at the wavevectors $(1/2, 1/2, 0)$ & $(1/2, 1/2, 1/2)$ are rather similar. Both give rise to large number of unique AFD/antipolar distortions similar to those described before. Notable also is the anisotropic behaviour of polar branches approaching the Γ -point from the different considered directions. Whilst the most imaginary TO branches are unaffected, discontinuity can be seen clearly when comparing the $[110]$ & $[111]$ directions for both PZT V & VI which is tabulated in Table 4.4. The fairly even distribution of states across the soft space results in a single island in the PDOS for both PZT V & VI, although, like other PZT arrangements, there is a higher density of antipolar states in the harder part of the soft-space. Remarkably, despite the near-dispersionless character of the most imaginary polar branch in PZT VI, the resulting peak in the PDOS is small as a result of its isolation from other bands in the spectra and its single-fold degeneracy.

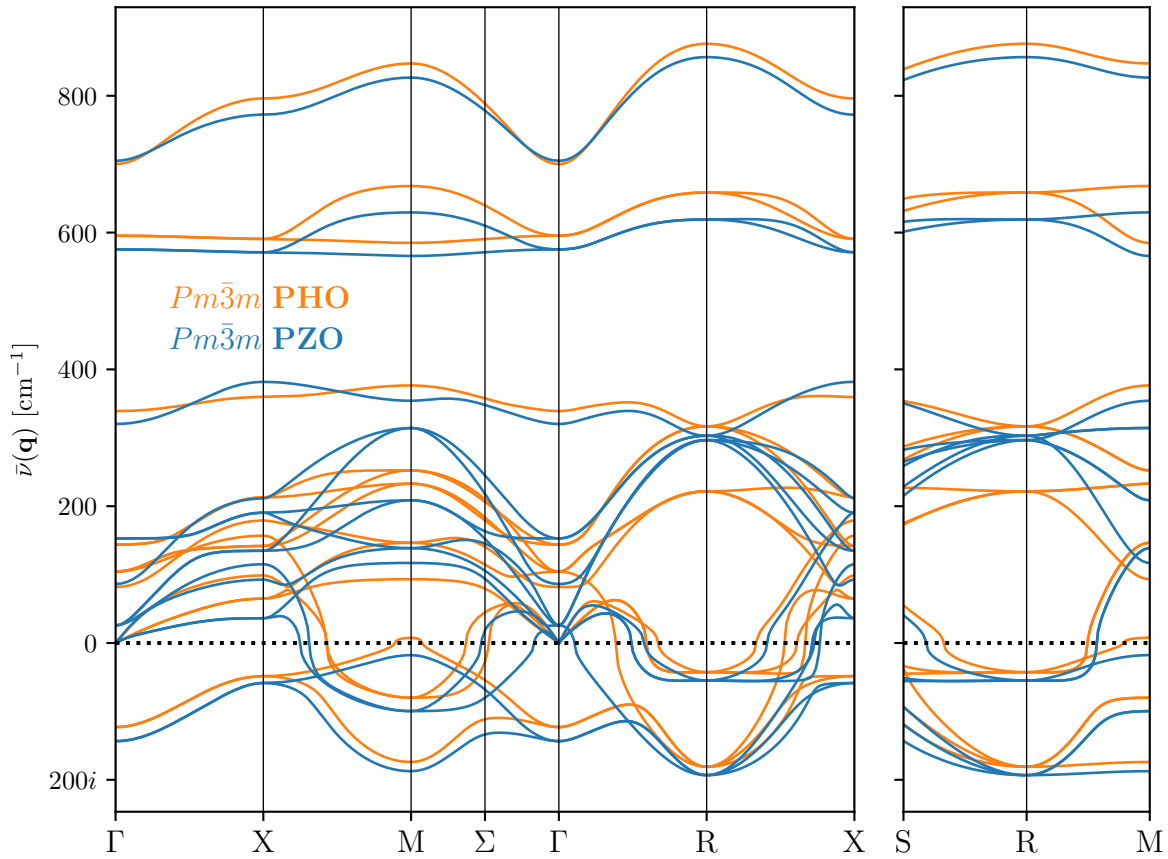


Figure 4.5: The phonon dispersions of primitive $Pm\bar{3}m$ PZO (blue) and PHO (orange).

4.4 PZO & PHO: a new ground state candidate

4.4.1 Comparison of phonon dispersions

Now having confirmed the presence of long wavelength soft modes in ordered cubic PZT 50/50 and PZO, some interesting questions naturally arise. Firstly, do these instabilities persist in PZO's isoelectronic and isostructural partner, PHO? If they do persist, how does their character compare to those in PZO? Lastly, given the ubiquity of these long wavelength modes, do any further modes of this type condense in the low temperature AFE phases of PZO and PHO? Figures 4.5 and 4.6 show the phonon dispersion relationships for PZO and PHO within the 1BZ. In contrast to the previous sections, these calculations have been performed using the *primitive* 5/40 atom cells for the $Pm\bar{3}m/Pbam$ phases. Also unlike the previous sections, we have included the real branches in these plots as they make for interesting visual comparisons. The majority of the discussion will once again, however, concentrate on the nature of the dynamical instabilities.

Focusing first on the cubic dispersions (Figure 4.5), we see some striking similarities between PZO and PHO. It is true that most of the imaginary and high (real; above $\approx 580 \text{ cm}^{-1}$) wavenumber optical branches follow similar dispersion paths across the 1BZ. Visually, the most

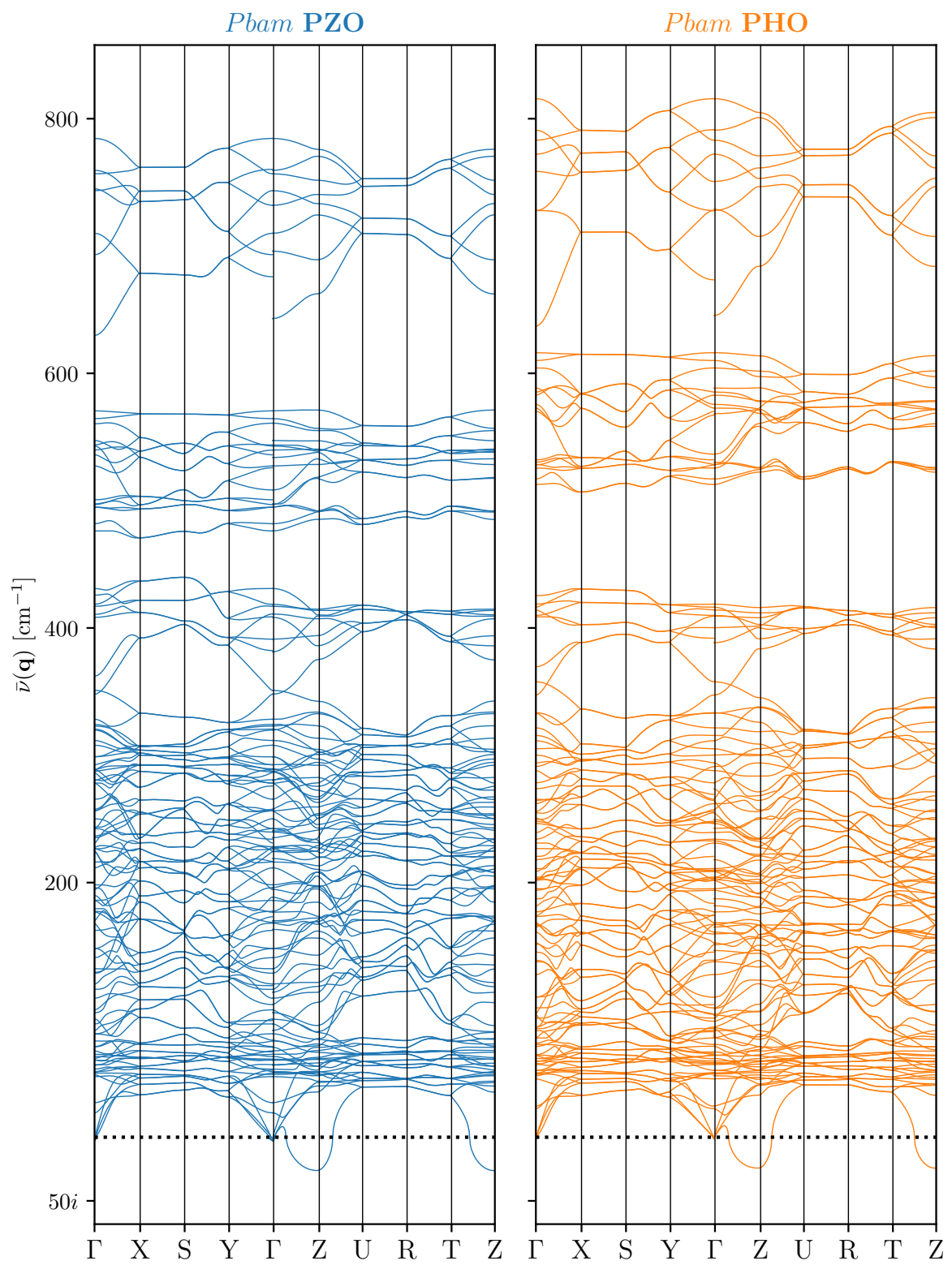


Figure 4.6: The phonon dispersions of primitive $Pbam$ PZO (blue) and PHO (orange).

discrepancy appears for those real branches in range $0 \text{ cm}^{-1} \leq \bar{\nu}(\mathbf{q}) \leq 250 \text{ cm}^{-1}$. It is likely that it is this region which is responsible for the differences in the thermal properties of the materials. Treating now the general nature of the dynamical instabilities, we see that PZO is systematically more unstable than PHO for most branches. This translates directly to the finding that the relative energy of the AFE $Pbam$ phase to $Pm\bar{3}m$ is much lower for PZO than PHO (Table 4.5). We also see that the important Σ_2 and R_4^+ modes have a larger amplitude in PZO than PHO; PHO is a weaker antiferroelectric (See Table 4.8). Following this, PZO and PHO are isostructural in the sense that they share the same irreps in the AFE phase, but, the magnitude of these irreps differ strongly between them. When analysing the eigendisplacements of the unstable modes at each high symmetry point, we find that the characters of *all* modes are shared between PHO and PZO. The only place we are unable to perform this comparison is at the M-point where the Pb-only antipolar mode M_2^- becomes real for PHO. A cautious observer may from Figure 4.5 suggest that some modes are also missing at the S-point, however, this is untrue. PHO and PZO simply possess nearly identical wavenumbers for some modes at and in the vicinity of this point. We do not describe the character of each instability in this section as, remarkably, they share identical character with the PBESol calculation for PZO in Section 4.3.2.1.

Looking now at the $Pbam$ dispersions of Figure 4.6, we see the two also share great similarities. The visible difference is perhaps the small upwards shift of the high wavenumber (above $\approx 550 \text{ cm}^{-1}$) optical branches of PHO versus PZO. One particular feature the eye is drawn towards is the instability of an optical branch in the vicinity of the Z-point ($\mathbf{q}_Z = (0, 0, 0.5)$). Since $Pbam$ is the purported low temperature ground state, this is surprising. The low temperature ground state (or more precisely, the 0K ground state) should have *no unstable modes*. Exactly at the Z-point, this mode has symmetry Z_4^+ for PZO and PHO with a wavenumber of $26.15i \text{ cm}^{-1}$ and $24.27i \text{ cm}^{-1}$ respectively. By convention, mode irreps are usually given as a decomposition of the $Pm\bar{3}m$ phase, so, we unfold the single Z_4^+ irrep (of $Pbam$) to five irreps: T_4 , T_2 , Λ_1 , Λ_3 and Δ_5 . It is interesting to point out that these distortions are also instabilities of the PZO and PHO $Pm\bar{3}m$ phases. The distortion pattern (though exaggerated) for T_4 and Λ_3 is shown in Figure 4.7. We do not discuss the character of the remaining modes here because, as we learn in Table 4.8, these modes only appear at a minuscule amplitude. T_4 (Figure 4.7a) is a long wavelength antiferrodistortive mode rotating about the pseudocubic \mathbf{b} axis. It is periodic over four perovskite units with two octahedra rotating clockwise and two anticlockwise. This mode is reminiscent of the *super-tilting* pattern observed in NaNbO_3 [324] and AgNbO_3 [325]. Λ_3 (Figure 4.7b) is a Pb-O antipolar mode. For the Pb displacements, it can be described as having a ‘two-up, two-down’ pattern in one PbO plane then a ‘two-left, two-right’ pattern in the next PbO plane. Within the PbO planes, O moves *antiparallel* to the Pb displacements. Within the $\text{ZrO}_2/\text{HfO}_2$ planes, O moves in a sinusoidal wave pattern with a period of four O sites. This pattern is reflected (about the Pb-O plane) in the next $\text{ZrO}_2/\text{HfO}_2$ plane.

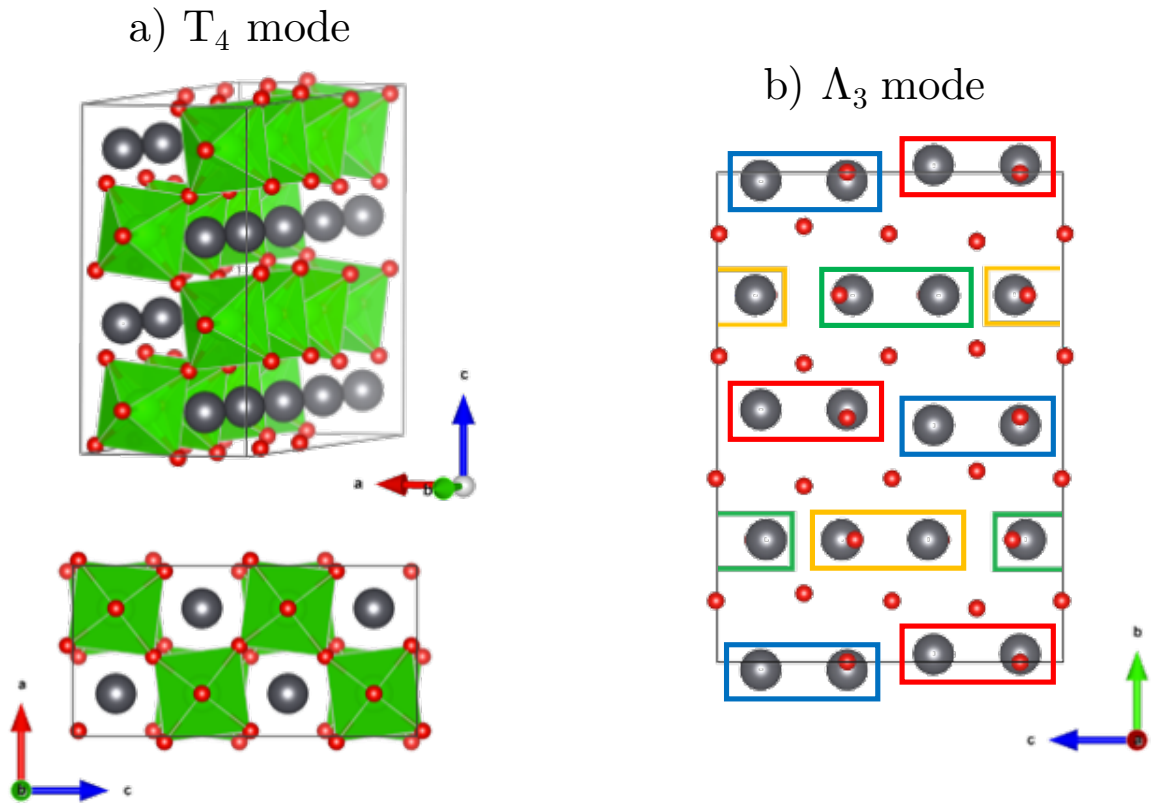


Figure 4.7: The two most important modes comprising the difference between the $Pbam$ and $Pnma$ crystals for PZO and PHO. The magnitude of the displacement is exaggerated. a) The T_4 mode. ZrO_6/HfO_6 octahedra rotate in antiphase about the pseudocubic b axis in *pairs*. b) The Λ_3 mode. Antipolar Pb displacements are grouped by a common displacement direction with coloured boxes (red: up, blue: down, orange: left, green: right). Zr/Hf (inactive in this mode) has been removed for clarity.

4.4.2 The antiferroelectric $Pnma$ phase

We now introduce the eigendisplacements associated with these new irreps into the $Pbam$ structure at a small amplitude, breaking the symmetry and pushing the crystal into a new minimum. After doing so, we relax the structure until the magnitude of all forces fall below 1×10^{-3} eV/Å. The result is new 80-atom $Pnma$ phase; marginally lower in energy than $Pbam$ and described by *eleven* distinct irreps. To corroborate this energy lowering and to ensure this new phase is not a mere artefact of the LDA, we perform the same procedure with the PBESol and SCAN[†] (strongly constrained and appropriately normed; meta-GGA [221].) functionals. The PBESol calculation was performed using the NCPP method used in Section 4.3. The relative stabilities are shown in Table 4.5 while the $Pbam$ and $Pnma$ crystal structures are described

[†]Calculations with the SCAN functional were received in private communications from J. K Shenton. VASP (v5.4.4) [270, 274, 326–328] was used with PBE PAWs [152, 234] (Zr_sv 04Jan2005, Hf_pv 06Sep2000, O 08Apr2002, Pb_d 06Sep2000). The effects of mismatching PBE PAWs with the SCAN functional are discussed in [329].

Table 4.5: The relative stability ΔE (in meV/FU) of the $Pbam$ and $Pnma$ phases compared to cubic $Pm\bar{3}m$ for PZO and PHO. $\Delta E = E(Pbam/Pnma) - E(Pm\bar{3}m)$.

	LDA-PW	PBESol	SCAN
$Pbam$ PZO	-310.744	-262.240	-258.943
$Pnma$ PZO	-311.878	-263.096	-259.138
$Pbam$ PHO	-95.309	-175.014	-205.946
$Pnma$ PHO	-96.026	-175.426	-206.186

in Tables 4.6 and 4.7 respectively. To quantify the strength of each distortion, we calculate the primitive cell normalised mode amplitude A_p for each irrep, shown in Table 4.8. To assign A_p , the atomic displacements are assigned (by symmetry) to an irrep and calculated as fractional displacements relative to the parent structure. We then normalise by a factor of $\sqrt{V_p/V_s}$ for primitive/supercell cell volumes V_p/V_s . A_p is then the root sum squared (RSS) of each of these displacements comprising the irrep. This is the format popularised by the ISODISTORT package [321].

From Table 4.5, we see that the new $Pnma$ phase is lower in energy than $Pbam$ for all three functionals used. $Pnma$ is more stable by ~ 1 meV/FU for most cases, but, this narrows to ≈ 0.2 meV/FU for the SCAN functional. The majority of this energy lowering comes from the condensation of the T_4 and Λ_3 modes which appear with an amplitude similar to the S_4 mode of $Pbam$ for the LDA-PW and PBESol calculations. For SCAN, the amplitudes of these modes are degraded, explaining the narrowing of the energy gap between $Pbam$ and $Pnma$ for this functional. This effect is particularly apparent for $Pnma$ PHO where the amplitudes of these two modes are $\approx 6\times$ smaller compared with LDA-PW and PBESol. Even more interesting, the RSS of $Pnma$ PHO for the SCAN functional is *lower* than $Pbam$ despite the introduction of the 5 new modes. This is the result of the reduced amplitude R_4^+ mode which likely competes with one of the new modes. Since the new irreps condensing in $Pnma$ couple only weakly to strain, it can be seen from Tables 4.6 and 4.7 that the lattice constants (per ABO_3 unit) of the two models are almost unchanged ($\sim 10^{-3}$ Å difference). Taking forward just the LDA-PW $Pnma$ PZO structure, we relax the forces further (to 1×10^{-6} eV/Å) and calculate the dynamical matrix exactly for five[‡] \mathbf{q} -vectors commensurate with a $5 \times 2 \times 3$ \mathbf{q} -point grid. At these points, we now find no unstable modes; it is *very unlikely* that there are further energy lowering subgroups of $Pnma$ as the result of symmetry lowering atomic distortions.

There are three possibilities we can conceive for the origin of this new phase which should all be considered. Firstly, it could be that what was observed as $Pbam$ in experiment was $Pnma$ all along. This could be forgiven since distinguishing between the two models in any given

[‡]We treated $\mathbf{q} = (0, 0, 0), (1/5, 0, 0), (2/5, 0, 0), (0, 1/3, 0)$ and $(0, 0, 1/2)$. Many perturbations were also treated for other \mathbf{q} on the $5 \times 2 \times 3$ mesh, but were intractable to compute for *all* atomic displacements. These additional perturbations also yielded real frequencies.

Table 4.6: The (fractional) Wyckoff positions (x, y, z) and orthorhombic lattice vectors for 40 atom $Pbam$ PZO and PHO. We compare LDA-PW, PBESol and the SCAN functionals complete with comparison to 10K neutron diffraction data.

Site	LDA-PW	PBESol	SCAN	Exp (10K) [330] [287]
<i>Pbam</i> PZO				
Pb 4g	(0.7035, 0.8770, 0.0000)	(0.7017, 0.8764, 0.0000)	(0.6951, 0.8762, 0.0000)	(0.6991, 0.8772, 0.0000)
Pb 4h	(0.2868, 0.1275, 0.5000)	(0.2893, 0.1282, 0.5000)	(0.2952, 0.1297, 0.5000)	(0.2944, 0.1294, 0.5000)
Zr 8i	(0.2431, 0.8754, 0.2497)	(0.2420, 0.8756, 0.2497)	(0.2401, 0.8760, 0.2497)	(0.2414, 0.8752, 0.2486)
O 4e	(0.0000, 0.0000, 0.7713)	(0.0000, 0.0000, 0.7714)	(0.0000, 0.0000, 0.7689)	(0.0000, 0.0000, 0.7707)
O 4f	(0.0000, 0.5000, 0.7999)	(0.0000, 0.5000, 0.7969)	(0.0000, 0.5000, 0.7974)	(0.0000, 0.5000, 0.7974)
O 4h	(0.6961, 0.0928, 0.5000)	(0.7010, 0.0941, 0.5000)	(0.6985, 0.0958, 0.5000)	(0.6989, 0.0956, 0.5000)
O 4g	(0.7230, 0.1587, 0.0000)	(0.7250, 0.1575, 0.0000)	(0.7237, 0.1560, 0.0000)	(0.7244, 0.1560, 0.0000)
O 8i	(0.2431, 0.8754, 0.2497)	(0.5316, 0.7616, 0.7188)	(0.5328, 0.7619, 0.7197)	(0.5317, 0.7378, 0.7202)
a (Å)	5.8098	5.8716	5.9028	5.8736
b (Å)	11.6864	11.7651	11.8129	11.7770
c (Å)	8.0993	8.1776	8.2078	8.1909
<i>Pbam</i> PHO				
Pb 4g	(0.7101, 0.8769, 0.0000)	(0.7092, 0.8764, 0.0000)	(0.7003, 0.8748, 0.0000)	(0.7114, 0.8768, 0.0000)
Pb 4h	(0.2840, 0.1281, 0.5000)	(0.2855, 0.1285, 0.5000)	(0.2920, 0.1300, 0.5000)	(0.2928, 0.1298, 0.5000)
Hf 8i	(0.2442, 0.8754, 0.2497)	(0.2434, 0.8756, 0.2497)	(0.2406, 0.8764, 0.2498)	(0.2421, 0.8745, 0.2455)
O 4e	(0.0000, 0.0000, 0.7714)	(0.0000, 0.0000, 0.7714)	(0.0000, 0.0000, 0.7669)	(0.0000, 0.0000, 0.7650)
O 4f	(0.0000, 0.5000, 0.7951)	(0.0000, 0.5000, 0.7927)	(0.0000, 0.5000, 0.7905)	(0.0000, 0.5000, 0.7932)
O 4h	(0.7049, 0.0950, 0.5000)	(0.7083, 0.0959, 0.5000)	(0.7065, 0.0995, 0.5000)	(0.6996, 0.0983, 0.5000)
O 4g	(0.7284, 0.1560, 0.0000)	(0.7303, 0.1551, 0.0000)	(0.7290, 0.1522, 0.0000)	(0.7329, 0.1561, 0.0000)
O 8i	(0.5282, 0.7609, 0.7195)	(0.2434, 0.8756, 0.2497)	(0.5271, 0.7599, 0.7234)	(0.5280, 0.7410, 0.7190)
a (Å)	5.7585	5.8181	5.8330	5.8404
b (Å)	11.5690	11.6580	11.6575	11.7057
c (Å)	8.0581	8.1344	8.13517	8.1751

Table 4.7: The (fractional) Wyckoff positions (x, y, z) and orthorhombic lattice vectors for 80 atom $Pnma$ PZO and PHO. We compare LDA-PW, PBESol and the SCAN functionals. We warn the reader, that by convention, the psuedocubic a and b axes are interchanged when compared to $Pbam$.

Site	LDA-PW	PBESol	SCAN
<i>Pnma</i> PZO			
Pb 8d	(0.7946, -0.0057, 0.8764)	(0.7963, -0.0061, 0.8757)	(0.8044, -0.0035, 0.8760)
Pb 4c	(0.7865, 0.2500, 0.8699)	(0.7883, 0.2500, 0.8689)	(0.7947, 0.2500, 0.8691)
Pb 4c	(0.2150, 0.2500, 0.1258)	(0.2122, 0.2500, 0.1260)	(0.2049, 0.2500, 0.1281)
Zr 8d	(0.7549, 0.1252, 0.6248)	(0.7554, 0.1252, 0.6246)	(0.7585, 0.1251, 0.6243)
Zr 8d	(0.2576, 0.6245, 0.8760)	(0.2589, 0.6246, 0.87636)	(0.2607, 0.6247, 0.8763)
O 8d	(0.5094, 0.8994, 0.4965)	(0.5105, 0.8978, 0.4962)	(0.5044, 0.8985, 0.4987)
O 8d	(0.4538, 0.8645, 0.7314)	(0.4571, 0.8649, 0.7326)	(0.4615, 0.8630, 0.7351)
O 8d	(0.4780, 0.3534, 0.7434)	(0.4815, 0.3542, 0.7451)	(0.4727, 0.3569, 0.7410)
O 8d	(0.7246, 0.4990, 0.6582)	(0.7267, 0.4990, 0.6569)	(0.7241, 0.4994, 0.6558)
O 8d	(0.0140, 0.6150, 0.5067)	(0.0152, 0.6150, 0.5071)	(0.0072, 0.6158, 0.5033)
O 4c	(0.6968, 0.2500, 0.5870)	(0.7010, 0.2500, 0.5887)	(0.6978, 0.2500, 0.5923)
O 4c	(0.3025, 0.2500, 0.3995)	(0.2967, 0.2500, 0.3985)	(0.3004, 0.2500, 0.4001)
a (Å)	5.8065	5.8671	5.9015
b (Å)	16.2246	16.3833	16.4237
c (Å)	11.6707	11.7505	11.8087
<i>Pnma</i> PHO			
Pb 8d	(0.7883, -0.0049, 0.8763)	(0.7895, -0.0049, 0.8758)	(0.7998, -0.0010, 0.8746)
Pb 4c	(0.7835, 0.2500, 0.8698)	(0.7846, 0.2500, 0.8692)	(0.7920, 0.2500, 0.8695)
Pb 4c	(0.2183, 0.2500, 0.1263)	(0.2161, 0.2500, 0.1263)	(0.2078, 0.2500, 0.1298)
Hf 8d	(0.7548, 0.1253, 0.6247)	(0.7551, 0.1251, 0.6246)	(0.7591, 0.1249, 0.6237)
Hf 8d	(0.2556, 0.6245, 0.8759)	(0.2571, 0.6246, 0.8761)	(0.2597, 0.6248, 0.8766)
O 8d	(0.5086, 0.8969, 0.4963)	(0.5092, 0.8958, 0.4963)	(0.5011, 0.8952, 0.4997)
O 8d	(0.4599, 0.8649, 0.7336)	(0.4639, 0.8646, 0.7350)	(0.4714, 0.8625, 0.7394)
O 8d	(0.4851, 0.3549, 0.7455)	(0.4862, 0.3561, 0.7463)	(0.4742, 0.3611, 0.7409)
O 8d	(0.7298, 0.4991, 0.6556)	(0.7317, 0.4992, 0.6546)	(0.7290, 0.4999, 0.6522)
O 8d	(0.0118, 0.6150, 0.5061)	(0.0128, 0.6150, 0.5063)	(0.0018, 0.6166, 0.5008)
O 4c	(0.7059, 0.2500, 0.5896)	(0.7085, 0.2500, 0.59180)	(0.7064, 0.2500, 0.5988)
O 4c	(0.2945, 0.2500, 0.3981)	(0.2901, 0.2500, 0.3983)	(0.2932, 0.2500, 0.3994)
a (Å)	5.7566	5.8147	5.8333
b (Å)	16.1342	16.2886	16.2713
c (Å)	11.5587	11.6482	11.6571

Table 4.8: The total decomposed mode amplitudes A_p (described in the text) for each irrep using the $Pm\bar{3}m$ phase as the parent and the $Pbam/Pnma$ phase as the daughter. Data is presented in the format “LDA-PW PBESol SCAN”. $RSS = \sqrt{\sum_i A_{p,i}^2}$.

Mode	$Pbam$ PZO			$Pbam$ PHO			$Pnma$ PZO			$Pnma$ PHO		
R_4^+	0.5504	0.5332	0.5138	0.5082	0.4969	0.4433	0.5380	0.5197	0.5088	0.4964	0.4841	0.4418
Σ_2	0.4233	0.4093	0.4462	0.3541	0.3416	0.3832	0.4098	0.3942	0.4440	0.3415	0.3308	0.3838
S_4	0.1412	0.1296	0.1424	0.1191	0.1094	0.1192	0.1443	0.1301	0.1427	0.1206	0.1114	0.1186
M_5^-	0.0096	0.0156	0.0257	0.0103	0.0155	0.0354	0.0159	0.0230	0.0265	0.0153	0.0197	0.0380
R_5^+	0.0277	0.0277	0.0376	0.0305	0.0302	0.0301	0.0267	0.0260	0.0349	0.0276	0.0268	0.0294
X_3^-	0.0191	0.0173	0.0169	0.0159	0.0137	0.0127	0.0135	0.0107	0.0153	0.0101	0.0092	0.0127
T_4	-	-	-	-	-	-	0.1337	0.1420	0.0641	0.1283	0.1261	0.0160
Λ_3	-	-	-	-	-	-	0.1275	0.1278	0.0735	0.1116	0.1007	0.0181
Λ_1	-	-	-	-	-	-	0.0264	0.0263	0.0155	0.0227	0.0201	0.0046
T_2	-	-	-	-	-	-	0.0046	0.0046	0.0028	0.0030	0.0026	0.0007
Δ_5	-	-	-	-	-	-	0.0113	0.0132	0.0092	0.0136	0.0086	0.0024
RSS	0.7094	0.6855	0.6969	0.6318	0.6139	0.5999	0.7172	0.6936	0.6988	0.6390	0.6196	0.5997

measurement is difficult (especially if you didn't know the $Pnma$ model existed): the new distortions are small in amplitude, so any measurement would likely have to be performed with high resolution equipment at cryogenic temperatures. Also, we find that the two models share the same Raman active modes[†] (Γ_2^+ , Γ_3^+ , Γ_4^+) so no new peaks would appear in the Raman intensity spectrum. Although one would expect the character and intensity of these peaks to differ between the models, the differences would be subtle. A ground state $Pnma$ structure would also be unsurprising seeing as we know the *vast majority* of perovskites condense this symmetry at low temperatures [332, 333]. The second origin we have conceived is that in some region below the measured AFE phase transition temperature, the crystal is $Pbam$, but, at some point before 0K there is a second transition to $Pnma$, previously undetected due to its small magnitude. At the time of writing this thesis, the group of Gustau Catalan are working on this origin in experiment. That is, they are checking for an anomaly in the functional properties of PZO (the dielectric loss, for example) down to low temperatures. While the presence of such an anomaly would indicate the presence of a phase transition, it does *not* present the symmetry of the new phase. It is perhaps only Neutron diffraction/scattering which would allow the determination of $Pnma$ over $Pbam$, although, X-rays *could* be successful in characterising the Λ_3 mode due to its strong Pb character. The third origin is that the new distortions are merely artefacts of the exchange & correlation functionals used in this chapter. While we have tried to minimize this cause by using three functionals at consecutively higher rungs (which *all* predict $Pnma$ as a more stable phase than $Pbam$) we cannot explicitly rule this out. Another reason this origin is unlikely is

[†]The shared nature of the Raman active modes for the $Pbam$ and $Pnma$ models was received in private communications with Mike Glazer as deduced by symmetry analysis using the program VIBRATE! (v2.7) [331]. In another private communication with Gustau Catalan, he confirms that no new Raman active modes appear in the Raman intensity spectrum between 295-83K.

that the new modes appear at a similar magnitude to the previously known S_4 mode (at least for LDA-PW and PBESol calculations) which is measured in experiment. Also, PZO and PHO are not materials where we would normally expect DFT to fail in the transition metal oxides. That is, they are not considered strongly correlated materials. Indeed, even if they were, the SCAN functional is known to perform well for strongly correlated systems [222] so this calculation most likely rules out this effect.

While this $Pnma$ phase appears exotic, it is more common than one might think. Similar 80-atom $Pnma$ phases are known to be metastable in $BiFeO_3$ (BFO); stabilised under pressure [334] or the correct electrostatic boundary conditions [335]. They are also known to appear in a whole host of other solid solutions, including $(Bi,La)FeO_3$ [285], $BiFe_{0.75}Mn_{0.25}O_3$ [284], $(Bi,Nd)FeO_3$ [281, 282] and $BiFe_{1/2}Sc_{1/2}O_3$ [283, 334]. We note that in all of these cases, the magnitude of the distortions defining $Pnma$ over $Pbam$ are stronger than what we find for PZO and PHO, making their experimental identification easier. Given that AFE phases of this type seem to be ubiquitous and it now appears (in DFT, at least) in the archetypal antiferroelectrics, the question must be asked: are 80-atom $Pnma$ phases the *most common* AFE arrangements in the perovskite oxides?

4.5 Summary

We have explored the soft mode lattice dynamics of PTO, PZO, PHO and $PbZr_{0.5}Ti_{0.5}O_3$ and determined the character of the most unstable modes of each arrangement. This has revealed a complex landscape of local minima and possible phase transition paths notably including competitive long wavelength distortions. It is important to emphasize that this work indicates that altering B-site ordering in a fixed concentration of Ti/Zr in PZT can in some special cases lead to the dominance of different order parameters. We find that, in general, (with the exception of PZT IV) higher symmetry models like PZT I and the VCA are dominated by rotational instabilities of the BO_6 octahedra which, like pure PZO and PHO, are able to couple with Pb antipolar modes at the Σ -point suggesting the stability of an AFE structure. Lower symmetry supercells are found to be more PTO-like implicated by the soft zone centre modes with a FE character. We suggest that this effect is the result of the presence of crystalline directions where continuous Ti-O-Ti chains exist or at least a direction where the Ti to Zr ratio is high. If this is not true (as is the case for PZT I) the more inert Zr sites act to dampen the FE distortion allowing for rotational instabilities to dominate. In the context of a realistic ordering of $PbZr_{0.5}Ti_{0.5}O_3$, these findings imply that for any given sample unless the Ti/Zr ordering is high symmetry (which is very unlikely) the dominant order parameters are likely be zone centre and FE in character. This finding agrees with the experimental observation that PZT is ferroelectric at this concentration [91]. Given the number of unique distortions in any one of the supercell models, however, it is unlikely that the ground state of these structures can be described *only* by a FE distortion.

This is supporting evidence for the experimentally observed coexistence of ferroelectricity and octahedral rotations [336]. Further work could include identification of the phase transition paths resulting in a mixed-mode ground state.

We find also that there is considerable competition with the routinely considered polar and Glazer-like rotational modes from longer wavelength antipolar modes and with non-Glazer-like AFD modes. In some cases non-Glazer-like isolated out-of-phase rotation of ZrO_6 octahedra is more unstable than Glazer $a^0a^0c^+$ and is either closely competitive with or more unstable than $a^0a^0c^-$ distortions. For PZT IV & V, we find *no* soft modes which result in Glazer type rotations. We find that some soft modes can give rise to distortions characteristic of more than one order parameter. It is found that in PZT IV, V and VI that FE order can appear simultaneously with antipolar Pb displacements. PZO, PHO and all PZT arrangements have long wavelength soft modes displaying a dual antipolar/AFD character. It is possible that such distortions are competitive in PZT IV suggesting complex local minima rivalling the softer FE distortion. Given the long wavelengths associated with these modes, there are a large number of participating atoms. It can then become costly to study their behaviour with conventional plane wave based DFT due to well known scaling issues. Accurate first principles simulations of these systems will then require large scale electronic structure methods [4].

The applicability of the VCA as a substitute for the supercell method has been investigated. Whilst the dispersion looks strikingly similar to that of PZT I, we find that the species specific character is considerably different. The alchemical Ti/Zr atom does not play a role in the lattice dynamics but rather is a site inert to displacement. Crucially, the softest Glazer type rotational modes have a different classification in the VCA becoming $a^-b^-c^-$ & $a^+b^+c^+$ as opposed to $a^0a^0c^-$ & $a^0a^0c^+$ like found in other PZT supercells and end members PTO & PZO. This quantitatively displays the inability of the VCA to represent local structural distortions.

Motivated by the appearance of long wavelength dynamical instabilities in PZO and PZT 50/50, we checked if these long wavelength modes were a shared characteristic of PHO. We studied the phonon dispersions of the cubic $Pm\bar{3}m$ and orthorhombic AFE $Pbam$ phases finding that PZO and PHO behaved *very* similarly. Notably, PZO and PHO shared the same instabilities (by character) in the $Pm\bar{3}m$ phase, but soft modes in PZO were more unstable. This results in the modes defining the AFE phases having a larger amplitude in PZO than PHO; they are isostructural in symmetry but not by distortion magnitude. Most remarkably, the phonon dispersions of the purported $Pbam$ AFE ground state, for both materials, were found to be dynamically unstable. The eigenvectors of the unstable modes describe an 80-atom $Pnma$ phase lower in energy than $Pbam$. Phonon analysis of this phase for PZO shows that, unlike $Pbam$, it is likely dynamically stable. While we cannot unequivocally declare that this is the ground state, from the perspective of DFT, $Pbam$ certainly isn't.

5 | Pseudoatomic Orbitals: Electronic and Structural Accuracy

Chapter abstract

A growing number of perovskite oxides are now known to become susceptible to structural distortions increasingly incommensurate with their parent cubic structures [43, 304, 305, 337]. From an *ab initio* simulation perspective, this requires accurate calculations including many thousands of atoms; a task beyond the remit of conventional plane wave-based density functional theory (DFT). We suggest that this void can be filled using the methodology implemented in the large scale DFT code, CONQUEST, using a local pseudoatomic orbital (PAO) basis. We begin by studying the structural accuracy (equilibrium volumes and bulk moduli) of the default basis sets compared with plane wave calculations using the same pseudopotentials. We survey a selection of important materials (*not* limited to the perovskite oxides) finding that modestly sized basis sets can reproduce plane wave accuracy for these properties to a high fidelity. Comparing two techniques for the generation of PAOs: the *equal energies* (EE) and *equal radii* (ER) constructions, we find that the latter slightly outperformed the former for these tests. Taking forward the ER construction, we further study the accuracy of this basis for a selection of perovskite oxides relevant to this thesis. We treat in detail the most fundamental quantity to DFT: the charge density $n(\mathbf{r})$ itself. An accurate description of $n(\mathbf{r})$ is vital for the perovskite FEs due to the crucial role played by short range restoring forces (characterised by bond covalency) and long range coulomb forces as suggested by the soft mode theory of Cochran and Anderson [1, 2, 52]. Comparing once more with plane waves and the same pseudopotentials, we analyse charge density differences and Bader partitioned charge assignments; matching PAO basis set sizes to calculations with plane wave cutoffs providing the same electronic and energetic accuracy. Finally, we study the amplitudes of condensed soft modes in the low temperature FE and AFE phases of PTO and PZO. We find that the lions share of these properties are impressively described with the default PAOs, but care has to be taken for FE PTO where a small basis incorrectly describes the balancing act between short range restoring and long range Coulomb forces propagating to a large super-tetragonality error.

5.1 Introduction

The ABO_3 perovskite oxides are well known for hosting a vast and rich variety of physical phenomena. These include interfacial two-dimensional electron gases [338, 339], negative capacitance [88, 340], high-temperature superconductivity [341, 342] and many more. A number of these are linked to a plethora of responsible order parameters and their competition/coupling with one another [343, 344]. Ferroelectric, ferromagnetic antiferroelectric & antiferromagnetic order are all commonplace in the perovskite oxides as well as antiferrodistortions (rotation of the BO_6 octahedra) and Jahn-Teller distortions. Some of these features are known to coexist with one another giving rise to the phenomena of multiferrocity [80]. In simulations, the onset of different competing order parameters can create a myriad of distinct local minima with similar energies. It is then of paramount importance that our simulation methodology produces accurate results such that we can distinguish them from one another in their energies but also accurately resolve their electronic & structural properties.

In addition to the requirement of high accuracy, the perovskite oxides present structural [43, 304, 337] and magnetic [345, 346] features over long wavelengths. From a simulation perspective, a supercell commensurate with these distortions could be large and require first principles simulations of thousands of atoms. For example, thin ferroelectric films are known to form *flux-closure domains* as a compensation mechanism for the depolarising field [32, 33]. The domain period of these films increases also with the depth of the film in question (the well known Kittel scaling law [176]) thus requiring simulations in excess of a thousand atoms. In the case of multiferroic $BiFeO_3$, the competition between various exchange interactions (described in [346]) manifests in the softening of a 64 nm non-collinear spin-cycloid [345, 346] and a unit cell of ~ 1000 atoms. Current simulations often bypass this fact and approximate this complex magnetic order as simple G-type antiferromagnetism. Studies of solid-solution families ($AB_xC_{1-x}O_3$, $(1-x)ABO_3 - xCDO_3$ and more) are popular in the field. Large supercell calculations can offer realistic experimental ordering in these alloys which can improve upon the accuracy of structural distortions predicted by smaller supercells and approximations like the virtual crystal approximation [43, 47, 48]. Further, longer wavelength dynamical instabilities are found to be competitive in the important piezoelectric solid solution $PbZr_{0.5}Ti_{0.5}O_3$ (PZT 50/50) requiring a large number of atoms to simulate the energetics [43]. Indeed, within the previous chapter, we found that such long wavelength distortions condense in the crystal structures of antiferroelectric $PbZrO_3$ and $PbHfO_3$ causing *even a single unit cell* to approach 100 atoms in size. Such long wavelength modulations are now expected to persist in other perovskites and a mechanism for their onset has been proposed [304]. The requirement for large supercell calculations is of course not limited to cases within the perovskite oxides. For example, large supercells are required for simulations of realistic doping (\sim parts-per-million) in semiconductor technologies, biological systems with or without solvent, compounds with dilute compositions and large scale defect

complexes such as dislocations.

Electronic structure calculations based on density functional theory (DFT) employing the plane wave pseudopotential method [347, 348] are known to achieve accurate results. This is in part due to the systematic and variational nature of the plane wave basis where increasing the number of basis functions is *guaranteed* to increase the level to which the total energy converges; free of empirical parameters. This method is not without its drawbacks. A plane wave by itself (the solution of the free electron [237]) bears little to no resemblance to the Kohn-Sham orbitals of the systems they are intended to represent. This is especially true for the localised 3d electrons of the transition metals, responsible for magnetic and orbital order. It is for this reason that many thousands of plane waves are required in the basis set expansion which can come at a large computational cost. Further, plane waves span the whole of the simulation cell which introduces wasteful grid calculations for systems including a vacuum region. These issues can be bypassed by replacing plane waves with physically intuitive local basis sets of pseudoatomic orbitals (PAOs) [6, 246–248, 349]. These are atomic-like orbitals for which the radial part is solved in the pseudopotential of each ionic species [249, 250]. PAOs are now regularly used in the *Siesta* [6], *OpenMX* [244], *ONETEP* [8], *FHI-AIMS*[†] [243] & *CONQUEST* [17] codes, the last of which is employed in this chapter. The construction and generation of such a basis is described in Section 5.2.3.

Our PAOs are designed with a cut-off in real space (where the basis function becomes zero) motivated by the desire to employ efficient sparse matrix algebra with high parallel efficiency [251]. Further, our formulation of DFT is based on the density matrix $\rho(\mathbf{r}, \mathbf{r}')$. Should we choose to truncate the range of this matrix (a requirement should we wish to use the linear scaling mode of operation), we are physically supported by the principle of near-sightedness; the assertion that the density matrix $\rho(\mathbf{r}, \mathbf{r}')$ decays to zero as $|\mathbf{r} - \mathbf{r}'| \rightarrow \infty$ [260]. Complete with a change in algorithm (described in Chapter 3, Section 3.4.6), this allows the well known $\mathcal{O}(N^3)$ scaling wall (where N is the number of atoms in the simulation) in standard DFT to be broken and replaced with a code which now scales as $\mathcal{O}(N)$. This method paves the way for full electronic structure calculations on systems of many thousands of atoms (or even millions [13]), well beyond what is possible with conventional plane wave methods. While the $\mathcal{O}(N)$ algorithm does allow for superior scaling, we find that for calculations involving a few thousand atoms (less than ≈ 4000) can be performed more quickly (and more accurately) through directly diagonalising the sparse Hamiltonian matrix. For less than a few hundred atoms, this diagonalisation can be performed on a primitive Hamiltonian with dimensions $N_{\text{PAO}} \times N_{\text{PAO}}$ (as we do in this chapter; N_{PAO} is the total number of PAOs used in the calculation) but for a few thousand atoms we must contract the basis set following the MSSF mode of operation discussed in Chapter 3, Section 3.4.5.

The accuracy of PAO basis sets has been reported in previous works [244, 247, 249, 250, 349–351] where structural and energetic properties have been discussed. Notably, none have

[†]*FHI-AIMS* typically uses the all-electron version of PAOs: numerical atomic orbitals (NAOs) [243].

reported on the effects to the most fundamental quantity in DFT; the charge density $n(\mathbf{r})$ itself. An accurate account of $n(\mathbf{r})$ is of high importance for the perovskite oxides. Not only because applications require it (like the simulation of 2DEGs [90]) but because of the possible ramifications for the soft mode theory of ferroelectricity [1, 2, 52]. That is, the ferroelectric transition is governed by a zone centre dynamical instability driven by the competition of short range covalent forces (preferring cubic symmetry) and long range Coulomb forces (favouring the ferroelectric state). The charge density $n(\mathbf{r})$ (and its derived quantities) is clearly a probe of bond covalency [352, 353] whilst electron-electron Coulomb terms feature explicit dependence on $n(\mathbf{r})$ in the calculation of the Hartree potential [202].

It is the purpose of this chapter to quantify the performance of PAOs versus plane waves using calculations with the same pseudopotential. We begin by comparing the two default PAO construction mechanisms implemented in the CONQUEST PAO generator code: the equal energies (EE) and equal radii (ER) constructions. We calculate the zero pressure equilibrium volumes and bulk moduli for these two methods and compare them to the plane wave result[†]. For this comparison, we use a broad selection of material test cases: elemental semiconductors (C, Si and Ge), Binary oxides (two SiO₂ structures: an α -quartz polymorph and stishovite, and, MgO) and cubic perovskite oxides (PTO, PZO and SrTiO₃, STO).

Taking forward only the ER construction (as we will later learn, this is marginally more successful for the structural properties), we perform a detailed comparison of the ground state charge densities and the order parameters controlling ferroelectric & antiferroelectric order in the perovskite oxides. We do so by considering PTO, PZO (in both their high temperature cubic and low temperature ferroelectric/antiferroelectric phases) and two cubic supercell arrangements of PZT 50/50. At low temperatures, PTO is a $P4mm$ ferroelectric formed from the softening of a single zone centre lattice mode (irrep) Γ_4^- [295]. In contrast, low temperature PZO is *thought to be* a $Pbam$ antiferroelectric described by a complex multi-mode picture comprised primarily of R_4^+ , Σ_2 & S_4 modes [85, 297]. A small part of the distortion is also due to the softening of R_5^+ , X_3^- & M_5^- (and, as we learnt from Chapter 4, perhaps also T_4 , Λ_3 , Λ_1 , T_2 and Δ_5 !) lattice modes [85, 297]. We quantify the amplitudes of each individual lattice mode and strain mode in the phase transitions of both perovskites as well determining the associated energetics for each of the considered PAO basis sets. Since the energy differences between structural polymorphs in the perovskite oxides are generally small (a few meV/atom), this is a *strict* test for the accuracy of PAOs.

The remainder of this chapter is now organized as follows. Within Section 5.2.1, we outline the general simulation method for both the plane wave and PAO DFT calculations and describe the crystal structures used in the study. Then, in Section 5.2.2, we outline the metrics we use

[†]Calculations presented in Section 5.3.1 (pertaining to equilibrium volumes and bulk moduli) were part of a collaborative project with many participants. The author was responsible for plane wave calculations of Si, Ge, C, STO, PTO and PZO and for PAO calculations of PZO. Other content was performed by the remaining authors of [51] and full credit is owed to them.

in comparison of PAO and PW calculations. In Section 5.2.3 we describe the method for the generation of the PAO basis sets and the details of the default basis sets used in this chapter. Section 5.3.1 discusses the accuracy of structural parameters; comparing the EE and ER PAO constructions. Past this point, our focus changes to treating only the perovskite oxides using the default ER PAOs. Section 5.3.2 provides charge density difference analysis between PAO calculations and plane waves while Section 5.3.3 presents Bader analysis of the ionic charges, volumes and average densities. In Section 5.3.4 we compare the amplitudes of the soft mode distortions responsible for the ferroelectric and antiferroelectric phase transitions in PTO & PZO including the energetics associated with crucial displacive modes. We closely examine the energetics over the phase transition paths by steadily increasing mode amplitudes until a maximal value, then, cumulatively add the remaining important modes. In Section 5.3.5 we discuss a simple method for optimising PAO basis sets when the defaults do not provide sufficient accuracy. We show the successful application of this method for describing ferroelectric PTO. We conclude this chapter in Section 5.4 with a broad overview of our findings. This includes a discussion of the impact this chapter has on the topic of local basis sets and the promise of accurate and large scale electronic structure calculations on the perovskite oxides.

5.2 Theoretical method

5.2.1 Simulation details

Calculations are performed using plane wave and local orbital DFT. Calculations using plane waves in Section 5.3.1 are performed with the PWSCF code (v6.4.1; part of the Quantum Espresso suite [354]) whilst those in the remaining sections are performed with the ABINIT code [310, 311] (v8.10.2). Local orbital calculations utilising PAOs are carried out using the CONQUEST code (v1.0) [7, 17, 355] with the direct diagonalisation of the primitive Hamiltonian matrix of dimensions $N_{\text{PAO}} \times N_{\text{PAO}}$. All three[†] codes are able to use the same norm-conserving pseudopotentials as produced by ONCVSP [233] (v3.3.1) where input parameters were taken from the library (v0.4) on the PseudoDojo website [230]. This library is known for its high accuracy results versus other pseudopotentials, projector augmented wave methods & all-electron results as characterised in the well known DFT *delta study* [348]. These pseudopotentials are scalar-relativistic and include partial core corrections. The orbitals treated as valence, for each species, can be found in Table 5.1. Exchange & correlation functionals are taken from the Libxc [218] (v3.0.0) library. For perovskite oxide and elemental semiconductor calculations we use the PBESol functional [356] while calculations of the binary oxides use the original and unmodified PBE functional [219]. While there is little difference between these

[†]While it is not ideal to use two different plane wave codes for the comparison to PAOs, in testing, we find that PWSCF and ABINIT produce *indistinguishable results* for the lattice constants of PTO, PZO and STO in the cubic phase. While this is to be expected since identical pseudopotentials are used, this level of reproducibility is laudable.

Table 5.1: The orbitals treated as valence by the pseudopotentials used in this work. Those orbitals in bold font are treated as semi-core in the PAO calculations (i.e, are described by only a single ζ regardless of the basis set size) and those which are underlined are *not* present in the pseudopotential but are treated as polarisation states in the PAO calculations.

Pb	5d, 6s, 6p, <u>6d</u>	Ge	3d , 4s, 4p, <u>4p</u>
Zr	4s , 4p, 5s, 4d, <u>5p</u>	C	2s, 2p, <u>3d</u>
Ti	3s , 3p, 4s, 3d, <u>4p</u>	Si	3s, 3p, <u>3d</u>
Sr	4s , 4p, 5s, <u>5p</u>	O	2s, 2p, <u>3d</u>
Mg	2s , 2p , 3s, <u>3p</u>		

functionals for many applications, PBESol is known to perform better than PBE for the structural properties of most solids, especially the perovskite oxides [171].

In Section 5.3.1 we consider six basis sets sizes in total for each of the test cases. That is, for the EE and ER constructions we treat the single- ζ plus polarisation (SZP), double- ζ plus polarisation (DZP) and triple- ζ plus triple-polarisation (TZTP) basis sets. Within the CONQUEST PAO generation code, these are the default `small`, `medium` and `large` basis sets respectively. In Sections 5.3.2, 5.3.3 and 5.3.4 we consider just three basis sets under the ER construction: SZP, double- ζ plus double-polarisation (DZDP) and TZTP. This approach allows us to study the effect of systematically adding an extra ζ per angular momentum channel; which for this section will allow us to more precisely assign where improvements to the electronic structure originate. We use different versions of the CONQUEST PAO generator code in this Chapter. We use `v1.01` in Section 5.3.1, `v1.02` in Sections 5.3.2, 5.3.3 and 5.3.4 and the beta version in Section 5.3.5. The basis sets and details of their generation are described fully in Section 5.2.3.

The different crystal structures treated in this study are shown in Figure 5.1. For the cubic $Pm\bar{3}m$ perovskites, $P4mm$ PTO and the elemental semiconductors, we use $9 \times 9 \times 9$ Monkhorst-pack [227] mesh for reciprocal space integrals. For Orthorhombic PZO and cubic PZT 50/50 arrangements we use a $7 \times 3 \times 5$ & $5 \times 5 \times 5$ mesh respectively. For α -quartz, stishovite and MgO we use $3 \times 2 \times 3$, $3 \times 3 \times 6$ and $4 \times 4 \times 4$ meshes, respectively. For calculations with plane waves, we use a 40Ha cutoff for all calculations apart from for MgO where a 60Ha cutoff was used. For calculations with PAOs, integrations must take place on a real space grid. A 300Ha cutoff grid was used for the perovskites, a 260Ha cutoff was used for the elemental semiconductors, stishovite/ α -quartz used a 200Ha cutoff and MgO used a 260Ha cutoff. All of these parameters were chosen to adequately converge the equilibrium volumes and bulk moduli of each test case. When optimised structures are needed, we relax the ionic positions until the magnitude of the force on every atom is less than 5×10^{-3} eV/Å. Stresses are relaxed until the magnitude of all elements of the Cartesian stress tensor fall below 1×10^{-4} GPa.

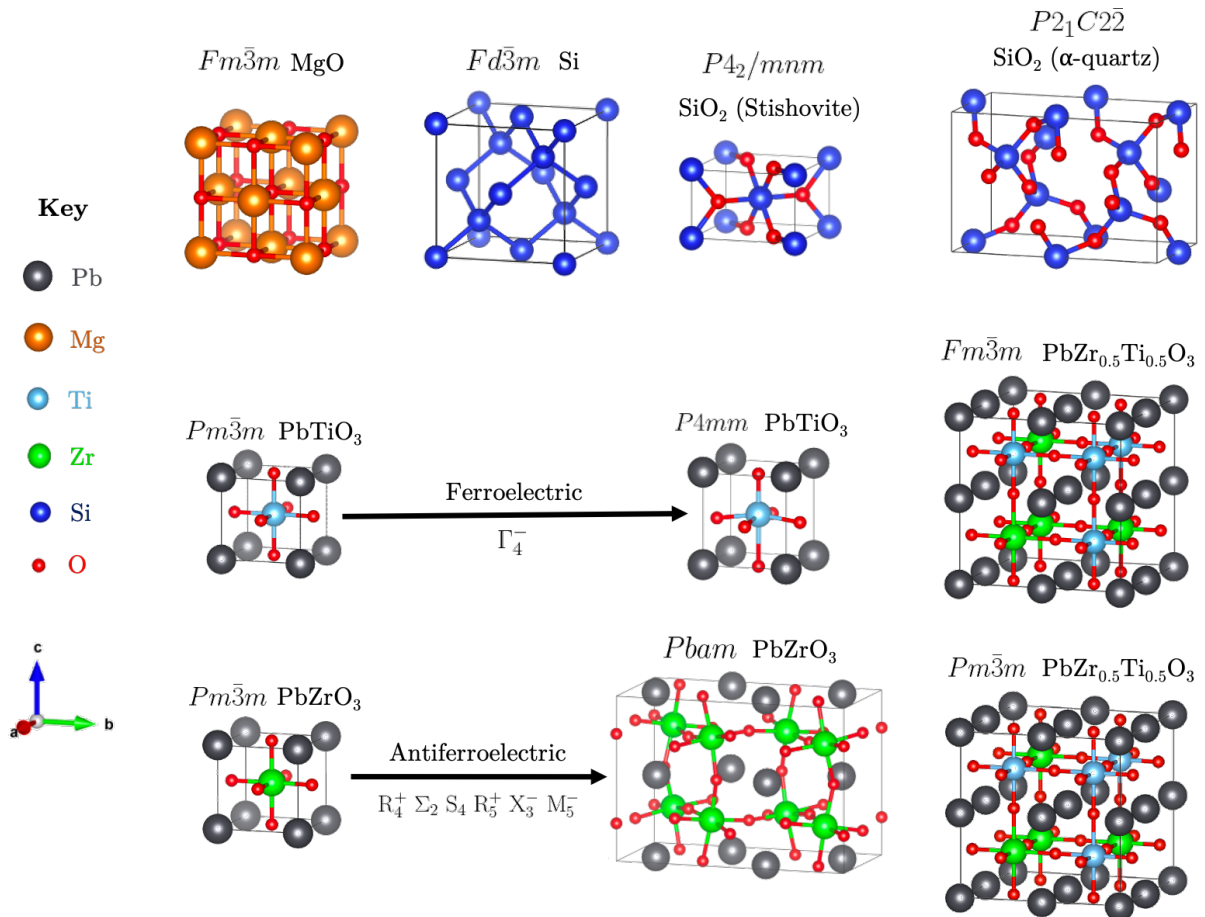


Figure 5.1: The crystal structures for all of the test cases in this chapter. We do not explicitly show C or Ge since they are isostructural with Si in this work. Similarly, we do not show STO since one only needs to exchange the A site of PTO for Sr. For PTO and PZO, we also illustrate the paraelectric to ferroelectric and paraelectric to antiferroelectric phase transitions, respectively. The responsible displacive soft modes for the transitions are also indicated.

5.2.2 Comparative metrics

To calculate the equilibrium volumes and bulk moduli in Section 5.3.1, we evenly scan volumes $V \pm 2\%$ of the equilibrium volume V_0 with static point energy calculations for the given test case. We use a total number of points which converges the bulk modulus B_0 of the Birch-Murnaghan [357] equation of state

$$E(V) = E_0 + \frac{9V_0B_0}{16} \left\{ \left[\left(\frac{V_0}{V} \right)^{\frac{2}{3}} - 1 \right]^3 B'_0 + \left[\left(\frac{V_0}{V} \right)^{\frac{2}{3}} - 1 \right]^2 \left[6 - 4 \left(\frac{V_0}{V} \right)^{\frac{2}{3}} \right] \right\} \quad (5.1)$$

for zero pressure energy E_0 and bulk modulus derivative B'_0 . Using the sampled $E(V)$, we perform a least squares fit to Equation 5.1 to extract V_0 and B_0 .

For calculations assessing the charge density (in Sections 5.3.2 and 5.3.3), we use a finer charge density grid with $100 \times 100 \times 100$ grid points/ABO₃ formula unit. For the orthorhombic $\sqrt{2}a \times 2\sqrt{2}a \times 2a$ PZO unit cell (where a is the $Pm\bar{3}m$ lattice constant), we use $150 \times 300 \times 200$ grid points. Each of these finer charge density calculations, for each basis, are performed using the optimised plane wave structure of each crystal. In order to assign ionic charges, volumes and average ionic densities, we use the Bader partitioning scheme as implemented in the `bader` code [358–361] (v1.03). This code partitions individual atoms in crystals using the zero-flux surface of the charge density. This is a 2-D surface for which the charge density is at a minimum perpendicular to the surface. We note that whilst there is no unequivocal definition for the assignment of ionic charge, we choose the Bader definition since it derives *only* from $n(\mathbf{r})$ thus introducing no new variables to our analysis. We define also a total integrated electronic error designed to quantify the level of disagreement in $n(\mathbf{r})$ for the plane wave and PAO calculations. This is defined by the integral

$$N_{\text{error}}^e = \int |n_{\text{PAO}}(\mathbf{r}) - n_{\text{PW}}(\mathbf{r})| d\mathbf{r} \quad (5.2)$$

for plane wave/PAO electronic charge density $n_{\text{PW}}(\mathbf{r})/n_{\text{PAO}}(\mathbf{r})$.

In Section 5.3.4 we assess the amplitudes of individual soft lattice modes in the phase transitions of PTO and PZO. To do so, we use the group symmetry analysis software made available in the ISOTROPY suite, in particular ISODISTORT [321] (6.7.0). This code is able to perform mode decompositional analysis when provided with the cubic $Pm\bar{3}m$ parent structures and the distorted daughter structures of PTO and PZO. In our calculations, the parent structures are the relaxed cubic $Pm\bar{3}m$ crystals for each basis set and daughter structures are the relaxed ferroelectric tetragonal PTO and antiferroelectric orthorhombic PZO cells for each basis. The soft mode amplitudes can then be extracted from the ionic displacements present in the daughter structures compared with the parents.

5.2.3 Generation of pseudoatomic orbitals

PAOs are a local basis with a simple construction of a radial function $R_{nl\zeta}(\mathbf{r})$ multiplied by an appropriate spherical harmonic $Y_m^l(\hat{\mathbf{r}})$

$$\chi_{nlm\zeta}(\mathbf{r}) = R_{nl\zeta}(\mathbf{r})Y_m^l(\hat{\mathbf{r}}) \quad (5.3)$$

for principal quantum number n , orbital angular momentum l and projection of orbital angular momentum m . The last subscript ζ is related to the number of functions per l -channel. Increasing the number of ζ 's adds flexibility to basis set and improves the accuracy of the total energy in a non-systematic manner. Since the spherical harmonics are analytic functions, the responsibility of the PAO generation code is to solve for the radial functions only. These radial functions are extracted as the eigenstates of the isolated pseudoatom confined within a spherical potential. While the confining potential can take on different forms [249], we use the hard confinement scheme first proposed by Sankey [248]. There is a question in this process with regards to how strongly each orbital should be confined. The approach used by the *Siesta* code is the concept uniform of energy shifts $\Delta\epsilon_l$; allowing for a consistent definition of confinement for all angular momentum channels across all PAOs. While our approach stems from this, by default, the CONQUEST PAO generator code (v1.02) specifies an energy shift for each PAO, $\Delta\epsilon_{nl\zeta}$, and solves for each $R_{nl\zeta}(r)$ explicitly as an eigenstate of the radial Schrödinger equation of the confined pseudoatom. That is,

$$\left(-\frac{1}{2r} \frac{d}{dr} r + \frac{l(l+1)}{2r^2} + V_l(r) \right) R_{nl\zeta}(r) = (\epsilon_{nl\zeta} + \Delta\epsilon_{nl\zeta}) R_{nl\zeta}(r). \quad (5.4)$$

We have implemented two schemes within the CONQUEST PAO generator code (v1.02) for setting $\Delta\epsilon_{nl\zeta}$. The first approach is the EE construction. Here, all radial functions of the same ζ share an energy shift. To add flexibility to multiple- ζ basis sets, we apply a large energy shift to one ζ , creating a highly confined function whilst others have progressively less confinement. The second approach is the ER construction. Here, we take the average r_c obtained for the same ζ from the EE construction. The radial functions are then solved once more using this average cutoff for all of the orbitals for a given ζ . This way, each ζ shares a cutoff radius. We use the default setting, applying energy shifts of 2 eV, 0.2 eV and 0.02 eV for $\zeta = 1, 2$ and 3, respectively. While these shifts are a heuristic, for most systems, they give three relatively evenly spaced confinement radii. Polarisation functions are solved in one of two ways. For equation of state fits in Section 5.3.1, species with semicore states use the explicit $l + 1$ excited solutions of the radial Schrödinger equation while those without semicore states use a perturbative scheme; considering the effect of a finite local electric field acting on the highest valence state [362]. In contrast, Section 5.3.2 uses the perturbative scheme for all atomic species. We note that the approach for evaluating polarisation states only differs between the two sections as perturbative

polarisation for species with semicore states has only recently been implemented in the PAO generation code (Section 5.3.1 predates this implementation). By default, all polarisation states share r_c with the highest occupied valence PAOs.

All of the cutoff radii for the default basis sets used in this chapter are displayed in Table 5.2. It can be seen that the ER method produces slightly more compressed functions than the EE method. These are generally more efficient as the Hamiltonian and overlap matrices become sparser with smaller r_c . We emphasize once more that the radial functions used in this chapter are the *defaults* of the PAO generator code. Any results here then should be regarded as *out-of-the-box* performance because in principle, it is possible to fit/optimize these functions for specific situations. For example, the approach made by the `Siesta` code is a downhill simplex minimisation of the total energy carried out on the material system to be studied with respect to the parameters of the PAO generation mechanism [249]. Another approach optimises the binding energy curve of dimers [363]. We discuss our own approach to optimisation in Section 5.3.5. Whilst these methods can produce good results, the possibility of many local minima in the optimisation is an issue as is the overfitting of smaller PAO bases such that their transferability is diminished. In this respect, a large basis set of default (and more general) PAOs *may be* more transferable.

Table 5.2: The cutoff radii r_c for the default PAOs used in this work under the equal energies and equal radii constructions for the PBE and PBESol functionals. Those table entries left blank appear for orbitals treated as semi-core (being described by only a single ζ).

		$r_c [a_0]$ Equal Energies (EE)			$r_c [a_0]$ Equal Radii (ER)		
		$\zeta = 1$	$\zeta = 2$	$\zeta = 3$	$\zeta = 1$	$\zeta = 2$	$\zeta = 3$
PBESol							
Pb	5d	4.46	3.51	2.61	6.85	5.34	3.78
	6s	6.54	5.21	3.87	6.85	5.34	3.78
	6p	9.57	7.19	4.85	6.85	5.34	3.78
	6d	9.57	7.19	4.85	6.85	5.34	3.78
Ti	3s	3.32	-	-	3.32	-	-
	3p	3.79	-	-	3.79	-	-
	4s	9.49	7.30	5.04	8.23	6.18	4.07
	3d	6.88	4.98	3.06	8.23	6.18	4.07
O	4p	6.88	4.98	3.06	8.23	6.18	4.07
	2s	4.31	3.40	2.46	4.86	3.74	2.58
	2p	5.47	4.06	2.71	4.86	3.74	2.58
Sr	3d	5.47	4.06	2.71	4.86	3.74	2.58
	4s	4.13	-	-	4.13	-	-

	4p	4.94	3.94	2.96	7.95	6.19	4.38
	5s	10.98	8.34	5.83	7.95	6.19	4.38
	5p	10.98	8.34	5.83	7.95	6.19	4.38
Zr	4s	3.52	-	-	3.52	-	-
	4p	4.06	-	-	4.06	-	-
	5s	9.04	7.21	5.28	8.22	6.39	4.52
	4d	7.38	5.54	3.78	8.22	6.39	4.52
	5p	7.38	5.54	3.78	8.22	6.39	4.52
Si	3s	6.55	5.16	3.69	7.65	5.81	4.02
	3p	8.62	6.47	4.31	7.65	5.81	4.02
	3d	8.62	6.47	4.31	7.65	5.81	4.02
Ge	3d	3.43	-	-	3.43	-	-
	4s	6.37	5.02	3.64	7.62	5.79	4.00
	4p	8.79	6.60	4.40	7.62	5.79	4.00
	4d	8.79	6.60	4.40	7.62	5.79	4.00
C	2s	5.48	4.26	3.05	6.25	4.69	3.17
	2p	6.96	5.16	3.28	6.25	4.69	3.17
	3d	6.96	5.16	3.28	6.25	4.69	3.17
PBE							
Si	3s	6.55	5.16	3.69	7.65	5.81	4.02
	3p	8.72	6.47	4.31	7.65	5.81	4.02
	3d	8.72	6.47	4.31	7.65	5.81	4.02
O	2s	4.31	3.35	2.46	4.91	3.74	2.58
	2p	5.47	4.11	2.67	4.91	3.74	2.58
	3d	5.47	4.11	2.67	4.91	3.74	2.58
Mg	2s	2.77	-	-	2.77	-	-
	2p	3.16	-	-	3.16	-	-
	3s	9.03	6.86	4.69	9.03	6.86	4.69
	3p	9.03	6.86	4.69	9.03	6.86	4.69

5.3 Results

5.3.1 Equilibrium volumes and bulk moduli

Table 5.3 details the equilibrium volumes and bulk moduli for all of the test materials calculated with plane waves and the default EE and ER PAOs. Before remarking on individual cases, it can be seen that in general, the EE and ER methods perform rather similarly in comparison to

plane waves for this metric. Default SZP basis sets offer between $\approx 2 - 5\%$ errors in equilibrium volumes (and $\approx 3\times$ less for lattice constants) and $\approx 1 - 11\%$ for bulk moduli (where this range is expanded due to the poor performance of B_0 for the SZP Ge basis sets). For DZP, these errors shrink to $\approx 1.5\%$ for equilibrium volumes and to $\approx 2\%$ for most bulk moduli with the exception of the SiO_2 polymorphs which still feature $\approx 10\%$ errors. For the default TZTP basis sets, we now see errors in equilibrium volumes falling in most cases below $\approx 1\%$ and bulk moduli accuracies between $\approx 1-2\%$ (with the notable exceptions of TZTP (ER) for STO and PZO which perform poorly).

Table 5.3: The equilibrium volumes V_0 and bulk moduli B_0 obtained from least-squares fits to the Birch Murnaghan equation of state [357] (Equation 5.1). EE indicates results from the equal energies PAO construction while ER indicates results from the equal radii method. PW is the converged plane wave result.

	PTO		PZO		STO	
	$V_0 [\text{\AA}^3]$	$B_0 [\text{GPa}]$	$V_0 [\text{\AA}^3]$	$B_0 [\text{GPa}]$	$V_0 [\text{\AA}^3]$	$B_0 [\text{GPa}]$
PW	60.14	191.1	70.98	169.7	58.79	186.4
SZP (EE)	61.22	183.0	73.35	163.5	60.76	182.6
DZP (EE)	61.06	186.2	71.84	169.4	60.52	180.0
TZTP (EE)	60.83	188.8	71.78	172.1	60.08	183.4
SZP (ER)	61.66	191.1	72.28	189.3	60.99	170.0
DZP (ER)	60.69	190.9	71.68	177.6	60.15	180.7
TZTP (ER)	60.2	190.3	71.22	158.0	59.67	169.9
	Si		C		Ge	
PW	160.19	93.28	45.04	449.3	182.86	67.47
SZP (EE)	169.39	93.28	46.66	425.4	189.22	59.73
DZP (EE)	161.52	92.58	45.65	441.1	185.58	65.73
TZTP (EE)	160.90	91.79	45.31	448.3	183.44	66.75
SZP (ER)	170.12	82.81	46.77	415.1	191.60	57.49
DZP (ER)	162.59	90.96	45.61	444.1	184.41	68.70
TZTP (ER)	160.72	91.70	45.19	452.9	184.22	64.99
	MgO		SiO_2 (Stishovite)		SiO_2 (α -quartz)	
PW	76.92	149.1	47.89	301.0	210.5	195.3
SZP (EE)	80.31	149.7	49.82	260.4	220.8	165.9
DZP (EE)	78.57	141.4	49.09	278.4	215.4	176.3
TZTP (EE)	78.50	148.4	48.26	291.8	212.6	190.9
SZP (ER)	80.32	137.2	49.95	283.9	222.0	160.4

DZP (ER)	78.49	141.5	49.16	289.2	215.6	177.1
TZTP (ER)	78.51	148.3	48.25	295.0	213.0	193.5

It can be seen in more cases than not, that the ER construction performs marginally better the EE construction for these tests. This is especially true for the tested perovskite oxides where the equilibrium volumes are *always* better described by ER PAOs. The performance for the elemental semiconductors is similar to the perovskites with the notable exception of Ge which for the SZP basis shows strong disagreements with the plane wave results. We show $E(V)$ for the ER PAOs in Figure 5.2. It can be seen from this figure that despite the large error in B_0 for the SZP basis, close to the equilibrium volume, it still very well matches the plane wave result. The performance begins to be poor when we reach high pressures for this basis.

A challenging test for the default PAOs is to compare the relative stabilities of the two SiO_2 polymorphs: equilibrium-pressure α -quartz and high pressure stishovite. Since stishovite has been artificially stabilised at equilibrium pressure, the correct ordering of the relative stabilities should show α -quartz having a lower energy than stishovite. Between these two polymorphs, the coordination Si also changes from four to six; the PAOs must be flexible to a new coordination environment. We compare the energy difference per formula unit (FU) for each basis set to the plane wave result (-0.28 eV/FU). The TZTP basis performs well (-0.20 eV/FU for EE and -0.22 eV/FU for ER). The DZP basis sets using perturbative polarisation (the default setting) gives the correct ordering (-0.08 eV/FU for EE, and -0.05 eV/FU for ER) with a less accurate magnitude. Generating the 3d polarisation orbitals simply as excited eigenstates of the confined pseudoatom gives the incorrect ordering for DZP (+0.15 eV/FU for EE and +0.19 eV/FU for ER) but the correct ordering for SZP (-1.46 eV/FU for EE and -0.52 eV/FU for ER). Testing further, we add a second perturbative polarisation state to the DZP basis (now DZDP), which now performs similarly to TZTP (-0.19 eV/unit for equal EE, and -0.20 eV/unit for ER). Clearly comparisons of stability of structures require radial flexibility in all angular momentum channels, and we would recommend using at least DZDP when considering this kind of problem with the default basis sets. For structural properties of the individual phases, however, the performance of the default DZP basis sets is reasonable, though not as accurate as for the elemental semiconductors, PTO, PZO and MgO. We see that the ER method also performs better not only for many of the structural properties, but also for the energetics. Indeed, in general, the total energy is lower for the ER basis sets compared to EE. It is also clear that perturbative polarisation states perform better than the excited eigenstates for the energetics. It is for this reason that Sections 5.3.2 and 5.3.3 use the ER construction with perturbative polarisation states.

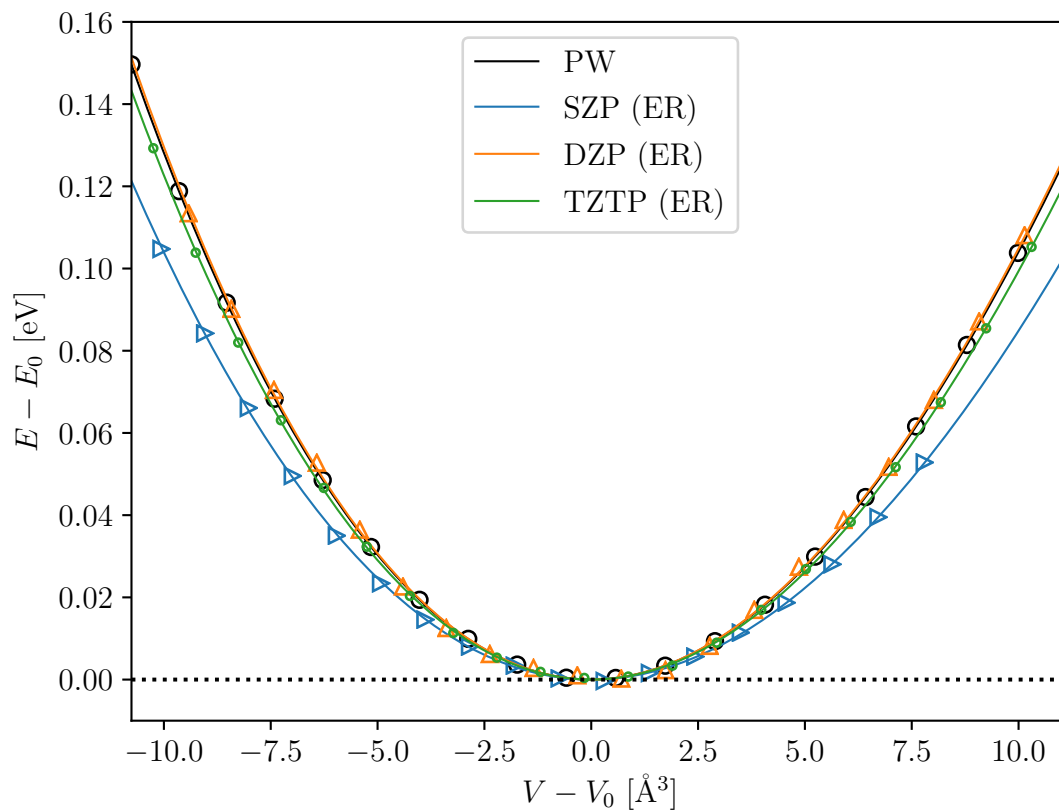


Figure 5.2: The Birch-Murnaghan equations of state for $Fd\bar{3}m$ Ge using plane waves (PW) and the default ER PAOs. This test case shows the *worst* agreement with plane waves. Each curve is shifted to the origin by the equilibrium energy and volume as this allows for clearer comparison of the bulk modulus.

	$N_{\text{error}}^e/\text{ABO}_3$ unit (44 electrons) [e]					
	$Pm\bar{3}m$ PTO	$Pm\bar{3}m$ PZO	$P4mm$ PTO	$Pbam$ PZO	$Fm\bar{3}m$ PZT 50/50	$Pm\bar{3}m$ PZT 50/50
SZP	0.719	0.768	0.730	0.772	0.739	0.743
DZDP	0.358	0.382	0.380	0.397	0.369	0.371
TZTP	0.246	0.276	0.257	0.282	0.257	0.259

Table 5.4: The total integrated electronic error N_{error}^e (normalized per 5-atom ABO_3 perovskite unit, containing 44 electrons) as defined in Equation 5.2 for the SZP, DZDP & TZTP PAO basis sets for each of the considered structures in Figure 5.1.

5.3.2 Charge density differences

Figures 5.3, 5.4 & 5.5 show the charge density differences $\Delta n(\mathbf{r}) = n_{\text{PAO}}(\mathbf{r}) - n_{\text{PW}}(\mathbf{r})$ for each PAO basis set and each crystal structure shown in the lowest two rows of Figure 5.1 (PTO, PZO and PZT 50/50). We show this quantity using both coloured isosurfaces and slices through chosen planes which are described in each figure. Before discussing the details of each case, we discuss some striking features shared by all cases. The range of $\Delta n(\mathbf{r})$ is similar between all crystals, extremal at around $0.25 \text{ electrons}/\text{\AA}^3$ with a very narrow region of negative $\Delta n(\mathbf{r})$, minimal at $\approx 0.07 \text{ electrons}/\text{\AA}^3$. Even when considering these extrema, their magnitudes are $\approx 50\times$ smaller than the extrema of any given $n(\mathbf{r})$. This is even more apparent when considering the mean absolute of $\Delta n(\mathbf{r})$ which is $\approx 0.01 \text{ electrons}/\text{\AA}^3$ for SZP falling to $\approx 0.004 \text{ electrons}/\text{\AA}^3$ by TZTP. This shows that even at first glance for all bases the electronic error versus plane waves is small. It is also clear that these regions of maximal $\Delta n(\mathbf{r})$ are small in volume and isolated close to each ionic site, especially the O anions. Further, error is almost vanishing proximal to the Pb cations and Pb-O bonds suggesting this chemistry is well reproduced from the plane wave calculations. Other than the aforementioned sites, $\Delta n(\mathbf{r}) \approx 0$ for the vast majority of the simulation box. Since all calculations are normalised to the same number of electrons (44/ ABO_3 unit) the localised surplus of electrons close to ionic sites *has to* result in an electron deficiency elsewhere. This manifests itself in two areas. Firstly, a small negative $\Delta n(\mathbf{r})$ appears in bonding areas, especially those characterising the BO_6 octahedra. Secondly, the remaining $\Delta n(\mathbf{r})$ spreads itself out as an even smaller negative background over the rest of the simulation box. Finally, we see that the effect of increasing the size of the PAO basis from SZP to DZDP results in a large reduction in $\Delta n(\mathbf{r})$. This effect is most clear when we examine the shrinking volumes enclosed by the isosurfaces present on any one of Figures 5.3, 5.4 or 5.5. This effect can also be seen as we increase the basis set size from DZDP to TZTP but is less drastic.

Table 5.4 shows the total integrated electronic error as defined in Equation 5.2. Much like the range of $\Delta n(\mathbf{r})$, the magnitude is similar across all crystals and decreases as we increase the basis set size. This improvement is once again greater between the SZP & DZDP basis sets as

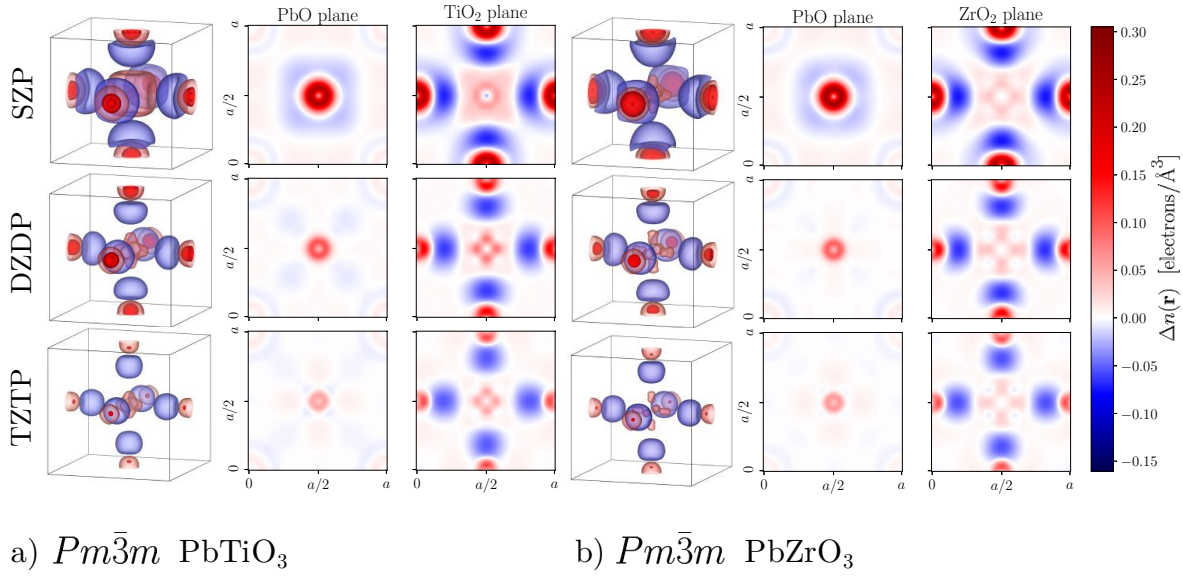


Figure 5.3: The charge density difference between PAO calculations and plane waves for increasing PAO basis set size for cubic PTO (a) and cubic PZO (b). For each case, we display the full 3d isosurfaces and slices through the PbO and BO_2 planes. Isosurfaces are plotted at the +0.10 (dark red), +0.020 (light red) and -0.020 (blue) electrons/ \AA^3 levels.

compared to the drop in N_{error}^e between DZDP & TZTP. What is notable, however, is that there is a noticeable (but small) gain in N_{error}^e as we break $Pm\bar{3}m$ symmetry for cubic PTO & PZO to the distorted $P4mm$ & $Pbam$ phases respectively. This gain is comparable for both compounds. This effect can be explained by a slight rigidity for each PAO local to sites which become low symmetry. The basis must now adapt to the distorted environment in a more asymmetrical manner which doesn't perform as well as the same process at a higher symmetry site. This effect can be seen clearly in Figure 5.4a when examining the TiO_2 panel for the SZP basis set. Close to the O 1b Wyckoff site we see firstly that $\Delta n(\mathbf{r})$ is now asymmetrical in the plane perpendicular to the pseudocubic c-axis as compared to the same panel in Figure 5.3a where $\Delta n(\mathbf{r})$ is symmetrical. We see also the $\Delta n(\mathbf{r})$ is now greater (and extremal) in the upper region of the O 1b site which is a primary source of the increase in the total integrated error as we break cubic symmetry. We see for the two PZT 50/50 configurations that N_{error}^e is comparable since both arrangements have a similar, cubic symmetry. It is also interesting to point out that the mean of N_{error}^e between cubic PTO & PZO for any basis *very closely* mirrors the value of N_{error}^e for either of the PZT 50/50 configurations. This suggests that the electronic structure local to PTO & PZO units in the alloy is similar to that of the pure compound. This is supported further when examining the BO_2 panels of Figure 5.5 where local PTO & PZO units are easily discernible when compared with the BO_2 panels of Figure 5.3. This suggests that approximations (like the virtual crystal approximation) designed to circumvent the need for large supercell calculations of alloys are unable to accurately account for local electronic structure. This is an explanation for the origin of the failings of the VCA pointed out in Chapter 4.

Figure 5.6a quantifies N_{error}^e for $Pm\bar{3}m$ PTO in terms of the same error produced by a given plane wave cutoff energy using the plane wave basis. We see that when increasing the number of PAOs to TZTP, we achieve the same accuracy as a 27.28 Ha cutoff plane wave calculation. Figure 5.6b makes the same comparison but for the convergence of the total energy difference ΔE . All PAO basis sets perform better using this metric (in particular, SZP makes a gain of +4.63 Ha in plane wave cutoff energy) with TZTP achieving the same convergence in energy as a 30.85 Ha plane wave cutoff. We note that these values are close to *double* those reported by the PAO basis sets in the `Siesta` code [6] but accept that a lot of this difference could be accounted for due to the softer (and lower accuracy) Troullier-Martins [364] type pseudopotentials used in [6] and the difference in material system used for the study (bulk Si).

5.3.3 Bader analysis

Table 5.5 shows the quantities derived from Bader partitioning of the charge densities calculated using the plane wave optimised geometries. These results reveal some fine features in the electronic structure. We see that for all basis sets, taking cubic PTO as an example, the Bader ionic charges q_B (obtained from the difference in the number of valence electrons treated by the pseudopotential and the Bader partitioned valence charge) *do not* coincide well with the nominal charges (Pb^{2+} , Ti^{4+} , O^{2-}) which are used frequently in the literature as a convenience rather than an *ab initio* assignment. We retrieve around half the nominal values suggesting a significant covalent character to the bonding, especially for the BO_6 octahedra. This is in contrast to the well known phenomenon of anomalous dynamical or *Born effective* charges (\mathbf{Z}^*) in the perovskite oxides, known to approximately *double* the nominal charges of ions in the perovskite oxides [162]. The reason for this discrepancy is that the dynamical nature of \mathbf{Z}^* accounts for the additional charge from counter motion of electrons/holes when an cation/anion is displaced. In comparison, the Bader charge calculated in this chapter is a static property. As we have previously noted, since static charges are not unequivocally defined, the given ionic charges in this section will vary between assignment methods.

We see that there is a cation \rightarrow anion negative charge transfer with increasing basis set size suggesting an increasing level of ionicity in bonding bringing q_B closer to their PW values. We see that the prediction of q_B is rather underestimated for cations and overestimated for anions in the SZP basis set. This suggests that the electronegativity of O is underestimated and/or electrons proximal to the metal ion sites are over-localised compared to plane waves. This fact first appears to be at odds with the observed effect of an electron surplus near O anions as seen in Figures 5.3, 5.4 & 5.5. This is however rationalised as we also observe a decrease in the Bader volume V_B for O anions which, in turn, increases the average valence charge density \bar{n}_B (as seen in Table 5.5) recovering the effect observed in the electron density difference plots. Whilst it can be seen that the Bader derived quantities are rather approximate (most notably in q_B) for the SZP basis, by DZDP (and *certainly* by TZTP) they are in good agreement with the values obtained from plane

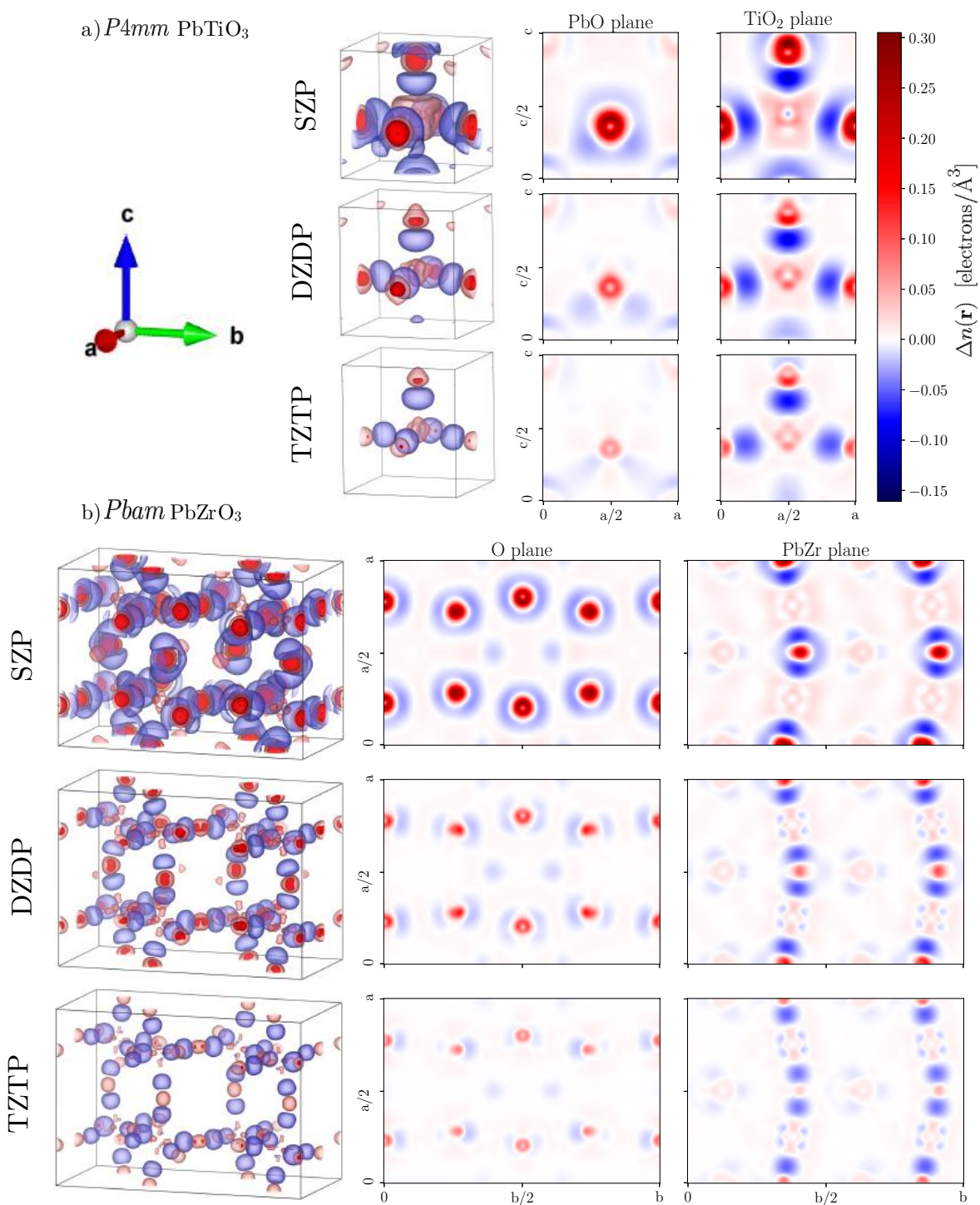


Figure 5.4: The charge density difference between PAO calculations and plane waves for increasing PAO basis set size for tetragonal PTO (a) and orthorhombic PZO (b). For each case, we display the full 3d isosurfaces and selected slices. Isosurfaces are plotted at the +0.10 (dark red), +0.020 (light red) and -0.020 (blue) electrons/ \AA^3 levels.

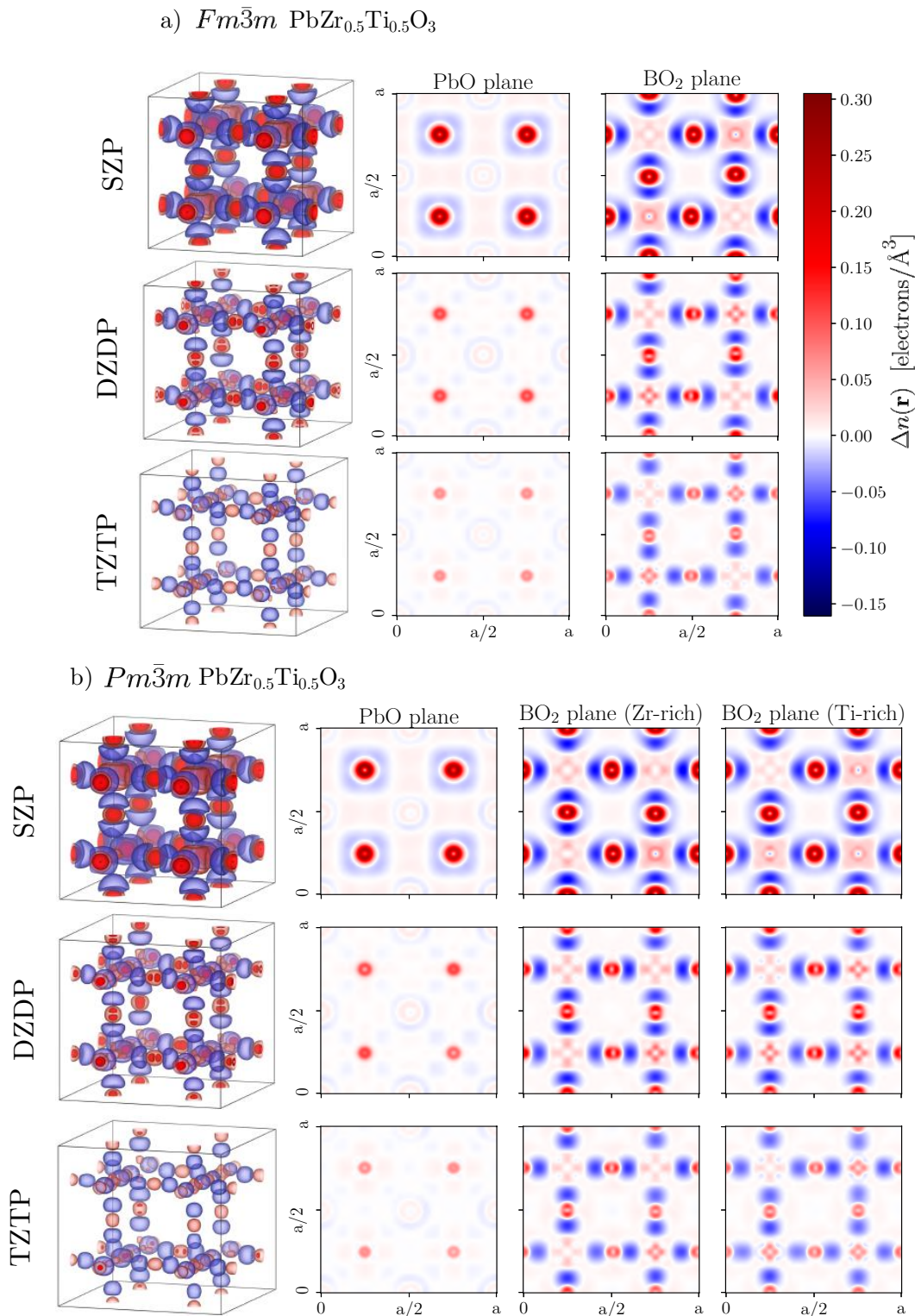


Figure 5.5: The charge density difference between PAO calculations and plane waves for increasing PAO basis set size for $Fm\bar{3}m$ cubic PZT 50/50 (a) and $Pm\bar{3}m$ cubic PZT 50/50 (b). For each case, we display the full 3d isosurfaces and selected slices. Isosurfaces are plotted at the +0.10 (dark red), +0.020 (light red) and -0.020 (blue) electrons/ \AA^3 levels.

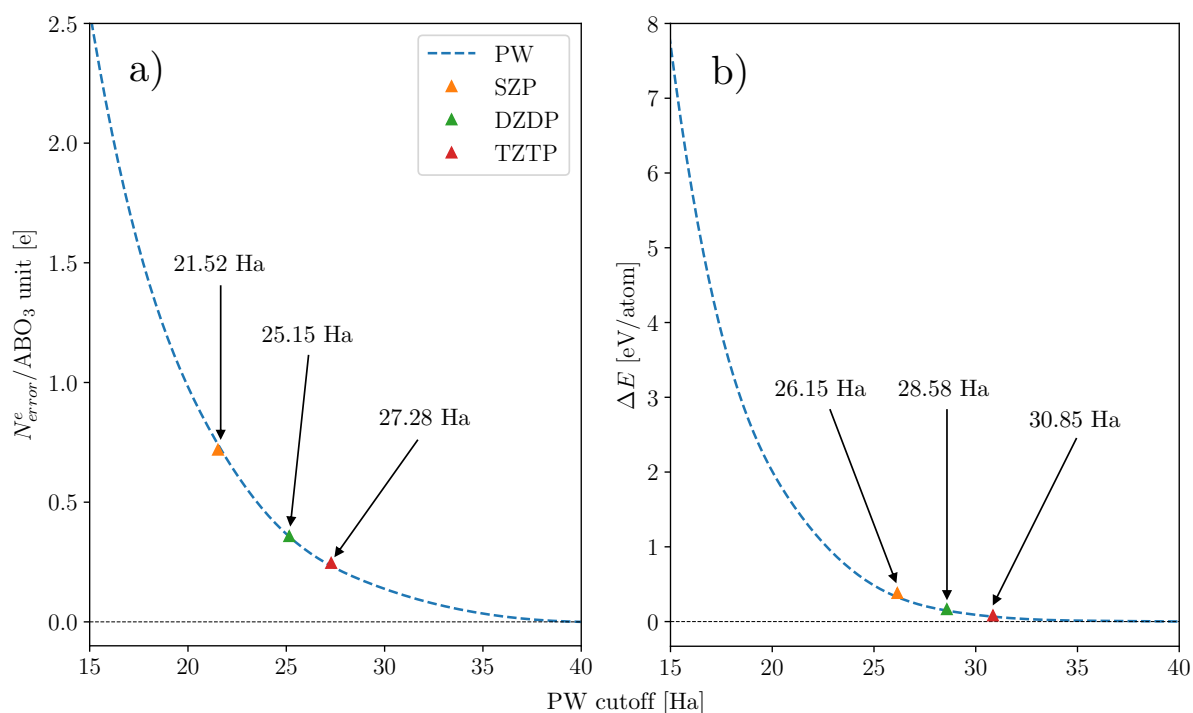


Figure 5.6: The convergence properties of plane wave calculations where PAO calculations featuring *the same error* have been overlaid for comparison. Calculations were performed on the $Pm\bar{3}m$ PTO structure. a) Convergence with respect to the total electronic error integral of Equation 5.2 b) Convergence with respect to ΔE , the energy difference between a given calculation and the energy obtained from the 40Ha plane wave cutoff.

	q_B [e]				V_B [\AA^3]				\bar{n}_B [$e/\text{\AA}^3$]			
<i>Pm$\bar{3}m$ PTO</i>												
	SZP	DZDP	TZTP	PW	SZP	DZDP	TZTP	PW	SZP	DZDP	TZTP	PW
Pb	1.29	1.37	1.39	1.38	18.81	18.40	18.39	18.41	0.676	0.686	0.686	0.686
Ti	2.01	2.08	2.12	2.15	7.68	7.54	7.42	7.35	1.300	1.315	1.331	1.344
O	-1.10	-1.15	-1.17	-1.18	11.22	11.40	11.45	11.46	0.633	0.627	0.6326	0.626
<i>Pm$\bar{3}m$ PZO</i>												
Pb	1.21	1.30	1.39	1.35	21.89	21.42	20.83	21.06	0.585	0.593	0.606	0.600
Zr	2.31	2.39	2.43	2.47	11.00	10.65	10.39	10.23	0.881	0.903	0.921	0.931
O	-1.17	-1.23	-1.27	-1.27	12.70	12.97	13.25	13.23	0.565	0.557	0.549	0.550
<i>P4mm PTO</i>												
Pb	1.27	1.35	1.39	1.37	19.70	19.26	19.07	19.16	0.646	0.657	0.661	0.659
Ti	2.03	2.10	2.13	2.16	7.83	7.67	7.56	7.48	1.273	1.291	1.306	1.315
O	-1.10	-1.15	-1.17	-1.18	11.76	11.96	12.07	12.06	0.603	0.597	0.594	0.595
<i>Pbam PZO</i>												
Pb	1.20	1.29	1.34	1.31	21.24	20.70	20.52	20.66	0.603	0.614	0.617	0.614
Zr	2.37	2.47	2.51	2.55	10.99	10.61	10.39	10.28	0.876	0.898	0.913	0.920
O	-1.19	-1.25	-1.28	-1.29	12.79	13.10	13.23	13.22	0.562	0.554	0.550	0.551
<i>Fm$\bar{3}m$ PZT 50/50</i>												
Pb	1.24	1.34	1.39	1.35	20.29	19.78	19.52	19.76	0.629	0.640	0.646	0.640
Zr	2.26	2.36	2.42	2.55	10.91	10.54	10.28	9.96	0.892	0.915	0.933	0.949
Ti	2.04	2.12	2.15	2.18	7.70	7.53	7.43	7.34	1.294	1.313	1.325	1.338
O	-1.13	-1.19	-1.22	-1.24	11.87	12.13	12.28	12.27	0.601	0.593	0.588	0.590
<i>Pm$\bar{3}m$ PZT 50/50</i>												
Pb	1.24	1.34	1.39	1.36	20.45	19.86	19.60	19.79	0.624	0.637	0.643	0.639
Zr	2.33	2.39	2.43	2.47	10.64	10.43	10.18	10.03	0.909	0.921	0.939	0.950
Ti	2.04	2.11	2.15	2.18	7.73	7.54	7.42	7.34	1.289	1.311	1.327	1.337
O	-1.14	-1.20	-1.23	-1.23	12.01	12.27	12.42	12.39	0.595	0.587	0.582	0.583
ϵ [%]	-7.55	-2.83	-0.26	-	2.45	1.20	0.37	-	-1.73	-0.89	-0.26	-
ϵ^{abs} [%]	7.55	2.83	1.45	-	4.27	1.84	0.84	-	2.82	1.25	0.60	-

Table 5.5: The Bader partitioned ionic charges q_B , volumes V_B and average valence charge densities \bar{n}_B for each ionic species and each of the considered crystal structures calculated for each basis set. Where ionic species have symmetry inequivalent sites, we take the mean value over all sites. We give also the mean relative error (MRE) ϵ and mean absolute relative error (MARE) ϵ^{abs} measured in % error versus plane waves.

waves. This once again emphasizes the electronic accuracy achievable with the default PAOs.

We have also examined the possibility that the errors in q_B could be an artefact of pressure using the particular case of $Pm\bar{3}m$ PZO. That is, the optimised lattice constants for the PAO bases overestimate the plane wave result by 0.99%, 0.46% and 0.34% for the SZP, DZDP and TZTP basis sets respectively. If we then perform simulations at the plane wave lattice constant (as was done for the results in Table 5.5) this imposes an isotropic pressure of -5.28 GPa (SZP), -2.63 GPa (DZDP) and -1.46 GPa (TZTP). Because of this fact, we calculated the Bader quantities once more using the zero pressure lattice constants. Remarkably, q_B changes only marginally (no more than $\pm 0.01e$). Since we are working at a larger volume, the V_B must of course increase, but, the ratios of the cationic to anionic volumes remains constant. Since roughly the same amount of charge is now enclosed within a larger V_B , we naturally see a decreased \bar{n}_B for all sites. We deduce then that the errors in q_B do not strongly respond to deviations from the equilibrium lattice constants. These errors are instead described by the incompleteness of the basis.

We see that the ratio of the cation to anion volumes is a decreasing function of basis set completeness, decreasing by ≈ 0.1 for V_B^B/V_B^O and ≈ 0.2 for V_B^{Pb}/V_B^O from SZP to TZTP. This implies that in the smaller basis set, O occupies a smaller ionic volume in comparison to the Pb and B-sites. This could result in small differences in lattice dynamics between the basis sets and could effect the Goldschmidt tolerance factor, depending explicitly on ionic radii [365, 366]. This effect could be responsible for some of the differences in the amplitudes of the soft modes discussed in Section 5.3.4.

5.3.4 Soft mode distortions

In this section we consider the soft modes known to drive the phase transitions in PTO and PZO. We consider the amplitude of each identifiable irrep in the relaxed structures for each basis set. We also consider the degree of energy lowering associated with each of these irreps and define phase transition energies. We display the displacive modes in Tables 5.6 and 5.7. Strain modes influence the phase transition in PZO only by a small amount so we include only discussion of strain modes in PTO (although all strain modes are tabulated in Table 5.8); coupling strongly to the displacive Γ_4^- mode. The phase transition energies are quoted in Table 5.10 and the linear evolution of mode energetics are shown in Figure 5.7.

Before discussing mode amplitudes, we must first carefully define them. We do so following the format of the ISODISTORT A_p amplitude normalised to the primitive cell [321]. Once an atomic displacement has been identified as belonging to a particular irrep, the displacement is calculated in fractional coordinates relative to the *parent* structure. This defines the amplitude of a specific displacement in the irrep. To calculate A_p we now normalise the amplitude by a factor of $\sqrt{V_p/V_s}$ for primitive/supercell cell volumes $V_{p/s}$. Now to calculate the amplitude of the irrep as a whole, we take the square root of the sum of the squares of the displacement amplitudes belonging to the irrep in question. If we wish to characterise the amplitude of the total distortion

			SZP	DZDP	TZTP	PW
$\Gamma_4^- \rightarrow \mathbf{q}_\Gamma = [0, 0, 0]$	Pb 1b	T_{1u}	0.000	0.000	0.000	0.000
	Ti 1a	T_{1u}	0.160	0.118	0.111	0.141
	O 3d	A_{2u}	0.659	0.458	0.370	0.446
	O 3d	E_u	0.842	0.646	0.550	0.651
Total distortion			1.081	0.800	0.672	0.802

Table 5.6: The mode amplitudes normalised to the parent cell A_p (described in the text) for the irreps characterising the $Pm\bar{3}m \rightarrow P4mm$ phase transition in PTO.

from the transition, we can take the square root of the sum of the squares for each irrep amplitude. Tables 5.6 and 5.7 are then tabulations of A_p .

We consider first the simpler phase transition of PTO. This is characterised by a single displacive mode Γ_4^- resulting in the ferroelectric $P4mm$ phase. Examining Table 5.6 we see that Pb 1b displacements are set to zero since we have chosen the Pb site as the origin. For the SZP basis set, the Γ_4^- distortion is rather approximate compared to plane waves, overestimated by $\approx 35\%$. This overestimate can be understood in simple terms by considering the arguments of Cochran and Anderson [1, 2, 52] in their seminal works on soft modes. It is suggested that the condition for stability against the ferroelectric distortion is that short range restoring forces (favouring the cubic phase) outweigh long range Coulombic forces (favouring ferroelectricity). This condition does not hold for PTO in 0K DFT hence the ferroelectric Γ_4^- mode is an energy lowering phase transition of the $Pm\bar{3}m$ phase. It is clear, however, that this delicate balance of short and long range forces is modified between the different PAO bases. As discussed in Section 5.1 (and displayed in Figure 5.3a), there are too few electrons in the covalent bonds defining the TiO_6 octahedra; an effect especially apparent for the SZP basis. This reduces the strength of short range restoring forces whilst the Coulombic Ewald contribution remains constant for a given ionic geometry. We suggest that this increased imbalance drives a much stronger ferroelectric distortion for the SZP basis. We note that whilst the Hartree forces (a functional of the charge density) from the coulomb interacting electrons will also play a role in this balancing act, their contribution is non-trivial. Indeed, the electrostatic contribution to the total energy from Ewald terms is in general *much* larger than the Hartree contribution in these systems so we expect the former to dominate.

Consider also the coupling to strain modes $\Gamma_{1\sigma}^+$ and $\Gamma_{3\sigma}^+$ (the subscript σ denotes a strain mode rather than a displacive one). The former is responsible for uniform isotropic expansions/contractions of the cell whilst the latter is responsible for tetragonality. Rather than quote the amplitude of each mode for each basis (shown in Table 5.8), it is more illuminating to examine the zero pressure lattice constants of Table 5.9. We see that for the SZP basis the c/a ratio is considerably overestimated at 1.24 when compared to the plane wave c/a of 1.084. This

			SZP	DZDP	TZTP	PW
$\mathbf{R}_4^+ \rightarrow \mathbf{q}_R = [1/2, 1/2, 1/2]$	O 3d	E_u	0.571	0.554	0.553	0.534
	Total \mathbf{R}_4^+ distortion		0.571	0.554	0.553	0.534
$\Sigma_2 \rightarrow \mathbf{q}_\Sigma = [1/4, 1/4, 0]$	Pb 1b	T_{1u}	0.213	0.214	0.239	0.256
	Zr 1a	T_{1u}	0.041	0.034	0.037	0.047
	O 3d	A_{2u}	-0.047	-0.042	-0.035	-0.035
	O 3d	E_{u_1}	0.253	0.250	0.224	0.227
	O 3d	E_{u_2}	-0.230	-0.222	-0.216	-0.217
	Total Σ_2 distortion		0.407	0.400	0.396	0.409
$\mathbf{S}_4 \rightarrow \mathbf{q}_S = [1/4, 1/2, 1/4]$	Pb 1b	T_{1u}	-0.049	-0.033	-0.026	-0.026
	O 3d	E_{u_1}	-0.013	-0.129	-0.103	-0.106
	O 3d	E_{u_2}	0.074	-0.083	-0.071	-0.070
	Total \mathbf{S}_4 distortion		0.154	0.157	0.128	0.129
$\mathbf{M}_5^- \rightarrow \mathbf{q}_M = [1/2, 1/2, 0]$	Pb 1b	T_{1u}	-0.006	-0.001	-0.009	-0.010
	Zr 1a	T_{1u}	-0.008	-0.003	-0.006	-0.008
	O 3d	E_u	0.012	0.013	0.009	0.009
	Total \mathbf{M}_5^- distortion		0.015	0.013	0.014	0.016
$\mathbf{R}_5^+ \rightarrow \mathbf{q}_R = [1/2, 1/2, 1/2]$	Pb 1b	T_{1u}	0.011	0.024	0.027	0.027
	O 3d	E_u	-0.001	-0.006	-0.007	0.008
	Total \mathbf{R}_5^+ distortion		0.011	0.025	0.028	0.028
$\mathbf{X}_3^- \rightarrow \mathbf{q}_X = [0, 1/2, 0]$	Zr 1a	T_{1u}	0.001	0.0003	0.002	0.003
	O 3d	E_u	-0.009	-0.009	-0.017	-0.017
	Total \mathbf{X}_3^- distortion		0.009	0.009	0.018	0.017
Overall distortion			0.718	0.702	0.693	0.686

Table 5.7: The mode amplitudes normalised to the parent cell A_p (described in the text) for the irreps characterising the $Pm\bar{3}m \rightarrow Pbam$ phase transition in PZO. The modes are listed in descending total distortion.

		Mode amplitude, A_p			
	irrep	SZP	DZDP	TZTP	PW
PTO	$\Gamma_{1\sigma}^+$	0.0667	0.0321	0.0166	0.0266
	$\Gamma_{3\sigma}^+$	0.1883	0.0867	0.0495	0.0674
PZO	$\Gamma_{1\sigma}^+$	-0.0037	-0.0037	-0.0037	-0.0029
	$\Gamma_{3\sigma}^+$	-0.0150	-0.0115	-0.0124	-0.0132
	$\Gamma_{5\sigma}^+$	0.0041	0.0049	0.0013	0.0014

Table 5.8: The strain mode amplitudes, A_p , for the $Pm\bar{3}m \rightarrow P4mm$ phase transition of PTO and the $Pm\bar{3}m \rightarrow Pbam$ phase transition of PZO.

	SZP [Å]			DZDP [Å]			TZTP [Å]			PW [Å]		
	a	b	c	a	b	c	a	b	c	a	b	c
<i>P4mm</i> PTO	3.799	3.799	4.710	3.865	3.865	4.282	3.890	3.890	4.128	3.870	3.870	4.194
<i>Pbam</i> PZO	5.919	11.907	8.241	5.877	11.835	8.223	5.886	11.793	8.206	5.871	11.765	8.178
<i>Fm$\bar{3}m$</i> PZT 50/50	8.124	8.124	8.124	8.091	8.091	8.091	8.080	8.080	8.080	8.050	8.050	8.050
<i>Pm$\bar{3}m$</i> PZT 50/50	8.143	8.143	8.143	8.112	8.112	8.112	8.096	8.096	8.096	8.069	8.069	8.069

Table 5.9: The optimised, mutually orthogonal, pseudocubic lattice constants a, b and c for the distorted PTO/PZO phases and the PZT 50/50 arrangements.

leads to the considerable overestimates of the amplitudes of $\Gamma_{1\sigma}^+$ and $\Gamma_{3\sigma}^+$. The amplitude of the ferroelectric Γ_4^- distortion is then increased as a result of the strong, mutual coupling to $\Gamma_{1\sigma}^+$ and $\Gamma_{3\sigma}^+$. A peculiarity of this transition for the default PAOs is their non-systematic nature. Despite the smaller number of basis functions, the DZDP basis performs better than TZTP for the amplitude of displacive modes, strain modes, the phase transition energy (Table 5.10) and lattice constants of the *P4mm* phase (Table 5.9). It is for this reason that great care must be taken when using PAOs to describe systems where the internal and cell degrees of freedom are strongly coupled. We note that using a basis other than the default can result in vast improvements for this transition. When tuning the confinement energies to fit the plane wave c/a , we can achieve a phase transition energy within 1 meV of the plane wave energy as we show in Section 5.3.5.

We have also computed the spontaneous macroscopic polarisation for the relaxed *P4mm* PTO structures. For the PAO calculations, we use the method developed by Resta [147, 367] (equivalent to the Berry phase formalism [64, 65] in the limit of large cells; we use 10 cells in the direction of the distortion) whilst we use the well known Berry phase formalism of King-Smith and Vanderbilt for the plane wave calculation. With plane waves, we find a polarisation of $92.74 \mu\text{C}/\text{cm}^2$ which compares very well with the TZTP value of $92.82 \mu\text{C}/\text{cm}^2$. We note that this is despite the underestimation of the displacive Γ_4^- mode (indicative of the ionic contribution, Table 5.6) meaning the electronic contribution to the polarisation is increased. The DZDP polarisation is found to be $104.15 \mu\text{C}/\text{cm}^2$ showing that despite the Γ_4^- mode amplitude closely adhering to the plane wave value, the electronic contribution is slightly overestimated. For the SZP basis, we find a polarisation of $95.93 \mu\text{C}/\text{cm}^2$ which at first glance indicates better agreement with plane waves than DZDP. We note that this is only because the significantly larger dipole moment (as indicated by the mode amplitude in Table 5.6) is normalised by the largely overestimated volume (+8.2% compared to plane waves).

The PZO transition is more difficult to unpack. Despite this, (perhaps due to only a weak coupling between displacive and strain modes) the material is impressively described by the default PAOs. The error in both the *Pm $\bar{3}m$* and *Pbam* lattice constants are smaller than 0.5% for the TZTP basis demonstrating that even highly distorted perovskites can be represented well by the default PAOs. We now examine Table 5.7 commenting on the individual contributions of each irrep in the transition. Beginning first with the R_4^+ mode we see that the accuracy

	PTO $Pm\bar{3}m \Rightarrow P4mm$ [meV/ABO ₃ unit]	PZO $Pm\bar{3}m \Rightarrow Pbam$ [meV/ABO ₃ unit]
SZP	-115.51	-295.78
DZDP	-58.40	-256.27
TZTP	-47.37	-258.71
PW	-69.83	-262.24

Table 5.10: The phase transition energies for the cubic to tetragonal/orthorhombic transitions in PTO/PZO. This quantity is defined by the difference in total energy between the relaxed cubic phase and the relaxed distorted phase for each basis.

improves with basis set size but accounts for the largest source of error in the overall distortion. Since the R_4^+ mode is AFD, this overestimation leads to a larger rotation angle of the oxygen octahedra compared to plane waves. For the antipolar Σ_2 distortion, we see that the total distortion is *further* from the plane wave value as we increase the number of basis functions. This is somewhat misleading however as when we examine the individual displacements, we see that O and Pb displacements are better described by the TZTP basis. The reason the SZP basis *appears* to perform better is because the underestimated Pb displacement balances with the O E_{u_2} displacement. Taking both the S_4 and X_3^- modes together, we see that an accurate description requires the TZTP basis. It should be noted, however, the X_3^- mode contributes very little to the energetics of the transition which is dominated by the R_4^+ , Σ_2 and S_4 modes. We note finally that although the amplitudes of some modes do not improve with basis set size, the overall distortion does. By TZTP, the distortion is within 0.1% of the plane wave distortion. This accuracy is seen also in the phase transition energy (Table 5.10) which improves with basis set size within 1% of the plane wave value by TZTP.

Figure 5.7 describes the energy difference ΔE between an initial, undistorted phase and a phase distorted by some fraction of a displacive or strain mode. For each basis, the maximum amplitude of an irrep is the amplitude found in the relaxed structure in Tables 5.6 and 5.7. In Figure 5.7a, the initial undistorted structure is the optimised $Pm\bar{3}m$ PTO structure for the basis in question. Since the displacive mode is coupled strongly to the strain modes, we linearly evolve the three modes (Γ_4^- , $\Gamma_{1\sigma}^+$ and $\Gamma_{3\sigma}^+$) simultaneously until their maximum amplitudes are reached. As was explained previously, the default DZDP basis best approximates the plane wave energetics since the TZTP basis retrieves a less accurate c/a ratio. A small energy barrier (at zero mode amplitude) exists for the transition for *all* cases. This is not true in reality, only existing here since we have assumed the displacive and strain modes are directly proportional on a 1:1 basis (the real coupling is non-linear). The size of this barrier for the SZP basis is larger at ≈ 35 meV. This is an artefact of the large strain modes and the highly non-linear coupling with the displacive mode. For curves along the plane wave optimised trajectory (explained in the Figure 5.7 caption), a minimum of energy is always reached before the mode maximum inferring that

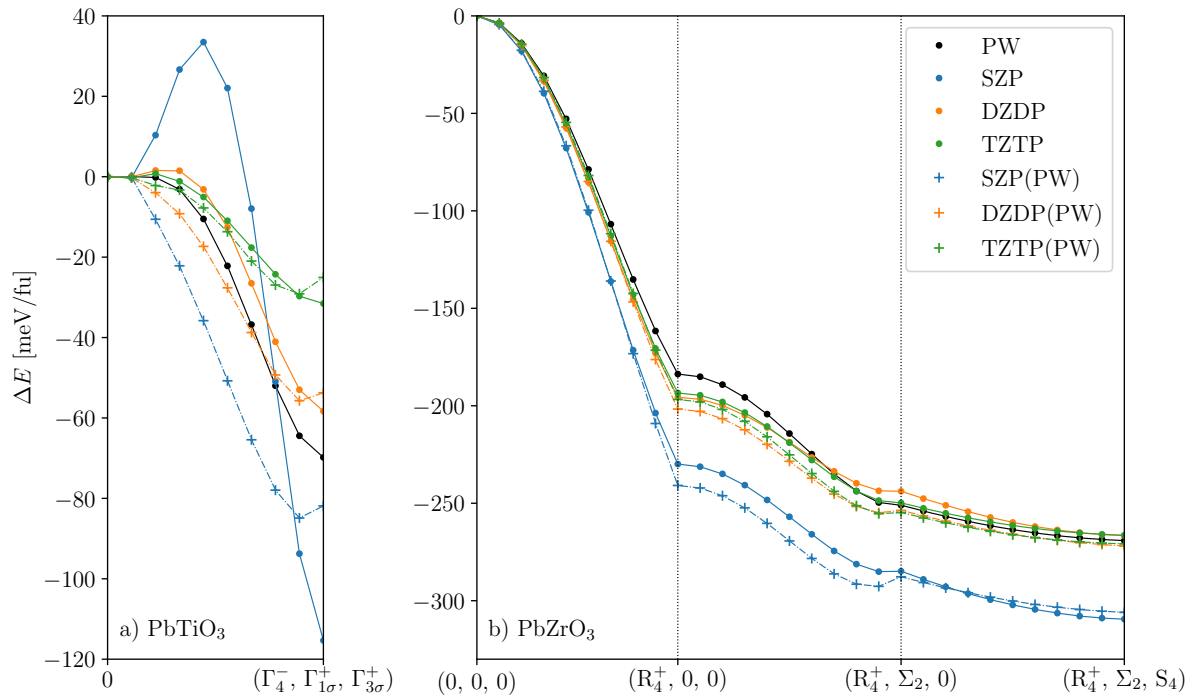


Figure 5.7: The phase transition energetics for PTO and PZO as function of normalised mode amplitude. Points/crosses are calculated data whereas lines are linear interpolations. Curves labelled with (PW) were calculated along the plane wave optimised trajectory. a) Seven curves indicating phase transition paths for the zone centre distortions in PTO. Modes with the subscript σ are strain modes coupled to the displacive Γ_4^- mode. b) Seven curves describing the phase transition path for the three most important modes in the $Pbam$ PbZrO₃ phase transition. Each path begins with the optimised orthorhombic cell for each basis such that strain modes are “pre-frozen”.

the optimised plane wave structure does not so well approximate the optimised structure of a given PAO basis. This, much like the phase transition energy, can be improved upon using a non-default basis.

In Figure 5.7b, our initial undistorted structure is the optimised orthorhombic $Pbam$ cell of PZO (with lattice constants described in Table 5.9) but with *zero* displacive mode amplitude. As a general trend, we see that there is a fair discrepancy between the SZP and plane wave curves. This almost disappears as we use a DZDP basis and even more so by TZTP. A clear source of error in our description for all bases is the overestimated amplitude of the R_4^+ mode. We see that along the $(0, 0, 0) \rightarrow (R_4^+, 0, 0)$ path, this overestimation results in *too much* energy lowering. Interestingly, for the DZDP and TZTP bases, this error seems to recover along the $(R_4^+, 0, 0) \rightarrow (R_4^+, \Sigma_2, 0)$ path and by the time all three displacive modes are present, the energetics are almost identical. For the plane wave optimised trajectories, we once again observe a minimum of energy before the maximal mode amplitude. This barrier appears just before the $(R_4^+, \Sigma_2, 0)$ point indicating that the plane wave Σ_2 mode (when coupled to R_4^+ at least) does not describe a stable structure. This effect does appear to diminish with basis set size, disappearing almost entirely for TZTP. At the (final) (R_4^+, Σ_2, S_4) point, we see that the DZDP, DZDP(PW), TZTP and TZTP(PW) curves very well represent the PW curve. This implies that in this case, the default PAOs could be used to describe a plane wave optimised structure with only a very small penalty in the energetics. This is valuable since this allows us take small plane wave optimised cells to build larger supercells for PAO calculations *without re-relaxing* the structure allowing for easy up-scaling of accurate DFT calculations.

5.3.5 Basis set optimisation

The mode decomposition amplitudes of Table 5.6 and the $Pm\bar{3}m \rightarrow P4mm$ phase transition energies for PTO in Table 5.10 show that there is some room for improvement on the default basis. We choose to optimise the c/a ratio of the tetragonal phase; minimising the difference in the c/a ratio obtained from the DZDP PAO basis with the plane wave result. Fitting to the c/a ratio is a good choice for the ferroelectric phases since strong strain-polarisation coupling ensures that the bulk polarisation will be implicitly optimised in the process. We choose the DZDP basis since this offers good flexibility whilst having few enough ζ 's (and therefore parameters in the optimisation process) to quickly (and more reliably) reach a minimum. Also, we use a different DFT functional in this section; LDA-CAPZ [215], as we use this optimised basis in Chapter 6 which makes use of this functional. In the optimisation process, the cutoff radii r_c (or equivalently, the confinement energies) of each PAO are the variables of the minimisation. The optimisation procedure can be described with three stages:

1. Solve for the radial functions $R_{nl\zeta}(r)$ for an initial set of r_c for each species for the confined pseudoatom. We choose the default ER PAOs as a starting point.

2. Using these PAOs, a full geometry optimisation of the atomic positions and cell size/shape is performed starting from the plane wave optimised $P4mm$ PTO structure.
3. If the resulting c/a ratio agrees with the plane wave value to some tolerance (we use 0.02), terminate. If not, return to stage 1 with a modified set of r_c in the direction of steepest descent according to the Nelder-Mead simplex [368].

Indeed, all three of the above steps are encapsulated within the Nelder-Mead simplex [368]; chosen simply because we have no information about the gradient of the objective function. The initial and optimised cutoff radii r_c are shown Table 5.11. It can be seen that the optimised cutoff radii are more compact than the defaults for Pb 5d, Pb 6d, Ti 4s, Ti 3d and Ti 4p while the remaining PAOs expand (especially O). The optimised DZDP phase transition energy for this functional (-47.91 meV) is accurate to the plane-wave calculation (-48.12 meV) to +0.44% whilst the optimised DZDP c/a ratio (1.036) is accurate to -0.19%. This is an improvement on the c/a obtained from the default DZDP basis (by the ER method; 1.30) and drastically improves on the phase transition energy (-17.95 meV). Much like the default TZTP PBESol basis used in the previous sections, the default TZTP LDA basis does *not* improve on the default DZDP basis; underestimating the c/a ratio further. We note that whilst our optimisation method clearly offers vast improvements for this application, we must make some serious caveats. Firstly, our approach is prone to encountering local minima (where the algorithm gets stuck) and is sensitive to the initial r_c . At this stage, then, we would describe this optimisation as being purely heuristic. Secondly, the optimisation interferes with the transferability of the basis. That is, although the structure of the $P4mm$ phase is better described with the optimised basis, the error in the equilibrium volume of the cubic $Pm\bar{3}m$ phase increases (the error is 1.5% for the default ER and is 1.9% for the optimised basis).

Table 5.11: The cutoff radii r_c for the default (ER; equal radii) and optimised LDA-CAPZ PTO basis described in the text. Unlike before, we now treat the Pb 5d states as semicore.

		Default r_c (ER) [a_0]		Optimised r_c [a_0]	
		$\zeta = 1$	$\zeta = 2$	$\zeta = 1$	$\zeta = 2$
Pb	5d	6.38	-	5.60	-
	6s	6.38	3.78	6.61	3.93
	6p	6.38	3.78	6.54	4.06
	6d	6.38	3.78	3.91	2.68
Ti	3s	3.32	-	4.53	-
	3p	3.79	-	5.11	-
	4s	8.13	4.07	5.75	3.22
	3d	8.13	4.07	5.68	3.14

	4p	8.13	4.07	4.02	3.01
O	2s	4.86	2.58	5.03	2.71
	2p	4.86	2.58	6.02	3.34
	3d	4.86	2.58	6.02	3.34

5.4 Summary

We have investigated the consequences of representing delicate features of the perovskite oxides and other materials with the default PAO basis sets packaged with CONQUEST in comparison to plane wave calculations using the same pseudopotential. For structural properties, most basis sets (although, with some glaring exceptions) described accurately the equilibrium volumes and bulk moduli of the elemental semiconductors, binary oxides and the perovskite oxides. We learnt that in most cases the ER PAO construction method marginally outperformed those made under the EE scheme for the structural properties and relative energetics. We learnt also that those default basis sets with perturbative polarisation functions outperformed those using simple excited states for describing relative stabilities. That is, in the case of the two SiO₂ polymorphs, the relative stability often had the wrong sign when using explicit excited states.

In the electronic structure, we were able to reproduce the plane wave electronic charge density with an error of $\approx 0.5\%$ using the total integrated electronic error integral of Equation 5.2. We found that the largest source of error to this integral is from a surplus of electronic density close to O anion sites as shown in electronic charge density difference plots. Even fine features derived from Bader partitioning (Bader charges, volumes and densities) agree well with plane wave calculations and once again demonstrates the small surplus in electronic density near O anion sites. We quantified the completeness of the PAO basis sets by providing plane wave cutoff energies offering the same accuracy in N_{error} and energy convergence as those using the plane wave basis. We found that although the two metrics disagree (by a small amount) on the cutoff, by TZTP we can achieve the accuracy of a 27.28-30.85 Ha plane wave cutoff, close to *double* what has previously been reported in the literature. We note that whilst this comparison is useful, the error cancellation in the plane wave basis (that is, errors in the core regions tend to cancel with one another) is not perfectly achieved when we consider the energy difference between plane wave and PAO calculations. Further, we expect these errors to be less system dependent in the case of plane waves than for PAOs, especially smaller basis sets (like SZ and SZP).

When investigating the condensation of soft modes, we found that larger basis sets of PAOs (DZDP and TZTP) well described the $Pm\bar{3}m \rightarrow Pbam$ phase transition in PZO, both structurally and energetically. Impressively, both the total distortion and phase transition energy when using the TZTP basis are within 1% of the plane wave figures. We found that more care

had to be taken for the $Pm\bar{3}m \rightarrow P4mm$ phase transition in PTO in part due to the need to accurately represent short range restoring forces and in part due to the strong coupling between displacive and strain modes. This, however, can be remedied by using a non-default optimised basis where we have laid out a heuristic method for the optimisation process. Remarkably, we find that using a default DZDP or TZTP basis set on a plane wave optimised geometry for PZO results in close to identical phase transition energies. This suggests that even highly distorted perovskites can be represented by basis sets of default PAOs.

This chapter suggests that even fine structural and electronic features of the perovskite oxides can be calculated to near plane wave accuracy using basis sets of PAOs. Since PAO-based calculations (in partnership with the correct algorithm) can scale to many thousands (and millions [13]) of atoms, this approach now offers a pathway for accurate large scale first principles simulations of perovskite systems using DFT. We note that whilst there is still progress to be made for the calculation of more demanding physical properties (like soft mode phase transition temperatures), some particularly valuable research questions (as discussed in Section 5.1) facing the perovskite oxides can now be addressed with this method using large scale structural relaxations, spin-polarised calculations with highly disordered magnetism and the extraction of electronic properties from systems with realistic defect concentrations.

6 | Ultrathin PbTiO_3 Films: Substrate Effects and Surface Defects

Chapter abstract

Low dimensional structures comprised of ferroelectric (FE) PbTiO_3 (PTO) and quantum paraelectric SrTiO_3 (STO) are hosts to complex polarisation textures such as polar waves, flux-closure domains and polar skyrmion phases [89, 174, 177–179, 369, 370]. Density functional theory (DFT) simulations can provide insight into this order, but are limited by the computational effort required. To circumvent this, we deploy two separate large scale DFT methods implemented in CONQUEST [7, 17] within two separate but complementary studies. In the first study, we treat PTO films on STO substrates using the novel multi-site support function (MSSF) method [18, 19]. This method reduces the solution time for the electronic ground state, preserves high accuracy and allows for simulations of systems $> 2,000$ atoms in size. At low dimensions, we find that the polar wave texture with cylindrical chiral bubbles emerges as an intermediate phase between full flux-closure domains and in-plane polarisation. This is driven by an internal bias field born of the compositionally broken inversion symmetry in the [001] direction. Tuning this built-in field could allow one to manipulate chiral order on the nanoscale through the careful choice of substrate, surface termination or use of overlayers. Antiferrodistortive (AFD) order locally interacts with these polar textures giving rise to strong FE/AFD coupling at the PbO terminated surface driving a $p(2 \times \Lambda)$ surface reconstruction; another pathway for the local control of ferroelectricity. In the second study, we scale up DFT beyond 5,000 atoms using the $\mathcal{O}(N)$ solver [16, 254, 255, 262, 266, 267] to simulate shallow, engineered surface trenches on free standing and polydomain PTO films. In line with experimental observations [32, 34, 55, 189], we find that surface trenches running parallel to domain walls (DW) are preferred to those running perpendicular to DWs. Also, trenches are found to be more stable positioned over the domain centroid compared to over the DW. We describe this preference with a principle of *least disturbance* to the underlying flux-closure domain structure. Finally, in agreement with experiment, we find large negative strain fields in the vicinity of our trenches [55]. This has been suggested to contribute to the DW alignment mechanism [55].

6.1 Introduction

With the advent of advanced deposition techniques [57, 371] has come a revolution in the engineering of thin film perovskite oxides and layered heterostructures for a variety of applications in nanoelectronics. These advancements have propelled research into the great variety of physical phenomena such systems can exhibit. These include enhanced colossal magnetoresistance [372], high-temperature superconductivity [373], the formation of interfacial two-dimensional electron and hole gases (2DEG/HG) [90, 338] and the emergence of negative capacitance [87, 88]. While these are becoming well documented [56, 58, 374], new emergent phenomena resulting from exotic electrical polarisation textures, including polar waves, vortices and polar skyrmion phases [89, 174, 177–179, 369, 370] are less well understood. The toroidal moment born from the chirality of these polar morphologies can give rise to strong electrotoroidic, pyrotoroidic and piezotoroidic effects [174, 180, 375] all of which show promise to be exploited in new low dimensional functional devices.

The ferroelectric (FE) domain walls (DWs) of related systems are also known to give rise to novel functionality. In some cases, it has been shown that FE DWs can become conducting within an otherwise insulating material [26, 376]: a promising avenue for the embedding of circuits in nanoelectronic devices [27, 28]. Indeed, this year (2020), a domain wall-enabled memristor was created in a thin film LiNbO_3 capacitor [29]. Following this, it is clear that polar textures and DWs can now be controlled and manipulated. However, current approaches rely on the delicate control of directed external fields [29–31, 89, 174] which can lack permanence once the field is switched off. In this chapter, we investigate alternative methods for controlling polar order on the nanoscale *without* use of these external fields. We perform two separate but complementary studies simulating the impact of substrate and engineered surface trenches on ferroelectric order in ultrathin PTO films. Because of the large number of atoms required for such simulations, we use the large scale DFT methods [7, 16, 18, 254, 255, 262, 266, 267] we detailed in Chapter 3, Section 3.4.

Another avenue for the control of ferroelectricity is through manipulating the interacting order parameters of the system. Notably, many perovskites (and heterostructures) are susceptible to both the antiferrodistortive (AFD) and FE distortions. In the bulk, these two modes were thought to suppress one another, although, recent evidence suggests that a cooperative regime may also exist [377, 378]. At surfaces and interfaces we see phase coexistence. For example, at the PbO terminated [001] surface of PTO, we observe the AFD $c(2 \times 2)$ surface reconstruction [379, 380]. This is characterised by strong antiphase rotations of the TiO_6 octahedra about the [001] axis (or $a^0a^0c^-$ in Glazer's notation [45, 46]) and is known to coexist with and mutually enhance in-plane ferroelectricity [379–381]. It is now popular to interface PTO with STO in the repeating $(\text{STO}_n/\text{PTO}_n)_N$ superlattice for n alternating perovskite unit cells repeated N times in a layered heterostructure. In the case of an ultrashort period ($n = 1$), hybrid-improper

ferroelectricity can arise from the coupling of AFD and FE modes [81].

The $(STO_n/PTO_n)_N$ heterostructure continues to be studied from a theoretical perspective. Most frequently considered is full periodic boundary conditions with infinitely repeated layers. This has been studied with first principles DFT [188] where the focus has been on the interactions of FE and AFD instabilities in the monodomain configurations. More recently, however, polydomain configurations have been studied and ferroelectric flux-closure domains have been shown to be stable [175]. Since [175] treats the bulk superlattice, the $c(2 \times 2)$ surface reconstruction wasn't considered. Polydomain simulations of pure TiO_2 terminated PTO films (which do not give rise to enhanced surface AFD modes [379, 380]) have been performed but do not treat the STO substrate by instead choosing to adopt the fictitious free standing film geometry [172]. This work then cannot make any account for substrate/interface effects or the intrinsically broken inversion symmetry for epitaxially deposited films on substrates. Indeed, inversion symmetry breaking is known to give rise to built-in bias fields [382, 383] in tricolor superlattices, which, to the authors knowledge, have so far *not* been investigated with DFT as a method for controlling FE domain structures. Also to the author's knowledge, there has been only a single DFT-based study treating both the PTO surface and the STO substrate. This study probed the nature of the theoretically proposed 2DEG/HG pair [90] where thicker films (≥ 14 unit cells) of the FE monodomain out-of-plane configuration were considered as large depolarising fields are known to suppress this configuration in thinner films [24]. Multiple FE domains are considered a competing phase but no 2DEG/HG pair emerges as the resulting flux closure domains are an alternative mechanism for screening the depolarising field [185].

Ferroelectric DWs have been experimentally observed in alignment with crystallographic step edges [32, 34] and surface defects (engineered or otherwise) [55, 189] in the PTO/STO system. While this promises control over the orientation and direction of (possibly conducting in similar systems) DWs, there are many open questions related to what drives the phenomenon. For example, it is not known *precisely* which part of the domain structure is pinned by the defect. One DFT study suggested that DWs themselves were pinned to the edges of crystallographic steps above a critical compressive strain [191]. In contrast to this, an effective Hamiltonian study [190] showed that it was the domain centroid (the area furthest from the DW with maximal out-of-plane polarisation) which was pinned by the step edge. In [190], unlike [191], the underlying polydomain nature of the film is treated, suggesting this approach provides the correct answer. Unfortunately, this clarity is muddied by the fact that [191] uses the more accurate full DFT approach while the approach taken in [190] is only *parameterised* by DFT. Another debate is related to the mechanism of the alignment. One study deployed time dependent Landau-Ginzburg-Devonshire (LGD) theory and suggested that the alignment mechanism is elastic. That is, the bulk and electrostrictive contributions to the free energy are lowered because lateral mechanical constraints are released in the vicinity of the surface defect [189]. In experiment, however, giant strains and strain gradients are found the vicinity of the surface defect [55]. This

opens the door to the possibility of strains and strain gradients coupling to the polydomain polarisation; piezoelectric and/or flexoelectric contributions to the alignment mechanism.

The polydomain configuration in itself is challenging to simulate from the perspective of DFT. The difficulty arises from the increased number of atoms N in the supercell as a result of treating a fixed domain period Λ . If we are also to treat a finite thickness of film t , the Kittel scaling law requires that the equilibrium Λ too increases since $\Lambda \propto \sqrt{t}$ [32, 34, 176]. If our simulations are to include the STO substrate, we could need a significant amount of atoms as the large ferroelectric polarisation of PTO may be able to polarise a few layers of STO. Finally, if we wish to include AFD modes in our simulations (like the $c(2 \times 2)$ surface reconstruction), the periodicity in the [010] direction must be doubled so as to not frustrate the octahedral rotations. To include all of these effects, calculations with a supercell containing *a few thousand atoms* are needed rather than the few hundred that conventional plane wave DFT is able to handle [4, 17]. When treating engineered surface trenches *even more* atoms may be required. While it is possible to treat a periodic array of surface trenches with a similar number of atoms to those discussed above, treating a trench in isolation may require several repeats of the polydomain structure to limit lateral trench-trench interactions. Further, if we are to unequivocally rule out the stability of trenches running perpendicular to the DW, *several thousand* atoms will be required in the supercell[†].

To overcome these limitations, some resort to alternative methods including phase fields, shell models, Monte Carlo and second principles [174, 369, 384–389]. Whilst these approaches each have their merits, they cannot *universally* serve as a replacement for full DFT. Most of these methods implicitly accept that DFT offers superior accuracy since they either are or can be parameterised by the theory [385, 388, 389]. Further, all of these methods make no account (or a limited account [385]) for the electronic structure, limiting the ability of simulations to adapt to new chemical environments like at surfaces and interfaces with a substrate. In this chapter, we utilise two separate novel variations on local orbital DFT. The first allows us to consider systems of a few thousand atoms with chemical accuracy rivaling plane wave calculations [18, 19] while the second allows us to treat very large systems [7, 17] (demonstrated for as many as 1 million atoms [13]) albeit with some loss of accuracy compared with the first approach.

This chapter is divided into two separate but complementary parts. In the first part, we provide a full first principles study on ultrathin films of PTO down to a single PbO monolayer ($N_z = 0$) up to 9 unit cells ($N_z = 9$) where $N_x/N_y/N_z$ is the number of perovskite unit cells included in the [100]/[010]/[001] direction. We treat explicitly the STO substrate and the PbO termination invoking the $c(2 \times 2)$ surface reconstruction. As well as treating paraelectric films, we treat two monodomain configurations of the polarisation ($\mathbf{P} \parallel [100]$ and $\mathbf{P} \parallel [110]$) and stripe domain patterns comprised of alternating $\mathbf{P} \parallel [001]$ and $\mathbf{P} \parallel [00\bar{1}]$ domains. We do not consider monodomain polarisation oriented in the out-of-plane directions ($\mathbf{P} \parallel [001]$ or $\mathbf{P} \parallel$

[†]This is as a result of increasing the supercell dimensions in the [010] direction as explained in Section 6.4.

[00 $\bar{1}$]) since a previous work has shown this is suppressed by the depolarising field within our range of thicknesses [90] (also verified to be true within our simulations). We characterise the competing energetics of the different film geometries as well detailing the resulting polar morphologies, interactions with the surface reconstruction and other structural features.

In the second part, we investigate the interaction of engineered surface trenches with the ferroelectric domain structure in an exemplar polydomain and free standing PTO film. Although we have previously noted that such a geometry is fictitious, its weakness is also its strength. That is, with this geometry, the effects of interfacial substrate chemistry are removed. Also, should we symmetrically terminate our films (the upper and lower surface feature a trench; as they do in this chapter), we can minimise effects from local inversion symmetry breaking in the out-of-plane directions. This way, we can study effects intrinsic to PTO itself, disentangled from these other effects, as we aim to do in this study. We choose the $N_z = 7$ film for this study since (for shallow trenches) it is thick enough to limit (although not eliminate) trench-trench interactions between the upper and lower surfaces of the film. We treat three arrangements for the orientation of the surface trenches: trenches running parallel to the DW positioned over the DW (\parallel^{wall}), trenches running parallel to the DW positioned over the domain centroid ($\parallel^{\text{centroid}}$) and trenches running perpendicular to the DW ($\perp + \text{AFD}$: the reason this orientation features AFD modes is discussed in Section 6.2.6.2). For each of these cases the width of the trench is held constant (two unit cells across) but we vary the depth at $d = 1, 2$ and 3 unit cells for each arrangement. We determine the most energetically favourable orientation of the trenches relative to the DW and report on the perturbations to the domain structure compared to the film without trenches.

The remainder of this chapter is organised as follows: Section 6.2.1 presents finer details associated with the simulation method. In Section 6.2.2, we provide a careful convergence study for the parameters of the multi-site support function (MSSF) expansion. Then, in Section 6.2.3, we perform convergence tests for the truncation range of the density matrix used in the $\mathcal{O}(N)$ calculations. Section 6.2.5 details the treated film geometries for PTO films on STO substrates (including a study for selecting the appropriate amount of STO substrate) while Section 6.2.6 details the geometries used in free standing film calculations with surface trenches. Section 6.3 discusses the results of the first study: PTO films on STO substrates. Within this study, in Section 6.3.1, we compare the competing energetics between each film geometry as a function of thickness. Next, in Section 6.3.2, we present the local polarisation fields of the various film geometries. The results of this first study finish in Section 6.3.3 where we detail the amplitudes of local AFD modes, including the $c(2 \times 2)$ surface reconstruction. Also in this section, we analyse the coupling of AFD modes with surface polarisation and the asymmetrical rumpling of surface/interfacial Pb cations. Section 6.4 pertains to the results of the second study: simulations of free standing PTO films with surface trenches. Within this study, in Section 6.4.1, we discuss the relative stabilities of the various trench orientations and trench depths. In Section 6.4.2, we discuss the contribution to the alignment mechanism from the minimisation of depolarising fields

near the trenches. Then, in Section 6.4.3, we consider the effects of the strain fields found in the vicinity of the trenches. We conclude this chapter in Section 6.5; marrying together the findings of each investigation, commenting on the impact this chapter has on the field and suggesting new areas for which our novel large scale DFT methods are applicable.

6.2 Theoretical method

6.2.1 General details

This Section provides details common to both the MSSF calculations and those using the $\mathcal{O}(N)$ approach, both implemented within the CONQUEST code[†] [7, 17]. Parameters specific to these two methods are described in Sections 6.2.2 and 6.2.3 respectively. Simulations use the local density approximation (LDA) as parameterised by Ceperley, Alder, Perdew and Zunger [215, 217] to describe exchange and correlation effects. This functional has recently been shown to perform well against higher rung functionals for describing some important features of the perovskite oxides [171]. Specifically, although both hybrid and meta-GGA functionals better predict the experimental structural properties, they still overestimate the bulk polarisation of PTO. Since this is the primary order parameter of our system, LDA is a good choice as the magnitude of the overestimate is much less. Optimised Vanderbilt norm-conserving pseudopotentials are used to replace core electrons [232, 233]. We use the scalar-relativistic variety available in the PseudoDojo library (v0.4) [230]. These are used as an input for the ONCVSP code (v3.3.1) [233]. These pseudopotentials include the Pb 5d 6s 6p, Sr 4s 4p 5s, Ti 3s 3p 4s 3d and the O 2s 2p states respectively. While many real-space integrals are performed using intuitive analytic operations [247], some are performed on a fine, regular integration grid with a plane wave equivalent cutoff of 300 Ha. Each of the structures in Sections 6.2.5 and 6.2.6 are fully relaxed with quenched molecular dynamics until the maximum absolute value of the force on every atom falls below 0.01 eV/Å. Supercells which feature asymmetric surface terminations can give rise to a small dipole moment in the out-of-plane direction which propagates to a small spurious electric field across the supercell. Those supercells suffering from this are corrected with the dipole correction scheme of Bengtsson [390].

6.2.2 Multi-site support functions

Simulations of PTO on an STO substrate presented in Section 6.3 use the MSSF method [18, 19] (as described in Chapter 3, Section 3.4.5) in tandem with $\mathcal{O}(N^3)$ scaling diagonalisation. These simulations require reciprocal space integrations which are performed on $6/N_x \times 6/N_y \times 1$ uniform meshes as described by Monkhorst & Pack [227] where $N_{x,y}$ are the number of

[†]The versions of CONQUEST and the basis generation code used in this chapter are from the beta which predates the official release.

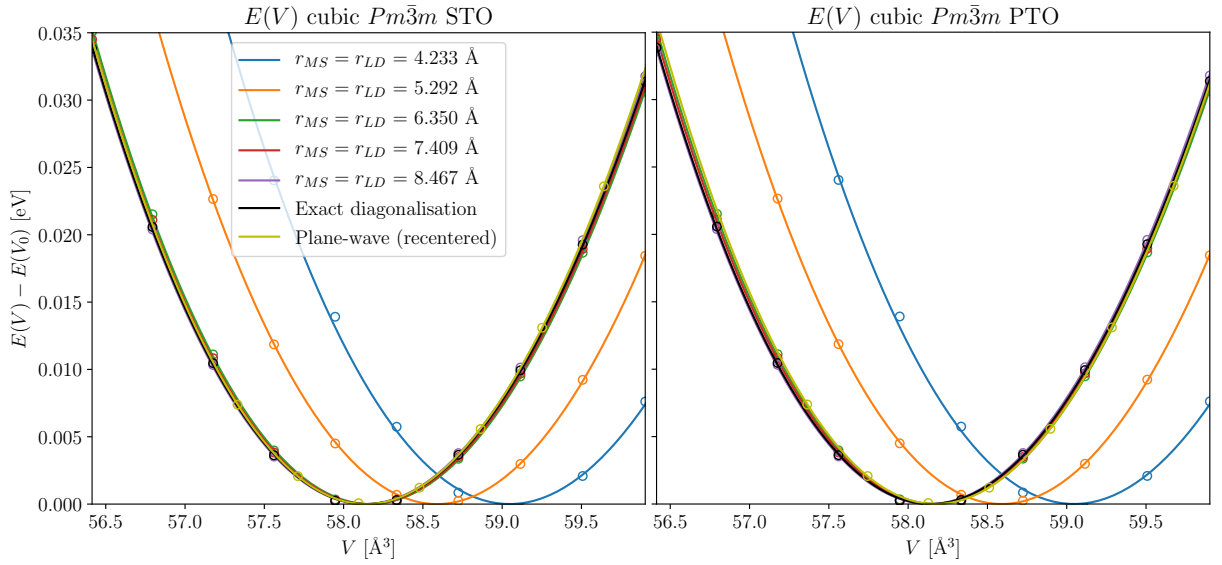


Figure 6.1: The equations of state $E(V)$ for the cubic phases of STO (left) and PTO (right) using different $r_{MS} = r_{LD}$. We also include $E(V)$ for the exact diagonalisation of PAOs (where the MSSF contraction has not been made) and the $E(V)$ (PW) result obtained from a plane wave calculation using the same pseudopotentials. The PW curve has V_0 shifted to agree with the minimum of the exact diagonalisation calculation so a better comparison can be made of the energetics. The true lattice constants can be found in Table 6.1.

perovskite unit cells included in the [100] and [010] directions of the supercell respectively[‡]. We use a double- ζ plus double-polarisation (DZDP) basis set of pseudo-atomic orbitals (PAOs) to expand the states of the pseudopotential. We also include the Pb 6d, Sr 4d, Ti 4p and the O 3d as polarisation orbitals aimed at increasing the angular flexibility of the basis. Ti 3s, Ti 3p and Pb 5d orbitals are treated as semi-core states described only with a single ζ . The exact details of the PTO basis sets used were described in Chapter 5, Section 5.3.5 while the Sr basis was generated with the default equal radii construction.

We have performed a convergence study for the parameters of the MSSF method. r_{MS} and r_{LD} were increased subject to $r_{MS} = r_{LD}$ and the Birch-Murnaghan [357] equations of state (Equation 5.1, Chapter 5) for cubic $Pm\bar{3}m$ PTO and STO were calculated. These curves are shown in Figure 6.1 and the fit parameters are recorded in Table 6.1. We also include on each figure the equation of state obtained with a plane wave basis set using the same pseudopotential as performed with the ABINIT code (v8.10.3) [310, 311]. We see that by $r_{MS} = r_{LD} = 6.350\text{\AA}$ there is excellent agreement with the exact diagonalisation and plane wave calculation. The lattice constants (calculated from the EOS fit - not lattice vector optimisation which produces a slightly different result) beyond $r_{MS} = r_{LD} = 6.350\text{\AA}$ also agree with the plane wave calculations, achieving errors of +0.51% and +0.52% for PTO and STO respectively. We see also that the Bulk modulus is well described by the PAO basis sets offering errors of -3.55%

[‡]We do not explicitly shift meshes with even in-plane dimensions to be centered on Γ while those with odd dimensions are naturally centered on Γ . The (marginal) effect of this choice is studied in Appendix A.2.

	V_0 [\AA^3]	a_0 [\AA]	B_0 [GPa]	B'_0
<i>Pm</i> $\bar{3}$ <i>m</i> PTO				
$r_{MS} = r_{LD} = 4.233\text{\AA}$	60.224	3.920	204.112	4.592
$r_{MS} = r_{LD} = 5.292\text{\AA}$	59.824	3.911	201.377	5.421
$r_{MS} = r_{LD} = 6.350\text{\AA}$	59.577	3.906	199.333	5.371
$r_{MS} = r_{LD} = 7.409\text{\AA}$	59.566	3.905	198.941	5.332
$r_{MS} = r_{LD} = 8.467\text{\AA}$	59.549	3.905	198.653	5.360
Exact diagonalisation	59.547	3.905	198.743	5.274
PW	58.616	3.885	206.659	4.656
<i>Pm</i> $\bar{3}$ <i>m</i> STO				
$r_{MS} = r_{LD} = 4.233\text{\AA}$	59.046	3.894	197.298	5.518
$r_{MS} = r_{LD} = 5.292\text{\AA}$	58.589	3.884	206.681	2.410
$r_{MS} = r_{LD} = 6.350\text{\AA}$	58.168	3.875	201.291	4.629
$r_{MS} = r_{LD} = 7.409\text{\AA}$	58.157	3.874	200.872	4.558
$r_{MS} = r_{LD} = 8.467\text{\AA}$	58.133	3.874	200.847	4.651
Exact diagonalisation	58.142	3.874	200.186	4.653
PW	57.225	3.854	201.395	4.095

Table 6.1: The values of the equilibrium volumes V_0 , equilibrium lattice constants a_0 , bulk moduli B_0 and bulk modulus derivatives B'_0 as obtained from a least squares fit of $E(V)$ to the Birch-Murnaghan equation of state. Exact diagonalisation refers to the result obtained without the MSSF contraction, i.e. the Hamiltonian is built with primitive PAOs with dimensions $N_{\text{PAO}} \times N_{\text{PAO}}$ like in Chapter 5.

and -0.05% respectively. Finally, we note that all PAO calculations overestimate (by a small amount) the bulk modulus derivative $B'_0 = (\partial B/\partial P)_{P=0}$. This is of little impact however since the Birch-Murnaghan equation of state is not particularly sensitive to B'_0 . Note, for example, that the exact diagonalisation and plane wave curves of Figure 6.1 are rather indistinguishable but differ by $\approx 13\%$ in B'_0 . We proceed using $r_{MS} = r_{LD} = 6.350\text{\AA}$. This yields the cubic $Pm\bar{3}m$ lattice constants of PTO and STO (a_{PTO} and a_{STO}) as 3.904\AA and 3.874\AA respectively. Further, the tetragonality (c/a) of FE $P4mm$ PTO is obtained as 1.036 producing a spontaneous polarisation of $79.02 \mu C/cm^2$ as calculated with Resta's method [66, 147] within the *modern theory of polarisation*. This method is equivalent to the Berry phase [64] formula of King-Smith and Vanderbilt [65] in the limit of large cells; we use 10 PTO unit cells in the direction of the FE distortion to achieve convergence.

6.2.3 Linear scaling

Simulations of free standing PTO films with surface trenches presented in Section 6.4 use the two part $\mathcal{O}(N)$ scaling algorithm [262, 266, 267] as implemented in the CONQUEST code [7, 17]. The full details of this method were described in Chapter 3, Section 3.4.6. The $\mathcal{O}(N)$ solver requires an inverted overlap matrix, \mathbf{S}^{-1} . This is completed with Hotelling's method [391] where we truncate the range of \mathbf{S}^{-1} to 6.35\AA . This choice inverts \mathbf{S} to a tight tolerance of 1×10^{-5} . For the second part of the algorithm (the density matrix minimisation (DMM) stage [262]), the minimisation tolerance is set to 1×10^{-6} . Self consistency is achieved in tandem with the second stage using the *mixed-L-SCF* scheme described in Chapter 3, Section 3.4.6.2. As we currently encounter problems with numerical instability when inverting the overlap matrix for multiple- ζ PAO basis sets, we instead use a single- ζ plus polarisation (SZP) basis set for these simulations. This basis set is comprised of the PAOs discussed in Section 6.2.2 with the second ζ removed. At the exact diagonalisation level, this returns the cubic $Pm\bar{3}m$ lattice constant of PTO as 3.909\AA and the c/a ratio of the FE $P4mm$ phase as 1.043. Both of these figures are only slightly enlarged when compared to the previously mentioned figures for the DZDP basis; use of the SZP basis retains structural accuracy. The same is not true for the relative stability of $P4mm$ versus $Pm\bar{3}m$, however. This is now underestimated at -88.86 meV/FU compared with same figure calculated with the DZDP basis (-47.91 meV/FU).

To allow for $\mathcal{O}(N)$ scaling, a further approximation must be made. That is, we must choose a truncation range for the density matrix (DM). We perform a careful convergence study for the total energy of the $Pm\bar{3}m$ and $P4mm$ phases and the energy difference between them. This is shown in Figure 6.2 where these energies are shown as function of increasing DM range using the structures optimised at the exact diagonalisation level. To find a balance between accuracy and efficiency, we choose to truncate the range of the DM at 10.58\AA ($20 a_0$). According to Figure 6.2, this decreases the energy difference to -106.89 eV/FU . This is not the complete story however as these calculations used the structures optimised at the exact diagonalisation

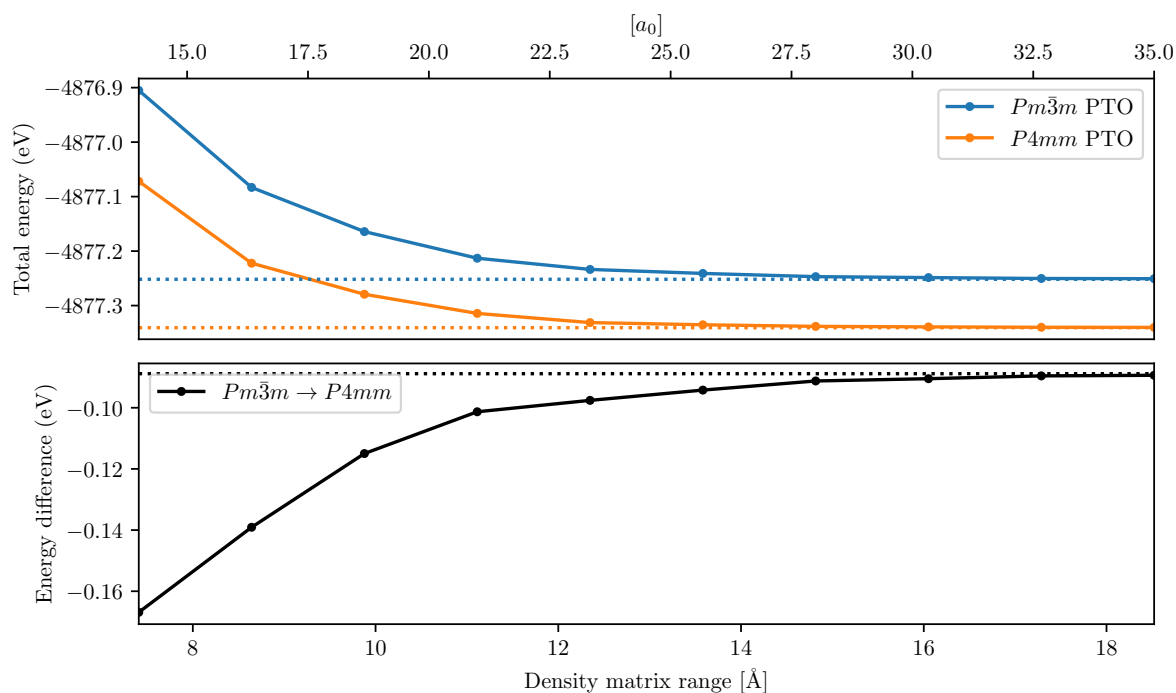


Figure 6.2: The total energy (upper) for $Pm\bar{3}m$ and $P4mm$ PTO and the energy difference (lower) between them as a function of increasing DM range. Horizontal dashed lines mark the total energy/energy difference from exact diagonalisation.

level. When we alter the DM range, we *slightly* alter the position of minima on the DFT total energy surface; DM truncation defines a (slightly) different optimal structure. At the new relaxed minima, the $Pm\bar{3}m$ lattice constant is 3.910 \AA and the tetragonality of the $P4mm$ phase is 1.046 . The energy difference also widens slightly to -113.33 meV . It is clear that the accuracy in precise figure for the energy difference is *not* retained with this smaller basis. However, the general hierarchy of the energetics *are* retained and the structures themselves do not deviate strongly from the DZDP level. When we assess the preferred orientation or surface trenches to the DW, this means we can have good confidence in the relaxed structure of the film and the energetic hierarchy of trench orientations. However, the precise energy difference between the different trench orientations will be only an estimate. Since we are only concerned with which orientation is the most favoured and with the atomistic structure, this is not an issue.

6.2.4 The local polarisation

To analyse the different polar morphologies within our ultrathin PTO films, it is useful to be able to access the magnitude of local dipole moments. One way for doing so is to use the linear approximation of Resta [66] (as was discussed in Chapter 2, Section 2.7) for the *local*

polarisation; the local dipole moment normalised by the volume of the local unit cell

$$\mathbf{P}^{(i)} = \frac{e}{\Omega_c} \sum_{\alpha} w_{\alpha} \mathbf{Z}_{\alpha}^* \cdot \mathbf{u}_{\alpha}^{(i)} \quad (6.1)$$

for local unit cell i , local unit cell volume Ω_c , atom index α , Born effective charge tensor \mathbf{Z}_{α}^* , local atomic displacements from the idealised *cubic* bulk positions $\mathbf{u}_{\alpha}^{(i)}$ and atomic weight factor w_{α} which is related to how many atoms α belong to the local cell i (which we choose to be 5). We must carefully note, however, that there are several choices for the local 5-atom unit cell i . These choices are discussed in [392]. We chose to work with two ABO_3 cells, the B-centered unit cell (where the A-site is at the origin) and the A-centered unit cell (where the B-site is at the origin). This allows for the calculation of local polarisation vectors centered at the both the metal cation sites. For the B-centered cells, we have the atomic weight factors $w_B = 1$, $w_A = 1/8$ and $w_O = 1/2$. For the A-centered cells we have $w_B = 1/8$, $w_A = 1$ and $w_O = 1/2$.

The Born effective charge tensors were calculated for cubic bulk PTO and STO using finite differences in the macroscopic polarisation. We do so by displacing each of the symmetry inequivalent sites within a $5 \times 5 \times 5$ supercell of PTO and STO a small amount (0.005 Å) and calculating the resulting polarisation with Resta's method [147]. For consistency, we use the $r_{MS} = r_{LD} = 6.35 \text{Å}$ MSSF contraction in the calculation. For PTO, the 3x3 symmetrical diagonal tensor has elements $\mathbf{Z}_{Pb, PTO}^* = 3.89$ and $\mathbf{Z}_{Ti, PTO}^* = 7.08$ while O is

$$\mathbf{Z}_{O, PTO}^* = \begin{bmatrix} -5.79 & 0 & 0 \\ 0 & -2.58 & 0 \\ 0 & 0 & -2.58 \end{bmatrix}.$$

For STO, the 3x3 symmetrical diagonal tensor has elements $\mathbf{Z}_{Sr, STO}^* = 2.55$ and $\mathbf{Z}_{Ti, STO}^* = 7.17$ while Oxygen is

$$\mathbf{Z}_{O, STO}^* = \begin{bmatrix} -4.95 & 0 & 0 \\ 0 & -1.92 & 0 \\ 0 & 0 & -1.92 \end{bmatrix}.$$

All of these tensors agree well with the plane wave result for this functional [162]. We note also the elements of the Oxygen tensors reorder based on which site in the local unit cell we are considering. We use these tensors for calculations of the local polarisation for the MSSF and linear scaling calculations. For the latter, we accept that these tensors will vary a small amount as we change basis set from DZDP to SZP and impose a truncation range for the DM. Since (i) we only expect this change to be small and (ii) this method is only used to provide an estimate, this is of little concern.

While this method is now used often in the field [175, 392], a drawback of this method is that a local unit cell cannot always be found. That is, at the film surface, there will always be an

incomplete unit cell. For this reason, our calculations always finish with a vector centered on Ti and *not* Pb, despite treating the PbO termination. At the PTO/STO interface, there is also a hybrid unit cell with half its A-sites being Pb and half being Sr. For this area, we define no local polarisation vectors.

6.2.5 Supercell configurations: PTO on STO

The film geometries treated for simulations of PTO on an STO substrate are displayed in Figure 6.3. Universal to all structures is a fixed amount of STO substrate. We must then perform a careful convergence study to identify the appropriate amount of included SrO/TiO₂ monolayers. We perform our tests on the paraelectric phase of the $N_z = 2$ film by including successively more SrO and TiO₂ monolayers in the substrate and relaxing each film to a force tolerance of 0.01 eV/Å. We then measure the vertical displacements Δz on the film metal cations from their initial positions and check for convergence as function of the number of substrate monolayers. The results are shown in Figure 6.4. It can be seen that Pb cations relax towards the substrate whilst Ti Cations relax away from it. This behaviour is only qualitatively achieved beyond $N_{ML} \approx 4$ with the exact positions stabilising beyond $N_{ML} \approx 11$. This suggests that $N_{ML} \geq 11$ should provide a sufficient amount of substrate for our simulations. We do, however, decide to include an additional 4 monolayers ($N_{ML} = 15$) to allow further ‘breathing room’ for ferroelectric distortions that could penetrate into the substrate when simulating polar phases. While this does come at the computational cost of an extra $10N_xN_y$ atoms, this is a necessary precaution.

An interfacial region $a_I = 1/2(a_{\text{STO}} + c_{\text{PTO}})$ exists between the first PbO layer and last SrO layer which we treat independently of the film and substrate. The in-plane components of the supercells are held to integer multiples of a_{STO} . The two bottom-most monolayers of the substrate have their atomic positions fixed in structural relaxations. These measures ensure we are applying a realistic mechanical strain to the PTO film as well as simulating the effects of a semi-infinite substrate. To limit unfavorable interactions between images of the film in the [001] direction, we introduce a total of 20Å of vacuum. These supercells have the generalised dimensions $\{N_x a_{\text{STO}}, N_y a_{\text{STO}}, 7a_{\text{STO}} + a_I + N_z c_{\text{PTO}} + 20\text{Å}\}$. We simulate films of thickness $N_z = 0, 1, 2, 3, 5, 7$ and 9 formula units of PTO where a thickness of 0 corresponds to a single PbO monolayer. Films of $N_z \geq 3$ unit cells were increased in steps of two unit cells such that the equilibrium domain period predicted by Kittel scaling could increase by an even integer number of unit cells (a requirement for domains to have an equal number of unit cells). This range of film thicknesses could encompass different energetically stable geometries including a transition between FE monodomain, polydomain and possible intermediate phases. It also spans low dimensional films with strong interface coupling with such effects decreasing with increased thickness.

We choose to treat the following supercell configurations with *and without* the influence of AFD modes (note also that structures treated without these modes do not show the $c(2 \times 2)$

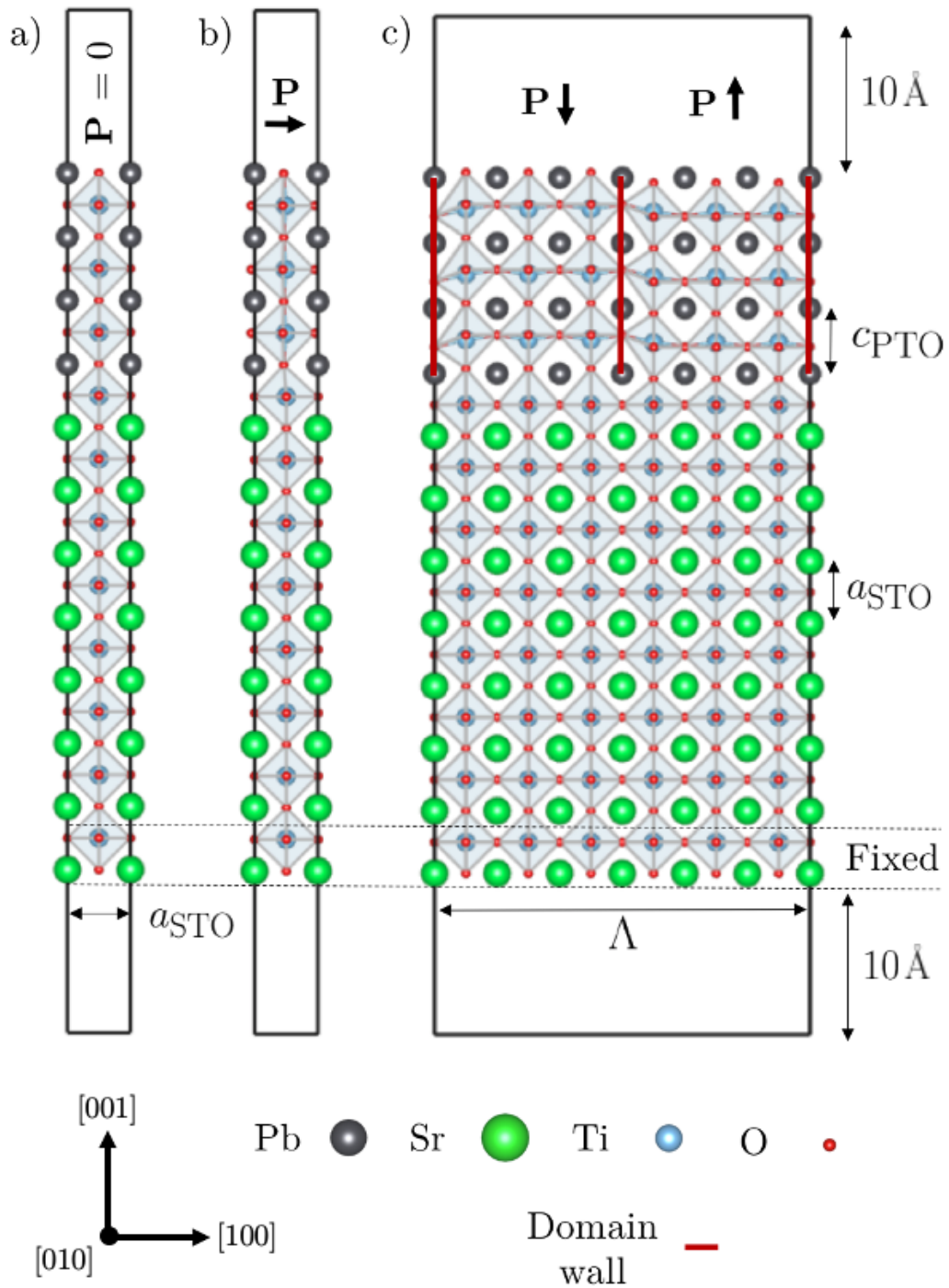


Figure 6.3: The initial supercell configurations for the $N_z = 3$ films before structural relaxation. Shown here are the supercells *not* including AFD modes. Each configuration is however also treated with AFD modes following the explanation in Section 6.2.5. a) The paraelectric supercell constrained such that spontaneous polarisation cannot emerge. b) The monodomain in-plane ferroelectric case ($\mathbf{P} \parallel [100]$ is shown here, but we also treat $\mathbf{P} \parallel [110]$) constrained such that spontaneous polarisation cannot develop in the out-of-plane direction. c) The polydomain ferroelectric case with equally sized up and down domains for the ferroelectric polarisation. Shown here is the $\Lambda = 6$ case.

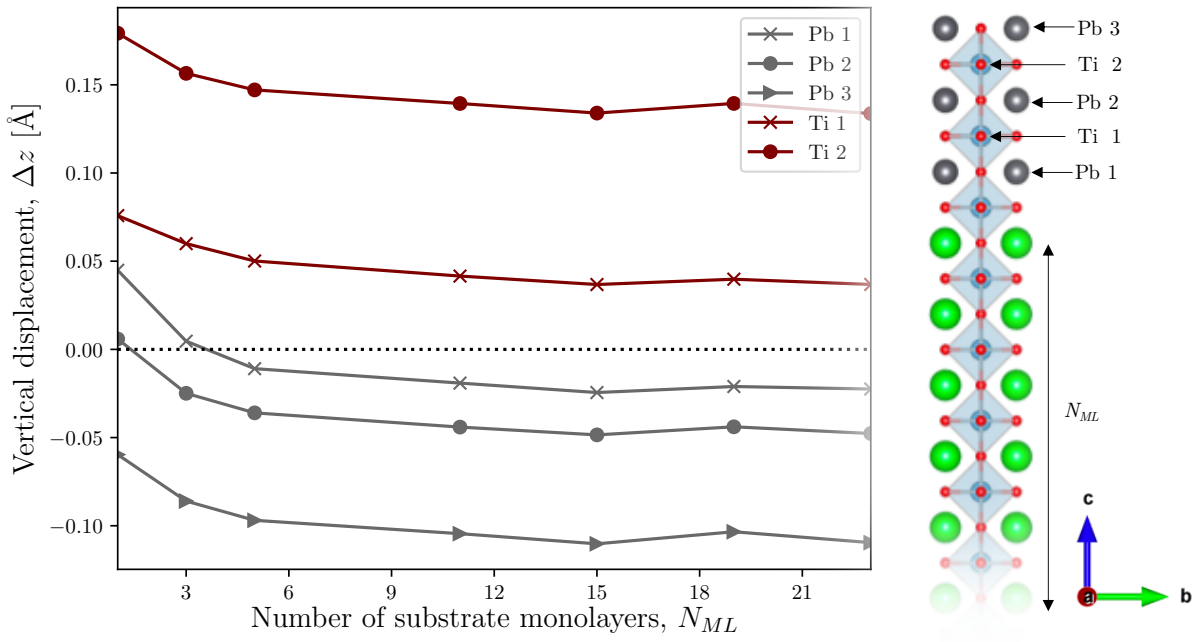


Figure 6.4: The displacements of metal cations from their initial positions (described in the main text) as a function of the number of included substrate monolayers, N_{ML} .

surface reconstruction). To do so, we must set $N_y = 2$ and have N_x set to multiples of 2. The important AFD distortions for both STO and PTO are the zone-boundary R_4^+ and M_3^+ modes. The former is equivalent to a $a^0a^0c^-$ Glazer tilt system [45, 46] while the latter is $a^0a^0c^+$. The former has been found previously to be the most energetically favorable so we do *not* treat the M_3^+ mode [393]. The R_4^+ mode can be defined with a single rotation angle θ_z as shown in the inset of Figure 6.5. We find that the angles $\theta_z = 6.21^\circ$ and $\theta_z = 4.52^\circ$ (Figure 6.5) define minima in the energy of the cubic supercells of STO and PTO respectively. Since simulations are performed with the in-plane lattice constants of STO, we initialise supercells with the optimal strained PTO rotation angle $\theta_{z,\sigma} = 5.20^\circ$ as found in the tetragonal supercell. These results indicate that strains of $< 1\%$ in PTO are able to both increase the optimal θ_z and increase the depth of the energy minima. These angles overestimate what is seen in experiment. For $I4/mcm$ STO, $\theta_z \approx 2.1^\circ$ [394] while AFD modes are not observed in the PTO bulk. Calculations using hybrid functionals have been able to improve this angle for STO ($\theta_z = 1.9^\circ$ [395]) but are not used in this study in part because of the computational cost but also due to the aforementioned overestimate in the bulk polarisation of PTO.

6.2.5.1 Paraelectric

First we consider films of the high symmetry, paraelectric, non-polar variety (Figure 6.3a). These supercells are initialised by PTO formula units with the high symmetry cubic fractional atomic positions and optimal cubic out-of-plane lattice constant $c_{\text{PTO}} = 3.904\text{\AA}$. Although spatial inversion symmetry is intrinsically broken by the composition of our supercells, we

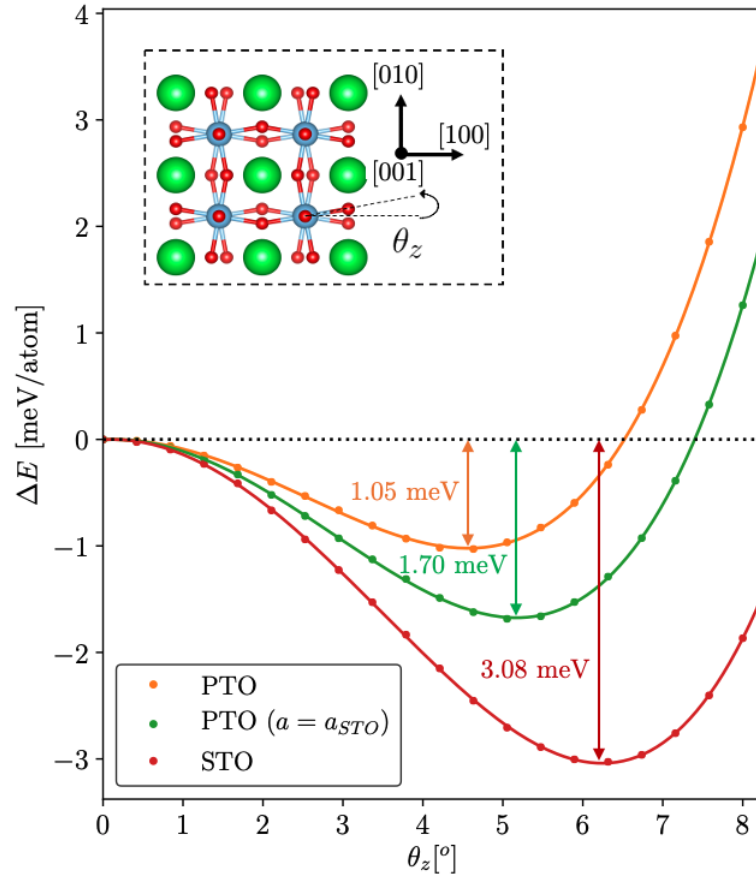


Figure 6.5: Energy versus the R_4^+ mode rotation angle θ_z for PTO at its bulk cubic lattice constants, strained PTO with $a = b = a_{STO}$ ($\sigma = -0.78\%$) and STO at its bulk cubic lattice constants. Calculations here are in full periodic boundary conditions in the infinite bulk crystal. The coefficients of quartic polynomials are evaluated with a least squares fitting procedure and plotted as lines. *Inset* An illustration demonstrating the R_4^+ rotation angle θ_z shown here for STO. The same angle persists in PTO.

constrain atomic relaxations of these films to the lowest symmetry space group ($P4mm$) carefully preventing any cation-anion counter motion. This allows for the most degrees of freedom in relaxations without incurring any intrinsic ferroelectric polarisation. It is the purpose of these films to provide a baseline for the relative stability of polar phases.

6.2.5.2 Monodomain in-plane ferroelectric

In this supercell, we allow monodomain ferroelectric polarisation to develop in the $[100]$ and $[110]$ directions (Figure 6.3b). PTO formula units retain the same c_{PTO} as the paraelectric case but atomic positions now correspond to the Γ_4^- mode of the primitive cubic PTO unit cell orientated in the $[100]$ direction. This induces a ferroelectric polarisation of $56.9 \mu C/cm^2$ in the infinite bulk as calculated with the method described in Section 6.2.1. To create $[110]$ polarisation, we simply displace the metal cations along the $[110]$ direction and displace Oxygen anions along the $[\bar{1}\bar{1}0]$ direction proportional to the magnitude of the bulk Γ_4^- mode. During structural relaxation, we apply symmetry constraints to prevent the development of out-of-plane polarisation [380], although, we expect that the non-trivial depolarising field that would result naturally suppresses it.

6.2.5.3 Polydomain ferroelectric

Here we consider films initialised with a striped domain structure consisting of alternating regions of PTO polarised in the $[001]$ and $[00\bar{1}]$ directions which we will from this point onwards refer to as up and down domains respectively (Figure 6.3c). Up and down domains are equal in size ($N_{up} = N_{down}$) and together form a full domain period Λ . Equivalently, $N_{up} + N_{down} = N_x \equiv \Lambda$. Domain walls are chosen to be centered on the PbO plane. This choice, however, is arbitrary as the energy difference between this and the TiO_2 centering is found to be ~ 1 meV per unit cell [172]. This is (slightly) beyond the resolution of our calculations, a fact noted in a comparable study [175].

It is found that there is a minimum thickness of film for this type of ferroelectricity to occur. Theoretical results of the free standing PTO film have shown that the polydomain ferroelectric film is lower in energy than the paraelectric configuration [172] but make no account of possible monodomain in-plane orientations for the polarisation. In experiments conducted with an STO substrate [33] it was found that that the polydomain configuration was only observed above 3 unit cells in thickness (in the temperature range of 311-644K). We also confirm that no out-of-plane component of \mathbf{P} remains after structural relaxation of polydomain $N_z = 1$ and 2 films ($\Lambda = 4$). We then only present results for this configuration for those films with thicknesses $N_z \geq 3$. PTO unit cells are initialised with the strained FE $P4mm$ unit cell. When the in-plane constants are constrained to a_{STO} , this results in $c = 4.049\text{\AA}$ and a slightly enhanced polarisation of $80.07 \mu C/cm^2$.

An accurate account for the polydomain structure requires us to work at the equilibrium domain period. To avoid the need to manually find this domain period for each thickness (which would require us to simulate several domain periods for each film thickness), we use knowledge from previous experimental and theoretical data. In particular, we find that both theory and experiment agree upon $\Lambda = 6$ when $N_z = 3$ [33, 172]. We use X-ray diffraction data [32] for the remaining film thicknesses. We choose the nearest even number of unit cells (to preserve the periodicity of the AFD rotation pattern) corresponding to the experimental domain periods. We then have for the $N_z = 3, 5, 7, 9$ films, domain periods of $\Lambda = 6, 8, 10, 12$ unit cells respectively. Films of this configuration are free from constraints during structural relaxation.

In a study of monodomain out-of-plane polarisation, it was found that $\mathbf{P} \parallel [00\bar{1}]$ (towards the STO substrate) becomes more polar than $\mathbf{P} \parallel [001]$ [90] (towards the vacuum). For polydomain films, this could mean that up domains are less polar than down domains. This would result in a small net dipole moment in the $[00\bar{1}]$ direction (and a spurious electric field) developing during structural relaxation which is corrected for using the scheme described in Section 6.2.1.

6.2.6 Supercell configurations: trenches on free standing PTO

Simulations assessing the impact of surface trenches are performed using the free standing film geometry of the $N_z = 7$ PTO film. Although no explicit STO substrate is present, we still choose to impose an in-plane strain equivalent to the experimental mismatch of the PTO and STO lattice constants (1.2%). This strains the system at a level coincident with the experimental observations of domain wall alignment [34]. At the PTO unit cell level, this sets the in-plane constants (a and b) of the $P4mm$ phase as $a'_{\text{STO}} = 3.848 \text{ \AA}$. Should we hold these constant and relax the c -axis and the atomic coordinates in the bulk, we obtain a PTO cell with a tetragonality of 1.077. A linear estimate of the polarisation (following the discussion in Section 6.2.4) is then $102.81 \mu\text{C}/\text{cm}^2$, increased from $87.75 \mu\text{C}/\text{cm}^2$ in the unstrained case. This strained unit cell is used to initialise the domain structure.

For these supercells (unlike the supercells described in Section 6.2.5) we choose to work at exactly the theoretical equilibrium domain period. We make this choice because in comparison with the films on substrates, there are fewer atoms in the supercell of a free standing film and only one thickness of film to treat; the task is much less labour intensive. To find this, we build four PbO terminated films with $\Lambda = 8, 10, 12$ and 14 where the domain wall (as before) is centered on the PbO plane and a vacuum space of 20 \AA is included. We relax each structure and compare the energy to the paraelectric film. The results are shown in Figure 6.6. We see that the equilibrium Λ is 12 unit cells, slightly larger than the period of 10 which we extrapolated for the films mounted on substrates in the previous section. This result gives us increased confidence in our theoretical method as, in line with experiment, we predict the polydomain phase to be more stable than the paraelectric phase. Indeed, we also find it to be lower in energy than monodomain polarisation oriented along the $[100]$ direction. The relaxed structure of the $\Lambda = 12$ film is used

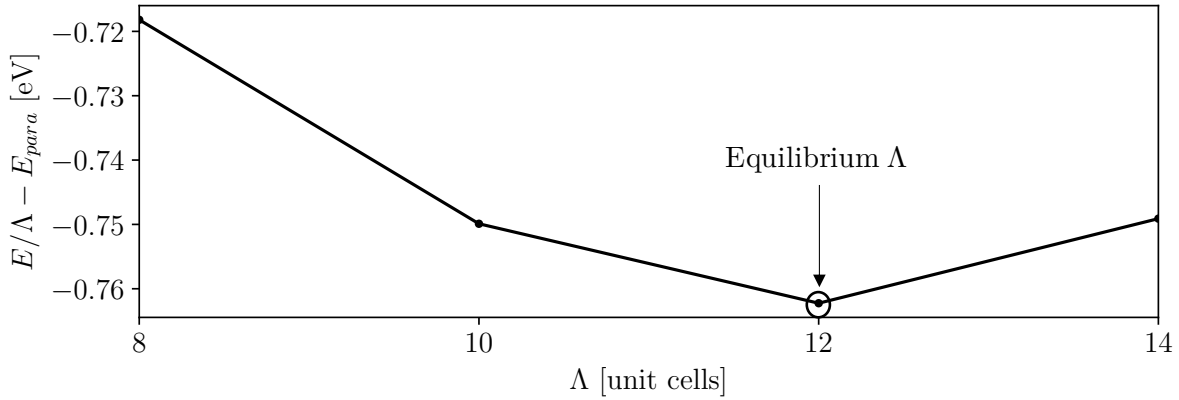


Figure 6.6: The energy difference between free standing $N_z = 7$ polydomain films and the paraelectric film as a function of domain period Λ . The equilibrium period is found at $\Lambda = 12$.

to prime the supercells in Sections 6.2.6.1 and 6.2.6.2. Like another work studying free standing films [172] we see the emergence of the flux-closure domain morphology. We show the local polarisation field of this relaxed structure in Figure 6.7. We draw the readers attention to the equal magnitudes of polarisation along the up and down domain centroids. This occurs since inversion symmetry is intact for this supercell; a symmetry which is compositionally broken when films are mounted on substrates in Section 6.3.

6.2.6.1 Trenches parallel to domain walls

We treat two types of film where the surface trench runs parallel to the domain wall. The first is shown in Figure 6.8a. Here, the trench is positioned above the domain wall and an identical trench is positioned on the other surface below the domain wall. We refer to this film as \parallel^{wall} . The second is shown in Figure 6.8b. This is the same as described for the first case but the trench has been shifted to run along a domain centroid. We refer to this film as $\parallel^{\text{centroid}}$. While Figure 6.8b shows the trench over the down domain, we remind the reader that our films feature trenches on both surfaces of the free standing film and that up and down domains are equivalent by symmetry in this arrangement. For both of these geometries, we treat trenches of depth $d = 1, 2$ and 3 unit cells. The $d = 1$ case is shown in Figure 6.8d. To increase d by one, we remove another PbO and TiO_2 layer from the floor of the trench. This set of d defines all of the possible depths in increments of one unit cell before the two symmetrical trenches would tunnel through the film entirely. Note how our choices of trench depth *always* leave the film uniformly terminated at the PbO layer. The trench width is set to two unit cells for all cases. This choice of width allows trenches to be satisfactorily separated in the $[100]$ direction when the supercell is only Λ unit cells across. We choose an even number for the width so trenches can be exactly centered on the central PbO chain of the domain wall or centroid. The general form for the geometry of these supercells is then $\{12a'_{\text{STO}}, a'_{\text{STO}}, L + 20 \text{ \AA}\}$ where L is the z -dimension

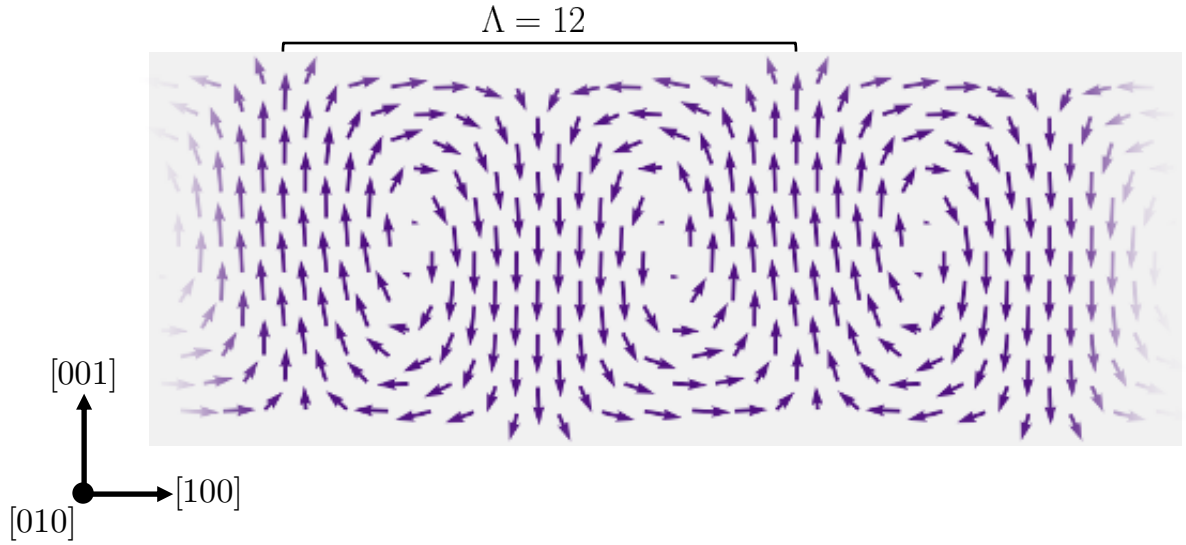


Figure 6.7: The local polarisation vector field of the relaxed $N_z = 7$ film at the equilibrium domain period $\Lambda = 12$ (as demonstrated in Figure 6.6).

of the relaxed and pristine $N_z = 7$ polydomain film. For each of the films listed so far, we also perform calculations with doubled [010] dimensions and break the symmetry at the surface as to invoke the $c(2 \times 2)$ surface reconstruction. We do this for a fair comparison in energy to the perpendicular arrangement (where the surface reconstruction naturally arises) described in the next section. The generalised dimensions of these films then become $\{12a'_{\text{STO}}, 2a'_{\text{STO}}, L + 20 \text{ \AA}\}$ which we denote as $\|\|_{4\Lambda}^{\text{wall}} + \text{AFD}$ and $\|\|_{4\Lambda}^{\text{centroid}} + \text{AFD}$.

We perform two further calculations greatly increasing the separation between trenches from Λ to 4Λ and treat both parallel arrangements ($\|\|_{4\Lambda}^{\text{wall}}$ and $\|\|_{4\Lambda}^{\text{centroid}}$). The general dimensions for this supercell then become $\{48a'_{\text{STO}}, a'_{\text{STO}}, L + 20 \text{ \AA}\}$. The goal here is to examine the effects of individual trenches rather than a short period array of them. With the trenches separated at this distance we will be able to see if strain and strain gradients at the surface of the film (resulting from the presence of a trench) persist at longer ranges. The [010] dimensions of these films do not permit AFD modes.

6.2.6.2 Trenches perpendicular to domain walls

We consider now a supercell where trenches run perpendicular to the domain wall, as shown in Figure 6.8c. As before, we treat trench depths of $d = 1, 2$ and 3 and hold constant the width at 2 unit cells. To achieve a trench separation consistent with the majority of the parallel trench arrangements, we must increase the supercell size in the [010] direction to give the generalised dimensions $\{12a'_{\text{STO}}, 12a'_{\text{STO}}, L + 20 \text{ \AA}\}$. These calculations are particularly demanding and can exceed 5,000 atoms in size. The even [010] periodicity and the broken symmetry resulting from the insertion of a trench naturally invokes the $c(2 \times 2)$ surface reconstruction for these films.

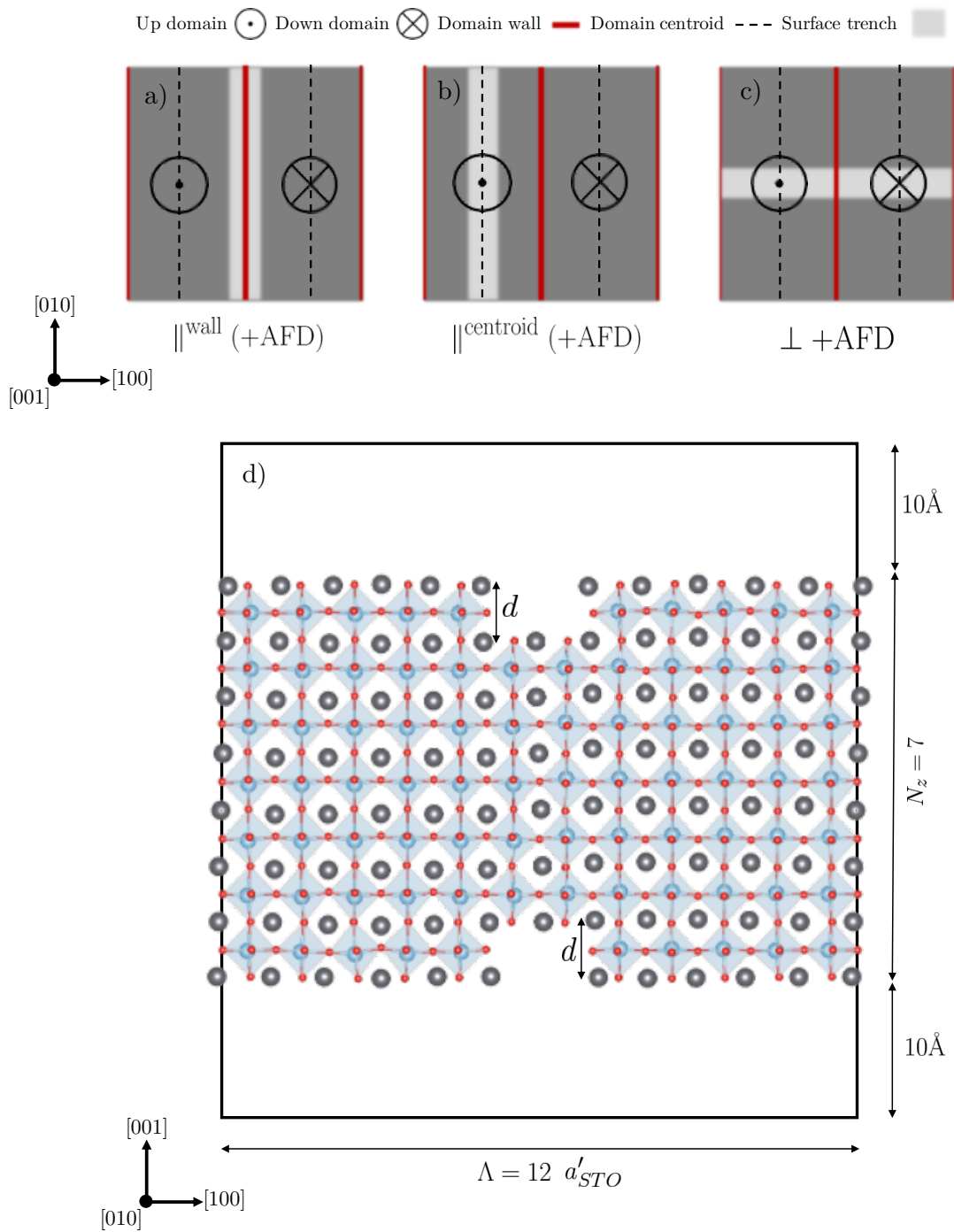


Figure 6.8: a-c) Bird's eye views for surface trenches on an ultrathin PTO film. Each trench arrangement is shown with its label which was assigned in the text. +AFD is bracketed in (a) and (b) as these trench configurations are treated with and without AFD modes. (a) Parallel to the domain wall, positioned over the domain wall: \parallel^{wall} . (b) Parallel to the domain wall, positioned over a domain centroid: $\parallel^{\text{centroid}}$. (c) Perpendicular to the domain wall: \perp +AFD. The reason this arrangement always includes AFD modes is discussed in the main text. d) Looking down the axis of a surface trench on the $N_z = 7$, $\Lambda = 12$ film. This example is the configuration shown in (a) looking down the [010] direction. Atom colouring follows the same key as Figure 6.3.

This must be considered when comparing the energetics to the parallel trench arrangements. We denote films of this type as $\perp + \text{AFD}$.

6.3 Results: PTO on STO

6.3.1 Competing phases

The relaxed film geometries considered in Section 6.2.5 have energetics which evolve as a function of film thickness. Figure 6.9 displays this behaviour indicating the favorability of different phases. We measure this favorability as the energy difference ΔE between the geometry of film in question and the paraelectric film. We choose to measure ΔE in meV/atom since the (more common) definition of meV/formula unit would vary with film thickness. This is because as the film thickness increases, the Pb/Sr fraction (upper axis of Figure 6.9) increases as an artefact of a fixed amount of STO substrate. As a result, we expect to see a component energy lowering from ferroelectric phases as we increase N_z since the energy of PTO is lowered with the onset of ferroelectricity (by 9.58 meV/atom in the bulk). We then expect to observe a rise in energy for purely AFD phases since the fraction of STO, favoring AFD modes, has decreased. The energetics of film thickness $N_z = 0$ are not present on Figure 6.9 since no ferroelectric phase was stable. Adding AFD rotations does however lower the energy compared to the paraelectric film by an amount similar to $N_z = 1$.

Considering first the monodomain in-plane ferroelectric films, Figure 6.9 shows that the favored axis for the polarisation is always [110] as was shown in a DFT study of the free standing film under compressive strain [396]. This is true with and without the influence of AFD modes. This favorable direction seems to diminish with film thickness becoming almost degenerate with [100] polarisation at $N_z = 7$ for the films *not* influenced by AFD modes. When AFD modes *are* taken into account, the degree of favorability for [110] polarisation (compared with [100]) almost doubles showing that [110] polarisation is far more compatible with $a^0a^0c^-$ rotations. We suggest that [110] polarisation is more favorable than [100] since $\mathbf{P} \parallel [100]$ is stunted by the epitaxial strain. An increased distortion along the longer diagonal axis of the supercell (of length $\sqrt{2}a_{\text{STO}}$) when compared with a distortion parallel to one of the pseudocubic axes (of length a_{STO}) relieves this stunting. We can also deduce whether coupling between AFD and FE modes is cooperative or competitive. The sum of ΔE for the FE [100] curve and the AFD curve (FE [100] + AFD (sum) on Figure 6.9) is always lower than the combined FE [100] + AFD curve (FE [100] + AFD (c) on Figure 6.9) where modes coexist. This indicates that the coupling is competitive with AFD modes suppressing FE ones and vice versa as is usually true for bulk modes. When making the same comparison for [110] polarisation (which is *not* observed in the bulk), however, the two curves are very similar. This suggests that FE and AFD modes are at worst independent of one another, but, for $N_z = 2$ or 3 are mildly cooperative, with the FE [110] + AFD (c) curve being lower in energy than the sum by ≈ 0.2 meV/atom (close to the resolution

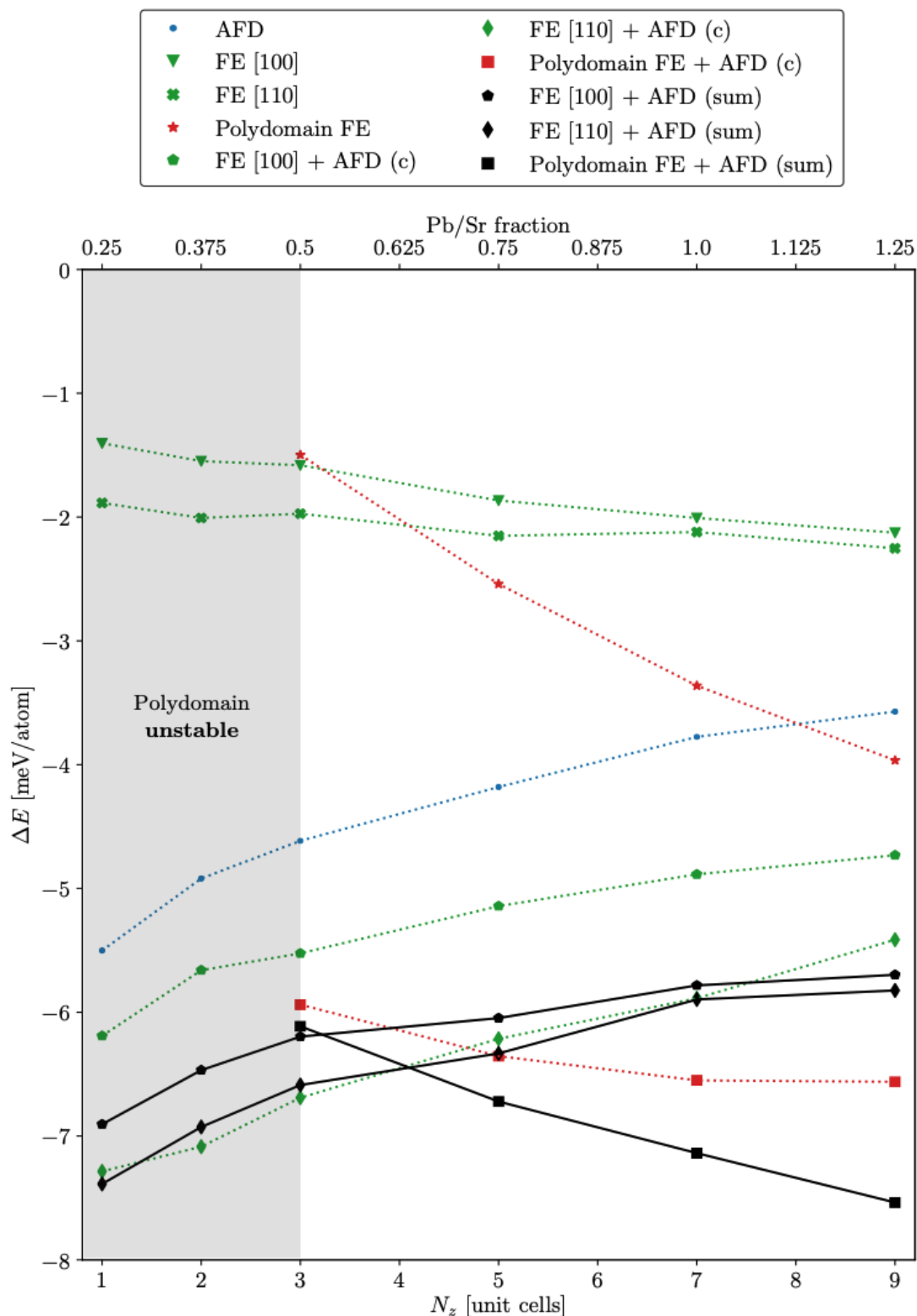


Figure 6.9: The energy difference of a given film ΔE compared with the non-polar paraelectric films versus the film thickness in PTO unit cells, N_z . Since we use a fixed amount of STO substrate, the formula unit of the film alters with N_z . This is accounted for by the upper x-axis indicating the Pb/Sr fraction. The area in grey indicates the domain of N_z for which the polydomain configuration was found to be unstable. In the key, entries followed by (c) indicate films where the mentioned modes coexist. Those followed by (sum) are simply the sum of the individual (isolated) contributions from the mentioned modes.

of the simulation).

Remarkably, the polydomain configuration is not universally the ground state. Monodomain [110] polarisation is the lowest in energy until a film thickness of 4-5 unit cells. This is close to the experimental observation of a polydomain structure at a thickness of 3 unit cells [33] with the difference perhaps being an artefact of finite temperature in experiment. We note also that these results agree with the theoretical findings of Shimada [172] in that at a thickness of 3 unit cells, the polydomain configuration is lower in energy than the paraelectric film. In our work within this chapter, however, while the energy is lowered by this geometry, monodomain in-plane [110] polarisation is favored at this depth. It is also important to note that this work treats the PbO termination whilst the work of Shimada treats the TiO_2 termination. As we discuss later (in Section 6.3.2), the $N_z = 3$ polydomain film *does not* condense the flux-closure domain morphology but instead shows a polar wave (Figure 6.11b). This clearly will have an impact on the energetics. Comparing the polydomain FE + AFD (c) curve with the polydomain FE + AFD (sum) curve, we find that the latter is always lower in energy (a gap which widens with increasing film thickness). This suggests that polydomain FE competes with AFD modes. This effect is not as drastic as the competition between FE modes and monodomain [100] polarisation however.

6.3.2 Polarisation morphologies

In this section we analyse and compare the polar morphologies of the PTO films on STO substrates using the local polarisation $\mathbf{P}^{(i)}$ we presented in Section 6.2.4. Vector fields of this quantity have been calculated for all polar structures and are presented in Figures 6.10 and 6.11.

In Figure 6.10a we show the Ti-centered local polarisation along the up and down domain centroids. The domain centroid here is a string of Ti centered unit cells in the vertical direction located at the centre of a domain. It is at the down domain centroid that the maximal local polarisation can be found, buried in the upper third of the PTO film. Indeed, there is a discrepancy in polarisation between the up and down domains throughout the entire film, leading to a small net dipole moment in the $[00\bar{1}]$ direction. This effect can be explained by the compositionally broken inversion symmetry present in even the highest symmetry films (the relaxed geometry described in Section 6.2.5.1). The result is that $\mathbf{P} \parallel [00\bar{1}]$ is favored by a built-in bias field directed towards the substrate. While we find that this field is local to the first few PTO surface monolayers, we suggest that the enhanced local $\mathbf{P} \parallel [00\bar{1}]$ modes at the surface spread to the rest of the domain due to a finite correlation length associated with the polar atomic displacements [397]. This leads to an indentation of the substrate (as seen in Figure 6.13) creating extra volume for the down domains and enhanced local tetragonality which mutually couples with the polarisation. The opposite argument is also true for the local $\mathbf{P} \parallel [001]$ modes within the up domain whereby the internal bias field is now depolarising. We predict that such a disparity between the up and down domains will diminish with increasing film thickness, tending to zero

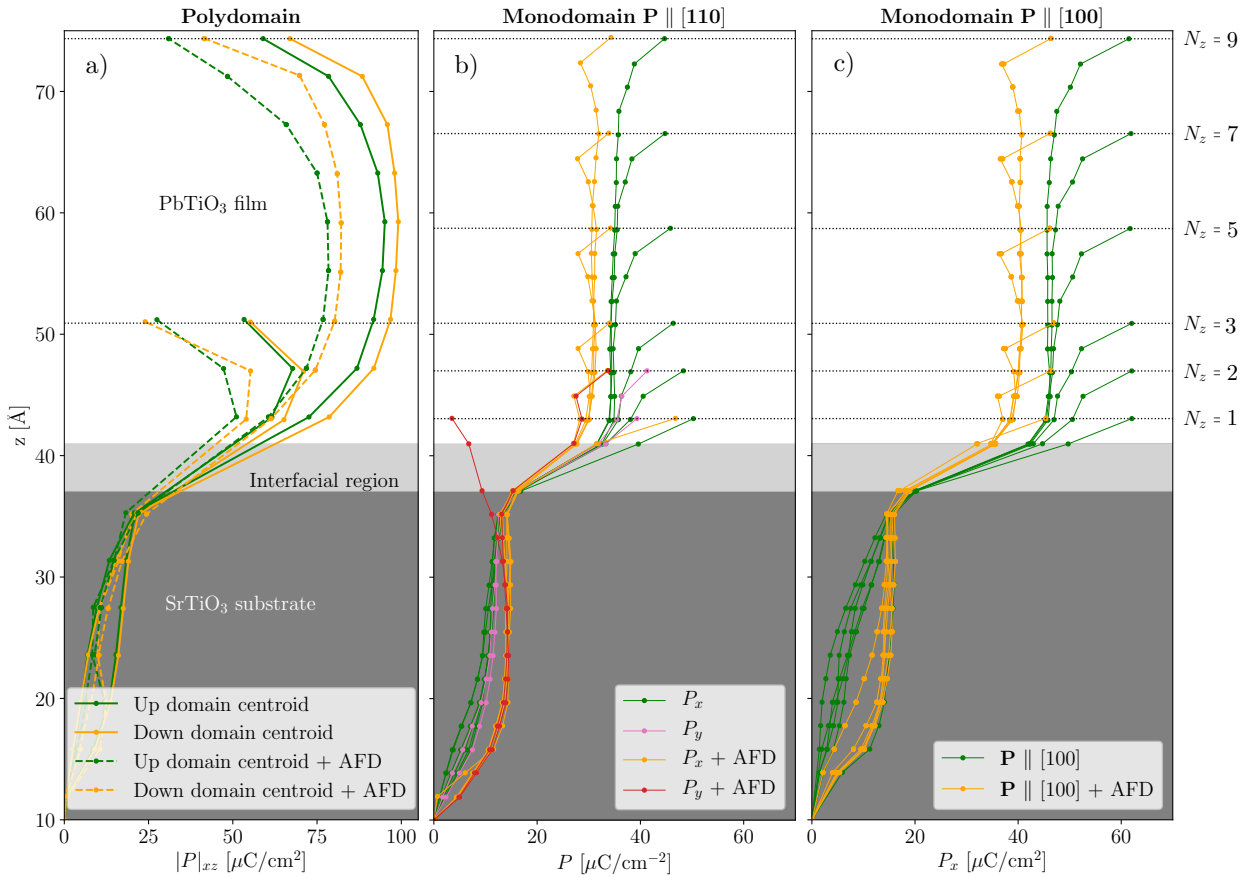


Figure 6.10: The local polarisation profiles as a function of film vertical position z for different film geometries with and without the interplay of AFD modes. a) The local polarisation ($|P|_{xz} = \sqrt{P_x^2 + P_z^2}$, which is $\approx P_z$ at the domain centroid apart from the $N_z = 3$ film which has a polar wave morphology) at the domain centroids for both the up and down domains of polydomain films. We display only $N_z = 3$ and $N_z = 9$ for clarity. b) The local polarisation of films initially in the $\mathbf{P} \parallel [110]$ configuration. Both P_x and P_y components are shown for $N_z = 1$ and $N_z = 2$ (where there is a finite size effect). Otherwise, $P_x \approx P_y$. c) The local polarisation (P_x) for films with $\mathbf{P} \parallel [100]$.

as the film thickness becomes much larger than the correlation length of the enhanced local polar modes. The scenario explained above is analogous to the observation of built-in bias fields present three component or *tricolor* superlattices [382, 383] where our third component is the vacuum region.

We find that the maximal polarisation increases with film thickness for the polydomain films. Although we only display $N_z = 3$ and $N_z = 9$ in Figure 6.10a, the rise is gradual when considering the maximal polarisation of the $N_z = 5$ and $N_z = 7$ films also. This reflects the results of synchrotron X-ray diffraction [33] whereby satellite peak intensity (indicative of domain polarisation) is an increasing function of film thickness. Such a phenomenon is likely a result of decreasing depolarising field strength with increasing film thickness as is observed for thicker $\mathbf{P} \parallel [001]$ films [398]. It is notable that by $N_z = 9$, this maximal polarisation (for the case *without* AFD modes) exceeds the strained PTO bulk figure by 26%. The same enhancement is not seen for the $N_z = 3$ film which suffers a 12% reduction. It can be seen for all film geometries that the influence of AFD modes tends to *reduce* the polarisation in the film. Figure 6.10a shows that allowing for AFD modes produces a local polarisation reduction of $\approx 15 \mu\text{C}/\text{cm}^2$ for all films. This reduction, however, becomes more severe as we reach the surface where we suggest that the enhanced local rotational modes at the surface reconstruction compete strongly with the polarisation.

The majority of the relaxed polydomain structures, as seen in similar works, form the flux closure morphology (Figure 6.11a). That is, the local polarisation gradually rotates through 180° across the domain wall at the top of the film and rotates through -180° at the bottom as a mechanism for screening the depolarising field. The result is counter-tilting vortex-like domain walls (Figure 6.11a, red areas), with a small vertical area for ≈ 0 polarisation at the vortex center. This domain morphology forms fully for the $N_z = 5, 7, 9$ films with and without the influence of AFD modes. We note that whilst these domain structures share similarities with other works, they do have some key differences. The vortex cores are not located centrally (in the z-direction) in the film. They are instead shifted towards the substrate. We also see that at the surface, flux is closed more abruptly than at the interface with the substrate. At the interface, the polarisation penetrates (≈ 2 unit cells) into the substrate helping to close the flux. Together with the previously mentioned tendency for a stronger polarisation in the $[00\bar{1}]$ direction, this makes for a more asymmetrical morphology than those observed in the superlattice or free standing film arrangement [172, 175]. In contrast to the work of Shimada [172], the $N_z = 3$ film does not appear to form complete a flux closure domain structure. Examining Figure 6.11b we see that the flux does not fully close at the interface with STO. Instead, the polar morphology is *S*-like or wave-like, in this case orientated in the $[\bar{1}00]$ direction giving the film a net in-plane macroscopic polarisation. We deduce that at the surface, the flux *does* close by analysing the displacements of the terminating PbO layer (whose polarisation vectors are not calculable with our method as explained in Section 6.2.4). This gives rise to small cylindrical vortices near the surface which

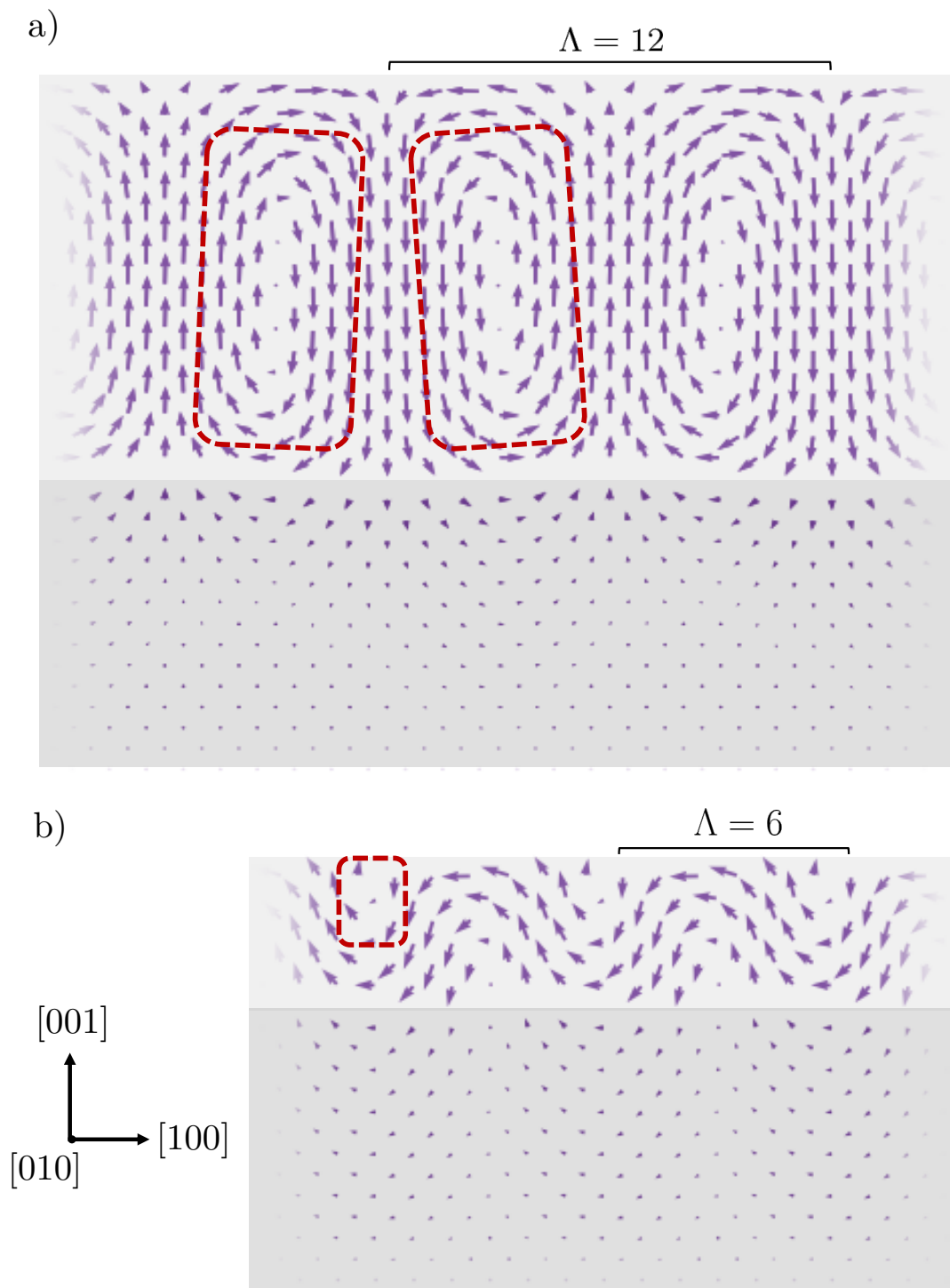


Figure 6.11: The local polarisation vector fields in the x - z plane for two film thicknesses not including AFD modes. a) The flux-closure domains of the $N_z = 9$, $\Lambda = 12$ film. The red area highlights a vortex/antivortex pair b) The polar wave morphology in the $N_z = 3$, $\Lambda = 6$ film. The red area indicates a cylindrical chiral bubble.

are sometimes known as *cylindrical chiral bubbles* [177, 369] (Figure 6.11b, red area).

Such an instability has been predicted as an intermediate phase in phase field simulations under applied electric fields in the superlattice arrangement [174] as well as at zero field in high-angle annular dark field (HAADF) images [177]. This polar topology is also observed in thin PZT films as predicted with Monte-Carlo simulations of a first principles-based Hamiltonian [369]. Although such a polar topology has not yet been observed in thin PTO films, we note that previous XRD studies do not explicitly rule out the coupling to the characteristic in-plane wavevectors for the $N_z = 3$ film [32, 33, 399]. In our work, the polar-wave morphology appears as an intermediate phase between full flux-closure domains and in-plane polarisation like in reference [174] but in the absence of an applied field. This is replaced by the built-in bias field which emerges from the compositionally broken inversion symmetry. Since this bias field is directed to suppress up domains but enhance down domains, up domains now have an decreased critical thickness for the absolute suppression of out-of-plane polarisation compared to down domains. We suggest that at $N_z = 3$, we are below this critical thickness for up domains (where in-plane FE modes are now favored) but still above it in down domains. The resulting polar wave texture is then emergent from the closing of flux between $\mathbf{P} \parallel [00\bar{1}]$ and $\mathbf{P} \parallel [\bar{1}00]$ (although $\mathbf{P} \parallel [100]$ is equally favored) domains as shown in Figure 6.11b. This finding suggests that control over polar morphologies can be achieved in ultrathin films by careful engineering of the boundary conditions. Specifically, we suggest that the built-in bias field can be manipulated through the choice of substrate, film surface termination or use of overlayers. This principle of design offers a promising avenue for the manipulation of chiral order in low-dimensional devices operating through the control of toroidal moments.

Figure 6.10b and 6.10c show the polarisation profiles for the films initialised with uniform polarisation oriented in the [110] and [100] directions respectively. For the former, we find that for most cases, $P_x \approx P_y$ (hence \mathbf{P} remains aligned along [110]) apart from the thinnest $N_z = 1$ and 2 films. In particular, when the $N_z = 1$ film is coupled with AFD modes, the polarisation rotates strongly to be mostly polarised in [001]. For both [110] and [100] polarised films, we see that these films become polar as we cross the STO/PTO interface, quickly adopting a bulk like value. Then, for films without AFD modes, we see a polar enhancement near the surface. For those with AFD modes, we see a polar reduction followed by enhancement near the surface contrasting with the strong reduction for the polydomain films. Computing the norm $\sqrt{P_x^2 + P_y^2}$ of the polarisation for the [110] and [100] films in the bulk-like region shows us that the [110] films have a slightly enhanced polarisation ($+2\mu\text{C}/\text{cm}^2$) compared to just [100] polarisation. What is notable for the monodomain films is that (past a thickness of two unit cells at least) there is no trend for the behaviour of the local polarisation for increasing film thickness. Each film shows the same bulk-like polarisation then the same surface reduction or enhancement.

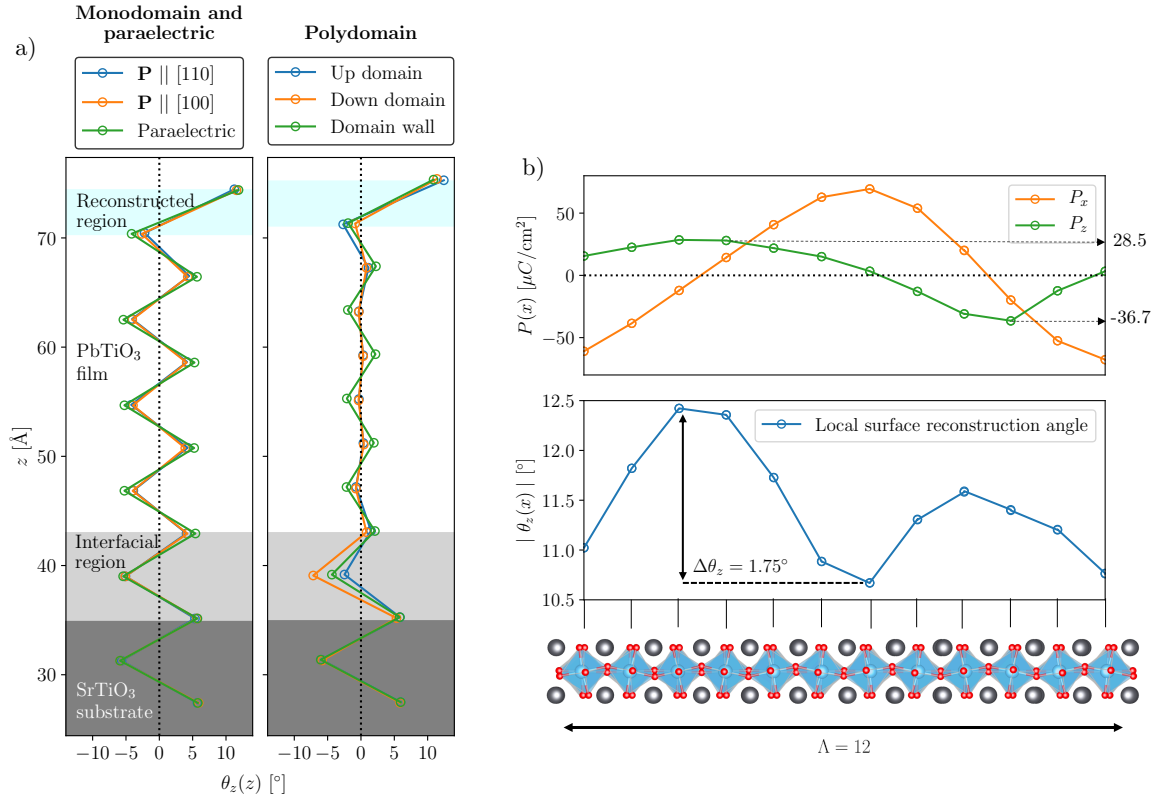


Figure 6.12: a) The $a^0a^0c^-$ TiO_6 octahedral rotation angle $\theta_z(z)$ for the different geometries of the $N_z = 9$ film. b) $\theta_z(x)$ and the x and z components of the local polarisation $P(x)$ across a domain period Λ of 12 unit cells for the $N_z = 9$ film. Since both the local polarisation and rotations are centered on Ti sites, as a visual guide, an aerial view of the film looking down $[00\bar{1}]$ is below b) aligned with the points on b).

6.3.3 The $p(2 \times \Lambda)$ surface reconstruction

An analysis of the competition between local FE and AFD modes can provide valuable insight into the design of new low dimensional devices whereby FE and AFD modes can be tuned to enhance their functional properties. In this section, we analyse the interaction of FE and AFD modes with a focus on strong coupling within the reconstructed surface layers of the PbO terminated films.

Figure 6.12 shows the local evolution of the R_4^+ octahedral rotation angle θ_z along the $[001]$ direction (Figure 6.12a) and across a domain period Λ in the $[100]$ direction (Figure 6.12b) for the $N_z = 9$ ($\Lambda = 12$) film. The rotational behaviour in Figure 6.12a (left) is similar to the behaviour reported by Bungaro [380] whereby the reconstructed area couples cooperatively with in-plane $[100]$ polarisation. We show that this is also true for $\text{P} \parallel [110]$ (polarisation is locally enhanced at the surface as shown by Figures 6.10b and 6.10c) with the rotation pattern $\theta_z(z)$ being almost indistinguishable from the $[100]$ polar film. We note that whilst this mutual AFD/FE enhancement is active at the surface, for the rest of the film, AFD/FE modes are mutually reduced when compared to the paraelectric structure and the bulk. The $\theta_z(z)$ trend for the polydomain

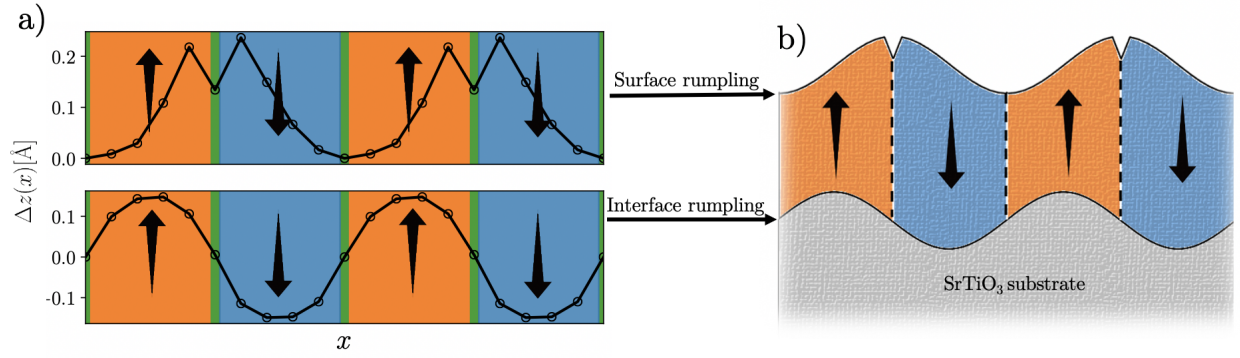


Figure 6.13: Surface and interface rumpling of the Pb cations for the $N_z = 7$ ($\Lambda = 10$) film *without* AFD modes. a) The vertical deviation of the surface (upper) and interface (lower) Pb atoms from the Pb atom located at the first domain wall (along the x -axis). b) An exaggerated schematic of the surface and interface rumpling including the boundary with the substrate.

films (Figure 6.12a, right) is more complex. Rotations are almost completely quenched (reduced to $\approx 2^\circ$) at the up and down domain centroids compared to the domain wall (apart from the reconstructed region). We suggest that this occurs since the maximal polarisation at the centroids outcompetes AFD modes. We see similar behaviour for all N_z for the effects listed above, even for the strength of the reconstruction angle. This is remarkably resistant to finite size effects: even at a single PbO monolayer ($N_z = 0$), θ_z persists at around 12° despite the change in chemical environment for the surface TiO_6 octahedra.

Figure 6.12b shows a coupling between local polarisation at the surface (upper) and the surface reconstruction angle (lower). Across a domain period Λ , we see that $\theta_z(x)$ modulates by 1.75° . $|\theta_z(x)|$ peaks close to $P_x = 0$ which is remarkable since this is precisely the *opposite* behaviour to the monodomain in-plane films where FE and AFD mutually support one another. Since $P_x(x)$ and $P_z(x)$ are $\pi/2$ radians out of phase with each other in the surface layer, it can also be said that the peaks in $|\theta_z(x)|$ coincide with extrema in $|P_z(x)|$. We see also the magnitude of $P_z(x)$ has an impact on the height of the peaks in $|\theta_z(x)|$. That is, since the down domains are more polar than the up domains, the larger down polarisation in the surface layer reduces the $|\theta_z(x)|$ peak and vice versa for the smaller polarisation in the up domain. We note that such AFD/FE couplings are different to those found in a recent shell model study of the free standing film [388]. In [388], the symmetrical [001] boundary conditions for the film modulate $\theta_z(x)$ over $\Lambda/2$ instead. We also note that whilst the strongest octahedral rotations θ_z are about the [001] axis, we also see smaller rotations of $\approx 2\text{-}3^\circ$ about the [100] axis in the surface reconstruction. In addition to this, at the surface of the polar wave film for $N_z = 3$, we observe rotations about *all three* pseudocubic axes in the surface reconstruction. The strongest rotations are still about the [001] axis however.

The broken inversion symmetry leads to further structural effects for the polydomain films. We can measure the distortion of the films in the vertical direction by considering the Pb

displacements in the terminating PbO layer with the vacuum and at the STO interface. Figure 6.13 shows an exemplar calculation for the $N_z = 7$ ($\Lambda = 10$) film. The other film thicknesses all resemble the behaviour of this film. With the exception of a small dip in Δz at the domain wall for the surface rumpling (a mechanism to reduce the domain wall formation energy), we see that interface and surface rumpling behave spatially like two sinusoids $\pi/2$ radians out-of-phase with one-another. This is in contrast to the PTO/STO superlattice configuration [175] where the intact inversion symmetry preserves symmetrical rumpling (in-phase sinusoids). Due to the periodicity of octahedral rotations and Pb cation surface rumpling in the [001] direction, it is clear that for the polydomain films we must reconsider the labelling of the surface reconstruction. For monodomain and paraelectric films, the Wood's notation [400] of $c(2 \times 2)$ remains correct but an analysis of the symmetry for the polydomain case reveals this must alter to become $p(2 \times \Lambda)$. We suggest that these fine FE/AFD interactions could now be observable in experiment thanks to recent advances in integrated differential phase contrast (iDPC) imaging [401]. In contrast to HAADF, iDPC images yield the positions of the metal cations *and* oxygen anions resolved at a subunit cell level [401]. This allows for the direct measurement of local FE and AFD modes offering an exciting new avenue for direct comparison with atomistic results.

6.4 Results: trenches on free standing PTO

6.4.1 The most favourable orientation

Table 6.2 shows the relative energies for each of the relaxed free standing films detailed in Section 6.2.6. The energies are displayed relative to the $\parallel^{\text{centroid}} + \text{AFD}$ film for each trench depth d . It is immediately clear that this is the most favoured trench orientation, independent of the d treated in this chapter. It is also clear that the relative ordering of the films is independent of d . That is, after $\parallel^{\text{centroid}} + \text{AFD}$ follows $\parallel^{\text{wall}} + \text{AFD}$, $\perp + \text{AFD}$ then the two films without AFD modes. Indeed, for those films treated without AFD modes ($\parallel^{\text{centroid}}$ and \parallel^{wall}), the favoured trench position remains over the centroid. It is also true that the trench is still favoured over the centroid compared to the wall when trenches are separated at 4Λ in the $\parallel_{4\Lambda}^{\text{centroid}}$ and $\parallel_{4\Lambda}^{\text{wall}}$ films. These findings are in line with the experimental [32, 34, 55, 189] and theoretical studies [180, 191] that have previously shown that DWs run parallel to surface defects. The clarification that the trench is most stable positioned over the centroid supports the predictions of [180] where the domain structure was pinned by step edges at the domain centroid. Explicitly, our study now also disagrees with [191] which found that a 180° DW formed directly under the surface defect.

The finding that the domain centroid is pinned by surface trenches (rather than other parts of the domain structure) informs design principles for DW nanoelectronic devices where the exact position of the DW needs to be controlled. That is, engineered surface trenches could be used to reliably control the position of a DW at a distance $\approx \Lambda/2$ from the trench. That being said, it is unknown how the insertion of a trench could affect the domain period. In the case of ultrathin

Table 6.2: The relative stabilities of the relaxed films with trenches as detailed in Section 6.2.6. The energy is measured relative to the $\parallel^{\text{centroid}} + \text{AFD}$ arrangement apart from films subscripted with 4Λ which are measured relative to $\parallel_{4\Lambda}^{\text{centroid}}$. Energies are normalised per formula unit. This is assigned as the number of atoms in the parallel trench arrangements with the *same* trench separation. That is, for $d = 1, 2$ and 3 , the energy is given per 428, 412 and 396 atoms, respectively, but, for the films subscripted 4Λ , the energy is given per 1760 atoms.

E - E($\parallel^{\text{centroid}} + \text{AFD}$) [eV/FU]							
	$\parallel^{\text{centroid}} + \text{AFD}$	$\parallel^{\text{wall}} + \text{AFD}$	$\perp + \text{AFD}$	$\parallel^{\text{centroid}}$	\parallel^{wall}	$\parallel_{4\Lambda}^{\text{centroid}}$	$\parallel_{4\Lambda}^{\text{wall}}$
$d = 1$	0	+0.219	+1.706	+3.852	+4.106	0	+0.359
$d = 2$	0	+0.361	+0.881	+4.089	+4.095	-	-
$d = 3$	0	+0.141	+1.951	+4.639	+4.878	-	-

films, this could be a troublesome effect because the film would now be *much* thinner in the area of the trench; decreasing the average thickness of the film with likely consequences for Kittel scaling. This could be an interesting focus of a future study. It is also important to consider how our results would change when substrate effects are present. That is, within Section 6.3.2, we found that the underlying domain structure becomes asymmetrical, manifesting mostly in down domains becoming more polar than up domains for films on substrates. Given this, it is likely that there will be a small difference in energy between a trench inserted over a down domain compared to over an up domain; it *could* only be possible to pin one type of domain. However, without explicit simulations, it is not possible to tell which is favoured. This is a further avenue to be explored in future works.

While we have now shown that $\parallel^{\text{centroid}} + \text{AFD}$ films are the most favoured orientation, the question of “*why?*” is a difficult one to answer. From our simulations, it appears that there are multiple factors which could contribute to the DW alignment mechanism by competing/coupling with local polar modes. These include: the presence of AFD modes, new depolarising fields at the trench edge and trench-induced strains and strain gradients. The influence of AFD modes are least likely to contribute. That is, the $\parallel^{\text{centroid}}$ film is *still* favoured over \parallel^{wall} without their presence. However, it is not possible to tell from our simulations how the $\perp + \text{AFD}$ film would be affected in the absence of AFD modes (see the discussion in Section 6.2.6.1) so we cannot rule them out completely. A discussion of the remaining factors are presented in Sections 6.4.2 and 6.4.3.

6.4.2 Depolarising field minimisation

For those trench orientations parallel to the domain wall, simple insights can be gleaned from the arrangement of the local polar modes in the vicinity of the surface trench. The general principle is that the orientation which is the most favoured is the one which is most able to minimise new depolarising fields near the trench; a principle we find that holds for all d treated in this

study. This is shown in Figure 6.14 for the $d = 1$, $\parallel^{\text{centroid}}$ film. It is clear to the eye that the local polarisation of the pristine film geometry (Figure 6.14a) is altered only a small amount for the remaining unit cells when the trench is positioned over the up domain centroid (Figure 6.14b; we also find a similar local polarisation pattern at the down domain centroid). While there is a reduction in magnitude, the direction and general pattern of the dipole moments are preserved. The same is not true when the trench is positioned over the wall (Figure 6.14b). We see that in this case, there is a reorientation of the local polarisation from the pristine film (Figure 6.14c) for the Ti sites of the uppermost unit cells. Specifically, these moments rotate in-plane along $[010]$ or $[0\bar{1}0]$ and turn towards the film. This is undoubtedly a mechanism to reduce the discontinuity of polarisation at the trench edge which would otherwise give rise to large depolarising fields. In the process of doing so, the upper Ti site in the dashed orange box of Figure 6.14d finds itself stuck between a rock and hard place. That is, although its relaxed geometry has reduced depolarising fields from polar discontinuity with the vacuum, it has found itself in an energetically unfavourable near-head-to-head[†] polar configuration with the Ti site below it. This will give rise to a penalty in the stability and is likely the reason the trench over the centroid is comparatively more stable. The origins of the favourability of the $\parallel^{\text{centroid}}$ film are independent of the presence of AFD modes. As was seen in Section 6.3 for the films on substrates, AFD modes tend to reduce to local magnitude of polar modes, but, their general pattern and direction is unchanged.

A scrupulous individual may ask: “Why do the local polar modes centered on the Ti sites within the purple dashed box in Figure 6.14b *not* rotate away from the vacuum in line with the mechanism described for Figure 6.14d?”. The answer to this has two parts. Firstly, closer inspection shows that they do *slightly* rotate in-plane (although are still largely out-of-plane). Indeed, the polarisation of these two Ti-centered unit cells look very much like the polarisation at the surface of the pristine film (Figure 6.14a). Secondly, it is clear from both Figures 6.14a and 6.11a that it is at exactly the domain centroid that out-of-plane polarisation is preserved without rotation in-plane (although, there is magnitude reduction near the surface, shown quantitatively in Figure 6.10a). This is permitted as the underlying flux-closure domain structure screens a large portion of the depolarising field.

The instability of the $\perp +$ AFD films can also be understood by changes in the local polarisation vector fields, but the description is more complex and cannot be understood by the unfavourable orientation of *isolated* polar modes. Overall, of the films studied, these films have their *ideal* domain structure perturbed the most by the insertion of a trench. Figure 6.15 shows the complex nature of the perturbed domain structure at a single vortex for the $d = 2$ film. Figure 6.15a shows the whole vortex looking down the $[010]$ direction for the area indicated on 6.15b.

[†]It has recently been shown from first principles that the depolarising field at 180° head-to-head and tail-to-tail domain walls can be screened with a 2DEG/HG pair [402]. No such gases form here so the energy cost for this near-head-to-head arrangement remains large.

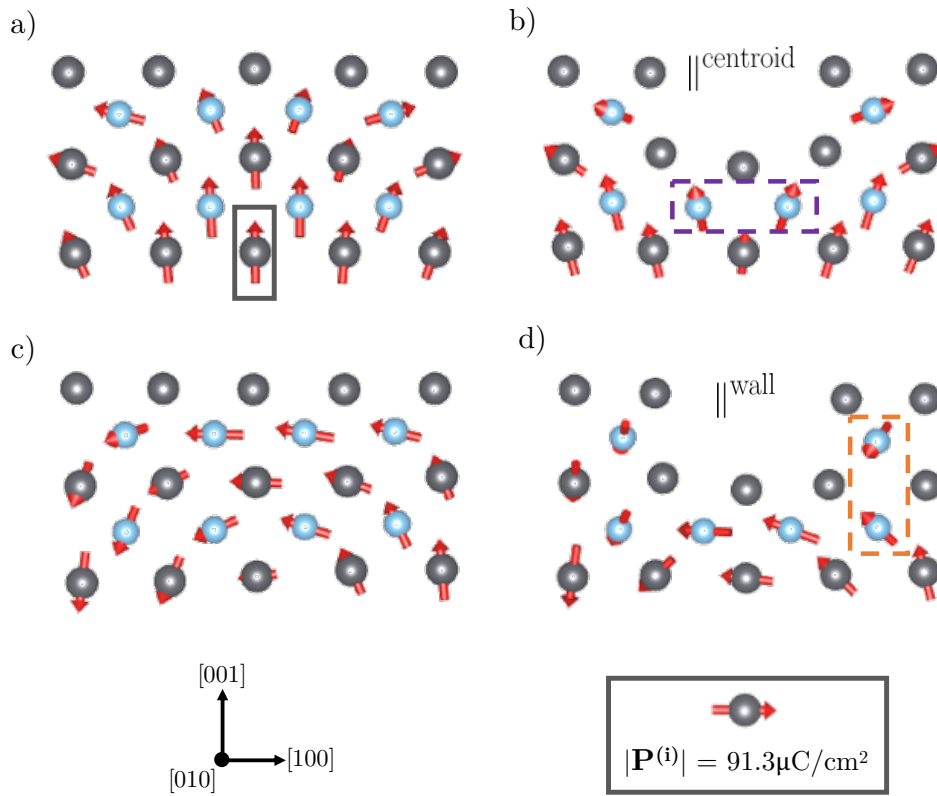


Figure 6.14: A close-up demonstration of the differences in the local polarisation before (a, c) and after (b, d) the introduction of a surface trench for those trench orientations running *parallel* to the domain wall. O sites are removed for clarity. a) Near the surface of the pristine film at the domain centroid. The Pb site contained within a grey box is the site used in the scale bar (lower right) b) The local polarisation near a $d = 1$ trench over the domain centroid ($\parallel^{\text{centroid}}$). The two Ti sites contained within the purple dashed box are discussed in the text. c) Near the surface of the pristine film at the domain wall. d) The local polarisation near a $d = 1$ trench over the domain wall (\parallel^{wall}). The two Ti sites contained within the orange dashed box show a near-head-to-head arrangement of local polar modes which are discussed in the text.

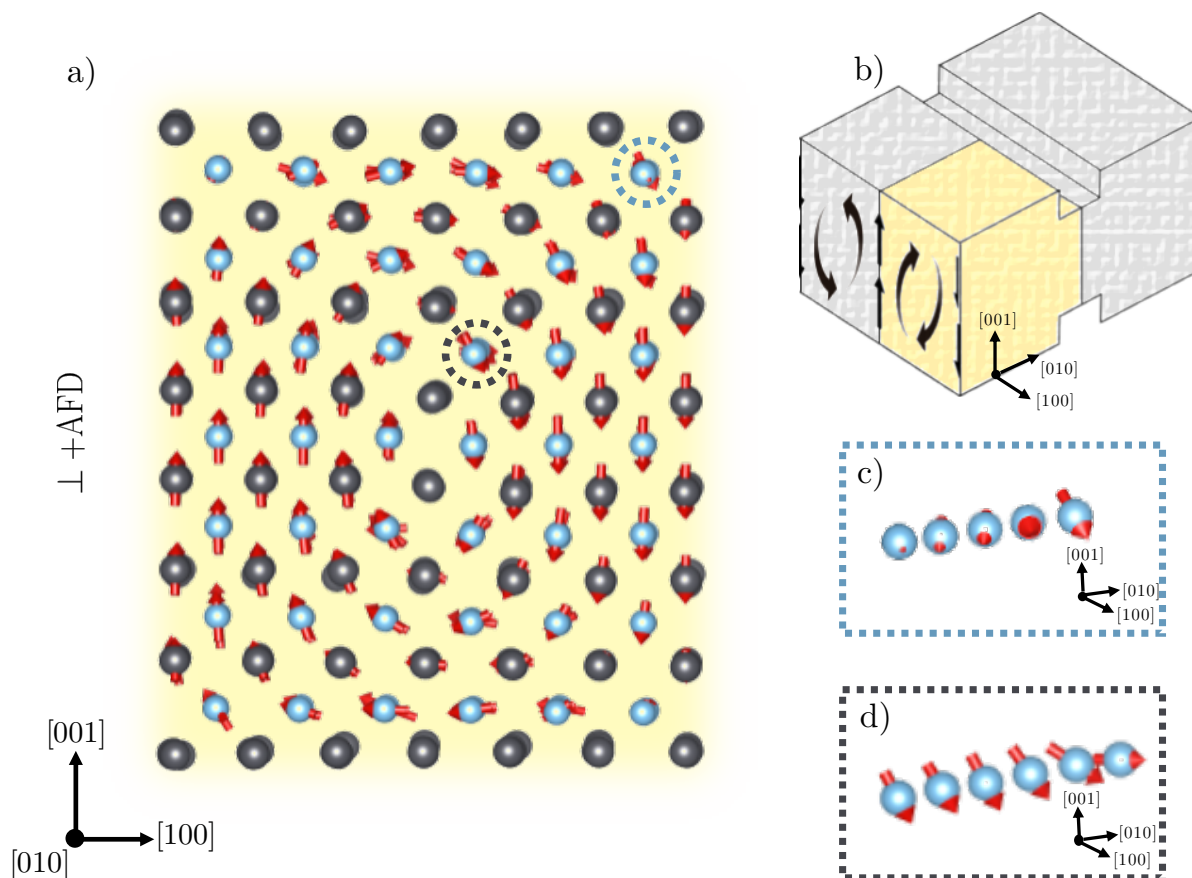


Figure 6.15: a) The local polarisation vector field of a single vortex in the relaxed $d = 2$, $\perp + \text{AFD}$ film looking down $[010]$. Oxygen has been removed for clarity. This figure also uses the same scale bar as Figure 6.14. b) A schematic of the $\perp + \text{AFD}$ film. The area shaded in cream/yellow indicates the segment of the film displayed in a). The arrows on the front of this shaded portion are a cartoon representation of a). c) A close up of the five local polar modes along $[010]$ at Ti-centered unit cells near the film surface (the area on a) circled in blue). The last Ti-site on the right is at the edge of the trench. d) A close up of six local polar modes along $[010]$ at Ti-centered unit cells near the vortex core (the area on a) circled in grey). The last Ti-site on the right is the Ti-site closest to the surface of the trench.

It is clear to the eye that at the rotating parts of the vortex, there are considerable modulations to the local polarisation as we travel in the [010] direction towards the trench site. Two examples of these modulations are shown close-up in Figures 6.15c and 6.15d. For Figure 6.15c, There is a strong turning of the polarisation away from the vacuum (and large increase in magnitude) for the site at the trench edge (the Ti-site furthest right in the figure). In Figure 6.15d, there is a continuous anticlockwise rotation of the local polar mode as we travel along [010] eventually becoming completely in-plane as we reach the site at the surface of the trench (the Ti-site furthest right in the figure). We can then deduce that, generally, sharp changes of the local polar modes near (or under) the trench destabilise the underlying domain structure at a longer range than the parallel trench arrangements, ultimately contributing to the instability of this trench arrangement compared with the others.

6.4.3 Strain fields

The study in reference [55] found large inhomogeneous strains and strain gradients for the out-of-plane lattice constants in the vicinity of Ar-ion milled trenches on the surface of a PTO/STO superlattice. This was enabled by the use of a nanofocussed X-ray beam which measured local three-dimensional maps of reciprocal space at different points around surface defects used to reconstruct images of the local lattice parameter. We showed these images in Chapter 2, Figures 2.11a and 2.11b. In this section, we compare our *ab initio* results to this study by calculating the local strain at the surface of our films with trenches.

First, we calculate a reference lattice constant which we take to be the average c for the pristine film (without trenches), $c^{\text{avg}} = 4.051 \text{ \AA}$. We choose this approach to be consistent with the experimental work of [55]. We then isolate each (Ti-centered) surface unit cell and calculate the two vertical Pb-Pb distances and the vertical apical O-O distance. Their average is the surface out-of-plane lattice parameter c^{surf} . The out-of-plane surface strain is calculated simply as

$$\epsilon_{33}^{\text{surf}} = \frac{c^{\text{surf}} - c^{\text{avg}}}{c^{\text{avg}}}. \quad (6.2)$$

This is shown in Figures 6.16 and 6.17 as we move along the [100] direction on the film surface. To remove the effect of AFD modes from the equation, in Figure 6.16, we choose to examine $\epsilon_{33}^{\text{surf}}$ on the bottom surface of the $\parallel^{\text{centroid}}$ film (where the trench is over an up domain). Since $\parallel^{\text{centroid}} + \text{AFD}$ is the most stable arrangement found in our work, this general orientation of trench *most likely* corresponds to experimental observations. It is clear immediately that in the vicinity of and at the floor of the trench, we see large negative strains which persist for $\approx 4 - 6$ unit cells, more than twice the width of the trench itself. Although, as can be seen from Figure 6.17, this range reduces to $\approx 3 - 4$ unit cells when the trench is over the down domain centroid on the bottom surface. The majority of this strain originates from changes in the Pb-Pb distances while O-O distances change only slightly. We can see from Figure 6.16 that the strain field

appears quite insensitive to d apart from for $d = 3$. For this case, there are giant strain anomalies at unit cell indexes 7 and 8. Also, at the trench floor for this film there is a reduction in the magnitude of the strain; a likely consequence of the limitations of our model as we discuss later in this section. Since our reference lattice constant for which we calculate the strain is an average value, we do not separate strain contributions of the underlying domain structure of the pristine film from those coming as the result of the trench. Following this, we can see from Figure 6.16 that the positive strain over the down domain centroid persists in the pristine film so is not a trench effect.

We see from Figure 6.17a that the range of the strain field doesn't alter in the $\|\|_{4\Lambda}^{\text{centroid}}$ films despite the increase in the lateral separation of trenches. We can also see from Figure 6.17 that there is distinctly different behaviour for the trench-induced strain between the $\|\|_{4\Lambda}^{\text{centroid}}$ and $\|\|_{4\Lambda}^{\text{wall}}$ films. For the former, we can see from Figure 6.17a that at the bottom surface (where the trench is over the up domain centroid) the trench-induced strain cooperates with the preexisting negative strain of the pristine film. On the opposite surface, the positive strain is reduced by the trench. This is in contrast with Figure 6.17b where we see no cooperation of strain but see sharp, discontinuous deviations from the strain field pattern of the pristine film even for those unit cells *not* at the trench floor. Also, the strain field alters from the pristine film at a longer range than the $\|\|_{4\Lambda}^{\text{centroid}}$ arrangement. We suggest that these effects contribute to the favourability of the $\|\|_{4\Lambda}^{\text{centroid}}$ film but it is difficult to quantify exactly their impact.

Most of the differences between our results and those seen in experiment can be inferred by the change in length scale. That is, the diameter of the nanofocused X-ray spot used in [55] was $\approx 60\text{nm}$; $\approx 13\times$ larger than the supercells discussed here. The trench treated in [55] was also much wider and much deeper (the width and depth were both $\sim 1\mu\text{m}$). This suggests that the range of the strain field is commensurate with the size of the defect. Directly simulating such a scenario from an atomistic basis would require ~ 100 million atoms. While this isn't necessarily beyond the scalability of our $\mathcal{O}(N)$ algorithm [13] the required computer power would be truly astronomical if were to meet our 10 – 20 atoms/core guideline for the operation of CONQUEST[†].

While it is now clear that large negative strains are seen in the vicinity of surface trenches both in theory and experiment, we must accept that our model has some shortcomings. That is, our choice of film thickness, for larger d , permits fictitious interactions between trenches along the vertical axis of the film (i.e. trenches on the top surface can interact with trenches on the bottom surface). While we expect this interaction to be small for $d = 1$, for $d = 2$ (and *certainly* by $d = 3$) the effect will be larger. We can therefore assume that the reliability of our results decrease with increasing d . These shortcomings aside, it is still not clear how the strain fields

[†]At the time of writing this thesis, the worlds largest supercomputer, Fugaku (with 7.3 million cores), comes close to meeting this guideline. As a ball-park estimate, I speculate that we could relax a ~ 100 million atom structure occupying the whole machine for ~ 1 month.

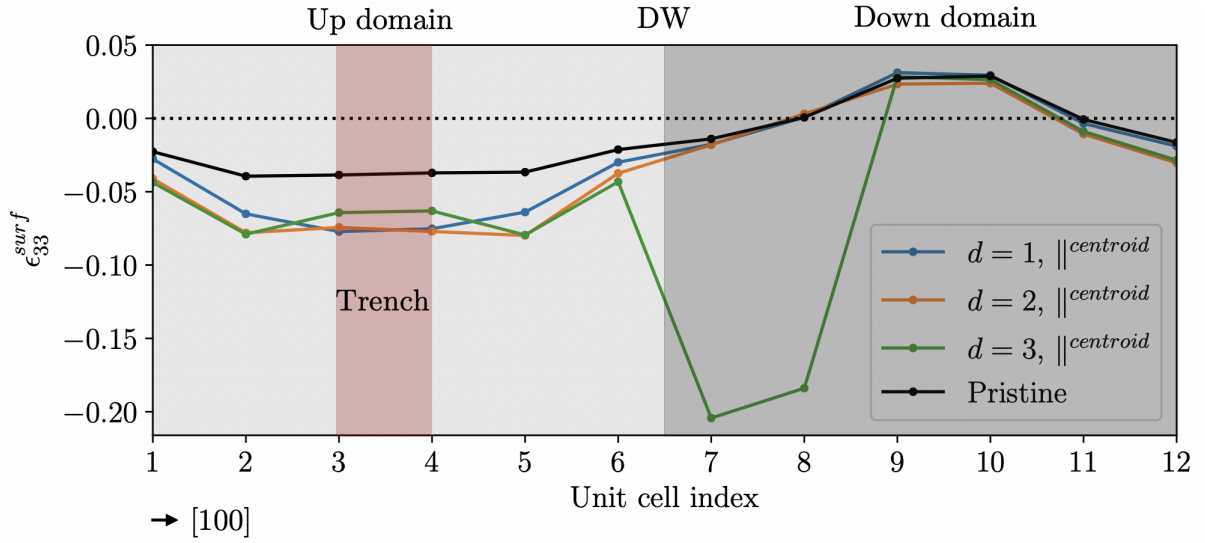


Figure 6.16: The out-of-plane strain for (bottom) surface unit cells $\epsilon_{33}^{\text{surf}}$ along the $[100]$ direction for the $\|\text{centroid}$ films. Both plots feature the underlying strain from the pristine film (the film without trenches) for comparison.

couple with the polarisation. As explained in the previous section, most of the changes in the local polarisation resulting from the introduction of a trench appear as a mechanism to minimise the depolarising field. Decoupling this contribution from possible contributions from strain (via the piezoelectric effect) or strain gradients (via the flexoelectric effect) is not possible with our method. Only the development of a scheme for disentangling these effects from one-another would provide insight into whether piezoelectric and flexoelectric effects play a role in the alignment mechanism. While *ab initio* calculations of the flexoelectric coefficients have recently become possible[†], such methods are still in a developmental stage and not yet applicable to the supercell sizes treated in this chapter. Certainly at the length scale studied here, the discussion of the previous section regarding the *least disturbance* of the local dipole moments provides a satisfactory description of the alignment mechanism. However, this description does not deal with how the local dipole moments would change with the width of the trench. When the trench width becomes much larger than Λ an alternate mechanism may dominate and the giant strain and strain fields seen in [55] and our study could become more important.

6.5 Summary and Conclusions

We have used large scale DFT calculations to simulate an array of polar morphologies present in thin PTO films. We studied their interaction with STO substrates, engineered surface trenches and

[†]The first principles theory of flexoelectricity is a hot topic. It was conceived in the early 2010's [403–405] and increasingly better implementations in code are beginning to emerge [406–408]. Thus far, however, these studies have reported only exemplar calculations in bulk systems.

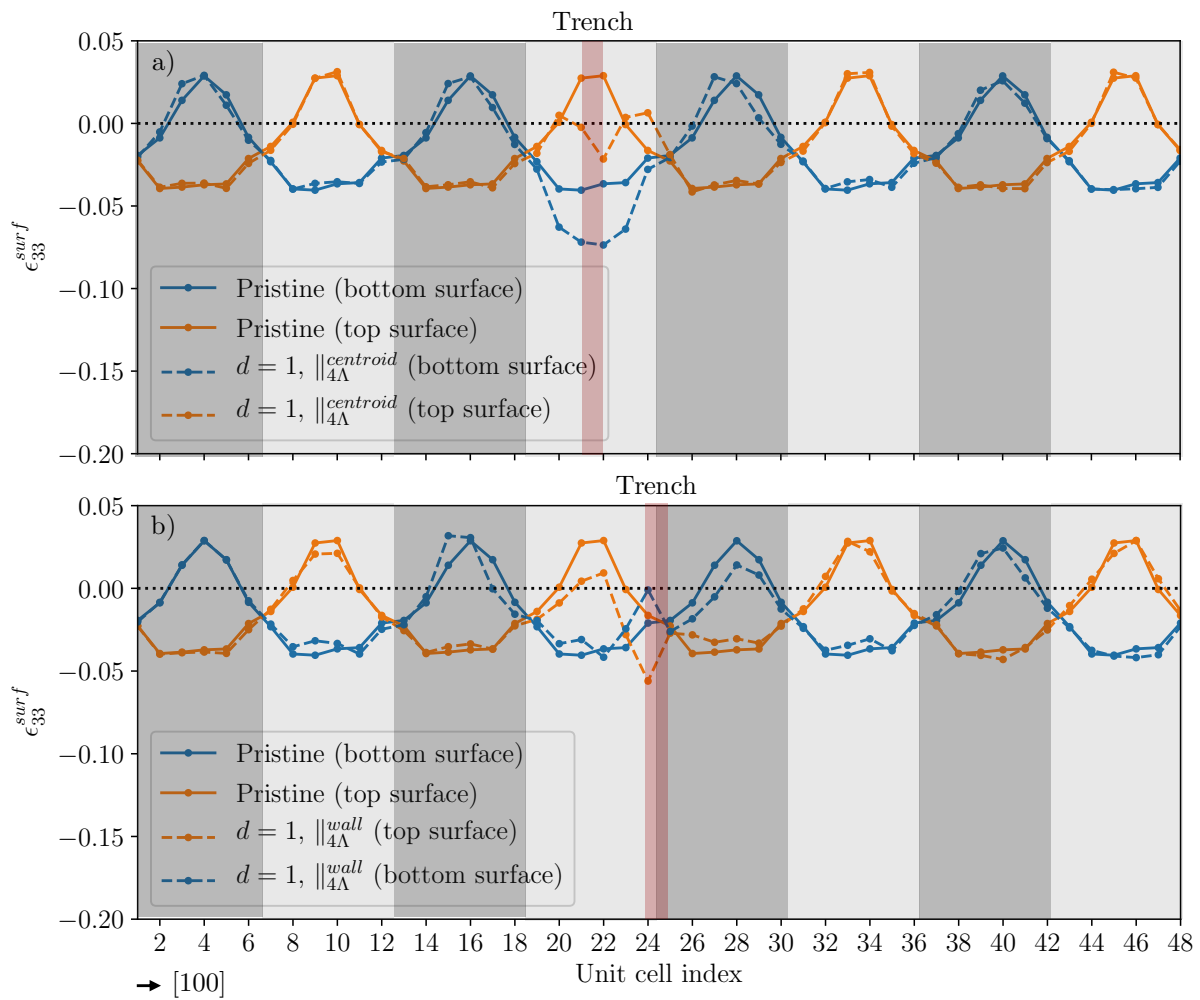


Figure 6.17: The out-of-plane strain for surface unit cells $\epsilon_{33}^{\text{surf}}$ along the $[100]$ direction for: a) the $\|_{4\text{\AA}}^{\text{centroid}}$ film and b) the $\|_{4\text{\AA}}^{\text{wall}}$ film. Both plots feature the underlying strain from the pristine film (the film without trenches) for comparison. Up domains are coloured light grey while down domains are dark grey.

AFD modes. In doing so, we have provided insight into mechanisms for controlling ferroelectric domain structures without the use of directed applied fields. Our methodology has been successful in providing first principles results for systems comprised of a few thousand atoms, well beyond what is feasible with traditional plane wave based methods, venturing towards systems sizes usually simulated with Monte Carlo, phase field or second principles techniques. Our simulations have allowed for the explicit simulation of a large amount of STO substrate, multiple ferroelectric domains and increased supercell dimensions in the [010] direction used include AFD modes, the surface reconstruction and to separate engineered surface trenches. For the majority of these simulations, this has ensured that we are able represent realistic experimental conditions when compared to previous works which neglect one or more of these features. In doing so we have showcased two effective algorithms for evaluating the electronic ground state as implemented in the CONQUEST code. When using the MSSF method in tandem with diagonalisation of the Hamiltonian, we have been able to perform high accuracy simulations involving $\approx 1,000 - 2,000$ atoms using $\approx 200 - 500$ physical cores; resources routinely available on standard HPC systems. Using the $\mathcal{O}(N)$ algorithm, we have performed useful calculations involving $>5,000$ atoms (albeit with some loss of accuracy) using $\sim 1,000$ physical cores; resources available on *most* HPC platforms.

We have demonstrated the stability of the polydomain film geometry compared to monodomain phases for freestanding PTO films and films on substrates. We find that the polydomain case becomes more energetically favorable between 4-5 unit cells in thickness, close to the experimental observation at 3 unit cells. We find that the general effect of including AFD modes is to lower the energy significantly (in most cases more than the FE distortion) and to suppress the amplitudes of local polar modes (apart from at the surface of monodomain in-plane FE films, where they are mutually cooperative).

The polydomain films display the flux-closure domain morphology for $N_z = 5, 7$ and 9 whilst the $N_z = 3$ film on an STO substrate shows the polar wave morphology with cylindrical chiral bubbles as an intermediate phase between full flux closure domains and in-plane ferroelectricity. Local polarisation is enhanced at the domain centroids when compared to PTO bulk; a trend which increases as a function of N_z . Most notably, down domains feature enhanced local polar modes promoted by the internal bias field born of the compositionally broken inversion symmetry present in any film-substrate system. Equally, this bias field acts to depolarise up domains leading to different critical thicknesses for the total suppression of out-of-plane ferroelectricity for the two domains. Since these critical thicknesses are the outcome of the strength and direction of the bias field, engineering this with a careful choice of substrate, surface termination or overlayers allows for control over polar textures at the nanoscale. This finding is especially important for next-generation functional devices reliant upon the control of toroidal order.

This bias field also has consequences for the periodicity of the AFD surface reconstruction. While we find that the reconstruction for the monodomain in-plane FE and paraelectric films is

$c(2 \times 2)$, we find that coupling between surface polarisation and AFD modes in the polydomain geometry modifies this. In addition to surface rumpling of Pb cations, the surface reconstruction angle modulates up to 1.75° across a domain period Λ . We then suggest that for the polydomain films, the correct label for the AFD surface reconstruction is $p(2 \times \Lambda)$ in Wood's notation. This provides direct evidence that the strength of AFD modes can be locally controlled by the strength of FE modes and vice versa. Such knowledge could motivate new principles of design in low dimensional functional devices whereby FE and AFD modes are locally tuned by their interactions.

In an investigation of engineered surface trenches on free standing PTO films, we have found that trenches running parallel to the domain wall and positioned over the domain centroid are more energetically favoured than those positioned over the wall and those running perpendicular to the domain wall. This is in agreement with the experimental observation that DWs run parallel to surface trenches, defects and other surface features in the PTO/STO system [32, 34, 55, 189]. While there are many different contributing factors, we suggest that a large portion of the alignment mechanism can be described based on a principle of *least disturbance* of the underlying domain structure. That is, the most favourable trench orientation is the one where the dipole moments in the vicinity of the trench are able to relax into a position where the energy penalty from depolarising fields is reduced the most. This is what occurs for the $\parallel^{\text{centroid}}$ films. Also in line with experiment [55], we find large negative strains and strain gradients in the vicinity of the trench. While [55] suggests that this likely contributes to the alignment mechanism, like [55], we are unable to disentangle strain and strain gradient coupling to the polarisation from polarisation rotation effects resulting from the minimisation of the depolarising field at the edges of the trench. Now with evidence suggesting that it is the domain centroid that is pinned (in agreement with [180]), it could be possible to control the exact position of DWs, which should appear $\approx \Lambda/2$ unit cells away from a small surface trench. This provides useful insights into the design of future DW nanoelectronic devices.

The large scale electronic structure methods implemented within the CONQUEST code now show promise to be used to solve a plethora of problems within the perovskite oxides. This could include the simulating other potentially possible polar morphologies in the PTO/STO system such as skyrmion phases [89, 178, 179] and disclinations [174]. The former has recently been observed in the PTO/STO superlattice [89, 178] supported by phase-field and second-principles simulations. A full first principles treatment using our method would provide accurate, valuable insights into the properties of these topological objects presenting a direction for future research should the necessary HPC resources be available. Since our method is general, we can extend to other problems in the perovskite oxides (and beyond) such as realistic defect concentrations and highly disordered configurations the popular solid solution families $\text{AB}_x\text{C}_{1-x}\text{O}_3$, $(1-x)\text{ABO}_3-x\text{CDO}_3$ where DFT methods used to circumvent the need for large supercell calculations fail in the reproduction of local structural distortions [43]. Indeed, within Chapter 4, we showed that

distortions increasingly incommensurate with the cubic ABO₃ unit are commonplace in PZT 50/50, PZO and PHO. Investigating the condensation of these modes could in a lot of cases require a large number of participating atoms. These are very fertile grounds to be exploited by large scale DFT in CONQUEST, able to provide vital insights into complex and incommensurate phase transitions [305, 337].

7 | Conclusions and Outlook

This thesis has offered new insights into the structure and function of technologically important ferroelectric and antiferroelectric perovskite oxides. We have studied materials renowned in industry and academia alike for being extremely versatile with properties that are either already exploited on a commercial scale (although, there is always room for improvement), or, for having a strong potential for utilisation in novel functional devices. We have been able to address the fundamental nature of the industrial piezoelectric, PZT, and assess functional ferroelectric domain textures in low-dimensional PTO films. Also, the crystal structure of the archetypal antiferroelectrics, PZO & PHO, has been brought into question, reopening a closed book with ramifications for other antiferroelectrics. At the same time, we have highlighted the need for large scale DFT simulations for many of these systems and demonstrated the readiness of the CONQUEST code to meet this requirement. We have shown that this method can be successfully applied for accurate simulations involving thousands of atoms; solving intractable problems for conventional codes.

In Chapter 4 we critically re-examined the $\text{Pb}(\text{Ti}, \text{Zr}, \text{Hf})\text{O}_3$ isoelectronic series and the PZT 50/50 solid solution. We began with an assessment of seven cubic constrained arrangements of PZT 50/50 (including the VCA) compared with end members PZO and PTO. For each case, we evaluated the phonon dispersions and densities of states throughout the 1BZ using accurate DFPT and FDM simulations. With a focus on the dynamical instabilities ($\tilde{\nu}(\mathbf{q}) \in i\mathbb{R}$), we mapped the possible energy and symmetry lowering phase transition pathways for the various arrangements. Using the dispersions, densities of states and the character of modes at high symmetry points, we were able to glean new insights into the nature of the phase transitions in these industrially important materials. In general, we found that those PZT configurations lacking continuous Ti-O-Ti chains (like the rock-salt ordered case) had lattice dynamics comparable to pure PZO whilst those *with* at least one of these chains intact (or at least a chain where the Ti:Zr ratio is high) behaved much more like pure PTO. This sends a word of warning to those wishing to simulate near-morphotropic PZT: the choice of cation ordering significantly alters the lattice dynamics (and likely the character of the ground state phase). This warning does come with a caveat. A simple analysis of the number of permutations for B-site order in PZT 50/50 (in a crystal of finite size) reveals that there are many more arrangements with at least one chain having a high Ti:Zr ratio than not. So, it is *much* more likely that any given sample will have a

PTO-like ferroelectric ground state, in line with experimental observation [91].

The character and wavelength of several important modes, above all, has informed us of two things. Firstly, the VCA cannot accurately represent distortions to the local atomic structure; a fact already suspected but now shown in quantitative manner. It is then highly likely that accurate lattice dynamics cannot be achieved with this approximation and increasingly large supercell calculations may be needed. Secondly, many phonon branches in the dispersions of PZT and PZO, unlike PTO, remain firmly unstable throughout much of the 1BZ, even at \mathbf{q} away from high symmetry points. This is strong evidence for the existence of long range order increasingly incommensurate with the parent cubic crystal. Since these instabilities have a large number of participating atoms, large scale DFT simulations are essential to study their energetics.

Given the complexity of the cubic PZO dispersion and the propensity for long range order, we were motivated to carefully study the (perhaps former!) groundstate antiferroelectric *Pbam* phase of PZO and PHO. Remarkably, the phonon dispersions of these phases, in both materials, are dynamically unstable at the \mathbf{Z} -point ($\mathbf{q}_Z = (0, 0, 1/2)$). Freezing in the eigendisplacements of this instability and relaxing the structure doubles the unit cell (to 80 atoms) and slightly lowers the energy (confirmed at the LDA, GGA and meta-GGA levels in DFT). This new phase is a lower symmetry *Pnma* structure, characterised by a NaNbO_3 -like [324] (or AgNbO_3 -like [325]) *super-tilting* pattern of the $\text{ZrO}_6/\text{HfO}_6$ octahedra and small Pb antipolar displacements perpendicular to the preexisting Pb antipolar displacements. When evaluating the stability of this this new *Pnma* phase with further phonon computations, we found that it was dynamically stable ($\bar{\nu}(\mathbf{q}) \in \mathbb{R}$) for the chosen set of \mathbf{q} -points. Then, from the perspective of DFT at least, it is most likely the ground state crystal structure of PZO and PHO. The outlook for experimental conformation of this is, however, difficult. Firstly, the differences between the *Pbam* and *Pnma* models are subtle. This distortion is small and *Pnma* is only lower in energy by $\sim 1\text{meV/FU}$. This suggests that near cryogenic temperatures may be required in any measurement to distinguish them. The low sensitivity of X-ray methods to oxygen positions likely precludes their use (although they may be able to resolve the Λ_3 Pb displacements), and, since the two models share the same Raman active modes, there will be no *smoking gun* in the Raman spectra. However, neutron methods (diffraction or inelastic scattering) could be used to great avail and high resolution TEM-HAADF/iDPC images have a chance to detect the new Pb displacements.

Having demonstrated that long wavelength order is ubiquitous (even in the bulk crystal) in these systems, we moved towards a suitable simulation method to study it. In Chapter 5, we demonstrated the readiness of compact & efficient basis sets of PAOs to perform accurate simulations of the perovskite oxides and other important materials. Since these are a vital ingredient for large scale DFT in the CONQUEST code, we have then shown it is possible to scale up DFT while retaining high chemical accuracy. We found this to be true *even for the perovskite oxides* which are expected to respond sensitively to small variations in the electronic structure. We began by performing a comparative study of the structural properties between

various PAO basis sets, reporting their accuracy with respect to plane wave calculations using the same pseudopotential. We focused on the PAO generation mechanism used to produce the default basis sets shipping with CONQUEST. We found that basis sets generated with the *equal radii* criterion, in most cases, *slightly* outperformed those created with the *equal energy* criterion for lattice constants and bulk moduli. This difference aside, most PAO basis sets were found to reproduce plane wave calculations to a high fidelity.

Taking forward the *equal radii* construction, we performed an in depth analysis of the electronic structure, phase transition energies and soft mode distortion amplitudes using PTO, PZO and two arrangements of PZT 50/50 as test cases. Once again, the performance of the PAO basis sets were bench-marked against plane wave calculations with the same pseudopotential. For the electronic structure, two metrics were selected. The first was a comparison of the charge density difference $\Delta n(\mathbf{r})$ between the PAO calculations and the plane wave obtained charge density. We examined this visually with charge density difference plots and quantified this by defining a *total electronic error* integral. We found that PAO charge densities obtained even with a small SZP basis were accurate to $\approx 1.7\%$ while the large TZTP basis was accurate to $\approx 0.5\%$. It became clear from the visualisations of the charge density differences that volumes of increased error appeared at sites with reduced symmetry, as evidenced in $P4mm$ tetragonal PTO. We found that most of the error in the charge density was related to oxygen, either by a surplus of charge density on oxygen sites or a deficiency in charge density in the bonding describing the TiO_6 octahedra. Secondly, we assigned charges to the atomic sites using the Bader partitioning method. We found that these assignments were similar in accuracy to the pure charge density with an obvious cation to anion electronic charge transfer as basis set size increased.

We finished by analysing the nature of the phase transitions from the high temperature cubic phases of PTO and PZO to the lower temperature ferroelectric and antiferroelectric phases. We reported impressive accuracy in both the phase transition energy and magnitude of the soft mode distortions for PZO using a moderately sized basis. We did, however, find that more care needed to be taken for the phase transition in PTO. Here, the default small basis set (SZP) could not adequately describe the delicate balancing act between short range restoring forces and long range Coulombic forces (as described in the soft mode theory of Cochran and Anderson [1, 2, 52]), leading to a large super-tetragonality error in the tetragonal phase. While this error can be negated through using a larger basis, we suggested that a ‘tuned’ basis be used instead.

Now with a tried and tested large scale DFT method, in Chapter 6, we moved towards describing the ferroelectric domain structures present in ultrathin PTO films. We focused first on the unaddressed problem of broken inversion symmetry for films on substrates. This problem *has* been addressed for tricolor superlattices where they are known to *self-pole* with the possible disappearance of minority domains [383, 392]. However, as we realised, full self-poling in this manner is prohibited in thin films by giant depolarising fields, so, the minority domains likely persist (which lines up with the experimental observation of polydomain ultrathin films in

film/substrate systems [32–34, 399]). Treating PTO deposited on a STO substrate, we used the MSSF method to investigate this problem, scaling high accuracy DFT beyond 2,000 atoms.

We found that multiple domains persisted down to low dimensions but were more asymmetrical than those previously reported in the literature. Domains directed towards the substrate were universally more polar than those directed away from it, driven by an internal bias field born of the compositionally broken inversion symmetry. When the film was just three unit cells thick, we found that there was a transition from full flux-closure domains to a polar wave phase with cylindrical chiral bubbles. We suggested that the formation of this phase was caused by the bias field creating different critical thicknesses (and different depolarising fields) for the suppression of out-of-plane ferroelectricity for up and down domains. Then, at some critical thickness, up domains become unstable whilst down domains remain stable. The resulting polar wave texture is then the result of the linked polar flux between areas of stable out-of-plane polarisation and areas where in-plane polarisation is now favoured. It was found that local polar modes coupled strongly with local AFD modes, especially at the surface. Here, strong inter-mode coupling drives a $p(2 \times \Lambda)$ surface reconstruction for polydomain films.

Also within Chapter 6, we scaled up DFT even further. Using the full $\mathcal{O}(N)$ scaling capabilities of CONQUEST, we investigated the mechanism for which ferroelectric domain walls align with surface defects in ultrathin films. With simulations exceeding 5,000 atoms in size, we confirm that ferroelectric domain walls preferentially align to run parallel to engineered surface trenches, pinned at the domain centroid. We suggest that this trench orientation is the most favoured as it causes only small modulations to the underlying flux-closure domain structure. Further, trenches as shallow as one unit cell in depth are found to give rise to strong strain gradients on the film surface in line with experimental observation [55]. These strain gradients are expected to play a role in the alignment mechanism for wider and deeper trenches.

Reflecting now on this thesis as a whole, there are certainly lessons to be learned and exciting new directions for future research. The emergence of an increased stability crystal structure of PZO and PHO, the supposed antiferroelectric archetypes, brings into question how much we know about the structure of other antiferroelectrics. A full first principles study of the phonon dispersions should then be performed on the other known antiferroelectrics. Only then could we rule out fine distortions at longer wavelength q contributing to their ground state structures. It is the opinion of the author that such a search for stability has not previously been completed due to the limitations of DFT. That is, antiferroelectric materials typically have large unit cells and low symmetry. This spells disaster for phonon calculations whose efficiency relies upon exploiting the symmetry operations of the crystal. For context, evaluating the stability of the $Pnma$ PZO phase required in excess of 500,000 core hours of DFPT calculations; access to HPC is clearly essential. Given the complexity of this new stable phase, it begs the question: are PZO and PHO *really* archetypal? It is the opinion of the author that they *are not*. The emergence of an antiferroelectric transition in $\text{Cu}_3\text{Bi}(\text{SeO}_3)_2\text{O}_2\text{Cl}$ (Francisite) described by a single antipolar

mode [132] is far more prototypical and will likely lead to great advances in the understanding of the antiferroelectric phenomenon.

Now that within Chapter 5 we have shown that *most* of the default PAOs shipping with CONQUEST rival plane wave accuracy, one may ask the question: why use plane waves at all? There are many answers to this question. We firstly must put emphasis on only *most* of the default PAOs performing well. Some notable examples performed rather poorly. Since we cannot be sure *exactly* when the default PAO constructions will fail, the preparatory step where one must carefully test the basis set remains. When one must optimise a basis, the performance becomes excellent, but, the very fact we have performed a fitting procedure (albeit fit to another *ab initio* result) makes the whole process feel a little less *ab initio*. By comparison, plane wave calculations suffer neither of these shortfalls. Also, at present, the maturity of plane wave packages is such that they are more feature rich than those operating with local orbitals. While this situation is improving, there is still much progress to be made.

Some interesting outlooks for controlling ferroelectric domains without external fields are made in Chapter 6. For films on substrates we suggested that the internal bias field generated from the broken inversion symmetry could be put to use. While it may already be possible to tune the strength of this field through the choice of substrate or overlayers, with the aid of ever-improving advanced deposition techniques, it could soon be possible to take this further. That is, ferroelectric domains could be contained within complex heterostructures offering tuned internal bias fields in more than one direction. This is one promising avenue for the development of future devices reliant on the control of toroidal order. We have also shown that engineered surface trenches as shallow as one unit cell are enough to preferentially align domain walls to run parallel to the trench in ultrathin films. This could inform design choices in the fabrication of domain wall nanoelectronic devices.

We hope that the work in Chapters 5 & 6 work will encourage more materials modellers to give large scale DFT a try. Within CONQUEST, we have shown that is possible to perform accurate simulations on a few thousands atoms using the HPC resources available at most universities and research laboratories. That being said, there are still teething problems for large scale DFT. One issue encountered within this thesis relates to difficulties in structural relaxation. That is, in the limit of a large system, the number of degrees of freedom f that must be optimised is $\approx 3N$ where N is the number of atoms. This causes problems for conventional optimisation procedures. Take for example the popular conjugate gradients method [409]. This is expected to reach a minimum after $\sim f$ steps; clearly unsatisfactory for systems comprised of a few thousand atoms. While we find that quenched molecular dynamics performs better for these larger structures, it is by no means perfect and has several adjustable parameters that one must tune for optimal performance. This is one area where machine learning techniques could offer improvements [410].

Since large scale DFT remains a compute intensive task, it must adapt to current hardware

trends in HPC. It was commonplace ten years ago to have supercomputers with only ≈ 10 physical cores per node. Examining some new systems (like Fugaku, Summit, ARCHER2 and Isambard) it is clear that this number has increased up to twelve-fold. In most cases, this will force further adoption of hybrid MPI/OpenMP communications. There is also a demand for these architectures to consume less power. Above all this has provided companies like ARM a slice of the HPC market. Indeed, the largest supercomputer in the world at the time of writing this thesis, Fugaku, is an ARM machine. This trend also means that GPU computation has become increasingly important. This creates a task for DFT code developers in working out which portions of code are suitable for porting to GPU. These issues aside, one thing is clear. Those who venture into the field of large scale DFT will surely reap the rewards through solving previously intractable problems, discovering new functional properties and ultimately informing advances in nanotechnology.

A | Appendices

Here we provide extra information in support of the main text of this thesis. Section A.1 contains standard tests for the convergence of plane wave calculations, a full wavenumber tabulation of the dynamical instabilities of PTO, PZO and PZT 50/50 and a demonstration of the equivalence of FDM and DFPT calculations. Section A.2 contains tests for convergence of PAO calculations for bulk and thin film calculations.

A.1 Plane waves and dynamical instabilities,

Figures A.1 and A.2 comprise a standard battery of convergence tests for the plane wave cutoff energies and BZ integrations relevant to Chapter 4. We remind the reader that the parameters used in production for NCPP/PAW (which used the PBESol [229]/LDA-PW [153] functionals) calculations were 1088.46/680.285 eV for the plane wave cutoff and Γ -centered $8/N_x \times 8/N_y \times 8/N_z$ and $6/N_x \times 6/N_y \times 6/N_z$ for Monkhorst-Pack meshes where $N_{x,y,z}$ is the number of repeated 5-atom perovskite units in the given Cartesian direction. For BZ integrations we considered only those meshes centred on the Γ -point so that important ferroelectric zone-centre instabilities were *not* interpolated in the subsequent DFPT phonon calculations.

Figure A.4 shows the DFPT & FDM dispersions of PTO & PZO using the primitive perovskite cell. DFPT calculations are performed using the implementation in ABINIT (v8.10.2) whilst FDM calculations are performed using `phonopy` (v2.1). We do not aim to prove the formal equivalence of the FDM and DFPT but rather demonstrate that in practicality, comparable results can be achieved between them. This test is a justification for the use of the FDM for VCA calculations in Chapter 4 when others are performed with DFPT.

We use a $4 \times 4 \times 4$ supercell and a displacement of 0.01 \AA for the FDM calculation and a Γ -centred $8 \times 8 \times 8$ q -point mesh for the DFPT calculation. We ensure that we achieve the same level of convergence in the electronic ground state for both cases. The parameters used represent what is feasibly possible (at present) for both methods for a modest computational cost. That is, convergence is very well achieved for DFPT with the chosen mesh of q -points, but, for the FDM, improvements can be made to some q -points but the supercell size of $4 \times 4 \times 4$ already contains 320 atoms, approaching the limits of plane wave DFT. This means that the DFPT calculation should be more accurate since the dense q -point mesh incorporates the exact calculation of

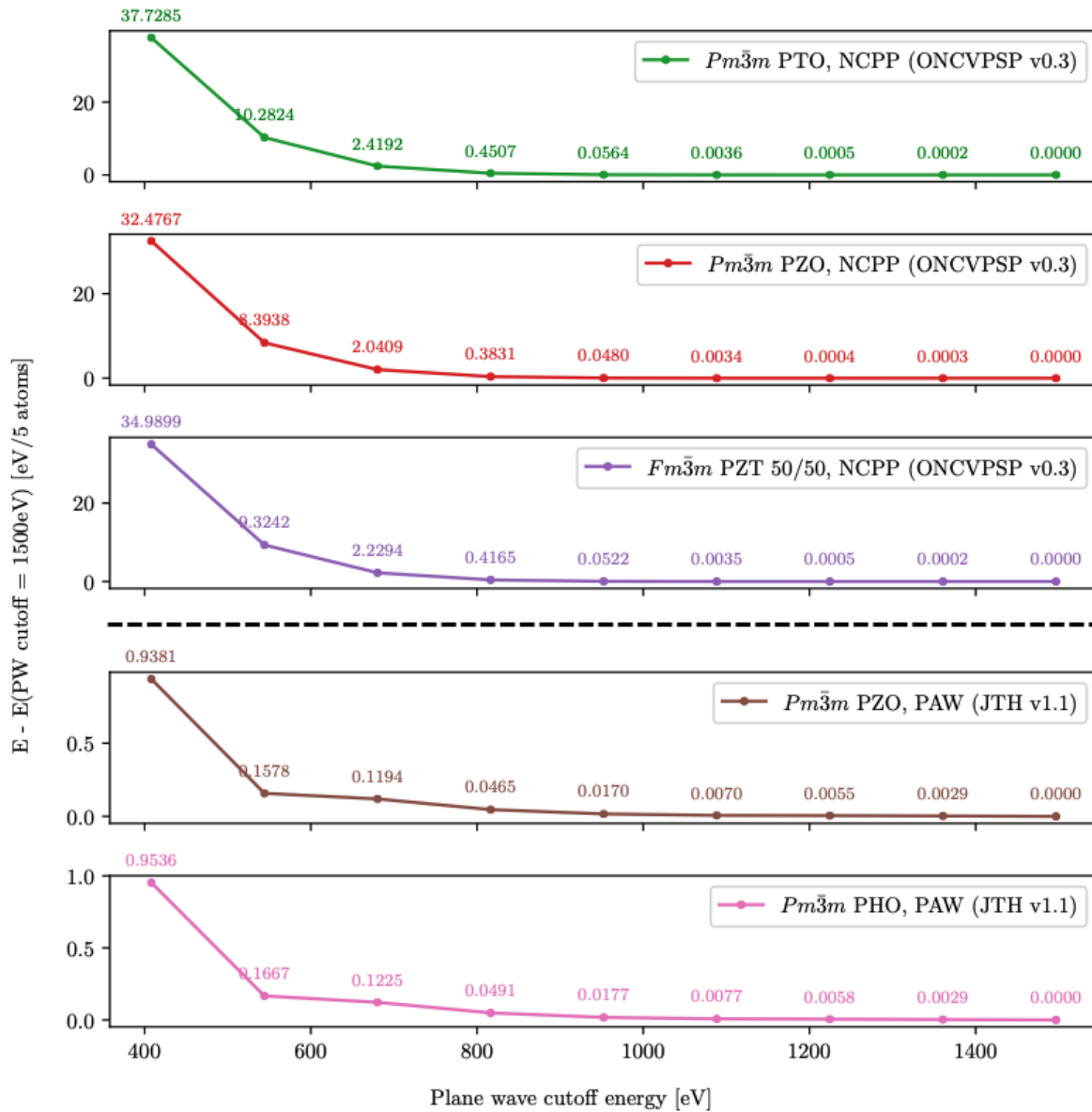


Figure A.1: The convergence of the total energy (compared to the total energy resulting from a highly converged 1500 eV calculation) as function of plane wave cutoff energy for the NCPP and PAW calculations. Plots on vastly different scales are separated by a black dashed line.

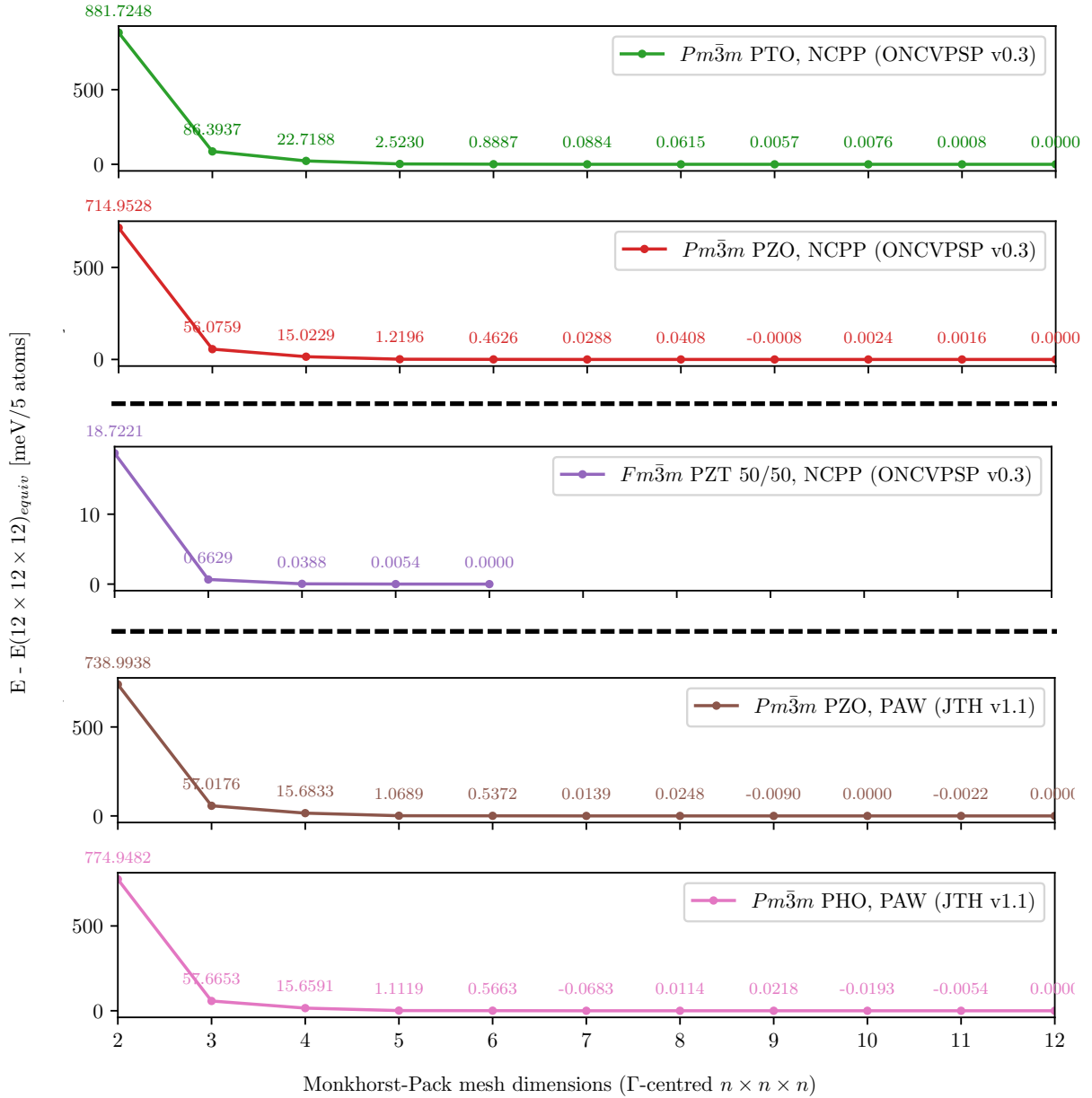


Figure A.2: The convergence of the total energy (compared to the total energy resulting from a highly converged $12 \times 12 \times 12$ calculation) as function of Γ -centred Monkhorst-Pack mesh dimensions for the NCPP and PAW calculations. Note that $Fm\bar{3}m$ PZT 50/50 is represented within a $2 \times 2 \times 2$ supercell of the primitive perovskite unit, so, the $6 \times 6 \times 6$ mesh of this calculation is designated as $12 \times 12 \times 12$ -equivalent. Plots on vastly different scales are separated by black dashed lines.

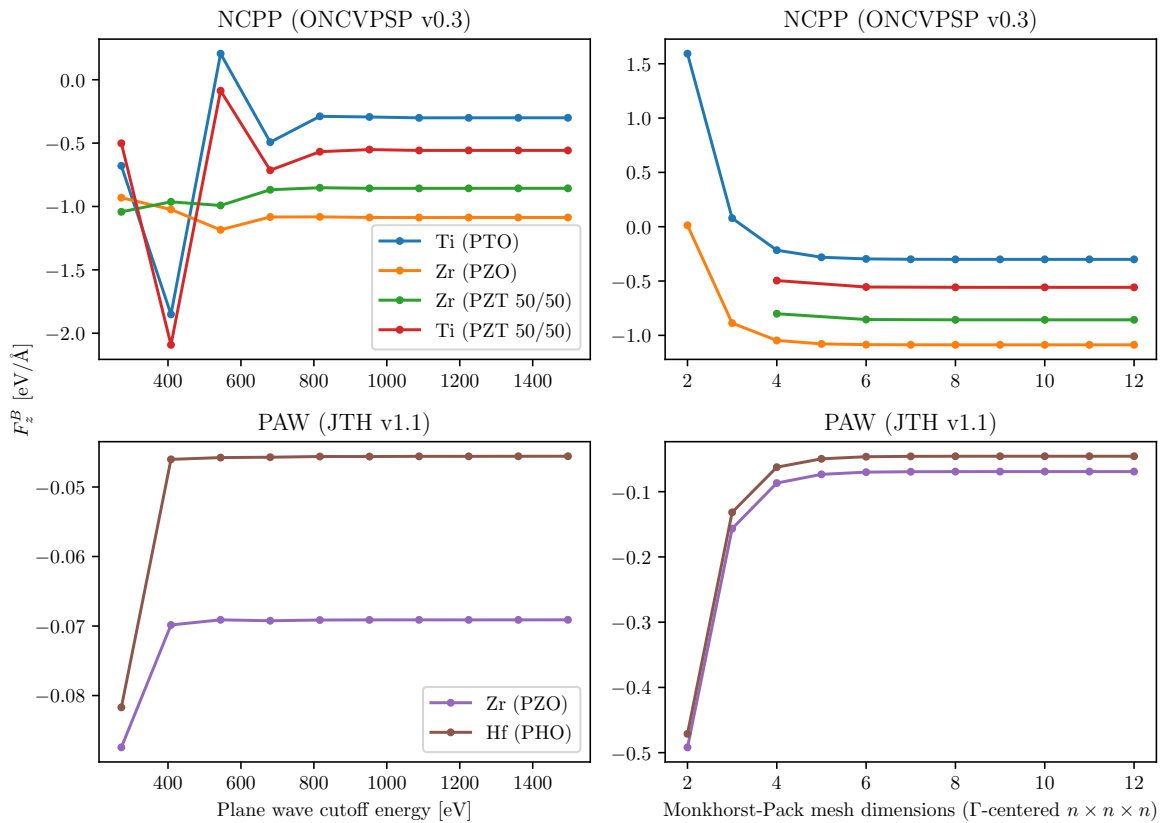


Figure A.3: The convergence of forces on the B-site ions in the cubic cell with the B-site displaced 0.1\AA in the $[001]$ direction. We show convergence as a function of fineness of Brillouin zone integration as well as the plane wave cutoff energy. Each plot has a different scale for the y-axis. For the upper right plot, PZT 50/50 calculations are plotted with their 5-atom perovskite unit cell equivalent MP mesh (i.e, a $2 \times 2 \times 2$ MP mesh in the 40-atom PZT supercell is equivalent to a $4 \times 4 \times 4$ mesh on the primitive perovskite unit cell).

phonons at longer wavelengths than what is possible within the $4 \times 4 \times 4$ supercell in the FDM.

Figure A.4 shows that there is clearly great agreement between the two methods across the whole of the 1BZ. The calculations are however not without discrepancy. Notably, at the M-point of the PTO calculation, the instabilities of the FDM are slightly greater than the DFPT calculation. Discrepancies of a similar magnitude also exist as we approach Γ for the PZO calculation. These errors are as the result of interpolation on a sparser grid of \mathbf{q} -points for the FDM calculation vs the DFPT calculation. This level of error is however small and does not affect the general hierarchy of modes.

		M	$\bar{\nu}$ [i cm $^{-1}$]		M	$\bar{\nu}$ [i cm $^{-1}$]		M	$\bar{\nu}$ [i cm $^{-1}$]
PTO	Γ_4^-	3	149.60	Δ_5^+	4	83.40	R_4^+	3	62.12
	T_4	2	45.40	Σ_3	4	37.61	Σ_2	4	27.05
	M_3^+	3	18.02						
PZO	R_4^+	3	181.52	T_4	2	178.75	M_3^+	3	176.09
	Γ_4^-	3	132.14	S_4	4	128.32	T_5	4	120.45
	Σ_2	4	119.69	Z_4	4	119.53	S_3	4	105.37
	Λ_2	8	103.13	Λ_3	16	101.82	Δ_5	4	93.38
	M_5^-	6	87.70	S_2	4	72.93	Σ_3	4	60.66
	Σ_2'	4	59.00	Z_4'	4	119.53	Z_1	4	56.19
	X_5^+	6	53.03	S_4'	4	50.60	R_5^+	3	49.96
	S_1	4	46.04	Z_2	4	36.84	T_5'	4	32.98
	T_3	2	29.33	M_2^-	3	12.25			
VCA	M_2^+	3	146.58	Δ_5	2	141.95	R_5^-	3	137.38
	Γ_4^-	3	101.18	S_1	4	71.78	T_2	4	52.87
	Z_1	4	52.18	T_5	4	52.14	Λ_3	16	49.55
	X_5^-	6	44.89	Σ_2	4	40.27	S_2	4	36.47
	Σ_3	4	28.90	M_5^-	6	21.80			
I	Γ_4^+	3	138.10	Δ_4	2	133.08	X_3^+	3	128.11
	Γ_4^-	3	111.99	Σ_2	4	73.53	Δ_5	4	62.02
	L_3^-	8	52.83	X_5^-	6	49.09	$L_3^{-'}$	8	48.70
	W_5	4	48.29	Δ_5'	4	47.02	Σ_3	4	40.64
	Σ_3'	4	30.35	X_5^+	6	23.23	Σ_4	4	15.71
	Σ_1	4	12.39						
II	Γ_3^-	1	242.28	M_3^-	1	227.52	Z_5^-	2	148.78
	Γ_5^-	2	144.78	A_5^-	2	140.02	Z_1^-	1	137.91
	Λ_4	2	132.92	Γ_3^+	1	127.97	C_1	4	105.26
	W_1	4	102.70	Λ_5	4	101.14	W_2	4	90.22

	M	$\bar{\nu}$ [$i \text{ cm}^{-1}$]		M	$\bar{\nu}$ [$i \text{ cm}^{-1}$]		M	$\bar{\nu}$ [$i \text{ cm}^{-1}$]	
	C ₂	4	81.83	V ₁	2	73.79	Γ_5^-	2	73.59
	V ₅	4	72.71	Λ_5'	4	63.59	A ₁ ⁺	1	62.46
	W ₄	4	58.47	C ₁ '	4	53.19	Γ_3^-	1	49.62
	A ₅ ⁺	2	48.45	C ₂ '	4	46.31	M ₂ ⁺	1	42.64
	Z ₅ ⁻	2	40.39	W ₃	4	40.28	W ₁ '	4	38.54
	V ₂	2	34.42	A ₂ ⁺	1	24.79	M ₅ ⁺	2	22.25
	A ₄ ⁺	1	20.43	C ₂ ^{''}	4	18.50			
III	Γ_5^-	2	196.63	M ₂ ⁺	1	190.76	Γ_3^-	1	174.29
	Δ_4	2	173.52	X ₂ ⁺	2	156.67	M ₅ ⁺	2	152.61
	Δ_3	2	150.97	X ₃ ⁺	2	149.79	Y ₃	2	147.85
	X ₂ ⁻	2	143.46	Γ_4^-	1	139.99	S ₃	4	129.31
	Y ₁	2	128.42	S ₄	4	125.00	Y ₂	2	121.06
	Σ_4	4	114.69	Σ_3	4	112.91	Δ_3'	2	112.14
	Σ_2	4	111.96	S ₂	4	106.31	M ₂ ⁺	1	86.98
	Γ_5^-	2	66.80	S ₄ '	4	63.81	X ₁ ⁺	2	57.29
	Σ_2'	4	51.92	M ₅ ⁻	2	44.99	S ₁	4	37.58
	Y ₄	2	37.45	Δ_1	2	36.77	Δ_3''	2	35.19
	Y ₁ '	2	33.47	Σ_1	4	31.52	Δ_4'	2	27.15
	X ₃ ⁻	2	21.52	X ₂ ⁻ '	2	21.52	Γ_5^+	2	19.61
	Σ_3'	4	1.48						
IV	Γ_4^-	3	181.41	Γ_4^+	3	169.33	X ₃ ⁺	1	168.90
	X ₅ ⁺	2	168.18	M ₂ ⁻	1	157.00	M ₃ ⁺	1	150.48
	R ₄ ⁺	3	148.69	X ₅ ^{+'}	2	130.13	M ₅ ⁺	2	129.20
	Γ_4^- '	3	114.61	X ₁ ⁻	1	113.97	Γ_4^+ '	3	113.65
	X ₅ ⁻	2	108.24	Γ_5^-	3	101.77	M ₅ ⁻	2	101.00
	R ₃ ⁻	2	97.56	M ₄ ⁻	1	93.31	M ₃ ^{+'}	1	92.85
	X ₅ ⁻ '	2	89.27	X ₄ ⁻	1	85.35	R ₄ ⁻	3	82.08
	M ₃ ⁻	1	76.93	X ₃ ⁻	1	74.61	M ₅ ⁻ '	2	66.98
	R ₅ ⁻	3	64.69	R ₅ ⁻ '	3	58.70	M ₂ ⁺	1	54.87
	M ₄ ⁺	1	53.23	X ₅ ^{+'''}	2	42.33	X ₅ ^{+'''}	2	38.24
	R ₅ ^{+'''}	3	38.04	Γ_4 ^{+'''}	3	37.69	R ₃ ⁺	2	32.38
	R ₄ ^{+'}	3	29.11	Γ_5^+	3	24.81	X ₅ ^{+''''}	2	22.41
	M ₃ ⁻ '	1	21.33	Γ_4 ^{+'''}	3	19.94	M ₅ ^{+'''}	2	19.92
	M ₁ ⁻	1	18.81	X ₅ ⁻ ''''	2	17.91	M ₂ ⁻ '	1	13.90
V	Γ_5^-	1	209.42	X ₃ ⁻	1	202.33	Γ_3^+	1	167.07

	M	$\bar{\nu}$ [$i \text{ cm}^{-1}$]		M	$\bar{\nu}$ [$i \text{ cm}^{-1}$]		M	$\bar{\nu}$ [$i \text{ cm}^{-1}$]			
			Γ_3^-	1	153.93	Γ_5^+	2	147.67	X_4^+	1	146.16
			X_1^-	1	132.83	$\Gamma_5^{+'}$	2	131.48	X_2^-	1	129.84
			M_3^+	1	126.85	A_3^+	1	124.13	A_3^-	1	117.20
			X_2^+	1	116.35	Γ_4^-	1	114.09	$\Gamma_3^{+'}$	1	113.55
			A_5^+	2	112.74	A_4^-	1	108.99	X_3^+	1	105.03
			M_5^+	2	99.94	$\Gamma_5^{-'}$	2	98.87	M_2^+	1	98.36
			$X_2^{-'}$	1	98.20	M_3^-	1	97.04	M_4^-	1	95.03
			M_5^-	2	86.16	$X_3^{-'}$	1	84.11	$A_4^{-'}$	1	75.27
			$\Gamma_3^{-'}$	1	74.54	A_5^-	2	67.07	$X_2^{+'}$	1	63.98
			$X_3^{+'}$	1	63.97	$\Gamma_5^{-''}$	2	62.67	A_2^-	1	60.47
			$A_5^{+'}$	2	57.86	X_4^-	1	56.88	M_2^-	1	50.65
			X_1^+	1	50.24	A_1^+	1	48.22	$A_5^{-'}$	2	47.63
			$X_2^{-''}$	1	47.30	$X_3^{-'}$	1	46.82	A_1^-	1	45.25
			$X_2^{-''''}$	1	44.10	$\Gamma_5^{-''''}$	2	43.75	A_2^+	1	43.00
			$M_5^{-'}$	2	42.70	A_4^+	1	42.11	$M_5^{+'}$	2	40.86
			$X_3^{''}$	1	39.51	$M_3^{-'}$	1	38.22	$M_3^{+'}$	1	37.50
			$\Gamma_5^{''}$	2	36.25	$A_3^{-'}$	1	35.66	$A_5^{''}$	2	35.53
			Γ_4^+	1	33.40	$X_2^{''}$	1	33.17	$M_5^{''}$	2	29.38
			$X_3^{-''''}$	1	28.07	X_1^-	1	26.36	M_4^+	1	26.31
			$X_4^{+'}$	1	25.02	$\Gamma_3^{''}$	1	24.40	$\Gamma_5^{''''}$	2	12.93
			$A_3^{+'}$	1	12.79	Γ_2^-	1	12.25	M_1^-	1	11.24
			$M_4^{-'}$	1	7.80						
VI			Γ_5^-	2	206.22	X_2^+	1	197.36	R_1^-	1	190.45
			Γ_3^-	1	180.33	Γ_5^+	2	167.85	X_4^+	1	167.42
			X_3^+	1	167.00	Γ_4^+	1	149.99	Γ_3^+	1	142.07
			R_4^+	1	141.00	A_3	2	137.71	$\Gamma_5^{-'}$	2	136.80
			R_3^-	1	123.60	A_2	2	120.70	$X_3^{+'}$	1	119.82
			X_3^-	1	115.84	X_1^-	1	114.49	$\Gamma_5^{+'}$	2	114.14
			R_4^-	1	106.06	$R_3^{+'}$	1	104.45	$X_2^{+'}$	1	102.38
			A_3'	2	101.82	R_2^+	1	98.40	$R_3^{-'}$	1	98.02
			$\Gamma_5^{-''}$	2	97.86	$\Gamma_3^{-'}$	1	96.82	X_4^-	1	92.87
			$X_3^{-'}$	1	89.47	X_2^-	1	88.45	R_4^+	1	88.45
			A_4	2	85.09	R_1^+	1	84.27	A_2'	2	83.99
			$X_2^{''}$	1	80.41	R_1'	1	80.04	$X_4^{-'}$	1	79.06
			$X_2^{-'}$	1	76.30	R_2^-	1	74.85	Γ_4^-	1	65.34
			$R_4^{-'}$	1	63.07	A_1	2	61.62	$\Gamma_5^{-''''}$	2	59.61

	M	$\bar{\nu}$ [i cm $^{-1}$]		M	$\bar{\nu}$ [i cm $^{-1}$]		M	$\bar{\nu}$ [i cm $^{-1}$]
$\Gamma_3^{-''}$	1	57.06	A_3''	2	48.35	A_4'	2	48.07
$X_2^{-''}$	1	46.95	$X_3^{-''}$	1	44.18	$X_3^{+''}$	1	41.42
$R_3^{+''}$	1	39.34	$X_2^{+''}$	1	39.27	$R_3^{-''}$	1	38.55
X_1^+	1	37.22	A_1'	2	36.53	$\Gamma_5^{+''}$	2	35.71
$R_1^{-''}$	1	35.39	$R_2^{+''}$	1	35.35	$R_4^{+''}$	1	35.01
A_2''	2	34.17	$\Gamma_3^{+''}$	1	33.14	$R_4^{+''}$	1	30.27
$X_2^{+''}$	1	25.71	$\Gamma_4^{+''}$	1	25.38	$R_2^{-''}$	1	24.39
$X_4^{+''}$	1	24.06	$X_3^{-''}$	1	23.84	$R_4^{+''}$	1	22.31
$R_2^{+''}$	1	20.26	A_3'''	2	19.30	$\Gamma_5^{+''}$	2	14.76
Γ_2^-	1	11.59						

Table A.1: The **analytical** phonon wavenumbers of dynamical instabilities at the considered wavevectors chosen in 4 for PTO, PZO and PZT 50/50. Modes are listed in descending order in imaginary wave number from left to right. Each mode is assigned a symmetry label and a multiplicity, M.

Table A.1 lists exhaustively the dynamical instabilities of the phonon calculations of PTO, PZO and PZT 50/50 in Chapter 4. Symmetry labels (irreps) are obtained by the following procedure: first, the eigendisplacement pattern of a given mode is superimposed (at a small amplitude) onto the parent crystal. This creates a daughter for which we use the mode decomposition analysis tools within the ISODISTORT [321] program. The result is the mode irrep and other useful symmetry information.

A.2 Pseudoatomic orbitals: bulk and thin films

In this section we show convergence in the total energy (per atom, to be consistent with Chapter 6) and energy differences for increasingly fine real-space integration grids [4] and Monkhorst-Pack [227] meshes. Figure A.5 shows energy convergence for the fineness of integration grid for the bulk phases of PTO. We see that our choice of a 300Ha cutoff achieves convergence to the (very fine) 1200Ha grid to 0.02 meV/atom in the energy difference between the $Pm\bar{3}m$ and $P4mm$ phases (A.5, Lower panel).

Figure A.6 shows the convergence in the total energy and energy differences with respect to the fineness of Monkhorst-Pack mesh for the bulk phases of PTO (left column) and the $N_z = 2$ film (right column, geometry explained in Chapter 5, Section 6.2.5). It is interesting to point out that energy convergence for the film geometry (a 2D mesh of $N \times N \times 1$) is achieved at a slightly coarser mesh (with smaller N , that is) than the bulk geometry (a 3D mesh of $N \times N \times N$). We suggest that this is because convergence in the the out-of-plane direction for the film geometry is (close to) perfectly achieved with a single k-point as ensured by the large vacuum region

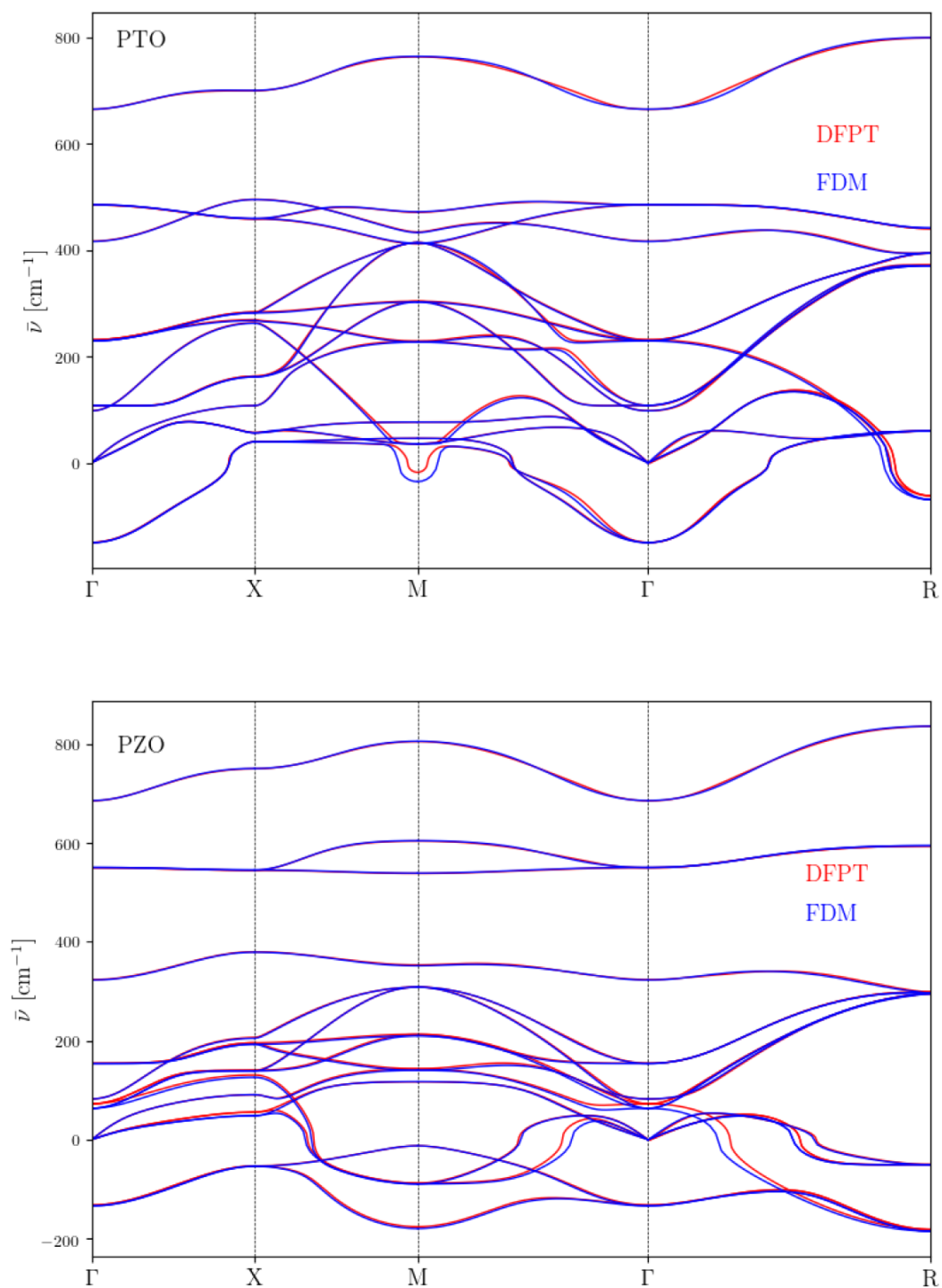


Figure A.4: Phonon dispersion curves using the FDM and DFPT for both PTO (top) and PZO (bottom). This calculation is performed across the primitive cell of $Pm\bar{3}m$ PTO & PZO.

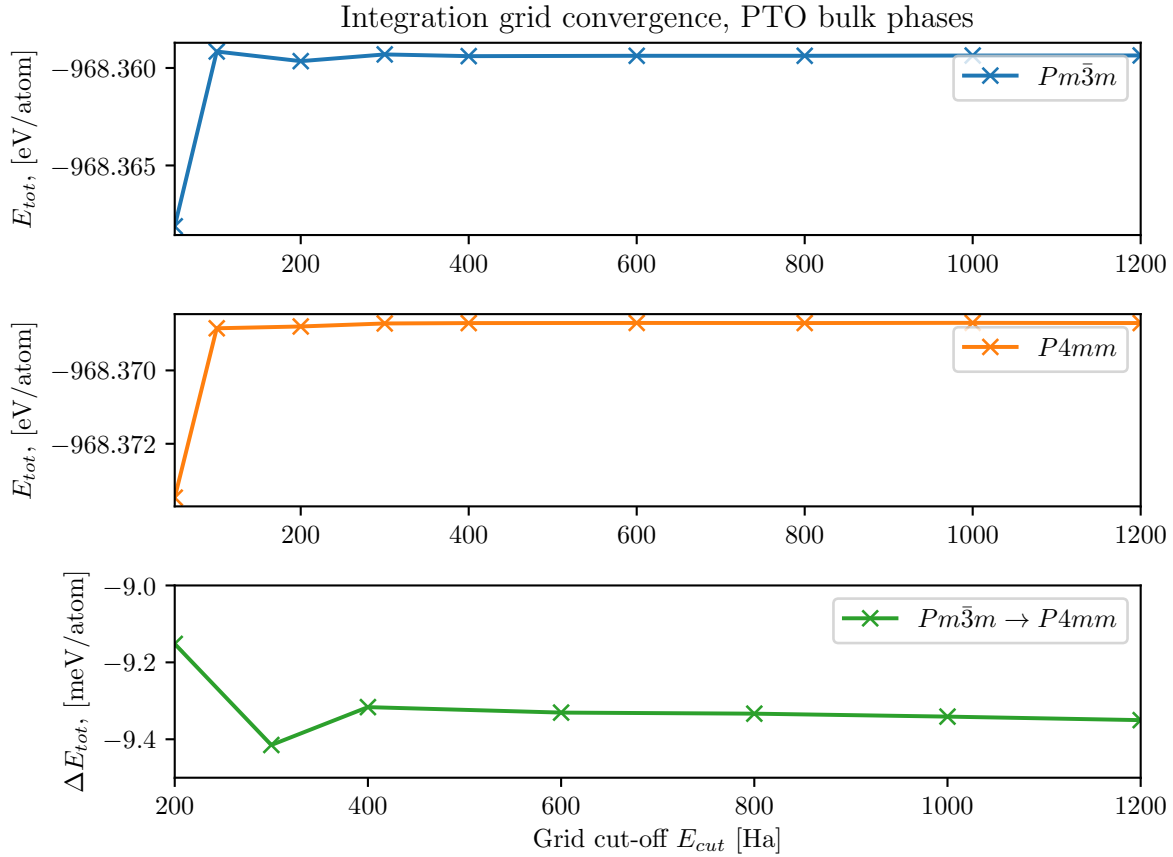


Figure A.5: A convergence study for the the fineness of integration grid (measured in plane-wave equivalent cut-off energy, E_{cut}) for the bulk $Pm\bar{3}m$ and $P4mm$ phases of PTO. The upper and middle panels are for convergence of the total energy whilst the lower panel measures the energy difference ΔE between the phases in meV/atom.

separating periodic images of the film. When we increase the fineness of the mesh, there is then no energy contribution from extra k -point sampling in the out-of-plane direction.

We note that there is a small effect related to energy differences between Γ -centered and non- Γ -centred meshes. For the film geometry, we see that the energy difference is lower by 0.19 meV/atom for the $6 \times 6 \times 1$ mesh (Figure A.6, bottom right) when one phase is Γ -centred and the other is not. This effect reduces to a difference of 0.1 meV/atom if we consider the energy difference between a paraelectric film (not centred on Γ) and a film with AFD modes, as we do in Chapter 6 (which is centered on Γ since we use a $6/N_x \times 6/N_y \times 1$ mesh and $N_x = N_y = 2$). We therefore conclude that energy differences between geometries without AFD modes and with AFD modes will all be lower in energy by ≈ 0.1 meV/atom. This extra degree of energy lowering should be taken into account when examining Figure 6.9 in 6, but, makes no difference to the conclusions drawn (i.e, the favourability hierarchy of different phases).

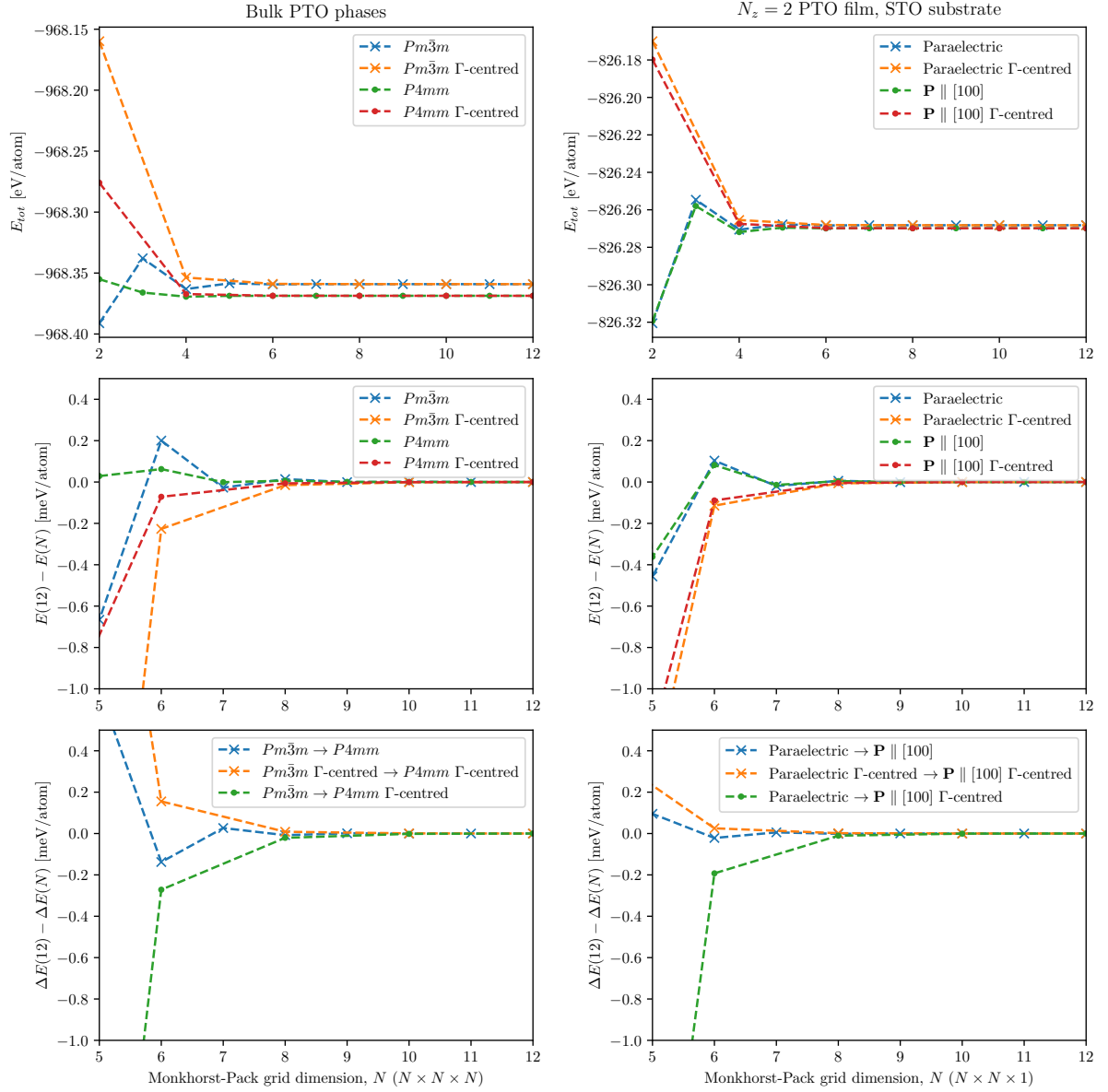


Figure A.6: The convergence of reciprocal space integrals using uniform Monkhorst-Pack meshes for the bulk phases of PTO and the $N_z = 2$ film (detailed in Chapter 6). The upper panels show the convergence of the total energy with increasing grid dimensions. The middle panel shows the same test but as a difference with the highly converged (to $\approx 5 \times 10^{-7}$ eV in the total energy) $12 \times 12 \times 12$ mesh. The lower panel also compares with the $12 \times 12 \times 12$ mesh, but measures the energy difference between the considered phases.

Bibliography

- [1] W. Cochran, “[Crystal Stability and the Theory of Ferroelectricity](#),” *Physical Review Letters*, vol. 3, no. 9, pp. 412–414, Nov. 1959.
- [2] W. Cochran, “[Crystal stability and the theory of ferroelectricity](#),” *Advances in Physics*, vol. 9, no. 36, pp. 387–423, Oct. 1960.
- [3] R. E. Cohen, “[Origin of ferroelectricity in perovskite oxides](#),” *Nature*, vol. 358, no. 6382, pp. 136–138, Jul. 1992.
- [4] D. R. Bowler and T. Miyazaki, “ [\$\mathcal{O}\(N\)\$ methods in electronic structure calculations](#),” *Reports on Progress in Physics*, vol. 75, no. 3, p. 036 503, Feb. 2012.
- [5] M. C. Payne, M. P. Teter, D. C. Allan, T. A. Arias, and J. D. Joannopoulos, “[Iterative minimization techniques for *ab initio* total-energy calculations: molecular dynamics and conjugate gradients](#),” *Reviews of Modern Physics*, vol. 64, no. 4, pp. 1045–1097, Oct. 1992.
- [6] J. M. Soler, E. Artacho, J. D. Gale, A. García, J. Junquera, P. Ordejón, and D. Sánchez-Portal, “[The SIESTA method for *ab initio* order-N materials simulation](#),” *Journal of Physics: Condensed Matter*, vol. 14, no. 11, pp. 2745–2779, Mar. 2002.
- [7] A. Nakata, J. S. Baker, S. Y. Mujahed, J. T. L. Poulton, S. Arapan, J. Lin, Z. Raza, S. Yadav, L. Truflandier, T. Miyazaki, and D. R. Bowler, “[Large scale and linear scaling DFT with the CONQUEST code](#),” *The Journal of Chemical Physics*, vol. 152, no. 16, p. 164 112, Apr. 2020.
- [8] J. C. A. Prentice, J. Aarons, J. C. Womack, A. E. A. Allen, L. Andrinopoulos, L. Anton, R. A. Bell, A. Bhandari, G. A. Bramley, R. J. Charlton, R. J. Clements, D. J. Cole, G. Constantinescu, F. Corsetti, S. M.-M. Dubois, K. K. B. Duff, J. M. Escartín, A. Greco, Q. Hill, L. P. Lee, E. Linscott, D. D. O’Regan, M. J. S. Phipps, L. E. Ratcliff, Á. R. Serrano, E. W. Tait, G. Teobaldi, V. Vitale, N. Yeung, T. J. Zuehlsdorff, J. Dziedzic, P. D. Haynes, N. D. M. Hine, A. A. Mostofi, M. C. Payne, and C.-K. Skylaris, “[The ONETEP linear-scaling density functional theory program](#),” *The Journal of Chemical Physics*, vol. 152, no. 17, p. 174 111, May 2020.

- [9] C.-K. Skylaris, P. D. Haynes, A. A. Mostofi, and M. C. Payne, “[Introducing ONETEP: Linear-scaling density functional simulations on parallel computers](#),” *The Journal of Chemical Physics*, vol. 122, no. 8, p. 084 119, Feb. 2005.
- [10] A. García, N. Papior, A. Akhtar, E. Artacho, V. Blum, E. Bosoni, P. Brandimarte, M. Brandbyge, J. I. Cerdá, F. Corsetti, R. Cuadrado, V. Dikan, J. Ferrer, J. Gale, P. García-Fernández, V. M. García-Suárez, S. García, G. Huhs, S. Illera, R. Korytár, P. Koval, I. Lebedeva, L. Lin, P. López-Tarifa, S. G. Mayo, S. Mohr, P. Ordejón, A. Postnikov, Y. Pouillon, M. Pruneda, R. Robles, D. Sánchez-Portal, J. M. Soler, R. Ullah, V. W.-z. Yu, and J. Junquera, “[Siesta: Recent developments and applications](#),” *The Journal of Chemical Physics*, vol. 152, no. 20, p. 204 108, May 2020.
- [11] T. D. Kühne, M. Iannuzzi, M. D. Ben, V. V. Rybkin, P. Seewald, F. Stein, T. Laino, R. Z. Khaliullin, O. Schütt, F. Schiffmann, D. Golze, J. Wilhelm, S. Chulkov, M. H. Bani-Hashemian, V. Weber, U. Borštnik, M. TAILLEFUMIER, A. S. Jakobovits, A. Lazzaro, H. Pabst, T. Müller, R. Schade, M. Guidon, S. Andermatt, N. Holmberg, G. K. Schenter, A. Hehn, A. Bussy, F. Belleflamme, G. Tabacchi, A. Glöß, M. Lass, I. Bethune, C. J. Mundy, C. Plessl, M. Watkins, J. VandeVondele, M. Krack, and J. Hutter, “[CP2K: An electronic structure and molecular dynamics software package - Quickstep: Efficient and accurate electronic structure calculations](#),” *The Journal of Chemical Physics*, vol. 152, no. 19, p. 194 103, May 2020.
- [12] S. Mohr, L. E. Ratcliff, P. Boulanger, L. Genovese, D. Caliste, T. Deutsch, and S. Goedecker, “[Daubechies wavelets for linear scaling density functional theory](#),” *The Journal of Chemical Physics*, vol. 140, no. 20, p. 204 110, May 2014.
- [13] D. R. Bowler and T. Miyazaki, “[Calculations for millions of atoms with density functional theory: linear scaling shows its potential](#),” *Journal of Physics: Condensed Matter*, vol. 22, no. 7, p. 074 207, Feb. 2010.
- [14] S. Smidstrup, T. Markussen, P. Vancraeyveld, J. Wellendorff, J. Schneider, T. Gunst, B. Verstichel, D. Stradi, P. A. Khomyakov, U. G. Vej-Hansen, M.-E. Lee, S. T. Chill, F. Rasmussen, G. Penazzi, F. Corsetti, A. Ojanperä, K. Jensen, M. L. N. Palsgaard, U. Martinez, A. Blom, M. Brandbyge, and K. Stokbro, “[QuantumATK: an integrated platform of electronic and atomic-scale modelling tools](#),” *Journal of Physics: Condensed Matter*, vol. 32, no. 1, p. 015 901, Oct. 2019.
- [15] Biovia, *Materials Studio*, Materials studio is a a user friendly interface to many atomistic modelling codes including CASTEP and ONETEP, Apr. 2020.
- [16] E. Hernández, M. J. Gillan, and C. M. Goringe, “[Linear-scaling density-functional-theory technique: The density-matrix approach](#),” *Physical Review B*, vol. 53, no. 11, pp. 7147–7157, Mar. 1996.

- [17] D. R. Bowler, R. Choudhury, M. J. Gillan, and T. Miyazaki, “Recent progress with large-scale *ab initio* calculations: the CONQUEST code,” *Physica Status Solidi (b)*, vol. 243, no. 5, pp. 989–1000, Apr. 2006.
- [18] A. Nakata, D. R. Bowler, and T. Miyazaki, “Efficient Calculations with Multisite Local Orbitals in a Large-Scale DFT Code CONQUEST,” *Journal of Chemical Theory and Computation*, vol. 10, no. 11, pp. 4813–4822, Oct. 2014.
- [19] A. Nakata, D. R. Bowler, and T. Miyazaki, “Optimized multi-site local orbitals in the large-scale DFT program CONQUEST,” *Physical Chemistry Chemical Physics*, vol. 17, no. 47, pp. 31 427–31 433, Mar. 2015.
- [20] E. Wainer and A. N. Salomon, “Titanium alloy manufacturing co,” *Electr. Rep*, no. 8, 1942.
- [21] E. Wainer and A. N. Salomon, “Titanium alloy manufacturing co,” *Electr. Rep*, no. 9, 1943.
- [22] A. von Hippel, R. G. Breckenridge, F. G. Chesley, and L. Tisza, “High dielectric constant ceramics,” *Industrial & Engineering Chemistry*, vol. 38, no. 11, pp. 1097–1109, Nov. 1946.
- [23] J. F. Scott and C. A. P. de Araujo, “Ferroelectric Memories,” *Science*, vol. 246, no. 4936, pp. 1400–1405, Dec. 1989.
- [24] J. Junquera and P. Ghosez, “Critical thickness for ferroelectricity in perovskite ultrathin films,” *Nature*, vol. 422, no. 6931, pp. 506–509, Apr. 2003.
- [25] Q. M. Zhang, H. Wang, N. Kim, and L. E. Cross, “Direct evaluation of domain-wall and intrinsic contributions to the dielectric and piezoelectric response and their temperature dependence on lead zirconate-titanate ceramics,” *Journal of Applied Physics*, vol. 75, no. 1, pp. 454–459, Jan. 1994.
- [26] J. Seidel, L. W. Martin, Q. He, Q. Zhan, Y.-H. Chu, A. Rother, M. E. Hawkrige, P. Maksymovych, P. Yu, M. Gajek, N. Balke, S. V. Kalinin, S. Gemming, F. Wang, G. Catalan, J. F. Scott, N. A. Spaldin, J. Orenstein, and R. Ramesh, “Conduction at domain walls in oxide multiferroics,” *Nature Materials*, vol. 8, no. 3, pp. 229–234, Jan. 2009.
- [27] G. Catalan, J. Seidel, R. Ramesh, and J. F. Scott, “Domain wall nanoelectronics,” *Reviews of Modern Physics*, vol. 84, no. 1, pp. 119–156, Feb. 2012.
- [28] P. S. Bednyakov, B. I. Sturman, T. Sluka, A. K. Tagantsev, and P. V. Yudin, “Physics and applications of charged domain walls,” *npj Computational Materials*, vol. 4, no. 1, p. 65, Nov. 2018.

- [29] J. P. V. McConville, H. Lu, B. Wang, Y. Tan, C. Cochard, M. Conroy, K. Moore, A. Harvey, U. Bangert, L.-Q. Chen, A. Gruverman, and J. M. Gregg, “[Ferroelectric Domain Wall Memristor](#),” *Advanced Functional Materials*, vol. 30, no. 28, p. 2000109, May 2020.
- [30] J. R. Whyte, R. G. P. McQuaid, P. Sharma, C. Canalias, J. F. Scott, A. Gruverman, and J. M. Gregg, “[Ferroelectric Domain Wall Injection](#),” *Advanced Materials*, vol. 26, no. 2, pp. 293–298, Oct. 2013.
- [31] R. G. McQuaid, M. P. Campbell, R. W. Whatmore, A. Kumar, and J. M. Gregg, “[Injection and controlled motion of conducting domain walls in improper ferroelectric Cu-Cl boracite](#),” *Nature Communications*, vol. 8, no. 1, p. 15105, May 2017.
- [32] S. K. Streiffer, J. A. Eastman, D. D. Fong, C. Thompson, A. Munkholm, M. V. R. Murty, O. Auciello, G. R. Bai, and G. B. Stephenson, “[Observation of Nanoscale 180° Stripe Domains in Ferroelectric PbTiO₃ Thin Films](#),” *Physical Review Letters*, vol. 89, no. 6, p. 067601, Jul. 2002.
- [33] D. D. Fong, “[Ferroelectricity in Ultrathin Perovskite Films](#),” *Science*, vol. 304, no. 5677, pp. 1650–1653, Jun. 2004.
- [34] C. Thompson, D. D. Fong, R. V. Wang, F. Jiang, S. K. Streiffer, K. Latifi, J. A. Eastman, P. H. Fuoss, and G. B. Stephenson, “[Imaging and alignment of nanoscale 180° stripe domains in ferroelectric thin films](#),” *Applied Physics Letters*, vol. 93, no. 18, p. 182901, Nov. 2008.
- [35] Z. Liu, T. Lu, J. Ye, G. Wang, X. Dong, R. Withers, and Y. Liu, “[Antiferroelectrics for Energy Storage Applications: a Review](#),” *Advanced Materials Technologies*, vol. 3, no. 9, p. 1800111, Jul. 2018.
- [36] G. Shirane, E. Sawaguchi, and Y. Takagi, “[Dielectric Properties of Lead Zirconate](#),” *Physical Review*, vol. 84, no. 3, pp. 476–481, Nov. 1951.
- [37] K. M. Rabe, “[Antiferroelectricity in Oxides: A Reexamination](#),” in *Functional Metal Oxides*, Wiley-VCH Verlag GmbH & Co. KGaA, Jul. 2013, pp. 221–244.
- [38] A. K. Tagantsev, K. Vaideeswaran, S. B. Vakhrushev, A. V. Filimonov, R. G. Burkovsky, A. Shaganov, D. Andronikova, A. I. Rudskoy, A. Q. R. Baron, H. Uchiyama, D. Chernyshov, A. Bosak, Z. Ujma, K. Roleder, A. Majchrowski, J.-H. Ko, and N. Setter, “[The origin of antiferroelectricity in PbZrO₃](#),” *Nature Communications*, vol. 4, no. 1, p. 2229, Jul. 2013.
- [39] P. Vales-Castro, K. Roleder, L. Zhao, J.-F. Li, D. Kajewski, and G. Catalan, “[Flexoelectricity in antiferroelectrics](#),” *Applied Physics Letters*, vol. 113, no. 13, p. 132903, Sep. 2018.

- [40] B. Xu, O. Hellman, and L. Bellaiche, “Order-disorder transition in the prototypical antiferroelectric PbZrO_3 ,” *Physical Review B*, vol. 100, no. 2, 020102(R), Jul. 2019.
- [41] Z. G. Fthenakis and I. Ponomareva, “Dynamics of antiferroelectric phase transition in PbZrO_3 ,” *Physical Review B*, vol. 96, no. 18, p. 184 110, Nov. 2017.
- [42] H. Fujishita, Y. Shiozaki, N. Achiwa, and E. Sawaguchi, “Crystal Structure Determination of Antiferroelectric PbZrO_3 - Application of Profile Analysis Method to Powder Method of X-ray and Neutron Diffraction,” *Journal of the Physical Society of Japan*, vol. 51, no. 11, pp. 3583–3591, Nov. 1982.
- [43] J. S. Baker and D. R. Bowler, “First-principles soft-mode lattice dynamics of $\text{PbZr}_{0.5}\text{Ti}_{0.5}\text{O}_3$ and shortcomings of the virtual crystal approximation,” *Physical Review B*, vol. 100, no. 22, p. 224 305, Dec. 2019.
- [44] B. Jaffe, *Piezoelectric ceramics*. Elsevier, 2012, vol. 3.
- [45] A. M. Glazer, “The classification of tilted octahedra in perovskites,” *Acta Crystallographica Section B Structural Crystallography and Crystal Chemistry*, vol. 28, no. 11, pp. 3384–3392, Nov. 1972.
- [46] A. M. Glazer, “Simple ways of determining perovskite structures,” *Acta Crystallographica Section A*, vol. 31, no. 6, pp. 756–762, Nov. 1975.
- [47] L. Bellaiche and D. Vanderbilt, “Virtual crystal approximation revisited: Application to dielectric and piezoelectric properties of perovskites,” *Physical Review B*, vol. 61, no. 12, pp. 7877–7882, Mar. 2000.
- [48] N. J. Ramer and A. M. Rappe, “Virtual-crystal approximation that works: Locating a compositional phase boundary in $\text{PbZr}_x\text{Ti}_{1-x}\text{O}_3$,” *Physical Review B*, vol. 62, no. 2, R743–R746, Jul. 2000.
- [49] S.-Y. Liu, Q.-S. Shao, D.-S. Yu, Y.-K. Lü, D.-J. Li, Y. Li, and M.-S. Cao, “First-principles study on the geometric and electronic structures and phase transition of $\text{PbZr}_x\text{Ti}_{1-x}\text{O}_3$ solid solutions,” *Chinese Physics B*, vol. 22, no. 1, p. 017 702, Jan. 2013.
- [50] C. Bungaro and K. M. Rabe, “Lattice instabilities of $\text{PbZrO}_3/\text{PbTiO}_3$ [1:1] superlattices from first principles,” *Physical Review B*, vol. 65, no. 22, p. 224 106, Jun. 2002.
- [51] D. R. Bowler, J. S. Baker, J. T. L. Poulton, S. Y. Mujahed, J. Lin, S. Yadav, Z. Raza, and T. Miyazaki, “Highly accurate local basis sets for large-scale DFT calculations in CONQUEST,” *Japanese Journal of Applied Physics*, vol. 58, no. 10, p. 100 503, Oct. 2019.

- [52] P. Anderson, “Translated from Russian: Qualitative constructions regarding the statistics of the phase transition in ferroelectric BaTiO₃,” *Izv. Akad. Nauk SSSR*, p. 290, 1960, We thank Mike Glazer for finding this Russian monograph. We are now both in possession of the original and would be grateful if a willing Russian translator would step forward!
- [53] J. S. Baker, T. Miyazaki, and D. R. Bowler, “[The pseudoatomic orbital basis: electronic accuracy and soft-mode distortions in ABO₃ perovskites](#),” *Electronic Structure*, vol. 2, no. 2, p. 025 002, Jun. 2020.
- [54] J. S. Baker and D. R. Bowler, “[Polar Morphologies from First Principles: PbTiO₃ Films on SrTiO₃ Substrates and the \$p\(2 \times \Lambda\)\$ Surface Reconstruction](#),” *Advanced Theory and Simulations*, vol. 3, p. 2 000 154, 9 Sep. 2020.
- [55] M. Hadjimichael, E. Zatterin, S. Fernandez-Peña, S. J. Leake, and P. Zubko, “[Domain Wall Orientations in Ferroelectric Superlattices Probed with Synchrotron X-Ray Diffraction](#),” *Physical Review Letters*, vol. 120, no. 3, p. 037 602, Jan. 2018.
- [56] M. Dawber, K. M. Rabe, and J. F. Scott, “[Physics of thin-film ferroelectric oxides](#),” *Reviews of Modern Physics*, vol. 77, no. 4, pp. 1083–1130, Oct. 2005.
- [57] D. G. Schlom, L.-Q. Chen, X. Pan, A. Schmehl, and M. A. Zurbuchen, “[A Thin Film Approach to Engineering Functionality into Oxides](#),” *Journal of the American Ceramic Society*, vol. 91, no. 8, pp. 2429–2454, Aug. 2008.
- [58] P. Zubko, S. Gariglio, M. Gabay, P. Ghosez, and J.-M. Triscone, “[Interface Physics in Complex Oxide Heterostructures](#),” *Annual Review of Condensed Matter Physics*, vol. 2, no. 1, pp. 141–165, Mar. 2011.
- [59] A. Devonshire, “[XCVI. Theory of barium titanate](#),” *The London, Edinburgh, and Dublin Philosophical Magazine and Journal of Science*, vol. 40, no. 309, pp. 1040–1063, Oct. 1949.
- [60] A. Devonshire, “[CIX. Theory of barium titanate—Part II](#),” *The London, Edinburgh, and Dublin Philosophical Magazine and Journal of Science*, vol. 42, no. 333, pp. 1065–1079, Oct. 1951.
- [61] P. Chandra and P. B. Littlewood, “[A Landau Primer for Ferroelectrics](#),” in *Physics of Ferroelectrics*, Springer Berlin Heidelberg, 2007, pp. 69–116.
- [62] J. C. Tolédano and P. Tolédano, *The Landau Theory of Phase Transitions*. World Scientific, Aug. 1987.
- [63] B. A. Strukov and A. P. Levanyuk, *Ferroelectric Phenomena in Crystals*. Springer Berlin Heidelberg, 1998.

- [64] M. V. Berry, “[Quantal phase factors accompanying adiabatic changes](#),” *Proceedings of the Royal Society of London. A. Mathematical and Physical Sciences*, vol. 392, no. 1802, pp. 45–57, Mar. 1984.
- [65] R. D. King-Smith and D. Vanderbilt, “[Theory of polarization of crystalline solids](#),” *Physical Review B*, vol. 47, no. 3, pp. 1651–1654, Jan. 1993.
- [66] R. Resta, M. Posternak, and A. Baldereschi, “[Towards a quantum theory of polarization in ferroelectrics: The case of \$\text{KNbO}_3\$](#) ,” *Physical Review Letters*, vol. 70, no. 7, pp. 1010–1013, Feb. 1993.
- [67] R. Resta, “[Quantum-Mechanical Position Operator in Extended Systems](#),” *Physical Review Letters*, vol. 80, no. 9, pp. 1800–1803, Mar. 1998.
- [68] R. Resta and D. Vanderbilt, “[Theory of Polarization: A Modern Approach](#),” in *Topics in Applied Physics*, Springer Berlin Heidelberg, 2007, pp. 31–68.
- [69] C. V. Raman and T. M. K. Nedungadi, “[The \$\alpha\$ - \$\beta\$ Transformation of Quartz](#),” *Nature*, vol. 145, no. 3665, pp. 147–147, Jan. 1940.
- [70] P. A. Fleury, “[The Effects of Soft Modes on the Structure and Properties of Materials](#),” *Annual Review of Materials Science*, vol. 6, no. 1, pp. 157–180, Aug. 1976.
- [71] M. Born and M. Goppert-Mayer, “Dynamic lattice theory in crystals,” *Handb. Phys.*, vol. 24, p. 623, 1933.
- [72] M. Born and K. Huang, *Dynamical theory of crystal lattices*. Clarendon press, 1954.
- [73] P. Ghosez, J.-P. Michenaud, and X. Gonze, “[Dynamical atomic charges: The case of \$\text{ABO}_3\$ compounds](#),” *Physical Review B*, vol. 58, no. 10, pp. 6224–6240, Sep. 1998.
- [74] A. Savoia, D. Paparo, P. Perna, Z. Ristic, M. Salluzzo, F. M. Granozio, U. S. di Uccio, C. Richter, S. Thiel, J. Mannhart, and L. Marrucci, “[Polar catastrophe and electronic reconstructions at the \$\text{LaAlO}_3/\text{SrTiO}_3\$ interface: Evidence from optical second harmonic generation](#),” *Physical Review B*, vol. 80, no. 7, p. 075 110, Aug. 2009.
- [75] S. Gariglio, N. Reyren, A. D. Caviglia, and J.-M. Triscone, “[Superconductivity at the \$\text{LaAlO}_3/\text{SrTiO}_3\$ interface](#),” *Journal of Physics: Condensed Matter*, vol. 21, no. 16, p. 164 213, Mar. 2009.
- [76] M. B. Shalom, M. Sachs, D. Rakhmilevitch, A. Palevski, and Y. Dagan, “[Tuning Spin-Orbit Coupling and Superconductivity at the \$\text{SrTiO}_3/\text{LaAlO}_3\$ Interface: A Magnetotransport Study](#),” *Physical Review Letters*, vol. 104, no. 12, Mar. 2010.
- [77] J. A. Bert, B. Kalisky, C. Bell, M. Kim, Y. Hikita, H. Y. Hwang, and K. A. Moler, “[Direct imaging of the coexistence of ferromagnetism and superconductivity at the \$\text{LaAlO}_3/\text{SrTiO}_3\$ interface](#),” *Nature Physics*, vol. 7, no. 10, pp. 767–771, Sep. 2011.

- [78] A. Tebano, E. Fabbri, D. Pergolesi, G. Balestrino, and E. Traversa, “[Room-Temperature Giant Persistent Photoconductivity in SrTiO₃/LaAlO₃ Heterostructures](#),” *ACS Nano*, vol. 6, no. 2, pp. 1278–1283, Jan. 2012.
- [79] L. Wang, Y. Li, A. Bera, C. Ma, F. Jin, K. Yuan, W. Yin, A. David, W. Chen, W. Wu, W. Prellier, S. Wei, and T. Wu, “[Device Performance of the Mott Insulator LaVO₃ as a Photovoltaic Material](#),” *Physical Review Applied*, vol. 3, no. 6, p. 064 015, Jun. 2015.
- [80] N. A. Spaldin and R. Ramesh, “[Advances in magnetoelectric multiferroics](#),” *Nature Materials*, vol. 18, no. 3, pp. 203–212, Feb. 2019.
- [81] E. Bousquet, M. Dawber, N. Stucki, C. Lichtensteiger, P. Hermet, S. Gariglio, J.-M. Triscone, and P. Ghosez, “[Improper ferroelectricity in perovskite oxide artificial superlattices](#),” *Nature*, vol. 452, no. 7188, pp. 732–736, Apr. 2008.
- [82] N. C. Bristowe, J. Varignon, D. Fontaine, E. Bousquet, and P. Ghosez, “[Ferromagnetism induced by entangled charge and orbital orderings in ferroelectric titanate perovskites](#),” *Nature Communications*, vol. 6, no. 1, p. 6677, Mar. 2015.
- [83] J. Varignon, N. C. Bristowe, E. Bousquet, and P. Ghosez, “[Coupling and electrical control of structural, orbital and magnetic orders in perovskites](#),” *Scientific Reports*, vol. 5, no. 1, p. 15 364, Oct. 2015.
- [84] J. Varignon, N. C. Bristowe, and P. Ghosez, “[Electric Field Control of Jahn-Teller Distortions in Bulk Perovskites](#),” *Physical Review Letters*, vol. 116, no. 5, p. 057 602, Feb. 2016.
- [85] J. Íñiguez, M. Stengel, S. Prosandeev, and L. Bellaiche, “[First-principles study of the multimode antiferroelectric transition in PbZrO₃](#),” *Physical Review B*, vol. 90, no. 22, 220103(R), Dec. 2014.
- [86] K. Momma and F. Izumi, “[VESTA 3 for three-dimensional visualization of crystal, volumetric and morphology data](#),” *Journal of Applied Crystallography*, vol. 44, no. 6, pp. 1272–1276, Oct. 2011.
- [87] A. M. Bratkovsky and A. P. Levanyuk, “[Very large dielectric response of thin ferroelectric films with the dead layers](#),” *Physical Review B*, vol. 63, no. 13, p. 132 103, Mar. 2001.
- [88] P. Zubko, J. C. Wojdeł, M. Hadjimichael, S. Fernandez-Pena, A. Sené, I. Luk’yanchuk, J.-M. Triscone, and J. Íñiguez, “[Negative capacitance in multidomain ferroelectric superlattices](#),” *Nature*, vol. 534, no. 7608, pp. 524–528, Jun. 2016.

- [89] S. Das, Z. Hong, V. A. Stoica, M. A. P. Gonçalves, Y. T. Shao, E. Parsonnet, E. J. Marksz, S. Saremi, M. R. McCarter, A. Reynoso, C. J. Long, A. M. Hagerstrom, D. Meyers, V. Ravi, B. Prasad, H. Zhou, Z. Zhang, H. Wen, F. Gómez-Ortiz, P. García-Fernández, J. Bokor, J. Íñiguez, J. W. Freeland, N. D. Orloff, J. Junquera, L. Q. Chen, S. Salahuddin, D. A. Muller, L. W. Martin, and R. Ramesh, “[Local negative permittivity and topological phase transition in polar skyrmions](#),” *Nature Materials*, Oct. 2020.
- [90] B. Yin, P. Aguado-Puente, S. Qu, and E. Artacho, “[Two-dimensional electron gas at the \$\text{PbTiO}_3/\text{SrTiO}_3\$ interface: An *ab initio* study](#),” *Physical Review B*, vol. 92, no. 11, p. 115 406, Sep. 2015.
- [91] Y. M. Jin, Y. U. Wang, A. G. Khachatryan, J. F. Li, and D. Viehland, “[Conformal Miniaturization of Domains with Low Domain-Wall Energy: Monoclinic Ferroelectric States near the Morphotropic Phase Boundaries](#),” *Physical Review Letters*, vol. 91, no. 19, p. 197 601, Nov. 2003.
- [92] J. C. Agar, R. V. K. Mangalam, A. R. Damodaran, G. Velarde, J. Karthik, M. B. Okatan, Z. H. Chen, S. Jesse, N. Balke, S. V. Kalinin, and L. W. Martin, “[Tuning Susceptibility via Misfit Strain in Relaxed Morphotropic Phase Boundary \$\text{PbZr}_{1-x}\text{Ti}_x\text{O}_3\$ Epitaxial Thin Films](#),” *Advanced Materials Interfaces*, vol. 1, no. 5, p. 1 400 098, May 2014.
- [93] B. Noheda, D. E. Cox, G. Shirane, J. A. Gonzalo, L. E. Cross, and S.-E. Park, “[A monoclinic ferroelectric phase in the \$\text{PbZr}_{1-x}\text{Ti}_x\text{O}_3\$ solid solution](#),” *Applied Physics Letters*, vol. 74, no. 14, pp. 2059–2061, Apr. 1999.
- [94] L. J. McGilly, P. Yudin, L. Feigl, A. K. Tagantsev, and N. Setter, “[Controlling domain wall motion in ferroelectric thin films](#),” *Nature Nanotechnology*, vol. 10, no. 2, pp. 145–150, Jan. 2015.
- [95] J. F. Scott, “[Ferroelectrics go bananas](#),” *Journal of Physics: Condensed Matter*, vol. 20, no. 2, p. 021 001, Dec. 2007.
- [96] Q. Huang, Z. Fan, L. Hong, S. Cheng, Z. Tan, G. Tian, D. Chen, Z. Hou, M. Qin, M. Zeng, X. Lu, G. Zhou, X. Gao, and J.-M. Liu, “[Machine Learning Based Distinguishing between Ferroelectric and Non-Ferroelectric Polarization-Electric Field Hysteresis Loops](#),” *Advanced Theory and Simulations*, p. 2 000 106, Jul. 2020.
- [97] J. Curie and P. Curie, “Development by pressure of polar electricity in hemihedral crystals with inclined faces,” *Bull. soc. min. de France*, vol. 3, p. 90, 1880.
- [98] C. A. Beevers and W. Hughes, “[The crystal structure of Rochelle salt \(sodium potassium tartrate tetrahydrate, \$\text{KNaC}_4\text{H}_4\text{O}_6 \cdot 4\text{H}_2\text{O}\$ \)](#),” *Proceedings of the Royal Society of London. Series A. Mathematical and Physical Sciences*, vol. 177, no. 969, pp. 251–259, Jan. 1941.
- [99] J. Valasek, “[Piezo-Electric and Allied Phenomena in Rochelle Salt](#),” *Physical Review*, vol. 17, no. 4, pp. 475–481, Apr. 1921.

- [100] M. D. Adams, “[The Genome Sequence of Drosophila melanogaster](#),” *Science*, vol. 287, no. 5461, pp. 2185–2195, Mar. 2000.
- [101] G. Busch and P. Scherrer, “[A new seignette-electric substance](#),” *Ferroelectrics*, vol. 71, no. 1, pp. 15–16, Jan. 1987, Originally published in 1935 in *Naturwissenschaften*.
- [102] J. West, “[XXVI. A quantitative X-ray Analysis of the Structure of Potassium Dihydrogen Phosphate \(KH₂PO₄\)](#),” *Zeitschrift für Kristallographie - Crystalline Materials*, vol. 74, no. 1-6, pp. 306–332, Jan. 1930.
- [103] J. C. Slater, “[Theory of the Transition in KH₂PO₄](#),” *The Journal of Chemical Physics*, vol. 9, no. 1, pp. 16–33, Jan. 1941.
- [104] W. P. Mason, “[The Elastic, Piezoelectric, and Dielectric Constants of Potassium Dihydrogen Phosphate and Ammonium Dihydrogen Phosphate](#),” *Physical Review*, vol. 69, no. 5-6, pp. 173–194, Mar. 1946.
- [105] A. C. Keller, “[Submarine Detection by Sonar](#),” *Transactions of the American Institute of Electrical Engineers*, vol. 66, no. 1, pp. 1217–1230, Jan. 1947.
- [106] C. Randall, R. Newnham, and L. Cross, “[History of the first ferroelectric oxide, BaTiO₃](#),” *Materials Research Institute, The Pennsylvania State University, University Park, Pa, USA*, pp. 1–11, 2004.
- [107] B. T. Matthias and J. P. Remeika, “[Ferroelectricity in the Ilmenite Structure](#),” *Physical Review*, vol. 76, no. 12, pp. 1886–1887, Dec. 1949.
- [108] S. Sawada, S. Nomura, and S. Fujii, “[Ferroelectricity in the Phase III of KNO₃](#),” *Journal of the Physical Society of Japan*, vol. 13, no. 12, pp. 1549–1549, Dec. 1958.
- [109] G. Shirane and S. Hoshino, “[On the Phase Transition in Lead Titanate](#),” *Journal of the Physical Society of Japan*, vol. 6, no. 4, pp. 265–270, Jul. 1951.
- [110] G. Shirane and K. Suzuki, “[Crystal Structure of Pb\(Zr,Ti\)O₃](#),” *Journal of the Physical Society of Japan*, vol. 7, no. 3, pp. 333–333, May 1952.
- [111] L. Egerton and D. M. Dillon, “[Piezoelectric and Dielectric Properties of Ceramics in the System Potassium-Sodium Niobate](#),” *Journal of the American Ceramic Society*, vol. 42, no. 9, pp. 438–442, Sep. 1959.
- [112] L. D. Landau, “[On the theory of phase transitions](#),” *Ukr. J. Phys.*, vol. 11, pp. 19–32, 1937.
- [113] V. L. Ginzburg, “[Phase transitions in ferroelectrics: some historical remarks](#),” *Physics-Uspekhi*, vol. 44, no. 10, pp. 1037–1043, Oct. 2001.
- [114] P. A. Fleury and J. M. Worlock, “[Electric-Field-Induced Raman Scattering in SrTiO₃ and KTaO₃](#),” *Physical Review*, vol. 174, no. 2, pp. 613–623, Oct. 1968.

- [115] I. P. Kaminow and T. C. Damen, “Temperature Dependence of the Ferroelectric Mode in KH_2PO_4 ,” *Physical Review Letters*, vol. 20, no. 20, pp. 1105–1108, May 1968.
- [116] R. A. Cowley, “Temperature Dependence of a Transverse Optic Mode in Strontium Titanate,” *Physical Review Letters*, vol. 9, no. 4, pp. 159–161, Aug. 1962.
- [117] W. G. Spitzer, R. C. Miller, D. A. Kleinman, and L. E. Howarth, “Far Infrared Dielectric Dispersion in BaTiO_3 , SrTiO_3 , and TiO_2 ,” *Physical Review*, vol. 126, no. 5, pp. 1710–1721, Jun. 1962.
- [118] S. Watarai, “Soft-Magnon Modes in Hematite,” *Journal of the Physical Society of Japan*, vol. 35, no. 3, pp. 696–705, Sep. 1973.
- [119] H. Chow and F. Keffer, “Soft surface magnons and the first-order magnetic phase transitions in antiferromagnetic hematite,” *Physical Review B*, vol. 10, no. 1, pp. 243–254, Jul. 1974.
- [120] K. Aizu, “Ferroelectrics Having an Irreversible (but Divertible) Spontaneous Polarization Vector,” *Journal of the Physical Society of Japan*, vol. 23, no. 4, pp. 794–797, Oct. 1967.
- [121] K. Aizu, “Possible Species of “Ferroelastic” Crystals and of Simultaneously Ferroelectric and Ferroelastic Crystals,” *Journal of the Physical Society of Japan*, vol. 27, no. 2, pp. 387–396, Aug. 1969.
- [122] K. Aizu, “Electrical, Mechanical and Electromechanical Orders of State Shifts in Nonmagnetic Ferroic Crystals,” *Journal of the Physical Society of Japan*, vol. 32, no. 5, pp. 1287–1301, May 1972.
- [123] K. Aizu, “Inferred Temperature-Dependences of Electrical, Mechanical and Optical Properties of Ferroelectric-Ferroelastic $\text{Gd}_2(\text{MoO}_4)_3$,” *Journal of the Physical Society of Japan*, vol. 31, no. 3, pp. 802–811, Sep. 1971.
- [124] A. P. Levanyuk and D. G. Sannikov, “Improper ferroelectrics,” *Soviet Physics Uspekhi*, vol. 17, no. 2, pp. 199–214, Feb. 1974.
- [125] G. Burns and F. H. Dacol, “Crystalline ferroelectrics with glassy polarization behavior,” *Physical Review B*, vol. 28, no. 5, pp. 2527–2530, Sep. 1983.
- [126] Y. Ishibashi and M. Iwata, “Considerations on Dielectric Properties of Relaxors,” *Journal of the Physical Society of Japan*, vol. 65, no. 3, pp. 853–857, Mar. 1996.
- [127] R. A. Cowley, S. N. Gvasaliya, S. G. Lushnikov, B. Roessli, and G. M. Rotaru, “Relaxing with relaxors: a review of relaxor ferroelectrics,” *Advances in Physics*, vol. 60, no. 2, pp. 229–327, Apr. 2011.
- [128] R. E. Cohen, “Origin of ferroelectricity in perovskites: The principal problems from a theoretical perspective,” *Ferroelectrics*, vol. 150, no. 1, pp. 1–12, Dec. 1993.

- [129] C. Kittel, “[Theory of Antiferroelectric Crystals](#),” *Physical Review*, vol. 82, no. 5, pp. 729–732, Jun. 1951.
- [130] G. Shirane, “[Ferroelectricity and Antiferroelectricity in Ceramic \$\text{PbZrO}_3\$ Containing Ba or Sr](#),” *Physical Review*, vol. 86, no. 2, pp. 219–227, Apr. 1952.
- [131] D. L. Corker, A. M. Glazer, W. Kaminsky, R. W. Whatmore, J. Dec, and K. Roleder, “[Investigation into the Crystal Structure of the Perovskite Lead Hafnate, \$\text{PbHfO}_3\$](#) ,” *Acta Crystallographica Section B Structural Science*, vol. 54, no. 1, pp. 18–28, Feb. 1998.
- [132] C. Milesi-Brault, C. Toulouse, E. Constable, H. Aramberri, V. Simonet, S. de Brion, H. Berger, L. Paolasini, A. Bosak, J. Íñiguez, and M. Guennou, “[Archetypal Soft-Mode-Driven Antipolar Transition in Francisite \$\text{Cu}_3\text{Bi}\(\text{SeO}_3\)_2\text{O}_2\text{Cl}\$](#) ,” *Physical Review Letters*, vol. 124, no. 9, p. 097 603, Mar. 2020.
- [133] S. Triebwasser, “[Study of the Second-Order Ferroelectric Transition in Tri-Glycine Sulfate](#),” *IBM Journal of Research and Development*, vol. 2, no. 3, pp. 212–217, Jul. 1958.
- [134] K. J. Choi, “[Enhancement of Ferroelectricity in Strained \$\text{BaTiO}_3\$ Thin Films](#),” *Science*, vol. 306, no. 5698, pp. 1005–1009, Nov. 2004.
- [135] J. A. Sanjurjo, E. López-Cruz, and G. Burns, “[High-pressure Raman study of zone-center phonons in \$\text{PbTiO}_3\$](#) ,” *Physical Review B*, vol. 28, no. 12, pp. 7260–7268, Dec. 1983.
- [136] J. H. Haeni, P. Irvin, W. Chang, R. Uecker, P. Reiche, Y. L. Li, S. Choudhury, W. Tian, M. E. Hawley, B. Craigo, A. K. Tagantsev, X. Q. Pan, S. K. Streiffer, L. Q. Chen, S. W. Kirchoefer, J. Levy, and D. G. Schlom, “[Room-temperature ferroelectricity in strained \$\text{SrTiO}_3\$](#) ,” *Nature*, vol. 430, no. 7001, pp. 758–761, Aug. 2004.
- [137] N. A. Spaldin, “[A beginners guide to the modern theory of polarization](#),” *Journal of Solid State Chemistry*, vol. 195, pp. 2–10, Nov. 2012.
- [138] C. B. Sawyer and C. H. Tower, “[Rochelle Salt as a Dielectric](#),” *Physical Review*, vol. 35, no. 3, pp. 269–273, Feb. 1930.
- [139] J. Bonini, D. Vanderbilt, and K. M. Rabe, “[Berry flux diagonalization: Application to electric polarization](#),” *Physical Review B*, vol. 102, no. 4, p. 045 141, Jul. 2020.
- [140] G. H. Wannier, “[The Structure of Electronic Excitation Levels in Insulating Crystals](#),” *Physical Review*, vol. 52, no. 3, pp. 191–197, Aug. 1937.
- [141] S. Gasiorowicz, *Quantum physics*. John Wiley & Sons, 2007, ch. 3.
- [142] E. Blount, “[Formalisms of Band Theory](#),” in *Solid State Physics*, Elsevier, 1962, pp. 305–373.
- [143] J. Zak, “[Berry’s phase for energy bands in solids](#),” *Physical Review Letters*, vol. 62, no. 23, pp. 2747–2750, Jun. 1989.

- [144] R. Resta, “[Manifestations of Berry’s phase in molecules and condensed matter](#),” *Journal of Physics: Condensed Matter*, vol. 12, no. 9, R107–R143, Feb. 2000.
- [145] X.-L. Qi and S.-C. Zhang, “[Topological insulators and superconductors](#),” *Reviews of Modern Physics*, vol. 83, no. 4, pp. 1057–1110, Oct. 2011.
- [146] N. Marzari, A. A. Mostofi, J. R. Yates, I. Souza, and D. Vanderbilt, “[Maximally localized Wannier functions: Theory and applications](#),” *Reviews of Modern Physics*, vol. 84, no. 4, pp. 1419–1475, Oct. 2012.
- [147] R. Resta, “[Macroscopic polarization from electronic wave functions](#),” *International Journal of Quantum Chemistry*, vol. 75, no. 4-5, pp. 599–606, Oct. 1999.
- [148] R. Car and M. Parrinello, “[Unified Approach for Molecular Dynamics and Density-Functional Theory](#),” *Physical Review Letters*, vol. 55, no. 22, pp. 2471–2474, Nov. 1985.
- [149] P. L. Silvestrelli, M. Bernasconi, and M. Parrinello, “[Ab initio infrared spectrum of liquid water](#),” *Chemical Physics Letters*, vol. 277, no. 5-6, pp. 478–482, Oct. 1997.
- [150] M. Sharma, R. Resta, and R. Car, “[Intermolecular Dynamical Charge Fluctuations in Water: A Signature of the H-Bond Network](#),” *Physical Review Letters*, vol. 95, no. 18, p. 187 401, Oct. 2005.
- [151] D. Alfè, “[PHON: A program to calculate phonons using the small displacement method](#),” *Computer Physics Communications*, vol. 180, no. 12, pp. 2622–2633, Dec. 2009.
- [152] P. E. Blöchl, “[Projector augmented-wave method](#),” *Physical Review B*, vol. 50, no. 24, pp. 17 953–17 979, Dec. 1994.
- [153] J. P. Perdew and Y. Wang, “[Accurate and simple analytic representation of the electron-gas correlation energy](#),” *Physical Review B*, vol. 45, no. 23, pp. 13 244–13 249, Jun. 1992.
- [154] P. Ghosez, E. Cockayne, U. V. Waghmare, and K. M. Rabe, “[Lattice dynamics of BaTiO₃, PbTiO₃, and PbZrO₃: A comparative first-principles study](#),” *Physical Review B*, vol. 60, no. 2, pp. 836–843, Jul. 1999.
- [155] C. H. Henry and J. J. Hopfield, “[Raman Scattering by Polaritons](#),” *Physical Review Letters*, vol. 15, no. 25, pp. 964–966, Dec. 1965.
- [156] R. H. Lyddane, R. G. Sachs, and E. Teller, “[On the Polar Vibrations of Alkali Halides](#),” *Physical Review*, vol. 59, no. 8, pp. 673–676, Apr. 1941.
- [157] G. Shirane, J. D. Axe, J. Harada, and J. P. Remeika, “[Soft Ferroelectric Modes in Lead Titanate](#),” *Physical Review B*, vol. 2, no. 1, pp. 155–159, Jul. 1970.
- [158] A. D. B. Woods, W. Cochran, and B. N. Brockhouse, “[Lattice Dynamics of Alkali Halide Crystals](#),” *Physical Review*, vol. 119, no. 3, pp. 980–999, Aug. 1960.

- [159] A. Pribram-Jones, P. E. Grabowski, and K. Burke, “[Thermal Density Functional Theory: Time-Dependent Linear Response and Approximate Functionals from the Fluctuation-Dissipation Theorem](#),” *Physical Review Letters*, vol. 116, no. 23, p. 233 001, Jun. 2016.
- [160] P. A. Tipler and G. Mosca, *Physics for scientists and engineers*. Macmillan, 2007, ch. 14, pp. 458–459.
- [161] M. S. Dresselhaus, G. Dresselhaus, and A. Jorio, *Applications of group theory to the physics of solids*, 2008.
- [162] W. Zhong, R. D. King-Smith, and D. Vanderbilt, “[Giant LO-TO splittings in perovskite ferroelectrics](#),” *Physical Review Letters*, vol. 72, no. 22, pp. 3618–3621, May 1994.
- [163] B. G. Dick and A. W. Overhauser, “[Theory of the Dielectric Constants of Alkali Halide Crystals](#),” *Physical Review*, vol. 112, no. 1, pp. 90–103, Oct. 1958.
- [164] X. Gonze and C. Lee, “[Dynamical matrices, Born effective charges, dielectric permittivity tensors and interatomic force constants from density-functional perturbation theory](#),” *Physical Review B*, vol. 55, no. 16, pp. 10 355–10 368, Apr. 1997.
- [165] S. Baroni, P. Giannozzi, and A. Testa, “[Green’s-function approach to linear response in solids](#),” *Physical Review Letters*, vol. 58, no. 18, pp. 1861–1864, May 1987.
- [166] S. Baroni, S. de Gironcoli, A. D. Corso, and P. Giannozzi, “[Phonons and related crystal properties from density-functional perturbation theory](#),” *Reviews of Modern Physics*, vol. 73, no. 2, pp. 515–562, Jul. 2001.
- [167] R. E. Cohen and H. Krakauer, “[Electronic structure studies of the differences in ferroelectric behavior of BaTiO₃ and PbTiO₃](#),” *Ferroelectrics*, vol. 136, no. 1, pp. 65–83, Nov. 1992.
- [168] C. Lichtensteiger, P. Zubko, M. Stengel, P. Aguado-Puente, J.-M. Triscone, P. Ghosez, and J. Junquera, “[Ferroelectricity in Ultrathin-Film Capacitors](#),” in *Oxide Ultrathin Films*, Wiley-VCH Verlag GmbH & Co. KGaA, Jan. 2012, pp. 265–230.
- [169] J. Guyonnet, “[Domain Walls in Ferroelectric Materials](#),” in *Springer Theses*, Springer International Publishing, 2014, pp. 7–24.
- [170] P. Aguado-Puente, “First-principles study of screening mechanisms of the depolarising field in nanosized capacitors,” PhD thesis, Universidad de Cantabria, 2011.
- [171] Y. Zhang, J. Sun, J. P. Perdew, and X. Wu, “[Comparative first-principles studies of prototypical ferroelectric materials by LDA, GGA, and SCAN meta-GGA](#),” *Physical Review B*, vol. 96, no. 3, p. 035 143, Jul. 2017.
- [172] T. Shimada, S. Tomoda, and T. Kitamura, “[Ab initio study of ferroelectric closure domains in ultrathin PbTiO₃ films](#),” *Physical Review B*, vol. 81, no. 14, p. 144 116, Apr. 2010.

- [173] A. K. Yadav, C. T. Nelson, S. L. Hsu, Z. Hong, J. D. Clarkson, C. M. Schlepütz, A. R. Damodaran, P. Shafer, E. Arenholz, L. R. Dedon, D. Chen, A. Vishwanath, A. M. Minor, L. Q. Chen, J. F. Scott, L. W. Martin, and R. Ramesh, “[Observation of polar vortices in oxide superlattices](#),” *Nature*, vol. 530, no. 7589, pp. 198–201, Jan. 2016.
- [174] A. R. Damodaran, J. D. Clarkson, Z. Hong, H. Liu, A. K. Yadav, C. T. Nelson, S.-L. Hsu, M. R. McCarter, K.-D. Park, V. Kravtsov, A. Farhan, Y. Dong, Z. Cai, H. Zhou, P. Aguado-Puente, P. García-Fernández, J. Íñiguez, J. Junquera, A. Scholl, M. B. Raschke, L.-Q. Chen, D. D. Fong, R. Ramesh, and L. W. Martin, “[Phase coexistence and electric-field control of toroidal order in oxide superlattices](#),” *Nature Materials*, vol. 16, no. 10, pp. 1003–1009, Aug. 2017.
- [175] P. Aguado-Puente and J. Junquera, “[Structural and energetic properties of domains in \$\text{PbTiO}_3/\text{SrTiO}_3\$ superlattices from first principles](#),” *Physical Review B*, vol. 85, no. 18, p. 184 105, May 2012.
- [176] C. Kittel, “[Theory of the Structure of Ferromagnetic Domains in Films and Small Particles](#),” *Physical Review*, vol. 70, no. 11-12, pp. 965–971, Dec. 1946.
- [177] L. Lu, Y. Nahas, M. Liu, H. Du, Z. Jiang, S. Ren, D. Wang, L. Jin, S. Prokhorenko, C.-L. Jia, and L. Bellaiche, “[Topological Defects with Distinct Dipole Configurations in \$\text{PbTiO}_3/\text{SrTiO}_3\$ Multilayer Films](#),” *Physical Review Letters*, vol. 120, no. 17, p. 177 601, Apr. 2018.
- [178] S. Das, Y. L. Tang, Z. Hong, M. A. P. Gonçalves, M. R. McCarter, C. Klewe, K. X. Nguyen, F. Gómez-Ortiz, P. Shafer, E. Arenholz, V. A. Stoica, S.-L. Hsu, B. Wang, C. Ophus, J. F. Liu, C. T. Nelson, S. Saremi, B. Prasad, A. B. Mei, D. G. Schlom, J. Íñiguez, P. García-Fernández, D. A. Muller, L. Q. Chen, J. Junquera, L. W. Martin, and R. Ramesh, “[Observation of room-temperature polar skyrmions](#),” *Nature*, vol. 568, no. 7752, pp. 368–372, Apr. 2019.
- [179] Z. Hong and L.-Q. Chen, “[Blowing polar skyrmion bubbles in oxide superlattices](#),” *Acta Materialia*, vol. 152, pp. 155–161, Jun. 2018.
- [180] S. Prosandeev, I. Ponomareva, I. Naumov, I. Kornev, and L. Bellaiche, “[Original properties of dipole vortices in zero-dimensional ferroelectrics](#),” *Journal of Physics: Condensed Matter*, vol. 20, no. 19, p. 193 201, Apr. 2008.
- [181] S. Prosandeev, A. Malashevich, Z. Gui, L. Louis, R. Walter, I. Souza, and L. Bellaiche, “[Natural optical activity and its control by electric field in electrotoroidic systems](#),” *Physical Review B*, vol. 87, no. 19, p. 195 111, May 2013.
- [182] C. Black and J. Welser, “[Electric-field penetration into metals: consequences for high-dielectric-constant capacitors](#),” *IEEE Transactions on Electron Devices*, vol. 46, no. 4, pp. 776–780, Apr. 1999.

- [183] P. Aguado-Puente and J. Junquera, “[Ferromagneticlike Closure Domains in Ferroelectric Ultrathin Films: First-Principles Simulations](#),” *Physical Review Letters*, vol. 100, no. 17, p. 177 601, Apr. 2008.
- [184] R. V. Wang, D. D. Fong, F. Jiang, M. J. Highland, P. H. Fuoss, C. Thompson, A. M. Kolpak, J. A. Eastman, S. K. Streiffer, A. M. Rappe, and G. B. Stephenson, “[Reversible Chemical Switching of a Ferroelectric Film](#),” *Physical Review Letters*, vol. 102, no. 4, p. 047 601, Jan. 2009.
- [185] P. Aguado-Puente, N. C. Bristowe, B. Yin, R. Shirasawa, P. Ghosez, P. B. Littlewood, and E. Artacho, “[Model of two-dimensional electron gas formation at ferroelectric interfaces](#),” *Physical Review B*, vol. 92, no. 3, p. 035 438, Jul. 2015.
- [186] K. D. Fredrickson and A. A. Demkov, “[Switchable conductivity at the ferroelectric interface: Nonpolar oxides](#),” *Physical Review B*, vol. 91, no. 11, p. 115 126, Mar. 2015.
- [187] M. Dawber, C. Lichtensteiger, M. Cantoni, M. Veithen, P. Ghosez, K. Johnston, K. M. Rabe, and J.-M. Triscone, “[Unusual Behavior of the Ferroelectric Polarization in \$\text{PbTiO}_3/\text{SrTiO}_3\$ Superlattices](#),” *Physical Review Letters*, vol. 95, no. 17, p. 177 601, Oct. 2005.
- [188] P. Aguado-Puente, P. García-Fernández, and J. Junquera, “[Interplay of Couplings between Antiferrodistortive, Ferroelectric, and Strain Degrees of Freedom in Monodomain \$\text{PbTiO}_3/\text{SrTiO}_3\$ Superlattices](#),” *Physical Review Letters*, vol. 107, no. 21, p. 217 601, Nov. 2011.
- [189] J. Park, J. Mangeri, Q. Zhang, M. H. Yusuf, A. Pateras, M. Dawber, M. V. Holt, O. G. Heinonen, S. Nakhmanson, and P. G. Evans, “[Domain alignment within ferroelectric/dielectric \$\text{PbTiO}_3/\text{SrTiO}_3\$ superlattice nanostructures](#),” *Nanoscale*, vol. 10, no. 7, pp. 3262–3271, Jan. 2018.
- [190] S. Prosandeev and L. Bellaiche, “[Influence of crystallographic steps on properties of ferroelectric ultrathin films: An *ab initio* study](#),” *Applied Physics Letters*, vol. 91, no. 7, p. 072 901, Aug. 2007.
- [191] T. Shimada, S. Tomoda, and T. Kitamura, “[First-principles study on ferroelectricity at \$\text{PbTiO}_3\$ surface steps](#),” *Journal of Physics: Condensed Matter*, vol. 22, no. 35, p. 355 901, Aug. 2010.
- [192] X. Wang, S. Tomoda, T. Shimada, and T. Kitamura, “[Local suppression of ferroelectricity at \$\text{PbTiO}_3\$ surface steps: a density functional theory study](#),” *Journal of Physics: Condensed Matter*, vol. 24, no. 4, p. 045 903, Jan. 2012.
- [193] D. R. Bowler, I. J. Bush, and M. J. Gillan, “[Practical methods for *ab initio* calculations on thousands of atoms](#),” *International Journal of Quantum Chemistry*, vol. 77, no. 5, pp. 831–842, Mar. 2000.

- [194] M. Gillan, D. Bowler, A. Torralba, and T. Miyazaki, “[Order-N first-principles calculations with the conquest code](#),” *Computer Physics Communications*, vol. 177, no. 1-2, pp. 14–18, Jul. 2007.
- [195] J. A. Wheeler and W. H. Zurek, “The present situation in quantum mechanics,” in *Quantum theory and measurement*, vol. 40, Princeton University Press, 2014, ch. 1, p. 152.
- [196] A. I. M. Rae, “The three dimensional Schrödinger equations,” in *Quantum Mechanics, Fifth Edition*, CRC Press LLC, 2007, ch. 3, p. 57.
- [197] A. S. Eddington, “The constants of nature,” in *The World of Mathematics*, 1956, 2007, ch. 2, pp. 1074–1093.
- [198] M. Born and R. Oppenheimer, “[Zur Quantentheorie der Molekeln \(ENG: Quantum theory of molecules\)](#),” *Annalen der Physik*, vol. 389, no. 20, pp. 457–484, Aug. 1927.
- [199] G. Grimvall, “[The Electron-Phonon Interaction in Normal Metals](#),” *Physica Scripta*, vol. 14, no. 1-2, pp. 63–78, Jul. 1976.
- [200] S. Pisana, M. Lazzeri, C. Casiraghi, K. S. Novoselov, A. K. Geim, A. C. Ferrari, and F. Mauri, “[Breakdown of the adiabatic Born–Oppenheimer approximation in graphene](#),” *Nature Materials*, vol. 6, no. 3, pp. 198–201, Feb. 2007.
- [201] A. W. Götz, “Overview of electronic structure methods,” in *Electronic Structure Calculations on Graphics Processing Units*, John Wiley & Sons, Ltd, Feb. 2016, pp. 39–66.
- [202] R. M. Martin, *Electronic Structure*. Cambridge University Press, Apr. 2004.
- [203] W. Y. Robert G. Parr, *Density-Functional Theory of Atoms and Molecules*. Oxford University Press, 1989.
- [204] R. M. Dreizler and E. K. U. Gross, *Density Functional Theory: An Approach to the Quantum Many-Body Problem*. Springer Berlin Heidelberg, 1990.
- [205] K. Burke, *The ABC of DFT*, Apr. 2007.
- [206] J. Kohanoff, *Electronic Structure Calculations for Solids and Molecules: Theory and Computational Methods*. Cambridge University Press, 2006.
- [207] P. Hohenberg and W. Kohn, “[Inhomogeneous Electron Gas](#),” *Physical Review*, vol. 136, no. 3B, B864–B871, Nov. 1964.
- [208] M. Levy, “[Universal variational functionals of electron densities, first-order density matrices, and natural spin-orbitals and solution of the \$v\$ -representability problem](#),” *Proceedings of the National Academy of Sciences*, vol. 76, no. 12, pp. 6062–6065, Dec. 1979.

- [209] A. I. M. Rae, “Time-independent perturbation theory and the variational principle,” in *Quantum Mechanics, Fifth Edition*, CRC Press LLC, 2007, ch. 7, p. 149.
- [210] W. Kohn and L. J. Sham, “Self-Consistent Equations Including Exchange and Correlation Effects,” *Physical Review*, vol. 140, no. 4A, A1133–A1138, Nov. 1965.
- [211] R. Feynman, “Statistical mechanics: A set of lectures (advanced book classics),” pp. 248–249, 1998.
- [212] P. Pulay, “Convergence acceleration of iterative sequences. The case of SCF iteration,” *Chemical Physics Letters*, vol. 73, no. 2, pp. 393–398, Jul. 1980.
- [213] P. Echenique and J. L. Alonso, “A mathematical and computational review of Hartree-Fock SCF methods in quantum chemistry,” *Molecular Physics*, vol. 105, no. 23-24, pp. 3057–3098, Dec. 2007.
- [214] V. Polo, E. Kraka, and D. Cremer, “Electron correlation and the self-interaction error of density functional theory,” *Molecular Physics*, vol. 100, no. 11, pp. 1771–1790, Jun. 2002.
- [215] J. P. Perdew and A. Zunger, “Self-interaction correction to density-functional approximations for many-electron systems,” *Physical Review B*, vol. 23, no. 10, pp. 5048–5079, May 1981.
- [216] T. Tsuneda and K. Hirao, “Self-interaction corrections in density functional theory,” *The Journal of Chemical Physics*, vol. 140, no. 18, 18A513, May 2014.
- [217] D. M. Ceperley and B. J. Alder, “Ground State of the Electron Gas by a Stochastic Method,” *Physical Review Letters*, vol. 45, no. 7, pp. 566–569, Aug. 1980.
- [218] M. A. Marques, M. J. Oliveira, and T. Burnus, “Libxc: A library of exchange and correlation functionals for density functional theory,” *Computer Physics Communications*, vol. 183, no. 10, pp. 2272–2281, Oct. 2012.
- [219] J. P. Perdew, K. Burke, and M. Ernzerhof, “Generalized Gradient Approximation Made Simple,” *Physical Review Letters*, vol. 77, no. 18, pp. 3865–3868, Oct. 1996.
- [220] J. P. Perdew, “Jacob’s ladder of density functional approximations for the exchange-correlation energy,” in *AIP Conference Proceedings*, vol. 577, AIP, Aug. 2001, p. 1.
- [221] J. Sun, A. Ruzsinszky, and J. Perdew, “Strongly Constrained and Appropriately Normed Semilocal Density Functional,” *Physical Review Letters*, vol. 115, no. 3, p. 036402, Jul. 2015.
- [222] K. Shenton, “First-principles investigations of structure-function relationships in bismuth ferrite,” The SCAN M-GGA is used heavily throughout this thesis to describe the properties of BiFeO₃, PhD thesis, University College London, London Centre for Nanotechnology, Aug. 2018.

- [223] A. P. Bartók and J. R. Yates, “[Regularized SCAN functional](#),” *The Journal of Chemical Physics*, vol. 150, no. 16, p. 161 101, Apr. 2019.
- [224] N. Ashcroft and D. Mermin, “The Born-von Karman boundary condition,” in *Solid state Physics*, Rineheart and Winston, 1976, ch. 8, p. 135.
- [225] N. Ashcroft and D. Mermin, “Bloch’s theorem,” in *Solid state Physics*, Rineheart and Winston, 1976, ch. 8, p. 133.
- [226] D. J. Chadi and M. L. Cohen, “[Special Points in the Brillouin Zone](#),” *Physical Review B*, vol. 8, no. 12, pp. 5747–5753, Dec. 1973.
- [227] H. J. Monkhorst and J. D. Pack, “[Special points for Brillouin-zone integrations](#),” *Physical Review B*, vol. 13, no. 12, pp. 5188–5192, Jun. 1976.
- [228] A. Togo and I. Tanaka, *Spglib: a software library for crystal symmetry search*, ArXiv eprint: 1808.01590, Aug. 2018.
- [229] J. P. Perdew, A. Ruzsinszky, G. I. Csonka, O. A. Vydrov, G. E. Scuseria, L. A. Constantin, X. Zhou, and K. Burke, “[Restoring the Density-Gradient Expansion for Exchange in Solids and Surfaces](#),” *Physical Review Letters*, vol. 100, no. 13, p. 136 406, Apr. 2008.
- [230] M. van Setten, M. Giantomassi, E. Bousquet, M. Verstraete, D. Hamann, X. Gonze, and G.-M. Rignanese, “[The PseudoDojo: Training and grading a 85 element optimized norm-conserving pseudopotential table](#),” *Computer Physics Communications*, vol. 226, pp. 39–54, May 2018.
- [231] D. R. Hamann, M. Schlüter, and C. Chiang, “[Norm-Conserving Pseudopotentials](#),” *Physical Review Letters*, vol. 43, no. 20, pp. 1494–1497, Nov. 1979.
- [232] D. Vanderbilt, “[Soft self-consistent pseudopotentials in a generalized eigenvalue formalism](#),” *Physical Review B*, vol. 41, no. 11, pp. 7892–7895, Apr. 1990.
- [233] D. R. Hamann, “[Optimized norm-conserving Vanderbilt pseudopotentials](#),” *Physical Review B*, vol. 88, no. 8, p. 085 117, Aug. 2013.
- [234] G. Kresse and D. Joubert, “[From ultrasoft pseudopotentials to the projector augmented-wave method](#),” *Physical Review B*, vol. 59, no. 3, pp. 1758–1775, Jan. 1999.
- [235] J. M. Worlock, J. F. Scott, and P. A. Fleury, “[Soft Phonon Modes and the 110° K Phase Transition in SrTiO₃](#),” in *Light Scattering Spectra of Solids*, Springer Berlin Heidelberg, 1969, pp. 689–696.
- [236] F. H. G. Arfken H. Weber, “Diagonalization of matrices,” in *Mathematical Methods for Physicists*, Elsevier, 2013, ch. 4, p. 217.
- [237] A. I. M. Rae, “The one-dimensional Schrödinger equations,” in *Quantum Mechanics, Fifth Edition*, CRC Press LLC, 2007, ch. 2, p. 19.

- [238] J. C. Slater, “[Atomic Shielding Constants](#),” *Physical Review*, vol. 36, no. 1, pp. 57–64, Jul. 1930.
- [239] J. E. Avery and J. S. Avery, “[Molecular integrals for slater type orbitals using coulomb sturmians](#),” *Journal of Mathematical Chemistry*, vol. 52, no. 1, pp. 301–312, Sep. 2013.
- [240] T. H. Dunning and P. J. Hay, “Gaussian basis sets for molecular calculations,” in *Methods of Electronic Structure Theory*, Springer US, 1977, pp. 1–27.
- [241] M. J. Frisch, G. W. Trucks, H. B. Schlegel, G. E. Scuseria, M. A. Robb, J. R. Cheeseman, G. Scalmani, V. Barone, G. A. Petersson, H. Nakatsuji, X. Li, M. Caricato, A. V. Marenich, J. Bloino, B. G. Janesko, R. Gomperts, B. Mennucci, H. P. Hratchian, J. V. Ortiz, A. F. Izmaylov, J. L. Sonnenberg, D. Williams-Young, F. Ding, F. Lipparini, F. Egidi, J. Goings, B. Peng, A. Petrone, T. Henderson, D. Ranasinghe, V. G. Zakrzewski, J. Gao, N. Rega, G. Zheng, W. Liang, M. Hada, M. Ehara, K. Toyota, R. Fukuda, J. Hasegawa, M. Ishida, T. Nakajima, Y. Honda, O. Kitao, H. Nakai, T. Vreven, K. Throssell, J. A. Montgomery Jr., J. E. Peralta, F. Ogliaro, M. J. Bearpark, J. J. Heyd, E. N. Brothers, K. N. Kudin, V. N. Staroverov, T. A. Keith, R. Kobayashi, J. Normand, K. Raghavachari, A. P. Rendell, J. C. Burant, S. S. Iyengar, J. Tomasi, M. Cossi, J. M. Millam, M. Klene, C. Adamo, R. Cammi, J. W. Ochterski, R. L. Martin, K. Morokuma, O. Farkas, J. B. Foresman, and D. J. Fox, *Gaussian~16 Revision C.01*, Gaussian Inc. Wallingford CT, 2016.
- [242] H. Shang, H. Xiang, Z. Li, and J. Yang, “[Linear scaling electronic structure calculations with numerical atomic basis set](#),” *International Reviews in Physical Chemistry*, vol. 29, no. 4, pp. 665–691, Oct. 2010.
- [243] V. Blum, R. Gehrke, F. Hanke, P. Havu, V. Havu, X. Ren, K. Reuter, and M. Scheffler, “[Ab initio molecular simulations with numeric atom-centered orbitals](#),” *Computer Physics Communications*, vol. 180, no. 11, pp. 2175–2196, Nov. 2009.
- [244] T. Ozaki, “[Variationally optimized atomic orbitals for large-scale electronic structures](#),” *Physical Review B*, vol. 67, no. 15, p. 155 108, Apr. 2003.
- [245] T. Ozaki and H. Kino, “[Numerical atomic basis orbitals from H to Kr](#),” *Physical Review B*, vol. 69, no. 19, May 2004.
- [246] S. Kenny, A. Horsfield, and H. Fujitani, “[Transferable atomic-type orbital basis sets for solids](#),” *Physical Review B*, vol. 62, no. 8, pp. 4899–4905, Aug. 2000.
- [247] A. S. Torralba, M. Todorović, V. Brázdová, R. Choudhury, T. Miyazaki, M. J. Gillan, and D. R. Bowler, “[Pseudo-atomic orbitals as basis sets for the O\(N\) DFT code CONQUEST](#),” *Journal of Physics: Condensed Matter*, vol. 20, no. 29, p. 294 206, Jun. 2008.

- [248] O. F. Sankey and D. J. Niklewski, “[Ab initio multicenter tight-binding model for molecular-dynamics simulations and other applications in covalent systems](#),” *Physical Review B*, vol. 40, no. 6, pp. 3979–3995, Aug. 1989.
- [249] J. Junquera, Ó. Paz, D. Sánchez-Portal, and E. Artacho, “[Numerical atomic orbitals for linear-scaling calculations](#),” *Physical Review B*, vol. 64, no. 23, p. 235 111, Nov. 2001.
- [250] E. Anglada, J. M. Soler, J. Junquera, and E. Artacho, “[Systematic generation of finite-range atomic basis sets for linear-scaling calculations](#),” *Physical Review B*, vol. 66, no. 20, p. 205 101, Nov. 2002.
- [251] D. Bowler, T. Miyazaki, and M. Gillan, “[Parallel sparse matrix multiplication for linear scaling electronic structure calculations](#),” *Computer Physics Communications*, vol. 137, no. 2, pp. 255–273, Jun. 2001.
- [252] E. H. Rubensson and E. Rudberg, “[Bringing about matrix sparsity in linear-scaling electronic structure calculations](#),” *Journal of Computational Chemistry*, vol. 32, no. 7, pp. 1411–1423, Feb. 2011.
- [253] P. Pulay, “[Ab initio calculation of force constants and equilibrium geometries in polyatomic molecules](#),” *Molecular Physics*, vol. 17, no. 2, pp. 197–204, Jan. 1969.
- [254] E. Hernández, M. J. Gillan, and C. M. Goringe, “[Basis functions for linear-scaling first-principles calculations](#),” *Physical Review B*, vol. 55, no. 20, pp. 13 485–13 493, May 1997.
- [255] E. Hernández and M. J. Gillan, “[Self-consistent first-principles technique with linear scaling](#),” *Physical Review B*, vol. 51, no. 15, pp. 10 157–10 160, Apr. 1995.
- [256] W. Hierse and E. B. Stechel, “[Order-N methods in self-consistent density-functional calculations](#),” *Physical Review B*, vol. 50, no. 24, pp. 17 811–17 819, Dec. 1994.
- [257] J. Poulton, “[A Density Functional Theory Study on the properties of Dopants in Silicon Nanostructures](#),” The OSSF method is developed and tested in this thesis, PhD thesis, University College London, London Centre for Nanotechnology, Nov. 2019.
- [258] M. J. Rayson and P. R. Briddon, “[Highly efficient method for Kohn-Sham density functional calculations of 500-10000 atom systems](#),” *Physical Review B*, vol. 80, no. 20, Nov. 2009.
- [259] M. J. Rayson, “[Rapid filtration algorithm to construct a minimal basis on the fly from a primitive Gaussian basis](#),” *Computer Physics Communications*, vol. 181, no. 6, pp. 1051–1056, Jun. 2010.
- [260] W. Kohn, “[Density Functional and Density Matrix Method Scaling Linearly with the Number of Atoms](#),” *Physical Review Letters*, vol. 76, no. 17, pp. 3168–3171, Apr. 1996.

- [261] S.-Y. Qiu, C. Z. Wang, K. M. Ho, and C. T. Chan, “[Tight-binding molecular dynamics with linear system-size scaling](#),” *Journal of Physics: Condensed Matter*, vol. 6, no. 43, pp. 9153–9172, Oct. 1994.
- [262] X.-P. Li, R. W. Nunes, and D. Vanderbilt, “[Density-matrix electronic-structure method with linear system-size scaling](#),” *Physical Review B*, vol. 47, no. 16, pp. 10 891–10 894, Apr. 1993.
- [263] X. Li, J. M. Millam, G. E. Scuseria, M. J. Frisch, and H. B. Schlegel, “[Density matrix search using direct inversion in the iterative subspace as a linear scaling alternative to diagonalization in electronic structure calculations](#),” *The Journal of Chemical Physics*, vol. 119, no. 15, pp. 7651–7658, Oct. 2003.
- [264] P. D. Haynes, C.-K. Skylaris, A. A. Mostofi, and M. C. Payne, “[Density kernel optimization in the ONETEP code](#),” *Journal of Physics: Condensed Matter*, vol. 20, no. 29, p. 294 207, Jun. 2008.
- [265] G. Galli, “[Linear scaling methods for electronic structure calculations and quantum molecular dynamics simulations](#),” *Current Opinion in Solid State and Materials Science*, vol. 1, no. 6, pp. 864–874, Dec. 1996.
- [266] D. Bowler and M. Gillan, “[Density matrices in O\(N\) electronic structure calculations: theory and applications](#),” *Computer Physics Communications*, vol. 120, no. 2-3, pp. 95–108, Aug. 1999.
- [267] A. H. R. Palser and D. E. Manolopoulos, “[Canonical purification of the density matrix in electronic-structure theory](#),” *Physical Review B*, vol. 58, no. 19, pp. 12 704–12 711, Nov. 1998.
- [268] R. McWeeny, “[Some Recent Advances in Density Matrix Theory](#),” *Reviews of Modern Physics*, vol. 32, no. 2, pp. 335–369, Apr. 1960.
- [269] J. H. Wilkinson, *The Algebraic Eigenvalue Problem*. Oxford University Press, 1965, pp. 71–72.
- [270] G. Kresse and J. Furthmüller, “[Efficient iterative schemes for ab initio total-energy calculations using a plane-wave basis set](#),” *Physical Review B*, vol. 54, no. 16, pp. 11 169–11 186, Oct. 1996.
- [271] N. Zein, “Density functional calculations of crystal elastic modula and phonon-spectra,” *Fizka Tverdogo Tela*, vol. 26, no. 10, pp. 3028–3034, 1984, I couldn’t find a DOI for this paper, sorry!
- [272] X. Gonze, “[Adiabatic density-functional perturbation theory](#),” *Physical Review A*, vol. 52, no. 2, pp. 1096–1114, Aug. 1995.

- [273] M. T. Yin and M. L. Cohen, “Theory of lattice-dynamical properties of solids: Application to Si and Ge,” *Physical Review B*, vol. 26, no. 6, pp. 3259–3272, Sep. 1982.
- [274] G. Kresse, J. Furthmüller, and J. Hafner, “Ab initio Force Constant Approach to Phonon Dispersion Relations of Diamond and Graphite,” *Europhysics Letters (EPL)*, vol. 32, no. 9, pp. 729–734, Dec. 1995.
- [275] K. Parlinski, Z. Q. Li, and Y. Kawazoe, “First-Principles Determination of the Soft Mode in Cubic ZrO_2 ,” *Physical Review Letters*, vol. 78, no. 21, pp. 4063–4066, May 1997.
- [276] D. Alfè, G. D. Price, and M. J. Gillan, “Thermodynamics of hexagonal-close-packed iron under Earth’s core conditions,” *Physical Review B*, vol. 64, no. 4, p. 045 123, Jul. 2001.
- [277] A. Togo and I. Tanaka, “First principles phonon calculations in materials science,” *Scripta Materialia*, vol. 108, pp. 1–5, Nov. 2015.
- [278] H. Hellman, “Einführung in die quantenchemie,” *Franz Deuticke, Leipzig*, vol. 285, 1937.
- [279] R. P. Feynman, “Forces in Molecules,” *Physical Review*, vol. 56, no. 4, pp. 340–343, Aug. 1939.
- [280] K. F. Riley, *Mathematical methods for physics and engineering*, eng, 3rd ed. Cambridge: Cambridge University Press, 2006, ch. 27, p. 1020.
- [281] I. Levin, M. G. Tucker, H. Wu, V. Provenzano, C. L. Dennis, S. Karimi, T. Comyn, T. Stevenson, R. I. Smith, and I. M. Reaney, “Displacive Phase Transitions and Magnetic Structures in Nd-Substituted BiFeO_3 ,” *Chemistry of Materials*, vol. 23, no. 8, pp. 2166–2175, Apr. 2011.
- [282] S. Karimi, I. M. Reaney, I. Levin, and I. Sterianou, “Nd-doped BiFeO_3 ceramics with antipolar order,” *Applied Physics Letters*, vol. 94, no. 11, p. 112 903, Mar. 2009.
- [283] D. D. Khalyavin, A. N. Salak, N. M. Olekhnovich, A. V. Pushkarev, Y. V. Radyush, P. Manuel, I. P. Raevski, M. L. Zheludkevich, and M. G. S. Ferreira, “Polar and antipolar polymorphs of metastable perovskite $\text{BiFe}_{0.5}\text{Sc}_{0.5}\text{O}_3$,” *Physical Review B*, vol. 89, no. 17, p. 174 414, May 2014.
- [284] A. A. Belik, A. M. Abakumov, A. A. Tsirlin, J. Hadermann, J. Kim, G. V. Tendeloo, and E. Takayama-Muromachi, “Structure and Magnetic Properties of $\text{BiFe}_{0.75}\text{Mn}_{0.25}\text{O}_3$ Perovskite Prepared at Ambient and High Pressure,” *Chemistry of Materials*, vol. 23, no. 20, pp. 4505–4514, Oct. 2011.
- [285] D. A. Rusakov, A. M. Abakumov, K. Yamaura, A. A. Belik, G. V. Tendeloo, and E. Takayama-Muromachi, “Structural Evolution of the BiFeO_3 - LaFeO_3 System,” *Chemistry of Materials*, vol. 23, no. 2, pp. 285–292, Jan. 2011.

- [286] M. Okuyama and Y. Hamakawa, “Ferroelectric PbTiO_3 thin films and their application,” *International Journal of Engineering Science*, vol. 29, no. 3, pp. 391–400, Jan. 1991.
- [287] V. Madigout, J. L. Baudour, F. Bouree, C. Favotto, M. Roubin, and G. Nihoul, “Crystallographic structure of lead hafnate (PbHfO_3) from neutron powder diffraction and electron microscopy,” *Philosophical Magazine A*, vol. 79, no. 4, pp. 847–858, Apr. 1999.
- [288] C. Oliveira, E. Longo, J. Varela, and M. Zaghete, “Synthesis and characterization of lead zirconate titanate (PZT) obtained by two chemical methods,” *Ceramics International*, vol. 40, no. 1, pp. 1717–1722, Jan. 2014.
- [289] N. Izyumskaya, Y.-I. Alivov, S.-J. Cho, H. Morkoç, H. Lee, and Y.-S. Kang, “Processing, Structure, Properties, and Applications of PZT Thin Films,” *Critical Reviews in Solid State and Materials Sciences*, vol. 32, no. 3-4, pp. 111–202, Dec. 2007.
- [290] T. Gururaja, W. A. Schulze, L. E. Cross, R. E. Newnham, B. A. Auld, Y. J. Wang, *et al.*, “Piezoelectric composite materials for ultrasonic transducer applications. Part I: Resonant modes of vibration of PZT rod-polymer composites,” *IEEE Trans. Sonics Ultrason.*, vol. 32, no. 19985, pp. 481–498, Jul. 1985.
- [291] Z. Chi and Q. Xu, “Recent Advances in the Control of Piezoelectric Actuators,” *International Journal of Advanced Robotic Systems*, vol. 11, no. 11, p. 182, Nov. 2014.
- [292] A. M. Kadin and S. B. Kaplan, “Dynamic Stimulation of Superconductivity With Resonant Terahertz Ultrasonic Waves,” *IEEE Transactions on Applied Superconductivity*, vol. 27, no. 4, pp. 1–5, Jun. 2017.
- [293] S. C. Pais, *Piezoelectricity-induced room temperature superconductor*, US patent application number: US 2019/0058105 A1, Feb. 2019.
- [294] G. Catalan, A. Lubk, A. H. G. Vlooswijk, E. Snoeck, C. Magen, A. Janssens, G. Rispens, G. Rijnders, D. H. A. Blank, and B. Noheda, “Flexoelectric rotation of polarization in ferroelectric thin films,” *Nature Materials*, vol. 10, no. 12, pp. 963–967, Oct. 2011.
- [295] R. Nelmes and W. Kuhs, “The crystal structure of tetragonal PbTiO_3 at room temperature and at 700 K,” *Solid State Communications*, vol. 54, no. 8, pp. 721–723, May 1985.
- [296] N. Sicron, B. Ravel, Y. Yacoby, E. A. Stern, F. Dogan, and J. J. Rehr, “Nature of the ferroelectric phase transition in PbTiO_3 ,” *Physical Review B*, vol. 50, no. 18, pp. 13 168–13 180, Nov. 1994.
- [297] B. K. Mani, S. Lisenkov, and I. Ponomareva, “Finite-temperature properties of antiferroelectric PbZrO_3 from atomistic simulations,” *Physical Review B*, vol. 91, no. 13, p. 134 112, Apr. 2015.

- [298] J. Hlinka, T. Ostapchuk, E. Buixaderas, C. Kadlec, P. Kuzel, I. Gregora, J. Kroupa, M. Savinov, A. Klic, J. Drahokoupil, I. Etxebarria, and J. Dec, “[Multiple Soft-Mode Vibrations of Lead Zirconate](#),” *Physical Review Letters*, vol. 112, no. 19, p. 197 601, May 2014.
- [299] P. Marton and C. Elsässer, “[First-principles study of structural and elastic properties of the tetragonal ferroelectric perovskite \$\text{PbZr}_{0.5}\text{Ti}_{0.5}\text{O}_3\$](#) ,” *Physica Status Solidi (b)*, vol. 248, no. 10, pp. 2222–2228, Mar. 2011.
- [300] J. L. Blok, D. H. A. Blank, G. Rijnders, K. M. Rabe, and D. Vanderbilt, “[Interplay of epitaxial strain and rotations in \$\text{PbTiO}_3/\text{PbZrO}_3\$ superlattices from first principles](#),” *Physical Review B*, vol. 84, no. 20, p. 205 413, Nov. 2011.
- [301] Z. Wu and H. Krakauer, “[First-principles calculations of piezoelectricity and polarization rotation in \$\text{PbZr}_{0.5}\text{Ti}_{0.5}\text{O}_3\$](#) ,” *Physical Review B*, vol. 68, no. 1, p. 014 112, Jul. 2003.
- [302] S. Kim, W.-J. Lee, Y.-H. Cho, M. Shim, and S. Kim, “[Piezoelectricity in \$\text{PbZr}_x\text{Ti}_{1-x}\text{O}_3\$ Studied by Density-Functional Perturbation Theory Supercell Calculations](#),” *Japanese Journal of Applied Physics*, vol. 52, no. 9R, p. 091 101, Sep. 2013.
- [303] I. Grinberg, V. Cooper, and A. Rappe, “[Oxide chemistry and local structure of \$\text{PbZr}_x\text{Ti}_{1-x}\text{O}_3\$ studied by density-functional theory supercell calculations](#),” *Physical Review B*, vol. 69, no. 14, p. 144 118, Apr. 2004.
- [304] K. Patel, S. Prosandeev, Y. Yang, B. Xu, J. Íñiguez, and L. Bellaiche, “[Atomistic mechanism leading to complex antiferroelectric and incommensurate perovskites](#),” *Physical Review B*, vol. 94, no. 5, p. 054 107, Aug. 2016.
- [305] R. G. Burkovsky, I. Bronwald, D. Andronikova, B. Wehinger, M. Krisch, J. Jacobs, D. Gambetti, K. Roleder, A. Majchrowski, A. V. Filimonov, A. I. Rudskoy, S. B. Vakhrushev, and A. K. Tagantsev, “[Critical scattering and incommensurate phase transition in antiferroelectric \$\text{PbZrO}_3\$ under pressure](#),” *Scientific Reports*, vol. 7, no. 1, p. 41 512, Jan. 2017.
- [306] A. J. Bell, “[Factors influencing the piezoelectric behaviour of PZT and other “morphotropic phase boundary” ferroelectrics](#),” *Journal of Materials Science*, vol. 41, no. 1, pp. 13–25, Jan. 2006.
- [307] A. Bogdanov, A. Mysovsky, C. J. Pickard, and A. V. Kimmel, “[Modelling the structure of Zr-rich \$\text{Pb}\(\text{Zr}_{1-x}\text{Ti}_x\)\text{O}_3\$, \$x = 0.4\$ by a multiphase approach](#),” *Physical Chemistry Chemical Physics*, vol. 18, no. 40, pp. 28 316–28 324, 2016.
- [308] R. G. Burkovsky, D. Andronikova, Y. Bronwald, M. Krisch, K. Roleder, A. Majchrowski, A. V. Filimonov, A. I. Rudskoy, and S. B. Vakhrushev, “[Lattice dynamics in the paraelectric phase of \$\text{PbHfO}_3\$ studied by inelastic x-ray scattering](#),” *Journal of Physics: Condensed Matter*, vol. 27, no. 33, p. 335 901, Aug. 2015.

- [309] R. G. Burkovsky, D. A. Andronikova, Y. A. Bronwald, A. V. Filimonov, and S. B. Vakhrushev, “[An analysis of the phonon dispersion curves of lead hafnate in the cubic phase using lattice-dynamical models](#),” *St. Petersburg Polytechnical University Journal: Physics and Mathematics*, vol. 2, no. 3, pp. 171–174, Oct. 2016.
- [310] X. Gonze, F. Jollet, F. A. Araujo, D. Adams, B. Amadon, T. Applencourt, C. Audouze, J.-M. Beuken, J. Bieder, A. Bokhanchuk, E. Bousquet, F. Bruneval, D. Caliste, M. Côté, F. Dahm, F. D. Pieve, M. Delaveau, M. D. Gennaro, B. Dorado, C. Espejo, G. Geneste, L. Genovese, A. Gerossier, M. Giantomassi, Y. Gillet, D. Hamann, L. He, G. Jomard, J. L. Janssen, S. L. Roux, A. Levitt, A. Lherbier, F. Liu, I. Lukačević, A. Martin, C. Martins, M. Oliveira, S. Poncé, Y. Pouillon, T. Rangel, G.-M. Rignanese, A. Romero, B. Rousseau, O. Rubel, A. Shukri, M. Stankovski, M. Torrent, M. V. Setten, B. V. Troeye, M. Verstraete, D. Waroquiers, J. Wiktor, B. Xu, A. Zhou, and J. Zwanziger, “[Recent developments in the ABINIT software package](#),” *Computer Physics Communications*, vol. 205, pp. 106–131, Aug. 2016.
- [311] X. Gonze, B. Amadon, P.-M. Anglade, J.-M. Beuken, F. Bottin, P. Boulanger, F. Bruneval, D. Caliste, R. Caracas, M. Côté, T. Deutsch, L. Genovese, P. Ghosez, M. Giantomassi, S. Goedecker, D. Hamann, P. Hermet, F. Jollet, G. Jomard, S. Leroux, M. Mancini, S. Mazevet, M. Oliveira, G. Onida, Y. Pouillon, T. Rangel, G.-M. Rignanese, D. Sangalli, R. Shaltaf, M. Torrent, M. Verstraete, G. Zerah, and J. Zwanziger, “[ABINIT: First-principles approach to material and nanosystem properties](#),” *Computer Physics Communications*, vol. 180, no. 12, pp. 2582–2615, Dec. 2009.
- [312] S. A. Mabud and A. M. Glazer, “[Lattice parameters and birefringence in PbTiO₃ single crystals](#),” *Journal of Applied Crystallography*, vol. 12, no. 1, pp. 49–53, Feb. 1979.
- [313] E. Sawaguchi, “[Ferroelectricity versus Antiferroelectricity in the Solid Solutions of PbZrO₃ and PbTiO₃](#),” *Journal of the Physical Society of Japan*, vol. 8, no. 5, pp. 615–629, Sep. 1953.
- [314] F. Jollet, M. Torrent, and N. Holzwarth, “[Generation of Projector Augmented-Wave atomic data: A 71 element validated table in the XML format](#),” *Computer Physics Communications*, vol. 185, no. 4, pp. 1246–1254, Apr. 2014.
- [315] G. Shirane and R. Pepinsky, “[Phase Transitions in Antiferroelectric PbHfO₃](#),” *Physical Review*, vol. 91, no. 4, pp. 812–815, Aug. 1953.
- [316] X. Gonze, “[First-principles responses of solids to atomic displacements and homogeneous electric fields: Implementation of a conjugate-gradient algorithm](#),” *Physical Review B*, vol. 55, no. 16, pp. 10 337–10 354, Apr. 1997.
- [317] P. Ghosez, “[First-principles study of lattice instabilities in Ba_xSr_{1-x}TiO₃](#),” in *AIP Conference Proceedings*, vol. 535, AIP, 2000, p. 102.

- [318] L. Vegard, “Die Konstitution der Mischkristalle und die Raumfüllung der Atome,” *Zeitschrift für Physik*, vol. 5, no. 1, pp. 17–26, Jan. 1921.
- [319] P. E. Blöchl, O. Jepsen, and O. K. Andersen, “Improved tetrahedron method for Brillouin-zone integrations,” *Physical Review B*, vol. 49, no. 23, pp. 16 223–16 233, Jun. 1994.
- [320] H. T. Stokes and D. M. Hatch, “FINDSYM: program for identifying the space-group symmetry of a crystal,” *Journal of Applied Crystallography*, vol. 38, no. 1, pp. 237–238, Jan. 2005.
- [321] B. J. Campbell, H. T. Stokes, D. E. Tanner, and D. M. Hatch, “ISODISPLACE: a web-based tool for exploring structural distortions,” *Journal of Applied Crystallography*, vol. 39, no. 4, pp. 607–614, Jul. 2006.
- [322] H. Miranda. (2019). Phonon website. <http://henriquemiranda.github.io/phononwebsite/>. A useful web-based visualisation tool for examining mode eigendisplacements., (visited on 04/10/2019).
- [323] M. I. Aroyo, J. M. Perez-Mato, C. Capillas, E. Kroumova, S. Ivantchev, G. Madariaga, A. Kirov, and H. Wondratschek, “Bilbao Crystallographic Server: I. Databases and crystallographic computing programs,” *Zeitschrift für Kristallographie - Crystalline Materials*, vol. 221, no. 1, p. 15, Jan. 2006.
- [324] J. Chen and D. Feng, “TEM study of phases and domains in NaNbO_3 at room temperature,” *Physica Status Solidi (a)*, vol. 109, no. 1, pp. 171–185, Sep. 1988.
- [325] M. Yashima, S. Matsuyama, R. Sano, M. Itoh, K. Tsuda, and D. Fu, “Structure of Ferroelectric Silver Niobate AgNbO_3 ,” *Chemistry of Materials*, vol. 23, no. 7, pp. 1643–1645, Apr. 2011.
- [326] G. Kresse and J. Hafner, “Ab initio molecular dynamics for liquid metals,” *Physical Review B*, vol. 47, no. 1, pp. 558–561, Jan. 1993.
- [327] G. Kresse and J. Hafner, “Ab initio molecular-dynamics simulation of the liquid-metal–amorphous-semiconductor transition in germanium,” *Physical Review B*, vol. 49, no. 20, pp. 14 251–14 269, May 1994.
- [328] G. Kresse and J. Furthmüller, “Efficiency of *ab-initio* total energy calculations for metals and semiconductors using a plane-wave basis set,” *Computational Materials Science*, vol. 6, no. 1, pp. 15–50, Jul. 1996.
- [329] Y. Yao and Y. Kanai, “Plane-wave pseudopotential implementation and performance of SCAN meta-GGA exchange-correlation functional for extended systems,” *The Journal of Chemical Physics*, vol. 146, no. 22, p. 224 105, Jun. 2017.

- [330] H. Fujishita, Y. Ishikawa, S. Tanaka, A. Ogawaguchi, and S. Katano, “Crystal Structure and Order Parameters in the Phase Transition of Antiferroelectric PbZrO_3 ,” *Journal of the Physical Society of Japan*, vol. 72, no. 6, pp. 1426–1435, Jun. 2003.
- [331] A. M. Glazer, “VIBRATE! A program to compute irreducible representations for atomic vibrations in crystals,” *Journal of Applied Crystallography*, vol. 42, no. 6, pp. 1194–1196, Oct. 2009.
- [332] M. W. Lufaso and P. M. Woodward, “Prediction of the crystal structures of perovskites using the software program SPUDS,” *Acta Crystallographica Section B Structural Science*, vol. 57, no. 6, pp. 725–738, Nov. 2001.
- [333] N. A. Benedek and C. J. Fennie, “Why Are There So Few Perovskite Ferroelectrics?” *The Journal of Physical Chemistry C*, vol. 117, no. 26, pp. 13 339–13 349, May 2013.
- [334] S. A. Prosandeev, D. D. Khalyavin, I. P. Raevski, A. N. Salak, N. M. Olekhovich, A. V. Pushkarev, and Y. V. Radyush, “Complex antipolar $\sqrt{2} \times 4 \times 2\sqrt{2}$ structure with $Pnma$ symmetry in BiFeO_3 and $\text{BiFe}_{1/2}\text{Sc}_{1/2}\text{O}_3$: First-principles calculations,” *Physical Review B*, vol. 90, no. 5, p. 054 110, Aug. 2014.
- [335] J. A. Mundy, C. A. Heikes, B. F. Grosso, D. F. Segedin, Z. Wang, B. H. Goodge, Q. N. Meier, C. T. Nelson, B. Prasad, L. F. Kourkoutis, W. D. Ratcliff, N. A. Spaldin, R. Ramesh, and D. G. Schlom, *A high-energy density antiferroelectric made by interfacial electrostatic engineering*, ArXiv eprint: 1812.09615, Dec. 2018.
- [336] F. Cordero, F. Craciun, F. Trequattrini, and C. Galassi, “Effects of coupling between octahedral tilting and polar modes on the phase diagram of the ferroelectric perovskites $\text{PbZr}_{1-x}\text{Ti}_x\text{O}_3$ and $(\text{Na}_{1/2}\text{Bi}_{1/2})_{1-x}\text{Ba}_x\text{TiO}_3$,” *Phase Transitions*, vol. 87, no. 3, pp. 255–270, May 2013.
- [337] R. G. Burkovsky, “Dipole-dipole interactions and incommensurate order in perovskite structures,” *Physical Review B*, vol. 97, no. 18, p. 184 109, May 2018.
- [338] H. Y. Hwang, Y. Iwasa, M. Kawasaki, B. Keimer, N. Nagaosa, and Y. Tokura, “Emergent phenomena at oxide interfaces,” *Nature Materials*, vol. 11, no. 2, pp. 103–113, Jan. 2012.
- [339] M. Huijben, A. Brinkman, G. Koster, G. Rijnders, H. Hilgenkamp, and D. H. A. Blank, “Structure-Property Relation of $\text{SrTiO}_3/\text{LaAlO}_3$ Interfaces,” *Advanced Materials*, vol. 21, no. 17, pp. 1665–1677, May 2009.
- [340] I. Mora-Seró, J. Bisquert, F. Fabregat-Santiago, G. Garcia-Belmonte, G. Zoppi, K. Durose, Y. Proskuryakov, I. Oja, A. Belaidi, *et al.*, “Implications of the Negative Capacitance Observed at Forward Bias in Nanocomposite and Polycrystalline Solar Cells,” *Nano Letters*, vol. 6, no. 4, pp. 640–650, Apr. 2006.

- [341] Y. Maeno, H. Hashimoto, K. Yoshida, S. Nishizaki, T. Fujita, J. G. Bednorz, and F. Lichtenberg, “[Superconductivity in a layered perovskite without copper](#),” *Nature*, vol. 372, no. 6506, pp. 532–534, Dec. 1994.
- [342] G. Xiao, M. Z. Cieplak, A. Gavrin, F. H. Streitz, A. Bakhshai, and C. L. Chien, “[High-temperature superconductivity in tetragonal perovskite structures: Is oxygen-vacancy order important?](#)” *Physical Review Letters*, vol. 60, no. 14, pp. 1446–1449, Apr. 1988.
- [343] Z. V. Gareeva and A. K. Zvezdin, “[Interacting antiferromagnetic and ferroelectric domain structures of multiferroics](#),” *Physica Status Solidi (RRL) - Rapid Research Letters*, vol. 3, no. 2-3, pp. 79–81, Mar. 2009.
- [344] N. A. Benedek and C. J. Fennie, “[Hybrid Improper Ferroelectricity: A Mechanism for Controllable Polarization-Magnetization Coupling](#),” *Physical Review Letters*, vol. 106, no. 10, p. 107 204, Mar. 2011.
- [345] I. Sosnowska, T. P. Neumaier, and E. Steichele, “[Spiral magnetic ordering in bismuth ferrite](#),” *Journal of Physics C: Solid State Physics*, vol. 15, no. 23, pp. 4835–4846, Aug. 1982.
- [346] S. R. Burns, D. Sando, B. Xu, B. Dupé, L. Russell, G. Deng, R. Clements, O. H. C. Paull, J. Seidel, L. Bellaiche, *et al.*, “[Expansion of the spin cycloid in multiferroic BiFeO₃ thin films](#),” *npj Quantum Materials*, vol. 4, no. 1, p. 18, Apr. 2019.
- [347] D. J. Singh and L. Nordstrom, *Planewaves, Pseudopotentials, and the LAPW method*. Springer Science & Business Media, 2006.
- [348] K. Lejaeghere, G. Bihlmayer, T. Bjorkman, P. Blaha, S. Blugel, V. Blum, D. Caliste, I. E. Castelli, S. J. Clark, A. D. Corso, *et al.*, “[Reproducibility in density functional theory calculations of solids](#),” *Science*, vol. 351, no. 6280, aad3000–aad3000, Mar. 2016.
- [349] M. J. Louwse and G. Rothenberg, “[Transferable basis sets of numerical atomic orbitals](#),” *Physical Review B*, vol. 85, no. 3, p. 035 108, Jan. 2012.
- [350] K. Lee, J. Yu, and Y. Morikawa, “[Comparison of localized basis and plane-wave basis for density-functional calculations of organic molecules on metals](#),” *Physical Review B*, vol. 75, no. 4, p. 045 402, Jan. 2007.
- [351] T. Otsuka, T. Miyazaki, T. Ohno, D. R. Bowler, and M. J. Gillan, “[Accuracy of order-N density-functional theory calculations on DNA systems using CONQUEST](#),” *Journal of Physics: Condensed Matter*, vol. 20, no. 29, p. 294 201, Jun. 2008.
- [352] S. T. Howard and O. Lamarche, “[Description of covalent bond orders using the charge density topology](#),” *Journal of Physical Organic Chemistry*, vol. 16, no. 2, pp. 133–141, Feb. 2003.

- [353] L. Zhang, F. Ying, W. Wu, P. Hiberty, and S. Shaik, “Topology of Electron Charge Density for Chemical Bonds from Valence Bond Theory: A Probe of Bonding Types,” *Chemistry - A European Journal*, vol. 15, no. 12, pp. 2979–2989, Mar. 2009.
- [354] P. Giannozzi, S. Baroni, N. Bonini, M. Calandra, R. Car, C. Cavazzoni, D. Ceresoli, G. L. Chiarotti, M. Cococcioni, I. Dabo, A. D. Corso, S. de Gironcoli, S. Fabris, G. Fratesi, R. Gebauer, U. Gerstmann, C. Gougoussis, A. Kokalj, M. Lazzeri, L. Martin-Samos, N. Marzari, F. Mauri, R. Mazzarello, S. Paolini, A. Pasquarello, L. Paulatto, C. Sbraccia, S. Scandolo, G. Sclauzero, A. P. Seitsonen, A. Smogunov, P. Umari, and R. M. Wentzcovitch, “QUANTUM ESPRESSO: a modular and open-source software project for quantum simulations of materials,” *Journal of Physics: Condensed Matter*, vol. 21, no. 39, p. 395 502, Sep. 2009.
- [355] D. R. Bowler, J. S. Baker, J. T. L. Poulton, S. Y. Mujahed, J. Lin, S. Yadav, Z. Raza, T. Miyazaki, M. Gillan, A. Nakata, L. Truflandier, A. Torralba, V. Brazdova, L. Tong, M. Arita, A. Sena, U. Terranova, R. Choudhury, C. Goringe, E. Hernandez, and I. Bush, *The CONQUEST code: Public release at <https://github.com/OrderN/CONQUEST-release>*, Jan. 2020.
- [356] J. P. Perdew, “Density functional theory and the band gap problem,” *International Journal of Quantum Chemistry*, vol. 28, no. S19, pp. 497–523, Jun. 2009.
- [357] F. Birch, “Finite Elastic Strain of Cubic Crystals,” *Physical Review*, vol. 71, no. 11, pp. 809–824, Jun. 1947.
- [358] M. Yu and D. R. Trinkle, “Accurate and efficient algorithm for Bader charge integration,” *The Journal of Chemical Physics*, vol. 134, no. 6, p. 064 111, Feb. 2011.
- [359] W. Tang, E. Sanville, and G. Henkelman, “A grid-based Bader analysis algorithm without lattice bias,” *Journal of Physics: Condensed Matter*, vol. 21, no. 8, p. 084 204, Jan. 2009.
- [360] E. Sanville, S. D. Kenny, R. Smith, and G. Henkelman, “Improved grid-based algorithm for Bader charge allocation,” *Journal of Computational Chemistry*, vol. 28, no. 5, pp. 899–908, Jan. 2007.
- [361] G. Henkelman, A. Arnaldsson, and H. Jónsson, “A fast and robust algorithm for Bader decomposition of charge density,” *Computational Materials Science*, vol. 36, no. 3, pp. 354–360, Jun. 2006.
- [362] E. Artacho, D. Snchez-Portal, P. Ordejn, A. Garca, and J. Soler, “Linear-Scaling *ab-initio* Calculations for Large and Complex Systems,” *Physica Status Solidi B*, vol. 215, no. 1, pp. 809–817, Sep. 1999.
- [363] J. Oroya, A. Martín, M. Callejo, M. García-Mota, and F. Marchesin, *Pseudopotential and Numerical Atomic Orbitals Basis Dataset*, An online database of numerical atomic orbitals compatible with the `Siesta` code., Feb. 2020.

- [364] N. Troullier and J. L. Martins, “Efficient pseudopotentials for plane-wave calculations,” *Physical Review B*, vol. 43, no. 3, pp. 1993–2006, Jan. 1991.
- [365] V. M. Goldschmidt, “The laws of crystal chemistry,” *Die Naturwissenschaften*, vol. 14, no. 21, pp. 477–485, May 1926.
- [366] C. J. Bartel, C. Sutton, B. R. Goldsmith, R. Ouyang, C. B. Musgrave, L. M. Ghiringhelli, and M. Scheffler, “New tolerance factor to predict the stability of perovskite oxides and halides,” *Science Advances*, vol. 5, no. 2, eaav0693, Feb. 2019.
- [367] R. Resta, “Macroscopic polarization in crystalline dielectrics: the geometric phase approach,” *Reviews of Modern Physics*, vol. 66, no. 3, pp. 899–915, Jul. 1994.
- [368] J. A. Nelder and R. Mead, “A Simplex Method for Function Minimization,” *Comput. J.*, vol. 7, no. 4, pp. 308–313, Jan. 1965.
- [369] D. Sichuga and L. Bellaiche, “Epitaxial Pb(Zr, Ti)O₃ Ultrathin Films under Open-Circuit Electrical Boundary Conditions,” *Physical Review Letters*, vol. 106, no. 19, p. 196 102, May 2011.
- [370] K. Du, M. Zhang, C. Dai, Z. N. Zhou, Y. W. Xie, Z. H. Ren, H. Tian, L. Q. Chen, G. V. Tendeloo, and Z. Zhang, “Manipulating topological transformations of polar structures through real-time observation of the dynamic polarization evolution,” *Nature Communications*, vol. 10, no. 1, p. 4864, Oct. 2019.
- [371] P. Willmott, “Deposition of complex multielemental thin films,” *Prog. Surf. Sci.*, vol. 76, no. 6-8, pp. 163–217, Oct. 2004.
- [372] K.-I. Kobayashi, T. Kimura, H. Sawada, K. Terakura, and Y. Tokura, “Room-temperature magnetoresistance in an oxide material with an ordered double-perovskite structure,” *Nature*, vol. 395, no. 6703, pp. 677–680, Oct. 1998.
- [373] A. W. Sleight, J. L. Gillson, and P. E. Bierstedt, “High-Temperature Superconductivity in the BaPb_{1-x}Bi_xO₃ System,” in *Ten Years of Superconductivity: 1980–1990*, Springer Netherlands, 1993, pp. 257–258.
- [374] J. Mannhart and D. G. Schlom, “Oxide Interfaces—An Opportunity for Electronics,” *Science*, vol. 327, no. 5973, pp. 1607–1611, Mar. 2010.
- [375] W. J. Chen, Y. Zheng, and B. Wang, “Large and Tunable Polar-Toroidal Coupling in Ferroelectric Composite Nanowires toward Superior Electromechanical Responses,” *Scientific Reports*, vol. 5, no. 1, p. 11 165, Jun. 2015.
- [376] A. Tselev, P. Yu, Y. Cao, L. R. Dedon, L. W. Martin, S. V. Kalinin, and P. Maksymovych, “Microwave a.c. conductivity of domain walls in ferroelectric thin films,” *Nature Communications*, vol. 7, no. 1, May 2016.

- [377] T. Gu, T. Scarbrough, Y. Yang, J. Íñiguez, L. Bellaiche, and H. J. Xiang, “Cooperative Couplings between Octahedral Rotations and Ferroelectricity in Perovskites and Related Materials,” *Physical Review Letters*, vol. 120, no. 19, p. 97 602, May 2018.
- [378] U. Aschauer and N. A. Spaldin, “Competition and cooperation between antiferrodistortive and ferroelectric instabilities in the model perovskite SrTiO_3 ,” *Journal of Physics: Condensed Matter*, vol. 26, no. 12, p. 122 203, Mar. 2014.
- [379] A. Munkholm, S. K. Streiffer, M. V. R. Murty, J. A. Eastman, C. Thompson, O. Auciello, L. Thompson, J. F. Moore, and G. B. Stephenson, “Antiferrodistortive Reconstruction of The PbTiO_3 (001) Surface,” *Physical Review Letters*, vol. 88, no. 1, p. 016 101, Dec. 2001.
- [380] C. Bungaro and K. M. Rabe, “Coexistence of antiferrodistortive and ferroelectric distortions at the PbTiO_3 (001) surface,” *Physical Review B*, vol. 71, no. 3, p. 035 420, Jan. 2005.
- [381] M. Sepiarsky, M. G. Stachiotti, and R. L. Migoni, “Surface reconstruction and ferroelectricity in PbTiO_3 thin films,” *Physical Review B*, vol. 72, no. 1, p. 014 110, Jul. 2005.
- [382] N. Sai, B. Meyer, and D. Vanderbilt, “Compositional Inversion Symmetry Breaking in Ferroelectric Perovskites,” *Physical Review Letters*, vol. 84, no. 24, pp. 5636–5639, Jun. 2000.
- [383] M. P. Warusawithana, E. V. Colla, J. N. Eckstein, and M. B. Weissman, “Artificial Dielectric Superlattices with Broken Inversion Symmetry,” *Physical Review Letters*, vol. 90, no. 3, p. 036 802, Jan. 2003.
- [384] P. Ghosez and J. Junquera, “First-Principles Modeling of Ferroelectric Oxide Nanostructures,” *eprint arXiv:cond-mat/0605299*, May 2006.
- [385] P. García-Fernández, J. C. Wojdeł, J. Íñiguez, and J. Junquera, “Second-principles method for materials simulations including electron and lattice degrees of freedom,” *Physical Review B*, vol. 93, no. 19, p. 195 137, May 2016.
- [386] L.-Q. Chen, “Phase-Field Models for Microstructure Evolution,” *Annual Review of Materials Research.*, vol. 32, no. 1, pp. 113–140, Aug. 2002.
- [387] P. Shafer, P. García-Fernández, P. Aguado-Puente, A. R. Damodaran, A. K. Yadav, C. T. Nelson, S.-L. Hsu, J. C. Wojdeł, J. Íñiguez, L. W. Martin, E. Arenholz, J. Junquera, and R. Ramesh, “Emergent chirality in the electric polarization texture of titanate superlattices,” *Proceedings of the National Academy of Sciences U.S.A.*, vol. 115, no. 5, pp. 915–920, Jan. 2018.

- [388] J. B. J. Chapman, A. V. Kimmel, and D. M. Duffy, “[Novel high-temperature ferroelectric domain morphology in PbTiO₃ ultrathin films](#),” *Physical Chemistry Chemical Physics*, vol. 19, no. 6, pp. 4243–4250, Jan. 2017.
- [389] M. Sepiarsky, M. G. Stachiotti, and R. L. Migoni, “[Interface Effects in Ferroelectric PbTiO₃ Ultrathin Films on a Paraelectric Substrate](#),” *Physical Review Letters*, vol. 96, no. 13, p. 137 603, Apr. 2006.
- [390] L. Bengtsson, “[Dipole correction for surface supercell calculations](#),” *Physical Review B*, vol. 59, no. 19, pp. 12 301–12 304, May 1999.
- [391] H. Hotelling, “[Some New Methods in Matrix Calculation](#),” *The Annals of Mathematical Statistics*, vol. 14, no. 1, pp. 1–34, Mar. 1943.
- [392] B. Meyer and D. Vanderbilt, “[Ab initio study of ferroelectric domain walls in PbTiO₃](#),” *Physical Review B*, vol. 65, no. 10, p. 104 111, Mar. 2002.
- [393] A. I. Lebedev, “[Ab initio calculations of phonon spectra in ATiO₃ perovskite crystals \(A = Ca, Sr, Ba, Ra, Cd, Zn, Mg, Ge, Sn, Pb\)](#),” *Physics of the Solid State*, vol. 51, no. 2, pp. 362–372, Feb. 2009.
- [394] F. W. Lytle, “[X-Ray Diffractometry of Low-Temperature Phase Transformations in Strontium Titanate](#),” *Journal of Applied Physics*, vol. 35, no. 7, pp. 2212–2215, Jul. 1964.
- [395] E. Heifets, E. Kotomin, and V. Trepakov, “[Calculations for antiferrodistortive phase of SrTiO₃ perovskite: hybrid density functional study](#),” *Journal of Physics: Condensed Matter*, vol. 18, no. 20, p. 4845, May 2006.
- [396] Y. Umeno, T. Shimada, T. Kitamura, and C. Elsässer, “[Ab initio density functional theory study of strain effects on ferroelectricity at PbTiO₃ surfaces](#),” *Physical Review B*, vol. 74, no. 17, p. 174 111, Nov. 2006.
- [397] M. D. Glinchuk, A. N. Morozovska, and E. A. Eliseev, “[Correlation Radius in Thin Ferroelectric Films](#),” *Ferroelectrics*, vol. 400, no. 1, pp. 243–254, Sep. 2010.
- [398] C. Lichtensteiger, J.-M. Triscone, J. Junquera, and P. Ghosez, “[Ferroelectricity and Tetragonality in Ultrathin PbTiO₃ Films](#),” *Physical Review Letters*, vol. 94, no. 4, p. 047 603, Feb. 2005.
- [399] G. Stephenson, D. Fong, M. R. Murty, S. Streiffer, J. Eastman, O. Auciello, P. Fuoss, A. Munkholm, M. Aanerud, and C. Thompson, “[In situ X-ray studies of vapor phase epitaxy of PbTiO₃](#),” *Physica B: Condens. Matter*, vol. 336, no. 1-2, pp. 81–89, Aug. 2003.
- [400] M. Prutton, *Introduction to surface physics*. Clarendon Press Oxford, 1994, p. 58.

- [401] Y. Sun, A. Y. Abid, C. Tan, C. Ren, M. Li, N. Li, P. Chen, Y. Li, J. Zhang, X. Zhong, *et al.*, “[Subunit cell-level measurement of polarization in an individual polar vortex](#),” *Science Advances*, vol. 5, no. 11, eaav4355, Nov. 2019.
- [402] J. Sifuna, P. García-Fernández, G. S. Manyali, G. Amolo, and J. Junquera, “[First-principles study of two-dimensional electron and hole gases at the head-to-head and tail-to-tail 180° domain walls in PbTiO₃ ferroelectric thin films](#),” *Physical Review B*, vol. 101, no. 17, p. 174 114, May 2020.
- [403] J. Hong and D. Vanderbilt, “[First-principles theory of frozen-ion flexoelectricity](#),” *Physical Review B*, vol. 84, no. 18, 180101(R), Nov. 2011.
- [404] J. Hong and D. Vanderbilt, “[First-principles theory and calculation of flexoelectricity](#),” *Physical Review B*, vol. 88, no. 17, p. 174 107, Nov. 2013.
- [405] M. Stengel, “[Flexoelectricity from density-functional perturbation theory](#),” *Physical Review B*, vol. 88, no. 17, p. 174 106, Nov. 2013.
- [406] C. E. Dreyer, M. Stengel, and D. Vanderbilt, “[Current-density implementation for calculating flexoelectric coefficients](#),” *Physical Review B*, vol. 98, no. 7, p. 075 153, Aug. 2018.
- [407] A. Schiaffino, C. E. Dreyer, D. Vanderbilt, and M. Stengel, “[Metric wave approach to flexoelectricity within density functional perturbation theory](#),” *Physical Review B*, vol. 99, no. 8, p. 085 107, Feb. 2019.
- [408] M. Royo and M. Stengel, “[First-Principles Theory of Spatial Dispersion: Dynamical Quadrupoles and Flexoelectricity](#),” *Physical Review X*, vol. 9, no. 2, p. 021 050, Jun. 2019.
- [409] M. R. Hestenes, E. Stiefel, *et al.*, “[Methods of conjugate gradients for solving linear systems](#),” *Journal of research of the National Bureau of Standards*, vol. 49, no. 6, pp. 409–436, Dec. 1952.
- [410] E. G. del Río, J. J. Mortensen, and K. W. Jacobsen, “[Local Bayesian optimizer for atomic structures](#),” *Physical Review B*, vol. 100, no. 10, p. 04 103, Sep. 2019.